UNIVERSIDADE ESTADUAL DE CAMPINAS
FACULDADE DE ENGENHARIA QUÍMICA

RODRIGO DE LIMA AMARAL

ANÁLISE DA QUALIDADE DE MEDIDAS 2D-2C E 2D-3C F-PIV DA VELOCIDADE DA FASE LÍQUIDA EM UMA COLUNA DE BOLHAS

QUALITY ANALYSIS OF 2D-2C AND 2D-3C F-PIV MEASUREMENTS OF THE LIQUID PHASE VELOCITY IN A BUBBLE COLUMN

Campinas, 2017

RODRIGO DE LIMA AMARAL

QUALITY ANALYSIS OF 2D-2C AND 2D-3C F-PIV MEASUREMENTS OF THE LIQUID PHASE VELOCITY IN A BUBBLE COLUMN

ANÁLISE DA QUALIDADE DE MEDIDAS 2D-2C E 2D-3C F-PIV DA VELOCIDADE DA FASE LÍQUIDA EM UMA COLUNA DE BOLHAS

Thesis presented to the School of Chemical Engineering of the University of Campinas as part of the in partial fulfillment of the requirements for the degree of Doctor in Chemical Engineering.

Tese apresentada à Faculdade de Engenharia Química da Universidade Estadual de Campinas como parte dos requisitos exigidos para a obtenção do título de Doutor em Engenharia Química.

Adviser: Prof. Dr. Sávio Souza Venâncio Vianna

Co-Adviser: Prof. Dr. Guilherme Jose de Castilho

ESTE EXEMPLAR CORRESPONDE À VERSÃO FINAL TESE DEFENDIDA PELO ALUNO RODRIGO DE LIMA AMARAL, ORIENTADA PELO PROF. DR. SÁVIO SOUZA VENÂNCIO VIANNA E CO-ORIENTADA PELO PROF. DR. GUILHERME JOSE DE CASTILHO

Campinas 2017

Agência(s) de fomento e nº(s) de processo(s): CAPES, 2296/2013

Ficha catalográfica
Universidade Estadual de Campinas
Biblioteca da Área de Engenharia e Arquitetura
Luciana Pietrosanto Milla - CRB 8/8129

Amaral, Rodrigo de Lima, 1988 -
Am13q Quality analysis of 2D-2C and 2D-3C F-PIV measurements of the liquid phase velocity in a bubble column. / Rodrigo de Lima Amaral. – Campinas, SP: [s.n.], 2017.

Orientador: Sávio Souza Venâncio Vianna.
Coorientador: Guilherme José de Castilho.
Tese (doutorado) – Universidade Estadual de Campinas, Faculdade de Engenharia Química.

1. Controle de qualidade. 2. Escoamento multifásico. 3. Velocidade. 4. Dinâmica dos fluídos - Médição. 5. Desenvolvimento experimental. I. Vianna, Sávio Souza Venâncio,1975-. II. Castilho, Guilherme José de,1983-. III. Universidade Estadual de Campinas. Faculdade de Engenharia Química. IV. Título.

Informações para Biblioteca Digital

Título em outro idioma: Análise da qualidade de medidas 2D-2C e 2D-3C F-PIV da velocidade da fase líquida em uma coluna de bolhas
Palavras-chave em inglês:
Quality control
Multiphase flow
Speed
Fluid dynamics - Measurement
Experimental development
Área de concentração: Engenharia Química
Titulação: Doutor em Engenharia Química
Banca examinadora:
Sávio Souza Venâncio Vianna [Orientador]
Ana Cristina Avelar Batista de Jesus
Erick de Moraes Franklin
João Felipe Mitre de Araujo
Dirceu Noriler
Data de defesa: 26-05-2017
Programa de Pós-Graduação: Engenharia Química

A Banca Examinadora composta pelos membros abaixo aprovou esta tese:

Prof. Dr. Sávio Souza Venâncio Vianna
Instituição: Universidade Estadual de Campinas (UNICAMP)

Profa. Dra. Ana Cristina Avelar Batista de Jesus
Instituição: Instituto Tecnológico da Aeronáutica/São José dos Campos (ITA)

Prof. Dr. João Felipe Mitre de Araujo
Instituição: Universidade Federal Fluminense/Niterói (UFF)

Prof. Dr. Erick de Moraes Franklin
Instituição: Universidade Estadual de Campinas (UNICAMP)

Prof. Dr. Dirceu Noriler
Instituição: Universidade Estadual de Campinas (UNICAMP)

A Ata de Defesa com as respectivas assinaturas dos membros encontra-se no processo de vida acadêmica do aluno

Aos meus pais, Roberta Lopes de Lima e Francisco de Assis Amaral Lopes, por tudo.

A Grasiela de Sousa Lopes, minha vó, por sempre ter sido uma referência na Família.

A Renata de Lima Amaral, minha irmã, e a Sophia de Lima Amaral, minha sobrinha.

Aos meus familiares e amigos pela torcida e incentivo.

AGRADECIMENTOS

Ao meu orientador, Prof. Dr. Sávio Souza Venâncio Vianna, pela oportunidade e por ter confiado no meu trabalho desde o começo. Também o agradeço pela orientação e por toda liberdade que me foi dada, fundamental no desenvolvimento deste trabalho.

Ao meu co-orientador, Prof. Dr. Guilherme Jose de Castilho, pela parceria desde 2011. Além da liberdade, sua contribuição foi fundamental no desenvolvimento desse e de todos os trabalhos relacionados a esse.

Ao Prof. Dr. Milton Mori, coordenador do projeto, por ter sido uma referência para mim. Além disso, pelas conversas e por todo suporte no desenvolvimento desse e de todos os trabalhos relacionados a esse.

À CAPES pelo suporte financeiro (2296/2013).

À Unicamp e à Faculdade de Engenharia Química pela estrutura e oportunidade cedida.

À PETROBRAS pelo suporte financeiro relativo ao projeto (0050.0070828.11.9).

Ao meu amigo/irmão, Helder Lima de Moura, por me acompanhar nessa luta desde 2005 e pela parceria nesse projeto. Sua contribuição foi decisiva no sucesso desse trabalho.

Aos amigos Raphael Ribeiro, Harrson Santana, Hugo Valença, Erik "China", Jean, Ivanei "Miguelis", Vicente, Alex "Plancknelson", Dira, Diogo "Balotelli", Ana "Chefa", Bruno Guzzo, Murilo Ferrari, Rhelvis Oliveira, "Clairone Cigano", Mateus "Tchê" e, em especial, a Carlos "Maranhão" pelo companheirismo, amizade, pelas risadas e pelas brincadeiras.

A Giovanna Melo e família por toda tranquilidade na etapa final desse projeto.

A Anna Csoknyai Guimarães, minha segunda mãe.

Aos meus colegas do laboratório de Processos Químicos e Gestão empresarial (LPQGe), Diana, Karina, João, José, Daniel, Tatiele e Victor.

A Fábio Savassi e Jairo Rotava da Quantum Tech pelo suporte técnico e por toda ajuda.

A Alcimar da Silveira pela parceria no desenvolvimento da estrutura das câmeras.

"A engenharia é fascinante: ou é 8 ou é 90!"

Celso Martins Ramos

RESUMO

A análise da fluidodinâmica em reatores de coluna de bolha é importante na compreensão dos mecanismos relacionados à transferência de calor, transferência de massa e taxa de reação química. A precisão das medições experimentais depende diretamente do domínio de medição. A Velocimetria por imagem de partículas (PIV) é uma técnica não intrusiva utilizada para determinar o campo de velocidade 2D ou 3D. Um campo 2D-3C (bidimensional, três componentes) pode ser determinado por duas câmaras com projeções diferentes numa disposição estereoscópica (PIV 2D-3C). A perda de correlação devido ao movimento fora do plano de pares de imagens de partículas, que é comum em aplicações PIV, pode ser reduzida usando o sistema PIV 2D-3C. Um problema encontrado nas aplicações 2D-3C PIV está relacionado com o acesso óptico em algumas instalações. Para determinar a velocidade da fase líquida, não é interessante registrar as bolhas no escoamento multifásico. Por conseguinte, as partículas traçadoras fluorescentes combinadas com um filtro passa-alta na câmara são utilizadas nos sistemas *Fluorescent* PIV (F-PIV). Este trabalho tem como objetivo avaliar a qualidade das medidas 2D-2C e 2D-3C F-PIV da velocidade da fase líquida no regime de escoamento homogêneo e de transição homogêneo-heterogêneo de uma seção de coluna de bolha. As imagens 2D-2C e 2D-3C F-PIV foram processadas utilizando *standard cross-correlation* (SCC), *ensemble correlation* (EC) e *sliding-average correlation* (SAC) para comparar a qualidade das medições. O coeficiente de correlação cruzada, a relação sinal-ruído (SNR) e a quantificação de incerteza PIV estimada por estatísticas de correlação foram utilizados como indicadores de qualidade. A baixa concentração de imagem de partícula (baixa *ppp*) e a baixa faixa dinâmica de velocidade (baixa DVR) foram identificadas como fontes de ruído dominante nas medidas PIV. O efeito do baixo *ppp* foi relacionado diretamente com o comportamento dos indicadores de qualidade baseados na conectividade de vizinhança espacial, erro de reconstrução 3C e no diâmetro do pico de correlação. Quanto às condições de qualidade da abordagem SCC, foram obtidos cinco limites que garantem que os *outliers* (falsos vetores) podem ser corrigidos sem que o campo vetorial perca a representatividade do escoamento. No regime de escoamento homogêneo, os ruídos randômicos causados pela baixa *ppp* foram consideravelmente reduzidos utilizando a abordagem SAC.

Palavras-chave: 2D-2C F-PIV; 2D-3C F-PIV; Ruído; Coluna de bolhas, Análise de qualidade.

ABSTRACT

The fluid dynamics analysis in bubble column reactors is important in understanding the mechanisms related to heat transfer, mass transfer and chemical reaction rate. The accuracy of the experimental measurements depends directly on the measurement domain. Particle image velocimetry (PIV) is a non-intrusive technique used to determine the 2D or 3D velocity field. A 2D-3C (two dimensional, three-component) field can be determined by two cameras with different projections in a stereoscopic arrangement (2D-3C PIV). The loss of correlation due to the out-of-plane motion of pairs of particle images, which is common in PIV applications, can be reduced using the 2D-3C PIV system. A problem encountered in 2D-3C PIV applications is related to optical access in some facilities. In order to determine the liquid phase velocity, it is not interesting to record bubbles in the multiphase flow. Therefore, fluorescent tracer particles combined with a high-pass filter on the camera are used in the Fluorescent PIV (F-PIV) systems. This work aims to evaluate the quality of the 2D-2C and 2D-3C F-PIV measurements of the liquid phase velocity in the homogeneous and homogeneous-heterogeneous transition flow regime of a bubble column. The 2D-2C and 2D-3C F-PIV images were processed using standard cross-correlation (SCC), ensemble correlation (EC), and sliding-average correlation (SAC) to compare the measurements quality. The cross-correlation coefficient, signal-to-noise ratio (SNR) and PIV uncertainty estimated by correlation statistics were used as quality indicators. The low particle image concentration (low *ppp*) and low dynamic velocity range (low DVR) were identified as dominant noise sources in the PIV measurements. The effect of the low *ppp* was directly related to the behavior of the quality indicators based on the spatial neighborhood connectivity, 3C reconstruction error, and correlation peak diameter. Regarding the quality conditions for SCC approach, five limits were obtained that guarantee that the outliers can be corrected without the vector field losing the representativeness of the flow. In the homogeneous flow regime, the random noise caused by low *ppp* was considerably reduced using the SAC approach.

Keywords: 2D-2C F-PIV; 2D-3C F-PIV; Noise; Bubble column, Quality analysis.

NOMENCLATURE

Roman symbols

d_i	Distance between the effective center of the lens and the image plane (m).
D_I	Interrogation window size (pixel)
d_o	Distance between the object and the effective center of the lens (m)
d_p	Diameter of the tracer particle (m)
d_t	Interframe time (s)
$d\tau$	Particle image diameter (pixel)
F_Δ	Loss of correlation due to local variation of the displacement
F_0	Loss of correlation due to the out-of-plane motion
F_I	Loss of correlation due to the in-plane motion
I	Intensities in the image (count)
L_X	Size of the recording medium in X direction (pixel)
L_Y	Size of the recording medium in Y direction (pixel)
M	Mapping function
M_0	Image magnification
N_I	Particle image density per interrogation window
ppp	Particle image concentration (particle per pixel)
r	Radial position (m)
R	Radius of the bubble column (m)
R_C	Average background correlation
R_D	Correlation peak of the particle images displacement
R_F	Correlation due to the random movement of particle images
s	Position vector in the correlation plane (m)
Sk	Stokes' number
t	Time (s)
u	Radial component in-plane of velocity (m/s)
u	Velocity modulus (m/s)
$\Delta\mathbf{u}$	Local variation of velocity
U_G	Superficial gas velocities (m/s)

$\Delta U_{max\text{-}min}$	Difference between the maximum and minimum velocity of the flow (m/s)
UQ	Quantification of PIV uncertainty (m/s)
$UQ_{\mathbf{u}}$	UQ for the velocity modulus (m/s)
UQ_x	UQ for the radial component in-plane of velocity (m/s)
UQ_x*	UQ_x normalized by the radial component in-plane of velocity (-)
UQ_y	UQ for the axial component in-plane of velocity (m/s)
UQ_y*	UQ_y normalized by the axial component in-plane of velocity (-)
v	Axial component of velocity (m/s)
w	Radial component out-of-plane of velocity (m/s)
$\Delta \boldsymbol{X}$	Particle image displacement (pixel)
$\Delta x_{p.max}$	Minimum scale can be resolved by PIV
ΔZ	Out-of-plane motion (pixel)
ΔZ_0	Thickness of the light sheet (m).

Greek Symbols

ε_{bias}	Bias error (pixel)
$\varepsilon_{Max3C\text{-}R}$	Allowed maximum error of 3C reconstruction (pixel)
ε_r	Ratio of the average random error of the out-of-plane component by in-plane component
ℓ	The smallest resolved length scale (m)
θ	Camera angle in a stereoscopic configuration (degrees)
λ	Wavelength (nm)
μ	Dynamic viscosity of the fluid (N s/m^2)
ρ	Density of the fluid (Kg/m^3)
ρ_p	Density of the tracer particle (Kg/m^3)
σ	Standard deviation
τ_f	Characteristic time scale of the flow (s)
τ_p	Relaxation time of the tracer particle (s)

Abbreviations

C	Component

CCC	Cross-correlation coefficient
CCD	Charge-coupled device
CFD	Computational fluid dynamics
CS	Correlation statistics
D	Dimension
DSR	Dynamic spatial range
DVR	Dynamic velocity range
EC	Ensemble correlation
FoV	Field of view
F-PIV	Fluorescent particle image velocimetry
IW	Interrogation window
LOS	Line-of-sight
Nd:YAG	Neodymium-doped yttrium aluminum garnet
PDF	Probability density function
PIV	Particle image velocimetry
PPR	Primary peak ratio
PTU	Programmable time unit
RMS	Root mean square
SAC	Sliding-average correlation
SCC	Standard cross-correlation
SCC*	SCC with PIV post-processing
SNR	Signal-to-noise ratio
SSM	Subtract sliding minimum

LIST OF FIGURES

LIST OF TABLES

CONTENTS

CHAPTER 1.

INTRODUCTION

Bubble columns are intensively used as multiphase contactors and reactors in chemical, biochemical and petrochemical industries. They offer several advantages in respect to the high heat and mass transfer rates, compactness and low cost of operation and maintenance. Among the main advantages of the use of bubble columns compared with other multiphasic contactors are the less maintenance due to the absence of moving parts and the achievement of high values of effective interfacial area, overall mass and heat transfer coefficients. Moreover, with the use of bubble columns it is possible to avoid any problem of clogging or erosion with solids handling besides occupying less floor space, making the reactors cheaper. A relevant characteristic of the bubble columns is that slow reactions can be performed due to the large residence time of the liquid phase (Levich, 1962; Shah *et al*., 1982; Hyndman *et al*., 1997; Kantarci *et al.*, 2005; Mudde, 2005). The accuracy and success of the design and scale-up of the bubble column requires a better understanding of the dynamics of multiphase flow and its influence on the bubble distribution (hold up), mixing and transport characteristics of the phases involved. Therefore, accurate investigations using computational fluid dynamics (CFD) and experimental data are needed (Degaleesan *et al.*, 2001). Particle image velocimetry (PIV) is a non-intrusive technique often employed in determining the velocity field of multiphase flows. PIV has been used for over 30 years as a non-intrusive measurement technique to analyze various types of flows, but there is still a lack of robust quantification of the measurement uncertainty to guarantee reliable experimental data (Wieneke, 2014; Wieneke, 2015).

According to Oberkampf and Roy (2010), the use of data with unknown uncertainty for validation of a numerical model exposes the researcher to two risks: (1) the rejection of a good model or, even more worrying (2) the acceptance of a bad model based on erroneous data, which can be used later in making a crucial decision. Most existing flows in industrial processes are completely 3D. The representation of the flow by a set of experimental measurements is directly related to the measurement domain. In general, PIV technique can be classified

depending on the measurement domain (dimension, D, and component, C) of the velocity distribution: 2D-2C (classic 2D PIV), 2D-3C (stereo-PIV) and 3D-3C PIV (holographic-PIV and tomographic-PIV). The PIV performance depends mainly on the concentration of tracer particles, particle image diameter, quality of the recorded images and processing. 2D-2C PIV uses one camera generally oriented at 90 degrees from the illuminated plane. The resulting 2D-2C vector field suffers from two deficiencies: (1) the out-of-plane velocity component is lost and (2) the in-plane velocity components present perspective error. Stereoscopic imaging (2D-3C PIV) eliminates both the deficiencies above. Simultaneous views from two different off-axis directions provide sufficient information to extract the out-of-plane component as well as to correct errors in the in-plane components. A problem encountered in 2D-3C PIV applications is the restricted optical access in some facilities allowing only the use of 2D-2C PIV (Prasad and Jensen, 1995; Prasad, 2000; Raffel *et al.*, 2007; Adrian and Westerweel, 2011).

In bubble columns, a major problem of PIV applications is the large laser light scattering by the bubbles in relation to the tracer particles, which may damage the camera sensor. To avoid this problem, fluorescent tracer particles and a high-pass filter on the camera are used to allow only the passage of light scattered by the tracer particles in the liquid phase. Even using a high-pass filter, usually recorded images still present an unequal intensity distribution in the frame (complete image) interfering on the accuracy of the velocity distribution (Northrup *et al*., 1991; Lindken and Merzkirch, 2002). The PIV technique that uses fluorescent tracer particles and high-pass filter is known as Fluorescent PIV (F-PIV). In addition, the presence of the bubbles contributes directly to uneven lighting inside the column forming regions with shadows mainly for high superficial gas velocities. In addition, the distortion caused by the curvature of the column can cause position and velocity errors.

1.1.GENERAL GOALS

This work aims to evaluate the quality of the 2D-2C and 2D-3C F-PIV measurements in a bubble column section. The velocity fields were determined by the standard cross-correlation (SCC) approach for a superficial gas velocity (U_G) of 0.152, 0.528, 2.106, and 4.212 cm/s. The quality of the velocity modulus and components of the liquid phase is analyzed by means of cross-correlation coefficient, signal-to-noise ratio (SNR), spatial coherence, and uncertainty estimated using correlation statistics. Besides that, the fields determined by the SCC and ensemble correlation (EC) approaches were compared to analyze the measurement quality. In

addition, the sliding-average correlation (SAC) was used to investigate in detail the noise effect in the average field. The effect of a spatial filter in post-processing was also investigated.

1.2.SPECIFIC GOALS

The specific goals of this work are:

- Optimize the PIV experimental set up;
- Determine the distribution of PIV quality indicators;
- Relate the PIV quality indicators with the false vectors present in the velocity field;
- Investigate the effect of the main noisy sources of the experiments;
- Investigate the quality of the PIV measurements for different U_G;
- Compare the 2D-2C and 2D-3C F-PIV measurements;
- Evaluate the effect and performance of the PIV post-processing on the velocity field;
- Investigate the noise effect on the instantaneous and average fields for both techniques.
- Optimize the PIV processing;

1.3.OUTLINE OF THIS THESIS

This work is divided in 7 chapters, according to the order summarized below:

Chapter 1 presents a brief introduction regarding the importance and challenges of the PIV applications in bubble column. The motivations and the aim of this study are also shown.

Chapter 2 presents the working principle and the main components of the 2D-2C and 2D-3C F-PIV systems. The main sources of noise and PIV quality indicators are also discussed.

Chapter 3 presents the main PIV applications in bubble column. Different experimental configurations, image processing and limitations of the technique are detailed.

Chapter 4 presents the characteristics of the investigated bubble column and the F-PIV systems used in this work. In addition to the experimental conditions, a preliminary test of the camera set up is discussed in detail.

Chapter 5 presents the image analysis settings. Parameters for the PIV preprocessing, processing and post-processing are detailed.

Chapter 6 presents the results and discussion of the quality analysis of the F-PIV measurements in the bubble column. The effects of the main noise sources are analyzed in the instantaneous and averaged fields for both techniques.

Chapter 7 presents the conclusions and recommendations for future work.

CHAPTER 2.

2D-2C AND 2D-3C PIV SYSTEM

This chapter presents the working principle and basic concepts of the image analysis of 2D-2C and 2D-3C PIV systems. In addition, errors and noise sources in PIV recording and analysis are detailed.

The imaging of 2D-3C systems to solve the perspective error in 2D-2C systems is discussed. Moreover, the principle of reconstruction of the third velocity component is detailed.

The method of uncertainty quantification based on correlation statistics and the propagation of uncertainty for the average fields are also presented and detailed.

All the concepts presented in this chapter are important in understanding the experimental set ups and in the image processing presented in Chapters 3, 4 and 5.

2.1.PRINCIPLE

The working principle of the 2D-2C and 2D-3C PIV system is schematically represented in Figure 2.1. Basically, the PIV analysis can be divided into five steps: calibration, recording, image preprocessing, processing (PIV correlation and 3C reconstruction), and post-processing (Raffel *et al.*, 2007; Adrian and Westerweel, 2011).

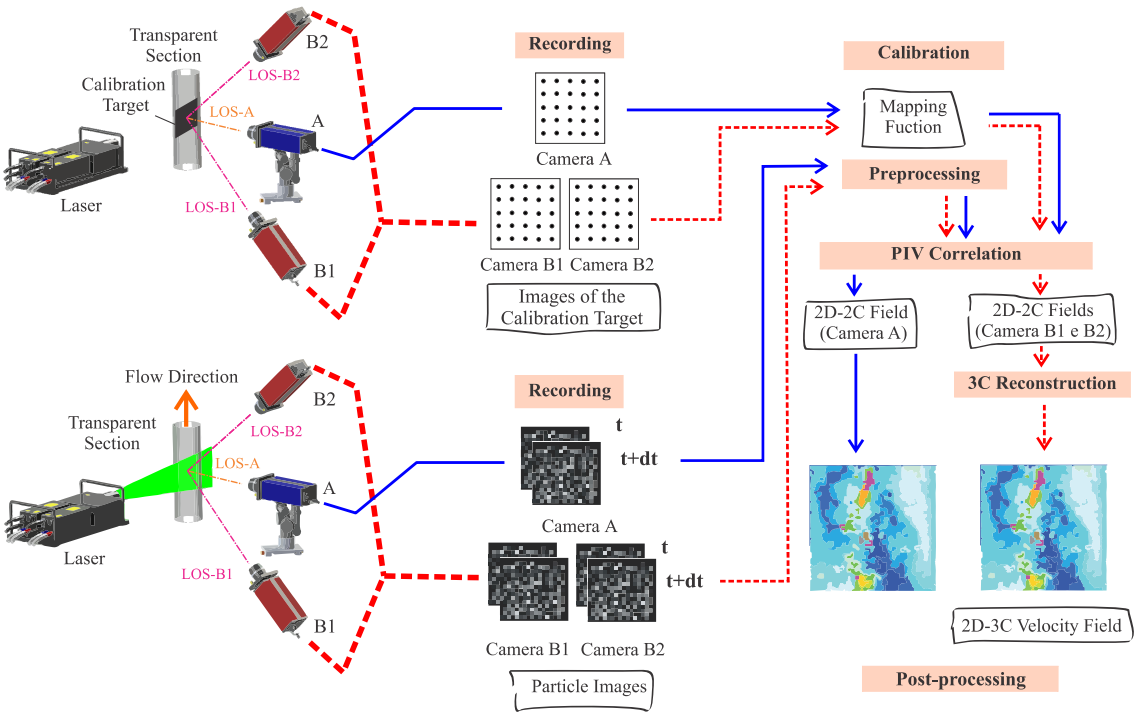

Figure 2.1 - Working principle of the (—) 2D-2C and (– –) 2D-3C PIV system.

The technique employs tracer particles that must faithfully follow the flow allowing for the calculation of the velocity based on the instantaneous position of the tracer population. Generally, the particles are illuminated by a laser light source and are homogeneously distributed in flow. The light scattered by the particles is registered on the camera sensor located at 90° from the light sheet so that the object plane in focus coincides with the slice illuminated in flow (Figure 2.2a). The recorded images are transferred to a computer for PIV analysis. Instead of determining the displacement of individual particle images, the PIV analysis determines the moving average of small populations of particle images contained in regions known as interrogation windows (IW) providing a displacement vector per window (Figure 2.2b). This procedure is known as PIV interrogation (Soloff *et al.*, 1997; Raffel *et al.*, 2007; Adrian and Westerweel, 2011).

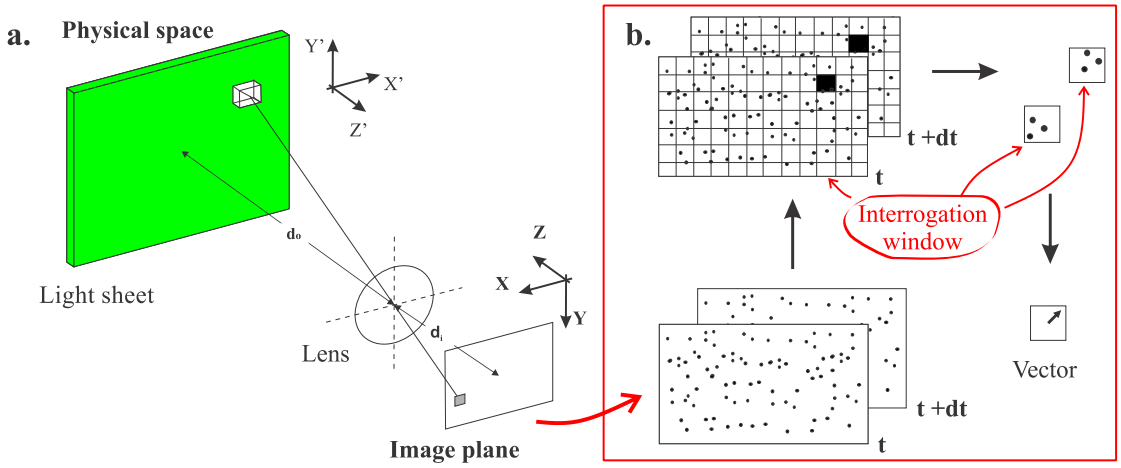

Figure 2.2 – Representation of the (a) geometric image and (b) PIV interrogation (Adapted from Amaral, 2013).

The essence of PIV image is precisely to map the location of each particle (object plane or physical space) in the image plane in a calibration procedure. The image magnification is defined as $M_0 = di/do$, where d_i is the distance between the effective center of the lens and the image plane and d_o is the distance between the object and the effective center of the lens (Figure 2.2a). The mapping should be an M function (known as mapping function) that relates the three-dimensional location of the particle in the flow field with the image plane. There are several ways to determine this function. For example, in a calibration procedure the least squares method can be used to determine a mapping function that approximates the data (the points of a target plate) and then minimize the mean square error (Soloff *et al.*, 1997; Raffel *et al.*, 2007; Adrian and Westerweel, 2011).

The calibration steps are shown in Figure 2.3. The calibration process can be performed manually by the previous orientation of the line-of-sight (LoS) of the camera targeting the calibration target. Therefore, the camera lens require adjustment in order to avoid the generation of blurry images. In general, different experiments may require different calibration targets. The inaccuracies in PIV calibration may be caused by optical distortion due to inaccurate optical alignment, imperfection in lens design, refraction of optical windows, fluid interfaces and other optical elements in an experiment. In 2D-3C PIV calibration, the mapping of two planes is needed for each camera, totaling two mapping functions per camera. Projections of the velocity vectors on each camera, which correspond to the same real displacements, are associated. The three velocity components are represented by the matrices M_{B1} and M_{B2} of each camera (Soloff *et al.*, 1997; Raffel *et al.*, 2007; Adrian and Westerweel, 2011).

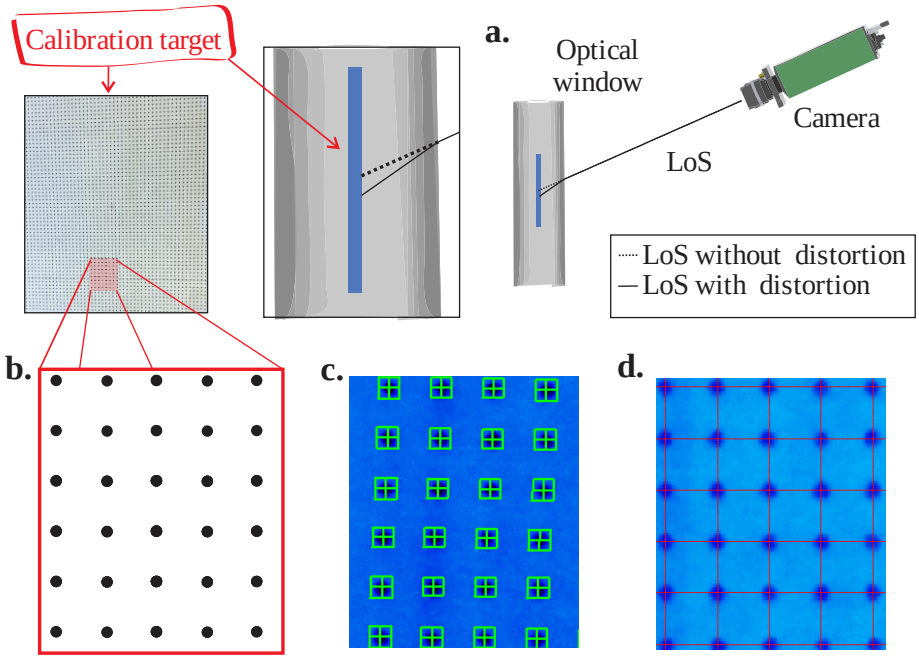

Figure 2.3 – Calibration steps. (a) PIV recording process for a single camera with nonzero distortion. (b) Points of the calibration plate. (c) Identification of the points and (c) and adjustment of the "mapping function" (red lines) by software Davis 8.2.

In the double-frame recording, a PIV algorithm (usually the standard cross-correlation, SCC) is used to correlate the particle images at two different instants of time. The PIV correlation plane (Figure 2.4) represents the probability distribution of all possible patterns of particle image displacement between consecutive frames and it may be written by Eq. 2.1. This plane presents a combination of the effects of various errors that govern the accuracy of the particle image displacement pattern. In Eq. 2.1, R_D is the correlation peak of the particle images displacement, R_C is the average background correlation and R_F is the correlation due to the random fluctuation in the interrogation window. The PIV preprocessing aims to increase the image quality obtained in recording before making the calculation of PIV cross-correlation in the processing. The choice of the image treatment using spatial and temporal filters performed in the preprocessing can improve or harm the information contained in recording. In 2D-3C PIV system, the 2D-2C vector fields of each camera are reconstructed to obtain the third velocity component. The reconstruction quality of the third velocity component (also called 3C reconstruction or Stereo reconstruction) depends on the accuracy of the 2D-3C PIV calibration. The 3C reconstruction is accurate when the calibrated image is aligned with the object plane (illuminated plane) (Adrian, 1991; Soloff *et al.*, 1997; Prasad, 2000; Raffel *et al.*, 2007; Adrian and Westerweel, 2011).

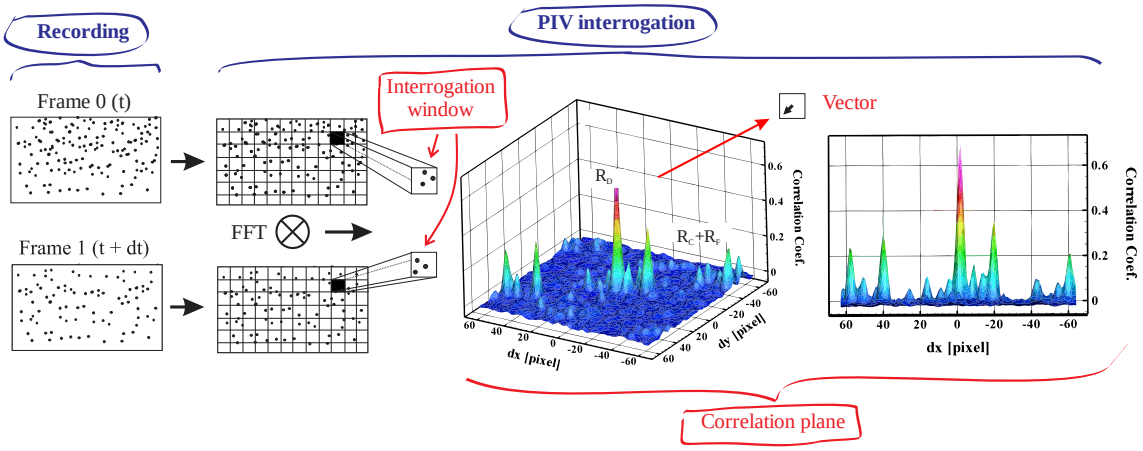

Figure 2.4 - Correlation peak of the particle images displacement (R_D) and noise sources (R_C and R_F) in the correlation plane for an interrogation window size of 128 pixels.

$$R(s,t) = R_C(s,t) + R_F(s,t) + R_D(s,t) \tag{2.1}$$

The SCC approach is used to determine the instantaneous flow fields for analysis of the turbulent parameters and average distribution. A disadvantage of the SCC approach is that the fields are easily degraded in the presence of noise. However, the ensemble correlation (EC) approach is more robust but only determines the average fields (Figure 2.5). This approach sums the $R(s,t)$ (Eq. 2.1) in time before the calculation of the vector field. The quality of the average field estimated by the EC depends directly on the number of frames used. The EC approach can be used to analyse the quality of the processing by the SCC one. If the fields processed by the SCC are free of noise, then the average fields determined by the SCC and EC are equal (Meihart *et al.*, 2000; Raffel *et al.*, 2007; Adrian and Westerweel, 2011).

The sliding-average correlation (SAC) approach was applied by Scarano *et al.* (2010) to increase the measurement accuracy of the velocity fluctuations. This approach can reduce the random component of the measurement error by averaging the correlation functions of a small temporal kernel, k (Figure 2.6). When $k\Delta t \ll \tau$ (is τ the characteristic time scale of the flow fluctuations), the result can be regarded as instantaneous (Sciacchitano, 2014). Effect of the SCC and SAC approach in a time series is presented in Figure 2.7.

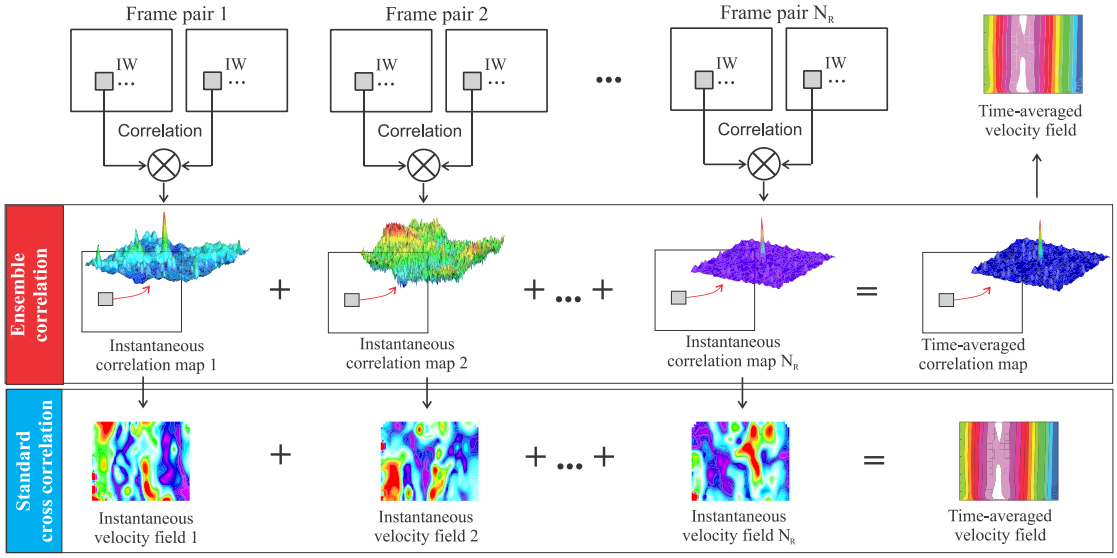

Figure 2.5 - Comparison between the ensemble correlation (EC) and standard cross-correlation (SCC) approach.

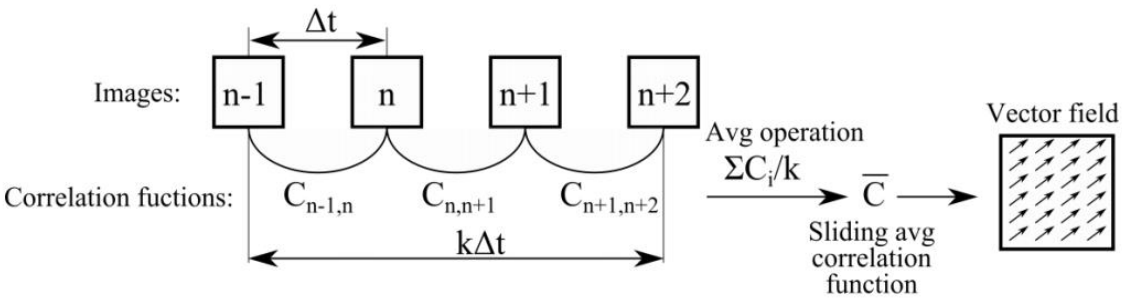

Figure 2.6 - Scheme of the sliding-average correlation (Sciacchitano, 2014)

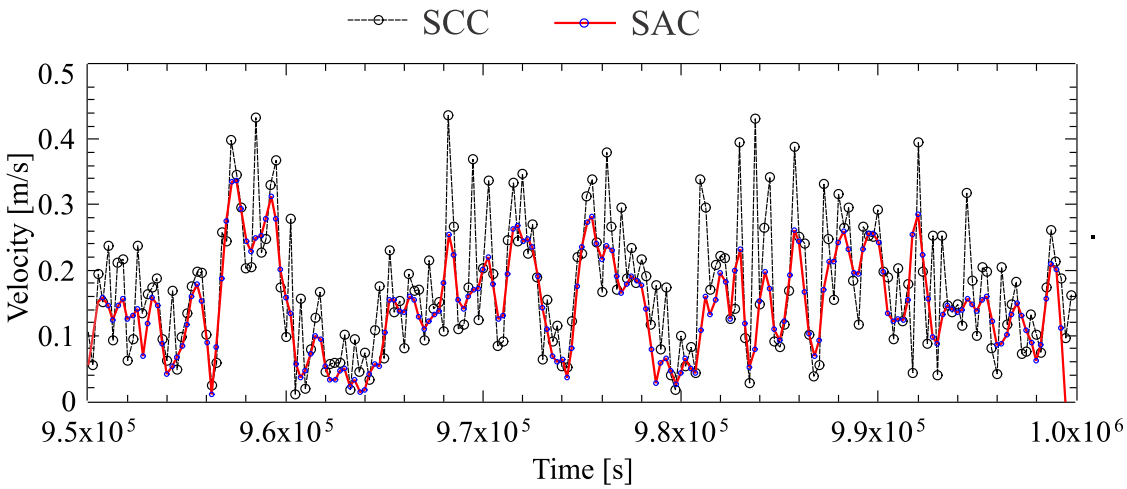

Figure 2.7 – Effect of the SCC and SAC approach in a time series.

In a noiseless field, the velocity value in the interrogation window varies smoothly between its neighborhoods. However, in PIV measurements it is difficult to avoid the presence of false vectors in the field. The neighborhood connectivity is the basis for the development of spatial and temporal filters in PIV post-processing. Post-processing filters based on the spatial and temporal coherence may fail in the presence of false vectors groups (outlier clusters). A measurement is said to be spatial and temporal coherent when its distribution varies smoothly (in space and time) between adjacent interrogation windows (Raffel *et al.*, 2007; Adrian and Westerweel, 2011; Sciacchitano, 2014; Masullo and Theunissen, 2016). The effect of the PIV post-processing on fields with outliers (false vectors that are easily detected) can be seen in Figure 2.8.

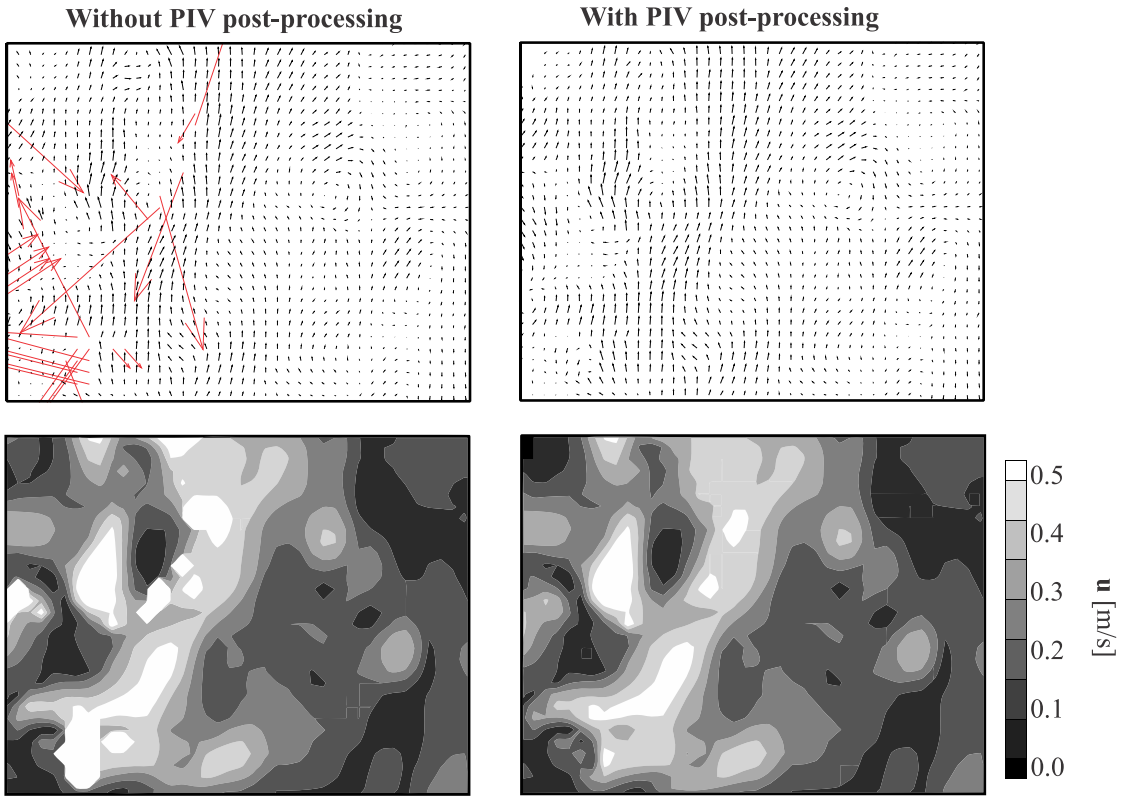

Figure 2.8 – Effect of the PIV post-processing on fields with outliers.

2.2. ERROR AND NOISE SOURCES

Errors are defined as the difference between the measurement and true value (unknown). Total errors consist of systematic (bias) and random errors (Coleman and Steele, 2009). Systematic errors are defined as errors that are fixed depending on their sources. The nature of these errors is that they follow a trend that makes them predictable. In PIV systems, systematic

errors include calibration errors and errors due to failure in adjusting the correlation peak when the particle image diameter is smaller than one pixel (peak-locking, Figure 2.9a), for example (Westerweel, 1997; Raffel *et al.*, 2007; Adrian and Westerweel, 2011; Sciacchitano, 2014).

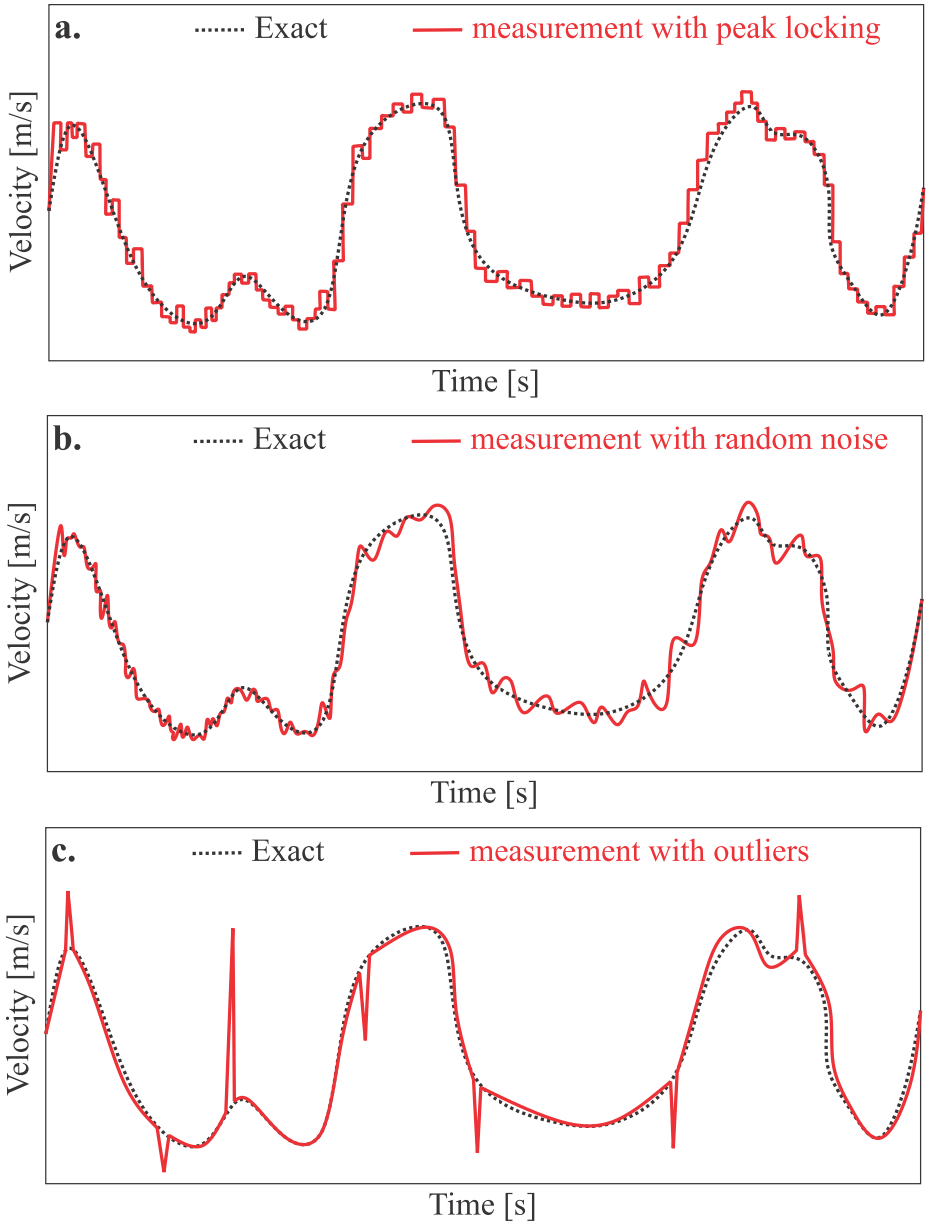

Figure 2.9 – PIV measurement with (a) peak locking, (b) random noise, and (c) outliers.

By tuning the PIV setup and processing, the systematic errors can be reduced or removed. Random errors are different for each measurement and are associated with noise in the recordings, out-of-plane motion, low concentration of tracers ("low density"), high concentration of tracers ("high density"), and displacement gradients among other sources of error (Figure 2.9b). These errors typically range between 0.03 and 0.1 pixel, which makes their identification difficult. In contrast, outliers are of the order of several pixels. Outliers are wrong

estimates of the displacement that occurs when the interrogation windows contain insufficient particle image pairs and a high noise level (Figure 2.9c). In general, an outlier may be defined as an observation (data point) which is very different from the rest of the data. Although this error may be considered acceptable for the instantaneous velocity, it can prevent the accurate evaluation of statistical quantities derived from fields such as the Reynolds stresses, acceleration, velocity gradient, divergence and vorticity (Westerweel, 1997; Raffel *et al*., 2007; Adrian and Westerweel, 2011; Sciacchitano, 2014).

2.2.1. Distortion of the particle image

Recorded images of the particles are subject to deformation (defocusing) and the individual particles can be recorded by the CCD (charge-coupled device) sensor as blurred. Optical windows as ducts, columns or complex geometries and fluids with different refractive indices produce distortion in the image. The distortion is directly related to the distribution of the refractive index on the environment, producing two types of systematic errors: position and velocity error. Before the recording of the particle images, the distortion caused by optical windows can be corrected by the image deformation using the mapping function obtained in PIV calibration. This mapping function is used to reconstruct the image compensating the distortion caused by the optical windows. However, the compensation of the defocusing of particle individual images in the flow is more difficult. Besides the defocus, the particle image can be shifted from its actual position because of refraction, which is designated as optical displacement.

According to Elsinga *et al.* (2005a, 2005b), the main disadvantage of the particle image blur is a consequent reduction in the particle image contrast and signal-to-noise ratio (SNR). Furthermore, the blur effect on the particle image can cause the enlargement of the correlation peak and can decrease the measurement accuracy. This peak elongation depends on the displacement of tracer particles in the recordings (Figure 2.10). If the tracer particle is moved from an undistorted region to a distorted (Figure 2.11), the cross-correlation map will be elongated resulting in an error of sub-pixel order (also known as bias). However, the map is symmetrical and without bias errors when the particles are blurred by the same amount on both recordings. According to the simulations carried out by Elsinga *et al.* (2005a), the particle images can be divided into four types in an environment with heterogeneous distribution of the refractive index: not distorted, blurred (elongated), duplicate, and duplicate with blurring

(Figure 2.12). Duplicate images of particles can further decrease the SNR since they may have different displacements of real particles (tracer particles).

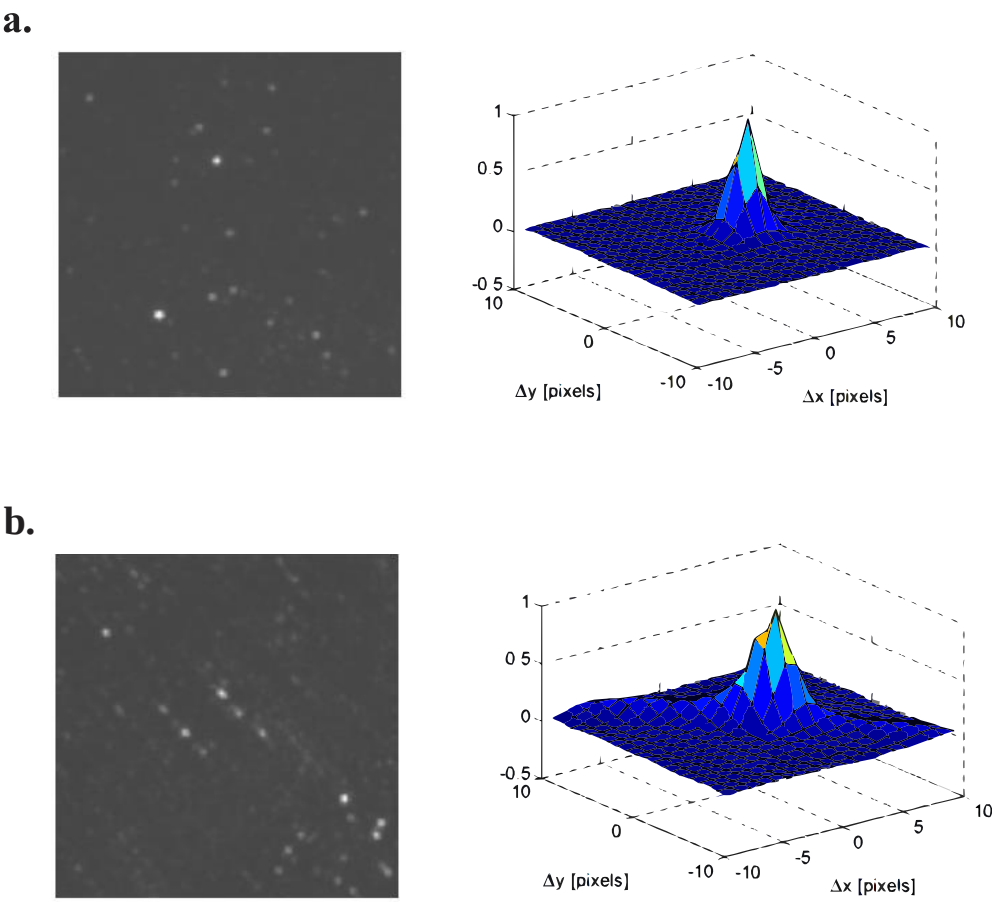

Figure 2.10 – Correlation plane for the image (a) without and (b) with the distortion effect (Adapted from Elsinga *et al*., 2005a).

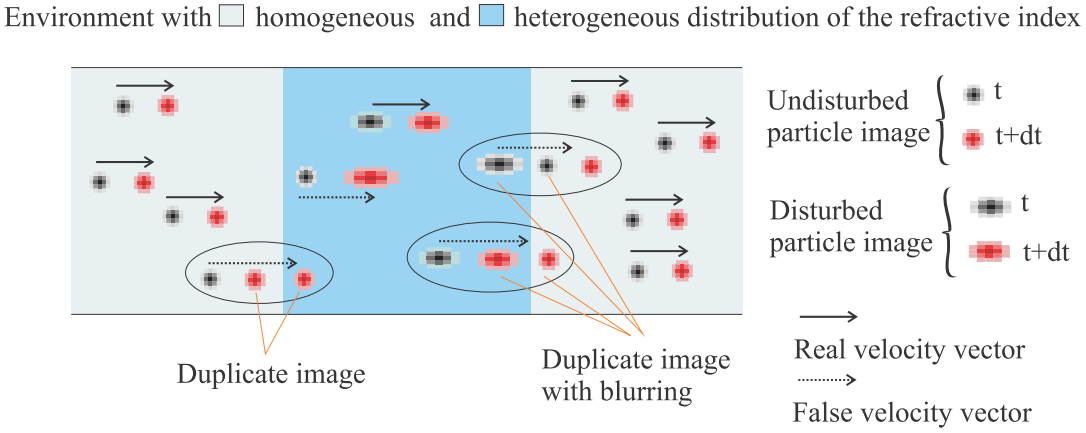

Figure 2.11 – Differences between distorted and undistorted medium (Adapted from Elsinga *et al*., 2005b).

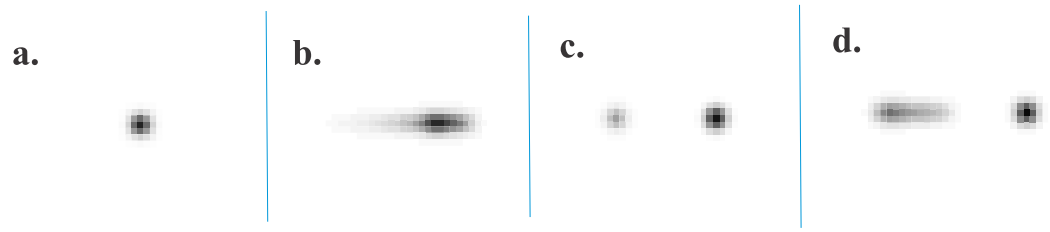

Figure 2.12 – Four types of particle image in an environment with heterogeneous distribution of refractive index: (a) not distorted, (b) blurred (elongated), (c) duplicate, and (d) duplicate with blurring (Adapted from Elsinga *et al*., 2005a).

2.2.2. Background noise

The quality of the images should normally be already guaranteed in the recording, optimizing the illumination of the particle tracers and positioning of the camera to eliminate the images background noise (Fincham and Spedding, 1997). Furthermore, a darkroom can be used to decrease or eliminate the background illumination. In practice, however, these conditions are hardly ever performed. The intensity of the laser light can vary in the frame or between the image frames due to differences in the two lasers (in the case of a Nd:YAG laser system). Furthermore, optical windows, objects in motion, and bubbles can introduce strong light reflections. Any light that is not the particle images contributes to the correlation plane as background intensity noise (R_C in Eq. 2.1) causing systematic errors. Several approaches such as temporal and spatial filters are available in the literature to reduce the effect of these problems (Northrup *et al*., 1991; Westerweel 1993; Raffel *et al*., 2007, Adrian and Westerweel, 2011)

In multiphase systems, the use of Fluorescent PIV (F-PIV) systems to solve this problem is quite common. This system uses fluorescent tracer particles and a high-pass filter on the camera to allow only the passage of light scattered by the tracer particles (Figure 2.13). Even using a F-PIV, usually recorded images still present an unequal intensity distribution in the frame interfering on the velocity accuracy (Lindken and Merzkirch, 2002; Honkanen and Nobach, 2005; Shavit *et al.*, 2007; Theunissen *et al.*, 2008; Seol and Socolofsky, 2008; Niels *et al.*, 2010).

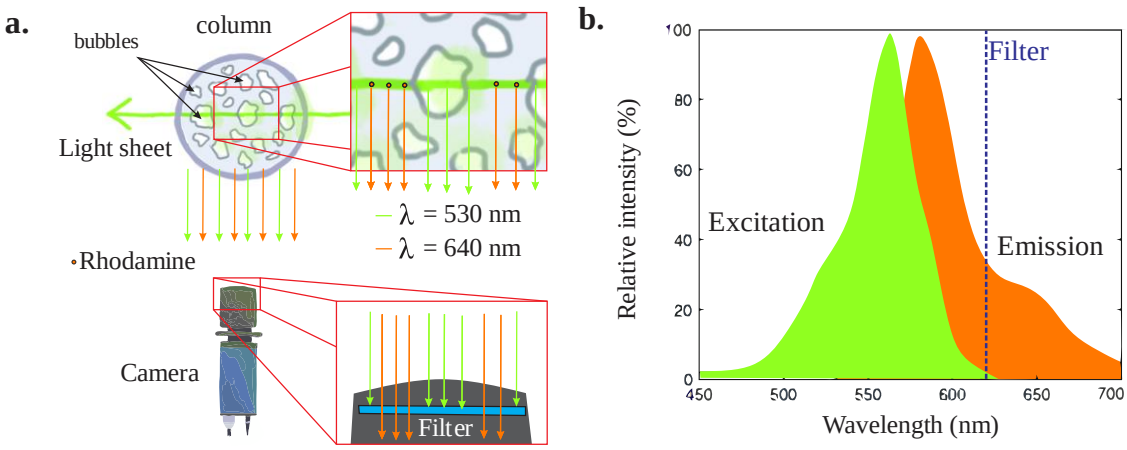

Figure 2.13 – (a) Representation of a Fluorescent PIV system (b) Excitation and emission spectrum of the Rhodamine B based on Wilson *et al.* (1986).

2.2.3. Noise in correlation

2D-2C PIV is based on matching two images to calculate a displacement field (dx, dy) as the best fit between the intensities in the frame 0, I_0, and frame 1, $I_1^*(x,y) = I_1(x+dx(x,y), y+dy(x,y))$, of the Figure 2.4. Typically, this involves maximizing the correlation given by the sum of $I_0 \cdot I_1$ (Wieneke, 2015). In PIV interrogation, the majority of the parameters are set considering a uniform displacement field (Westerweel, 1993; Westerweel, 1997; Olsen and Adrian, 2001; Adrian and Westerweel, 2011). Under these conditions, it was shown that the width of the correlation peak is proportional to the particle image diameter, dτ (Westerweel, 2000; Westerweel, 2008). However, PIV is applied to study the flow fields that are typically non-uniform.

The parameters that influence the measurement error attributable to PIV interrogation is the dτ, particle image density per interrogation window (N_I), particle image contrast, out-of-plane and in-plane motion associated with the velocity gradient (Scarano, 2002). For uniform displacement, the detection of the correlation peak is proportional to $N_I \cdot F_I \cdot F_O \cdot F_\Delta$, where F_I, F_O, and F_Δ are the loss of correlation due to the in-plane motion, out-of-plane motion and due to local variation of the displacement, respectively. Unfortunately, N_I, F_I, F_O, and F_Δ are unknown in the measurements of flow velocity (Keane and Adrian, 1990; Hain and Kahler, 2007; Westerweel, 2008).

An extensive study using Monte Carlo simulation for double-exposure single-frame, multiple-exposure single-frame, and single-exposure double-frame was performed by Keane

and Adrian (1990, 1991, 1992). This study resulted in four practical design rules for PIV measurements: $N_I > 10$, $|\Delta \boldsymbol{X}| < D_I/4$, $|\Delta Z| < \Delta Z_0/4$, and $a \equiv M_0|\Delta \mathbf{u}|\Delta t \ll d_\tau$, where a is the velocity gradients, $|\Delta \boldsymbol{X}|$ is the particle image displacement, D_I is the interrogation window size, $|\Delta Z|$ is the out-of-plane motion, ΔZ_0 is the thickness of the light sheet, and $|\Delta \mathbf{u}|$ is the local variation of velocity. A practical measure of cross-correlation quality that can be associated with the $N_I \cdot F_I \cdot F_O \cdot F_\Delta$ is the signal-to-noise ratio (SNR), which is defined as the ratio of the highest correlation peak and the second highest peak (Kahler and Kompenhans, 2000; Pereira *et al.*, 2004). Numerical investigations show that a correlation coefficient of 0.5 and an SNR of 2.0 are ideal to avoid errors in the field vector (Hain and Kahler, 2007).

In PIV interrogation, a discrete window shift technique (Westerweel *et al.*, 1997) can be used to increase the SNR by offsetting the interrogation windows according to the mean displacement (Figure 2.14b).

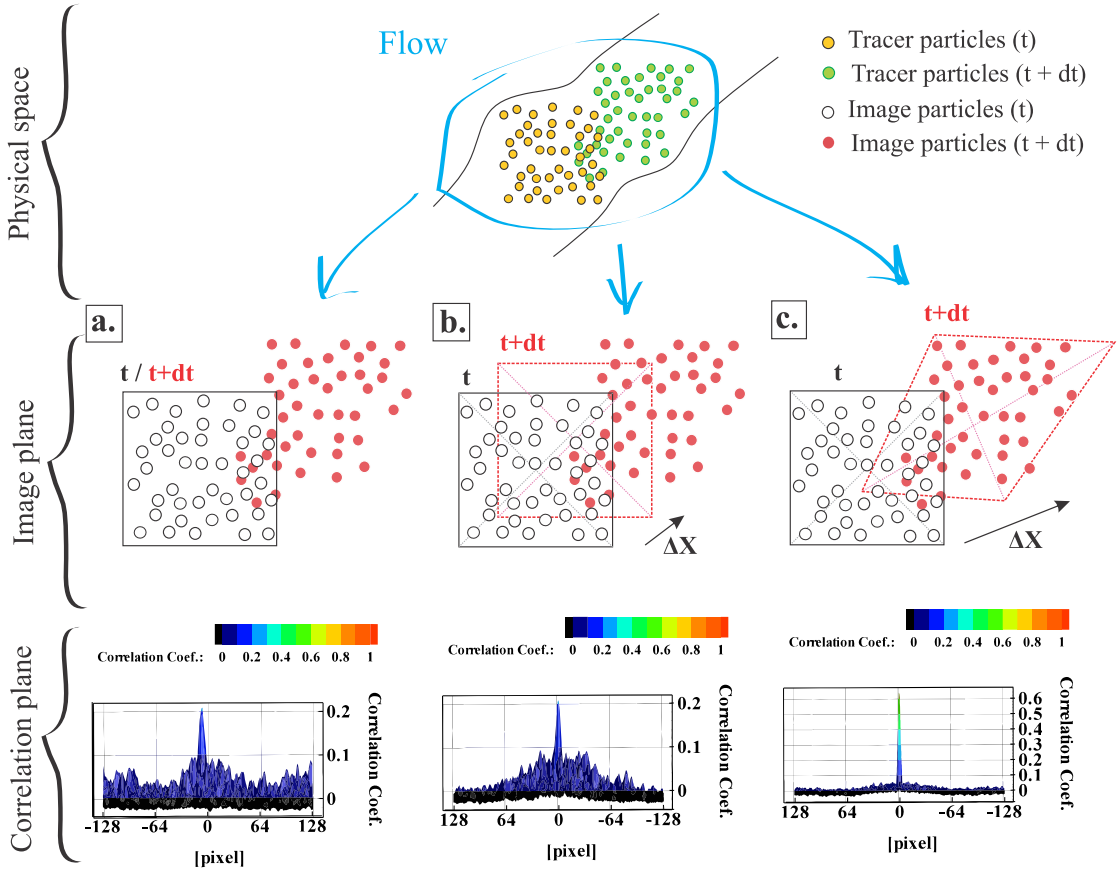

Figure 2.14 – PIV Interrogation: (a) Without and (b) with the offseting the interrogation window. (c) Iterative technique based on the offseting and deformation of the interrogation window

Analysis of the cross-correlation may be performed with an iterative technique based on the deformation of the interrogation window (Scarano, 2002), where the interrogation windows are deformed based on the result of the previous interrogation (Figure 2.14c). Moreover, multiple steps may be employed in which the size of the interrogation window can be progressively decreased (Raffel *et al*., 2007; Adrian and Westerweel, 2011).

The PIV performance may be associated with the multiplication of the dynamic velocity range (DVR) and dynamic spatial range (DSR). L_X and L_Y are the size of the recording medium, then the field of view in the fluid is given by $\ell_x = L_X/M_0$ and $\ell_y = L_Y/M_0$, then $\mathrm{DSR} = \mathrm{Min}\left(L_X/\left(M_0 \cdot \Delta x_{p,\max}\right), L_Y/\left(M_0 \cdot \Delta x_{p,\max}\right)\right)$, where $\Delta x_{p,\max}$ is the resolved minimum scale. DSR can be increased by increasing the number of pixels, or by using smaller interrogation windows. On the other hand, DVR is defined as the ratio between the maximum and minimum velocity which can be solved as $\mathrm{DVR} = \Delta x_{p,\max}/\sigma_{\Delta x}$. For PIV conventional systems, DVR usually reaches values up to 200-300 (Adrian, 1997; Hain and Kahler, 2007).

2.2.4. Perspective error and 3C reconstruction

A major limitation in 2D-2C PIV systems is caused by the perspective error on the in-plane velocity components. This problem can be solved by using a 2D-3C PIV system that applies two cameras with different projections to record simultaneously the same field of view to determine the out-of-plane motion of the tracer particles providing a 2D-3C velocity field (Figure 2.15) (Raffel *et al.*, 2007; Adrian and Westerweel, 2011).

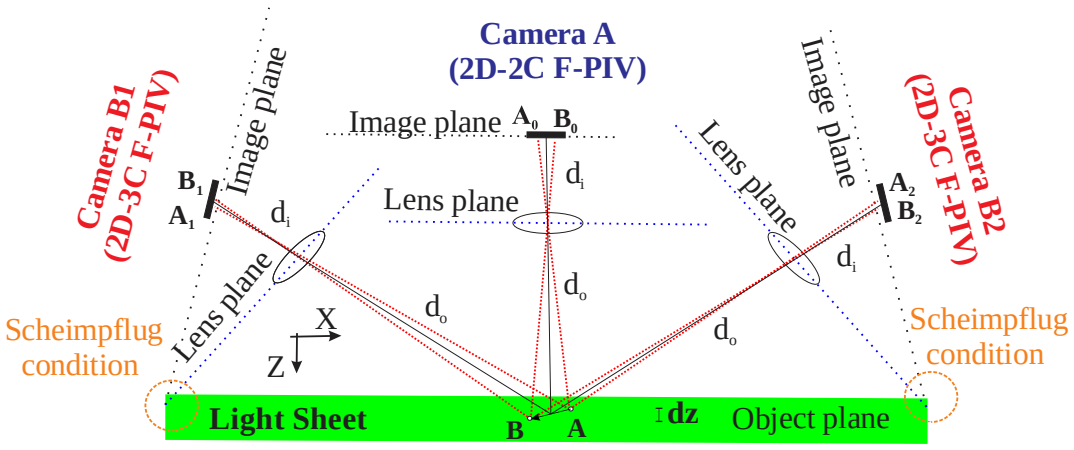

Figure 2.15 - Schematic representation of the 2D-2C and 2D-3C PIV imaging.

Lawson and Wu (1997) analyzed the best angle for 3C reconstruction through a geometric model. The authors investigated the ratio of the average random error of the out-of-plane component by in-plane component ($\varepsilon_r = \varepsilon_{RMSz}/\varepsilon_{RMSx}$) as a function of the camera angle (2θ) in a stereoscopic configuration. The lowest ε_r is obtained when 2θ = 90 degrees (Figure 2.16). This condition requires a high optical access of the investigated area and large image distortion due to curvatures of optical windows or fluid interfaces. In various practical situations, 2θ between 60 and 80 degrees provide an out-of-plane component with high accuracy. The Scheimpflug condition is used as a method to obtain images in good focus over the entire image plane. This condition requires that the object plane, lens plane, and image plane are colinear. The use of the Scheimpflug condition results in a significantly non-uniform magnification (di/do) across the image plane. Besides that, the presence of out-of-plane motion or the non-overlapping of the two laser sheets change the relative intensity between particle images at first and second exposure. This difference of intensity was demonstrated to be the source of large errors (Raffel *et al.*, 2007; Nobach and Bodenschatz, 2009; Adrian and Westerweel, 2011).

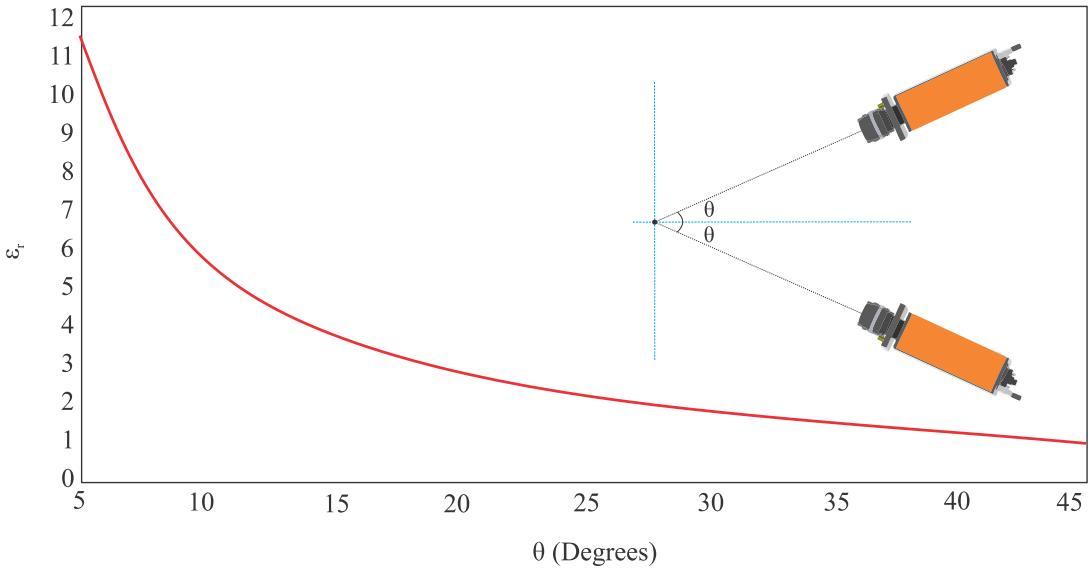

Figure 2.16 - Ratio of the average random error of the out-of-plane component by in-plane component ($\varepsilon_r = \varepsilon_{RMSz}/\varepsilon_{RMSx}$) as a function of the camera angle (θ) in a stereoscopic configuration investigated by Lawson and Wu (1997).

In 2D-2C fields, multiple passes decreasing the interrogation window size (multiple steps) can be used to increase the SNR in the PIV interrogation. Usually, the 2D-2C vector fields converge sufficiently (match between the particle images) after four passes at the final interrogation window size. The image dewarping and image deformation are done

simultaneously before each step in the multi-pass iterative scheme. The image dewarping is performed to compute the 2D-2C fields in the correct positions of the spatial coordinates. A sub-pixel interpolation is required during this process. The image deformation aims to compensate the distortion caused by the environment. The size and shape of the interrogation windows for both cameras must be the same, i.e., the correlation must be done on the same particle images. A preliminary stereo reconstruction is done to remove the false vectors in the 2D-2C fields. Usually, these false vectors produce larger reconstruction errors (larger than 1 pixel). Then, the stereo reconstruction is performed solving a system of four linear equations with three unknowns (u, v, w). The deviation (reconstruction error) from the measured (u_{i1}, v_{i1}) and (u_{i2}, v_{i2}) reconstructed in image plane can be calculated from (u_1, v_1) and (u_2, v_2) components in 2D-2C vector field. Usually, the reconstruction error is below 0.5 pixels when the 2C vector error is less than 0.1 pixel. The reconstruction is accurate when the calibrated image is aligned with the object plane (illuminated plane) (Calluaud and David, 2004; Wieneke, 2005).

2.3. UNCERTAINTY QUANTIFICATION: CORRELATION STATISTICS METHOD

Currently, four methods of quantification of PIV uncertainty have been in focus: uncertainty surface (Timmins *et al.*, 2012), primary peak ratio (Charonko and Vlachos, 2013), particle disparity (Sciacchitano *et al.*, 2013), and correlation statistics (Wieneke, 2014, Wieneke, 2015). Sciacchitano *et al.* (2013, 2014) experimentally analyzed the four methods of uncertainty quantification and observed that the correlation statistics (CS) approach provides the most accurate estimates using the standard cross-correlation (SCC). The CS method analyzes the overall contribution of pixel intensity to the shape of the correlation function. Furthermore, this method is based on the assumption that the PIV interrogation algorithm should always produce a symmetric correlation peak after convergence. In this case, the image in frame 1, I_1, is dewarped back onto image in frame 0 using the displacement field u (Eq. 2.2) keeping image in frame 0, I_0, constant.

$$I_1^*(x) = I_1(x+u) \tag{2.2}$$

In Figure 2.17, $C_+ = C(u+\Delta x)$ should be equal to $C_- = C(u-\Delta x)$ for a small distance $\pm\Delta x$ away from u (Eq. 2.3). However, the contribution of the unmatched particle images and image noise produces the asymmetrical shape of the correlation peak (Figure 2.18). In this case,

fitting a Gaussian curve through the three points leads to the residual displacement δu given by Eq. 2.4. A measured displacement error is obtained when δu is optimized by the PIV predictor–corrector scheme as ΔC equals zero again (Eq. 2.5). The uncertainty estimation of the displacement field is obtained from δu and the standard deviation of ΔC_i .

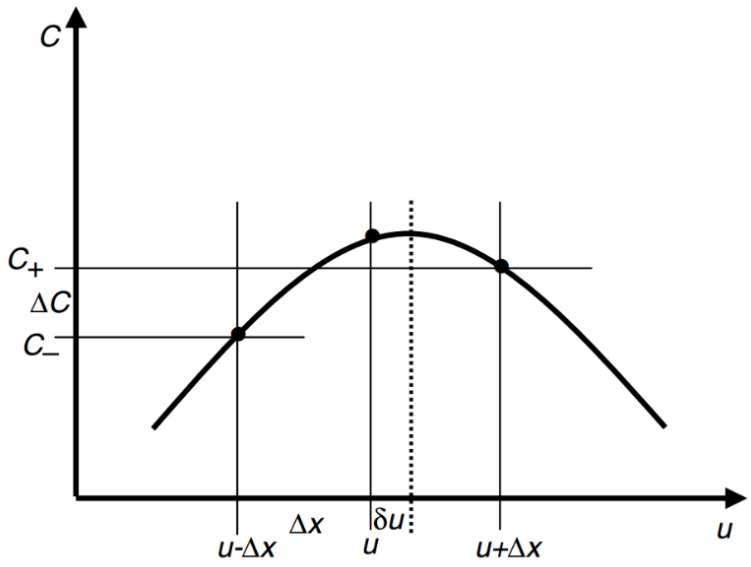

Figure 2.17 - Correlation function, C(u) (Wieneke, 2015).

$$\Delta C = C_+ - C_- = \sum \left(I_0(x,y) I_1^*(x+\Delta x, y) - I_0(x,y) I_1^*(x-\Delta x, y) \right) \cong 0 \tag{2.3}$$

$$\delta u = \frac{\Delta x}{2} \left(\frac{\log(C_+) - \log(C_-)}{2\log(C_0) - \log(C_+) - \log(C_-)} \right) \tag{2.4}$$

$$\Delta C = \sum \Delta C_i \tag{2.5}$$

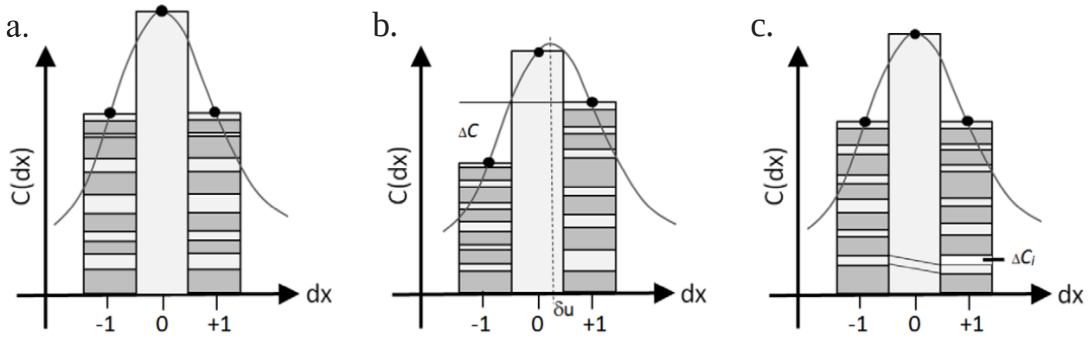

Figure 2.18 - Correlation function for (a) ideal noise-free image and (b) with added noise. (c) Correlation peak shifted by the PIV predictor–corrector scheme (Wieneke, 2015).

Assuming that the samples are independent and follow a normal distribution of the standard deviation σ_x, the standard uncertainty of the time-averaged value is defined by Eq. 2. 6 (Benedict and Gould, 1996; Bendat and Piersol, 2010), where N is the number of samples. Ahn and Fessler (2003) reported that for $N \geqslant 30$ the Eq. 2.6 presents precision of 1% (Coleman and Steele 2009). When the samples are not independent, the parameter N must be substituted with the effective number of independent samples N_{eff} (Eq. 2.7), where the autocorrelation coefficient between two samples $\rho(n\Delta t)$ is considered for an interval Δt and time step *n*.

$\sum_{-\infty}^{+\infty} \rho(n\Delta t) > 1$ and consequently $N_{Feff} < N_F$ when the measurements are correlated. In Equation 2.6, the systematic errors due to spatial modulation errors or peak locking are not taken into account. The standard deviation σ_u (Eq. 2.8) contains both the true velocity fluctuations ($\sigma_{u,\,fluct}$) and the measurement errors ($\sigma_{u,err}$), where U_u is the uncertainty of the instantaneous velocity component and $\overline{U_u^2}$ is the mean-square of U_u^2 (Sciacchitano and Wieneke, 2016).

$$U_{\bar{x}} = \frac{\sigma_x}{\sqrt{N}} \tag{2.6}$$

$$N_{eff} = \frac{N}{\sum_{n=-\infty}^{+\infty} \rho(n\Delta t)} \tag{2.7}$$

$$\sigma_u^2 = \sigma_{u,\,fluct}^2 + \sigma_{u,err}^2 \approx \sigma_{u,\,fluct}^2 + \overline{U_u^2} \tag{2.8}$$

CHAPTER 3.

PIV APPLICATIONS IN BUBBLE COLUMNS

This chapter presents a brief review of the literature on flows in bubble column. The flow characteristics of the liquid and gaseous phase are discussed in each flow regime. In addition, the shape of the bubbles in different conditions is detailed.

Examples of different configurations of PIV systems in bubble column are also presented in this chapter. The adaptations and purpose of each PIV application are detailed.

3.1. FLOW IN BUBBLE COLUMN

3.1.1. Flow regimes

The characterization of the fluid dynamics has a significant effect on the operation and performance of the bubble column reactor. The regimes in these reactors are classified according to the gas superficial velocity. Basically, three regimes can be observed (Figure 3.1): homogeneous (bubbly flow), heterogeneous (churn-turbulent), and slug flow (Shah *et al.,* 1982). The bubbly flow regime is characterized by the quasi-uniform distribution of the bubbles through the column radius. Typically, this regime occurs when the gas superficial velocity is less than 0.05 m/s (aqueous solution) and the rising velocity of the bubbles is between 0.18 and 0.30 m/s. The turbulent regime is achieved as the gas superficial velocity in the column increases. The gas-liquid dispersion leads to an unstable flow pattern with increasing velocity. This heterogeneous regime presents large bubbles moving with high velocities in the presence of small bubbles. The random velocity distribution induced by the bubbles when no turbulent production occurs is defined as "pseudo-turbulence" (Lance and Bataille, 1991). The slug regime occurs in columns of smaller diameters and high gas rates. In this regime, the bubbles are stabilized near the column wall, causing to formation of large bubbles (Slug). In addition, there is a homogeneous-heterogeneous transition regime, in which the interaction between the gaseous and liquid phases varies considerably (Levich, 1962; Shah *et al.,* 1982; Hyndman *et al.,* 1997; Kantarci *et al.,* 2005; Mudde, 2005).

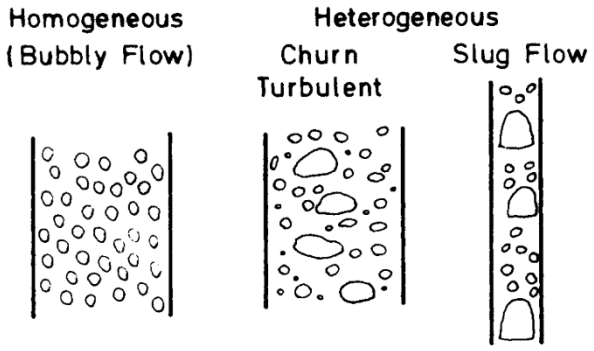

Figure 3.1 – Flow regimes in bubble columns (Shah *et al.,* 1982)

The effect of the column dimensions on flow regimes is important for the scale-up, design, and optimization of real apparatus. The effect of the column diameter, D, is often related to the turbulence scale, intensity of circulations, backmixing, axial dispersion, wall friction, and turbulent viscosity (Mersmann, 1978; Ueyama and Miyauchi, 1979; Shah *et al.,* 1982; Tinge

and Drinkenburg, 1986; Deckwer, 1992, Kastanek *et al.*, 1993; Groen *et al.*, 1996; Zahradnik *et al.*, 1997; Krishna *et al.*, 1999, Baten and Krishna, 2001; Ruzicka *et al.*, 2001). Flow regime in function (approximate dependency) of the gas superficial velocity, U_G, and column diameter, D_C (water and dilute aqueous solutions) is presented in Figure 3.2

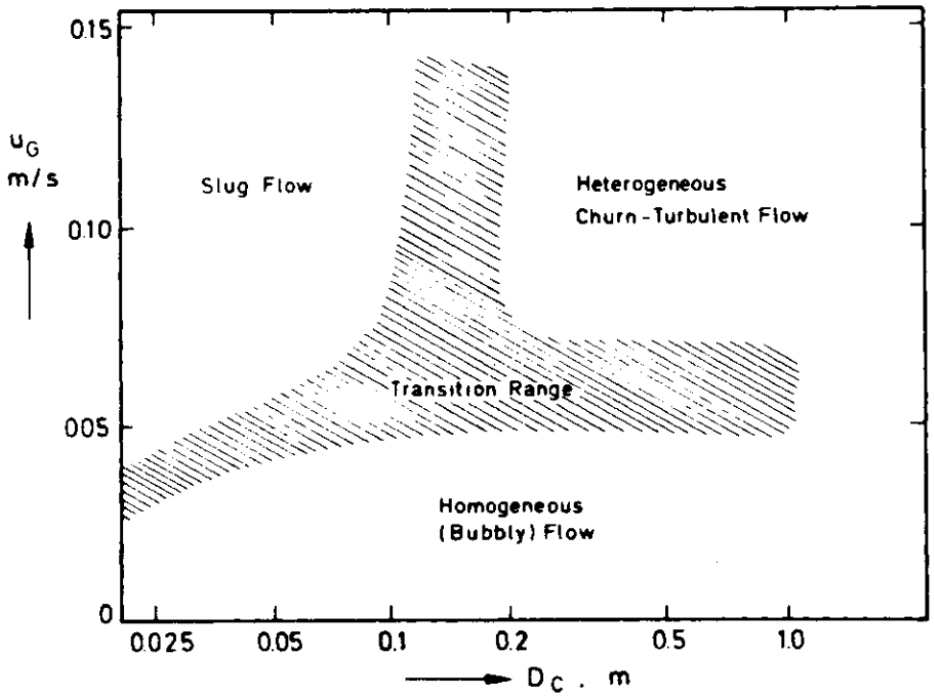

Figure 3.2 – Flow regime in function (approximate dependency) of the gas superficial velocity, U_G, and column diameter, D_C (water and dilute aqueous solutions) (Shah *et al.*, 1982).

3.1.2. Shape of the bubbles

The shape of the bubble under the influence of the gravity are generally classified into three categories: spherical, ellipsoidal, and spherical-cap or ellipsoidal-cap. The “spherical” form is obtained when inertial forces become significant in respect to viscous forces (creeping flow or stokes flow). The “ellipsoidal” bubbles presents convex interface (viewed from inside) around the entire surface. In addition, bubbles with ellipsoidal shapes exhibit periodic dilation or random oscillation movements. The “spherical-cap” form is observed in large bubbles tend to adopt flat bases and asymmetric (Cliff *et al.*, 1978).

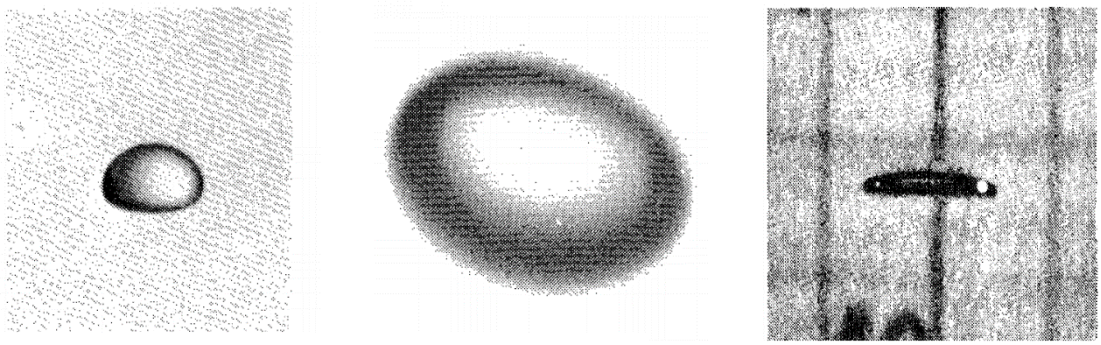

Figure 3.3 – Ellipsoidal bubbles (Adapted from Cliff *et al*., 1978).

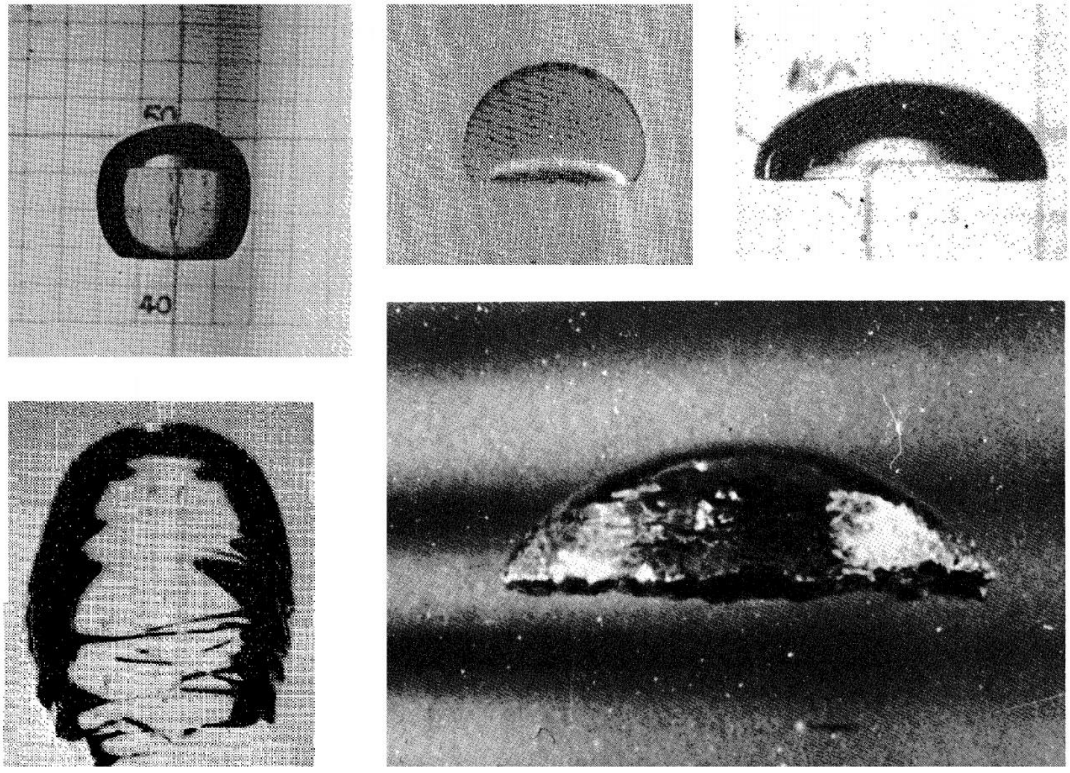

Figure 3.4 - Spherical-cap bubbles (Adapted from Cliff *et al*., 1978).

The shape of the bubble can be correlated in terms of the Eötvös number (Eq 3.1), Morton number (Eq 3.2), and Reynolds number (Eq 3.3) in Figure 3.5. In Eq. 3.1-3.3, d_e is the diameter of volume-equivalent sphere for the bubble, g is the gravitational acceleration, σ is the interfacial or surface tension, μ is the viscosity of continuous, U is the velocity of the bubble in relation to the fluid phase, and $\Delta\rho = |\rho_b - \rho|$ is the absolute value of density difference between the bubble and continuous phase (Cliff *et al*., 1978).

$$Eo = g \cdot \Delta\rho \cdot d_e / \sigma \tag{3.1}$$

$$M = g \cdot \mu^4 \cdot \Delta\rho / \rho^2 \cdot \sigma^3 \tag{3.2}$$

$$\mathrm{Re} = \rho \cdot d_e \cdot U / \mu \tag{3.3}$$

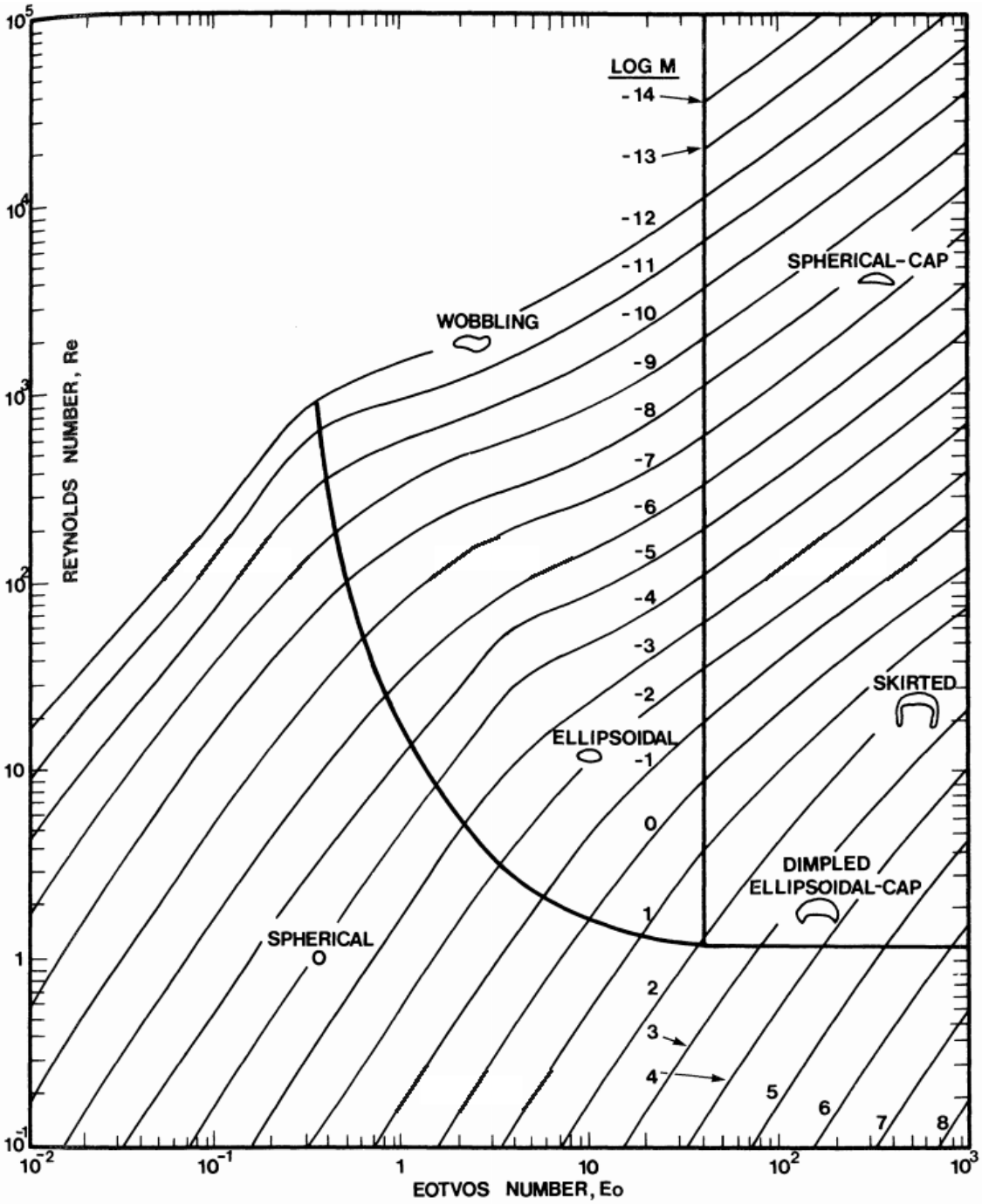

Figure 3.5 - Shape regimes for bubbles in terms of the Eötvös number (Eo), Morton number (M), and Reynolds number (Re) (Adapted from Cliff *et al*., 1978).

The homogeneous flow regime is characterized by a narrow bubble size distribution and the bubble coalescence is insignificant. In addition, the radial and axial distribution of bubble size is uniform. In heterogeneous regime, large and small bubbles are observed, that is, this regime presents a wide distribution of bubble size. In addition, bubble coalescence predominates. In the slug regime, the shape of the bubble is affected by the wall of the column (Levich, 1962; Shah *et al.,* 1982; Hyndman *et al.,* 1997; Kantarci *et al*., 2005; Mudde, 2005).

3.2. PIV IN BUBBLE COLUMN

Most PIV applications in bubble columns are from adaptations of 2D-2C classical PIV systems. These adaptations mainly sought to solve the problems associated with the great scattering of light caused by the bubbles. In addition, the adapted PIV systems sought to simultaneously determine the velocity of the two phases.

3.2.1. 2D-2C measurements.

Deen *et al.* (2000) used PIV/LIF, PIV, and LDA systems to investigate the multiphase flow in a bubble column (Figure 3.6). The PIV/LIF system combines the particle image velocimetry and laser induced fluorescence methods. This method uses two cameras and fluorescent tracer particles. Optical filters are used to obtain images of solely tracer particles with one camera and images of the dispersed phase with the other camera. The column used had a square cross-section of 0.15 x 0.15 m and a height of 1 m. The column was filled with distilled water and 4 g of sodium chloride per litre was added to obtain a non-coalescing system. In the PIV/LIF system, 300 image-pairs were recorded during a period of 900 s considering a superficial gas velocity of 0.5 cm/s. The interrogation window size was 64 x 64 pixel (0.01 x 0.01 m). Some outliers in the velocity fields were detected and removed with two subsequent tests. The instantaneous velocity fields of both phases obtained by PIV/LIF are shown in Figure 3.7. The bubble plume showed large random oscillations and most of the outliers were observed in the gas velocity field (Deen *et al*., 2000).

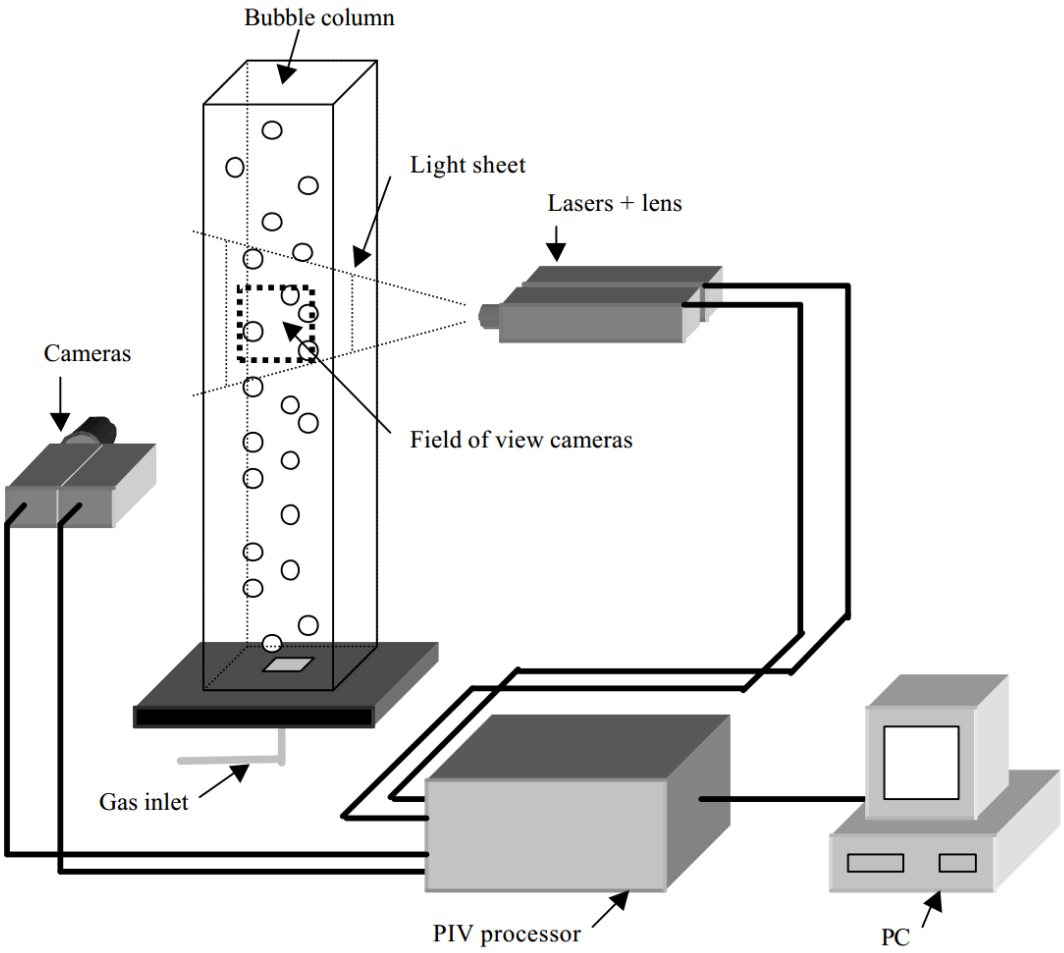

Figure 3.6 – Experimental PIV/LIF set-up used by Deen *et al.* (2000).

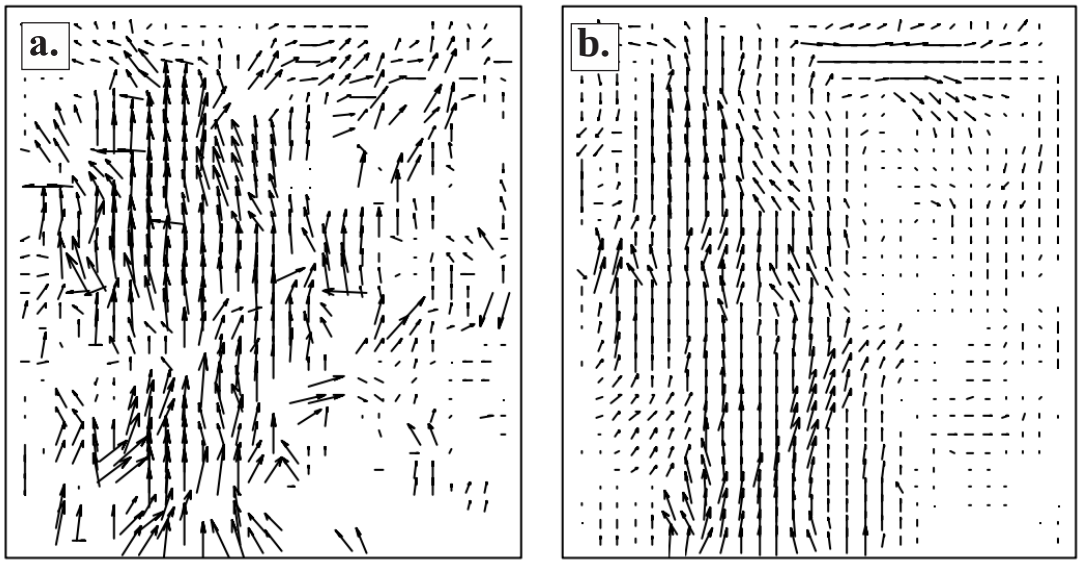

Figure 3.7 – Instantaneous velocity field of (a) gas and (b) liquid phase. The measurement was made in the centre plane of the column at a height of 0.26-0.41 m (Deen *et al.*, 2000).

Lindken and Merzkirch (2000) used PIV system and high-speed camera to investigate the 2D-2C velocity field of the liquid phase and 3D velocity of the bubbles for low U_G. For the PIV system, a double-pulsed Nd:YAG laser (532 nm) was used as light source and the particle images were recorded with a CCD sensor (Figure 3.8). For determining the 3D positions of the bubbles, a 2.5-W cw Ar^+ laser was also used as light source providing a light sheet orthogonal to the PIV light sheet. In addition, a digital high-speed camera (576 Hz) was positioned above the column to reconstruct the bubbles in the image space. In PIV evaluation, the digital mask technique was applied to separate the images of particles and bubbles. The images of the bubbles were processed, binarized, and reconstructed using the cameras projection in time. An instantaneous velocity field with 2D-2C for the liquid phase and 3D for the bubbles are presented in Figure 3.9a. Wake regions were observed using an interrogation window size of 29 x 29 pixels (Figure 3.9b) for an average bubble diameter of 5.5 10^{-3} m.

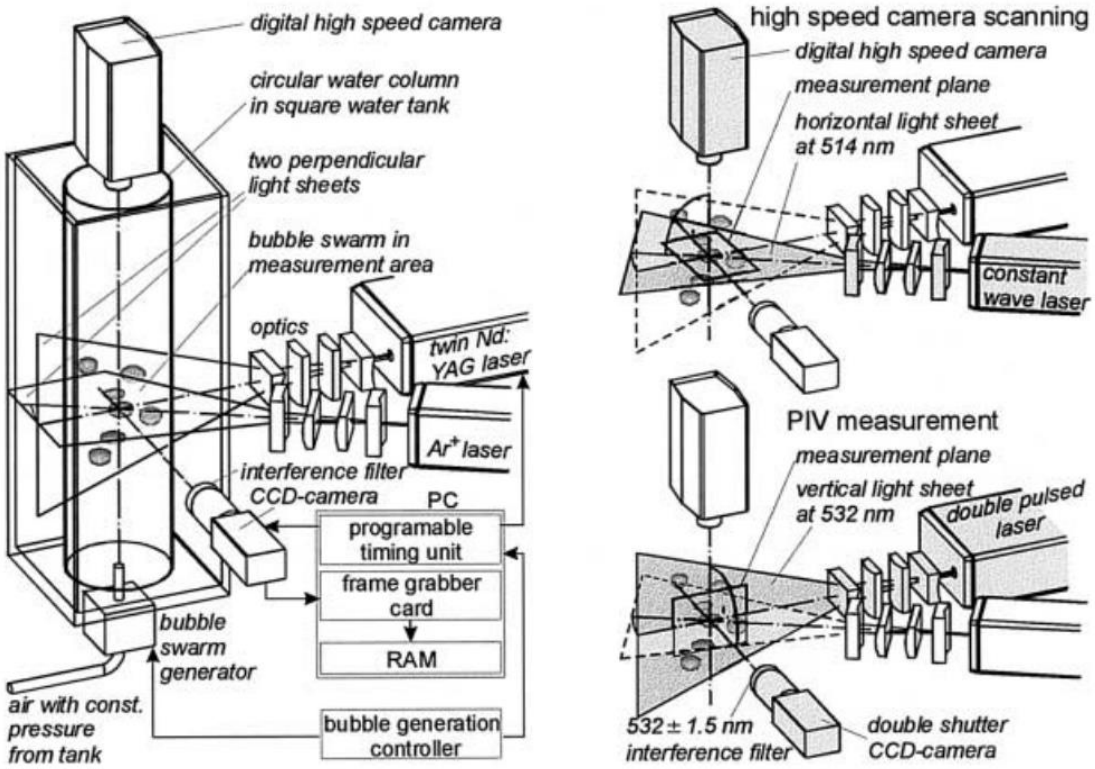

Figure 3.8 – Experimental set-up for simultaneous PIV measurements and 3D bubble visualization (Lindken and Merzkirch, 2000).

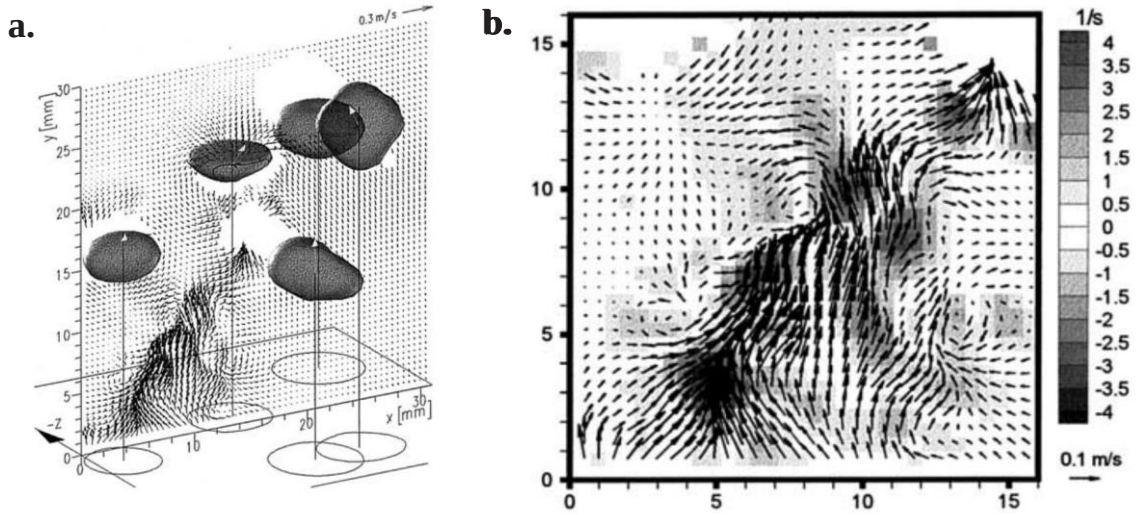

Figure 3.9 – (a) Velocity field with 2D-2C for the liquid phase and 3D for the bubbles. (b) Vorticity and velocity distribution in the wake region (Lindken and Merzkirch, 2000).

Delnoij *et al*. (2000) developed the ensemble correlation approach that enables the simultaneous measurement of the tracer particles and bubbles velocities using a PIV system with a single CCD camera. In the correlation map (Figure 3.10), the ensemble cross-correlation function contains two distinct peaks: one associated with the displacement of the bubbles ($R_D^{(BB)}$) and the other related to the displacement of the tracer particles ($R_D^{(TT)}$). In addition, the amplitude of this bubble displacement component is proportional to the mean effective number of the bubble image pairs in the interrogation window.

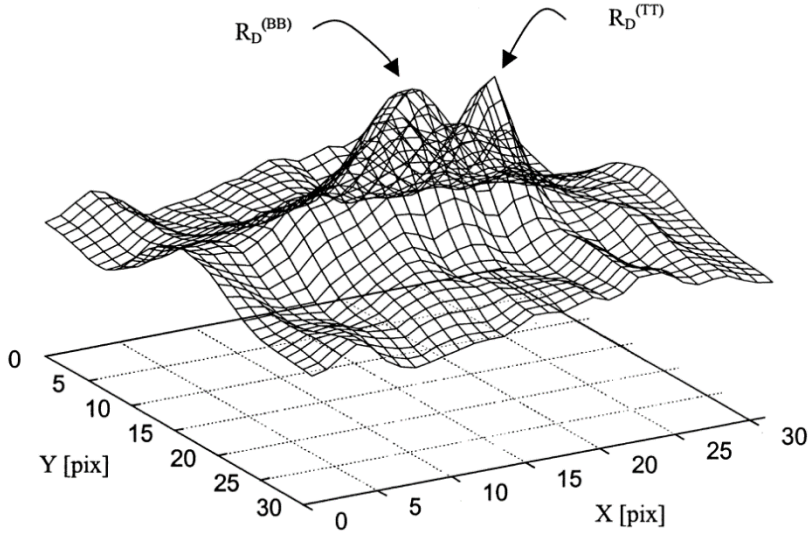

Figure 3.10 – Cross-correlation function (interrogation window size of 32 x 32 pixels) in two-phase single-exposure, double-frame PIV (Delnoij *et al*., 2000).

The authors studied the performance of the ensemble correlation approach using synthetic bubble-tracer particle patterns (Monte Carlo simulation). Moreover, the approach was tested by studying experimentally the two-phase flow in a pseudo-two-dimensional bubble column (Figure 3.11a). The image density of the tracers and their velocity were assumed to be constant and the image density of the bubbles was varied from 1 to 10. The authors did not investigate the effect of the bubble-tracer size difference. The particle and bubble images diameters were set as 2 pixels. The valid detection probability (number of correct measurements) was defined as the probability that a single interrogation window produces a bubble velocity measurement that is within 0.5 pixel of the bubble velocity specified as an input parameter for the Monte Carlo simulation. The valid detection probability increased as the number of images in the ensemble correlation set increased because the bubble displacement correlation peak was amplified. The overall noise level was decreased due to the mutual extinction of random noise peaks. The random noise level decreased by a factor $2^{1/2}$ as the size of the ensemble correlation set increased by a factor of 2.

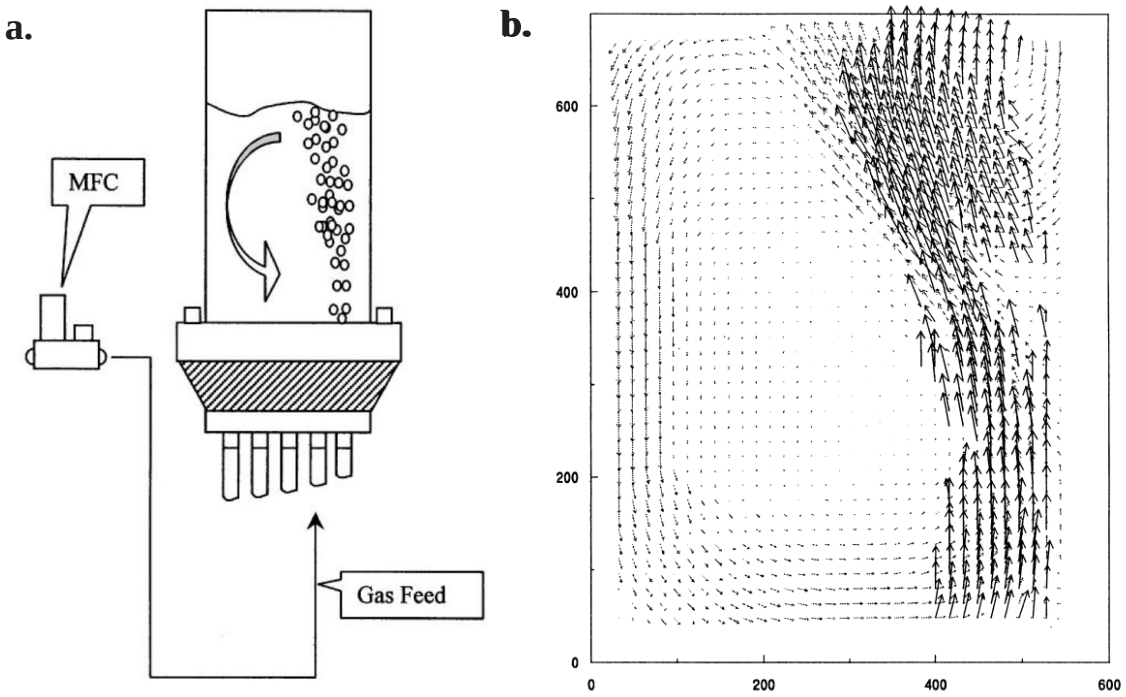

Figure 3.11 – (a) Schematic representation of the pseudo two-dimensional bubble column used in the test experiments. (b) Liquid and bubble velocity field (Delnoij *et al*., 2000).

The viewing section of the column (200 mm wide, 500 mm high and 8 mm deep) was constructed with ordinary glass. The gas was injected through five gas distributors. Low concentration of tracer particles was observed near the bubble plume. On the other hand, there

were also distinct regions with a high concentration of tracer particles. The liquid and bubble velocity field in the pseudo two-dimensional bubble column is presented in Figure 3.11b. The experimental results revealed the capability of the PIV technique to measure simultaneously the whole field characteristics of the gas-liquid two-phase flow (Delnoij *et al*., 2000).

Deen *et al.* (2001) used synthetic PIV images to derive theoretical rules that relate the maximum gas hold-up to the measurement accuracy in the flow of a bubble column. In addition, PIV images from an actual experiment were also used. The authors investigated the valid detection probability (number of correct measurements) under conditions existing in different regions of the flow (Figure 3.12). In the R1 area the bubble concentration is rather low and the valid detection probability is high. In the R3 area the bubble concentration is rather high and the valid detection probability is low. According to the authors, the measurement accuracy is not only a function of the gas fraction, but it also depends on the analysis technique.

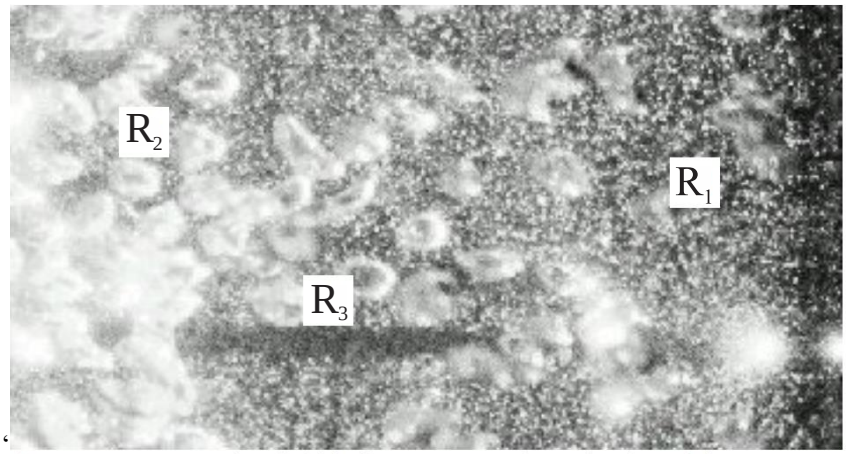

Figure 3.12 - Raw image at a gas volume fraction of about 1% (Deen *et al*., 2001).

Lindken and Merzkirch (2002) developed a novel PIV system to determine phase-separated velocity measurements in a two-phase flow of a bubble column (Figure 3.13). This system is a combination of the three PIV techniques most used in multiphase flows: PIV with fluorescent tracer particles, shadowgraphy, and the digital phase separation with a masking technique. For the recording of the particle images a double-pulsed Nd:YAG laser (532 nm) was used. Fluorescent tracer particles in the flow reflect part of the light and they emit light at a wavelength of 555–585 nm with an emission peak at 566 nm. A double-pulsed high-power light emitting diode (LED, 675 nm) array illuminates the multiphase flow for the recording of the bubbles. The flow is back-illuminated and the bubbles produce shadows. Both sets of information from the tracers and from the bubbles were recorded simultaneously in the same frame of the CCD sensor. The method is based on shifting the background intensity to higher

intensity values (Figure 3.14). The shadow image with light of wavelength 675 nm passes the optical high pass filter and the shadow image is recorded on the detector. They do not interfere with each other, because they are spatially separated in the object field as well as in the image field. Figure 3.14c shows a typical PIV/shadowgraphy image. The measurements showed that the method developed by Lindken and Merzkirch (2002) is able to measure velocities in two-phase flows with high precision for low U_G. Figure 3.15 shows an instantaneous velocity field for multiphase PIV measurement.

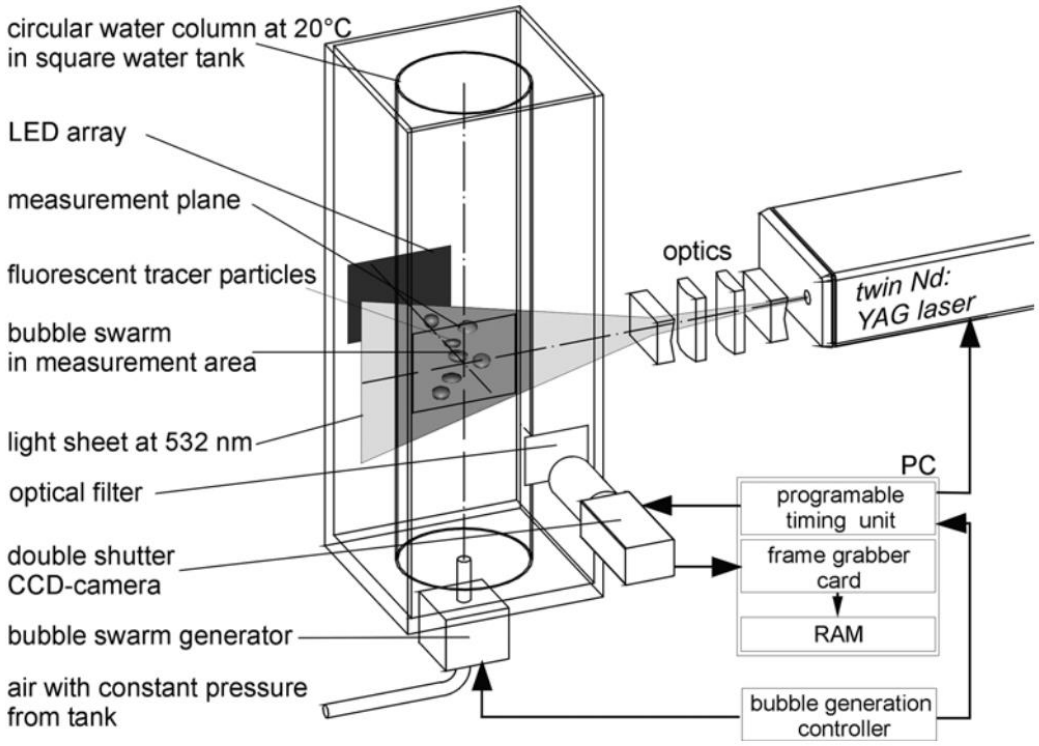

Figure 3.13 - Set-up and triggering of the combined PIV/shadowgraphy experiment (Lindken and Merzkirch. 2002).

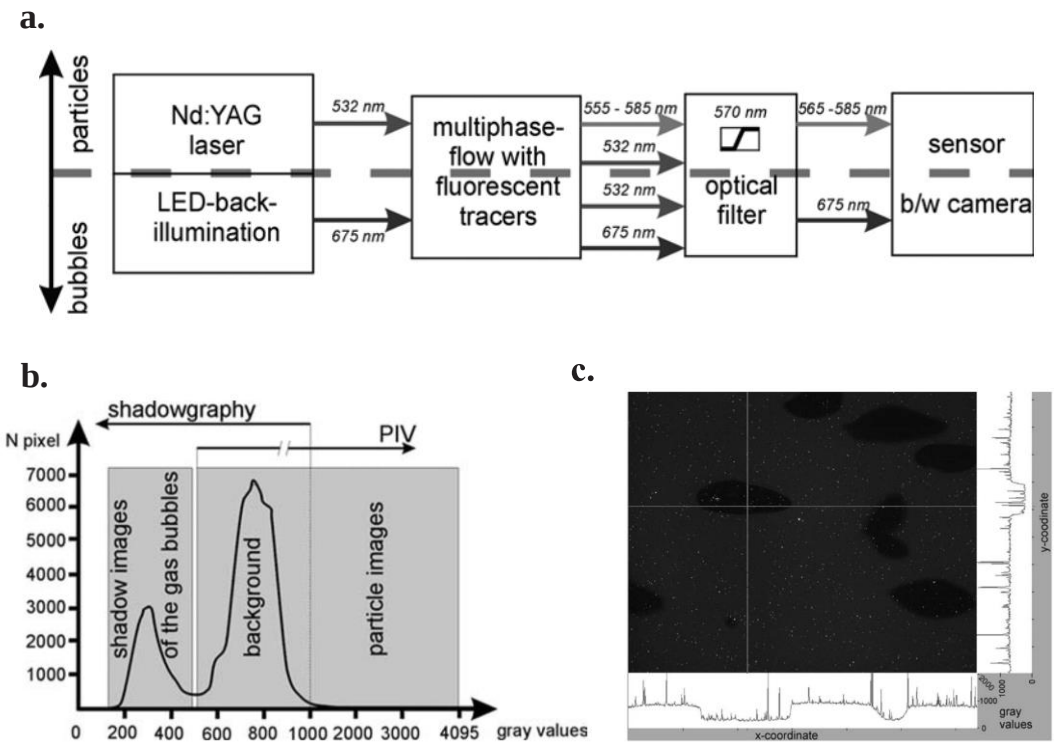

Figure 3.14 – (a) Principle of the combined PIV/shadowgraphy experiment (b) Histogram of the intensity (gray) values of the pixels. (c) Raw image (Lindken and Merzkirch. 2002).

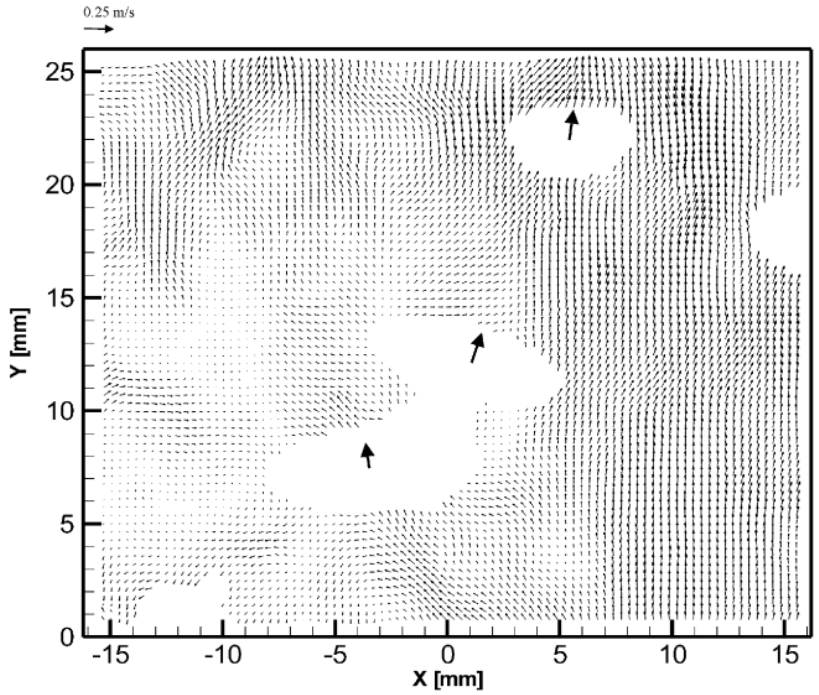

Figure 3.15 – Instantaneous velocity field for multiphase PIV measurement (Lindken and Merzkirch. 2002).

The two-phase pulsed-light velocimetry (PLV) system was developed by Bröder and Sommerfeld (2002) to evaluate instantaneous flow fields of both rising bubbles and the

continuous phase. Basically, the system consists of a classic PIV coupled to a Fluorescent-PIV, where the cameras were placed in a non-perpendicular arrangement with respect to the light sheet to improve the phase separation (Figure 3.16). The arrangement of the cameras was based on the scattering intensity of the bubbles using geometrical optics (Figure 3.17). The different scattering components obtained from geometrical optics were plotted for spherical bubbles. The raw images for each camera are presented in Figure 3.18a. The camera with the filters of 532 nm and 585 nm was used to determine the velocity of the liquid phase and bubbles, respectively. The acquired images were evaluated with the minimum-quadratic-difference (MQD) algorithm. The bubbles velocity was obtained using the particle tracking velocimetry (PTV) approach. The local resolution (i.e. the size of the smallest interrogation area) was 1.9 x·3.7 mm for the tracers and 2.8·x 5.4 mm for the bubbles. The distortion of the images due to the non-perpendicular arrangement of the CCD cameras was removed by the geometric transformation based on a perspective projection (similar to PIV calibration). The time series of the bubble and liquid velocities in a section located 500 mm above the aerator are presented in Figure 3.18b.

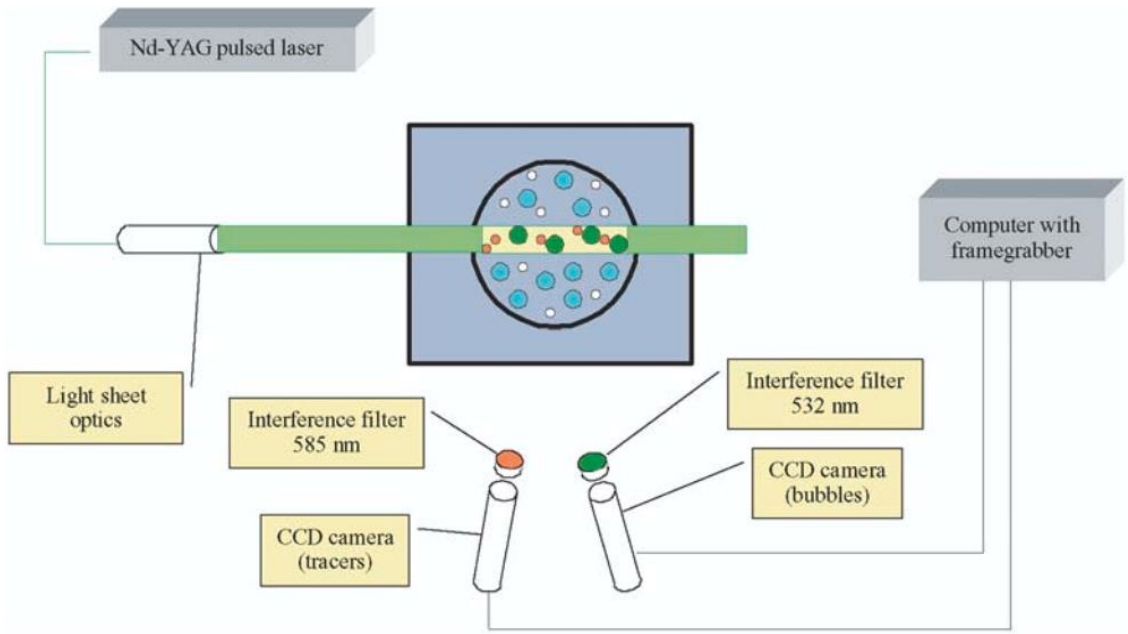

Figure 3.16 - Experimental setup (Bröder and Sommerfeld, 2002).

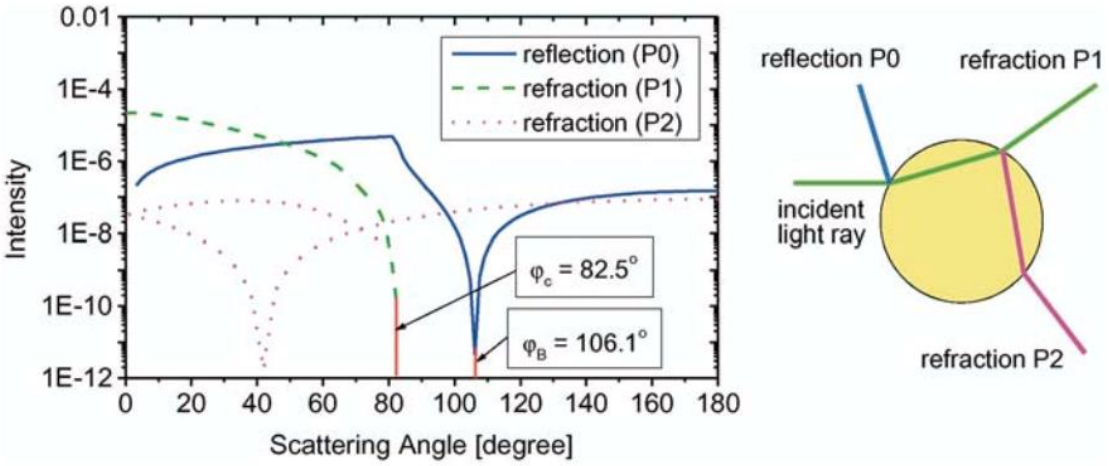

Figure 3.17 - Intensity of the different scattering modes as a function of scattering angle (measured from the forward scattering direction) for air bubbles in water (relative refractive index m=0.75) obtained by geometrical optics (φ_B: Brewster's angle, φ_c: critical angle) (Bröder and Sommerfeld, 2002).

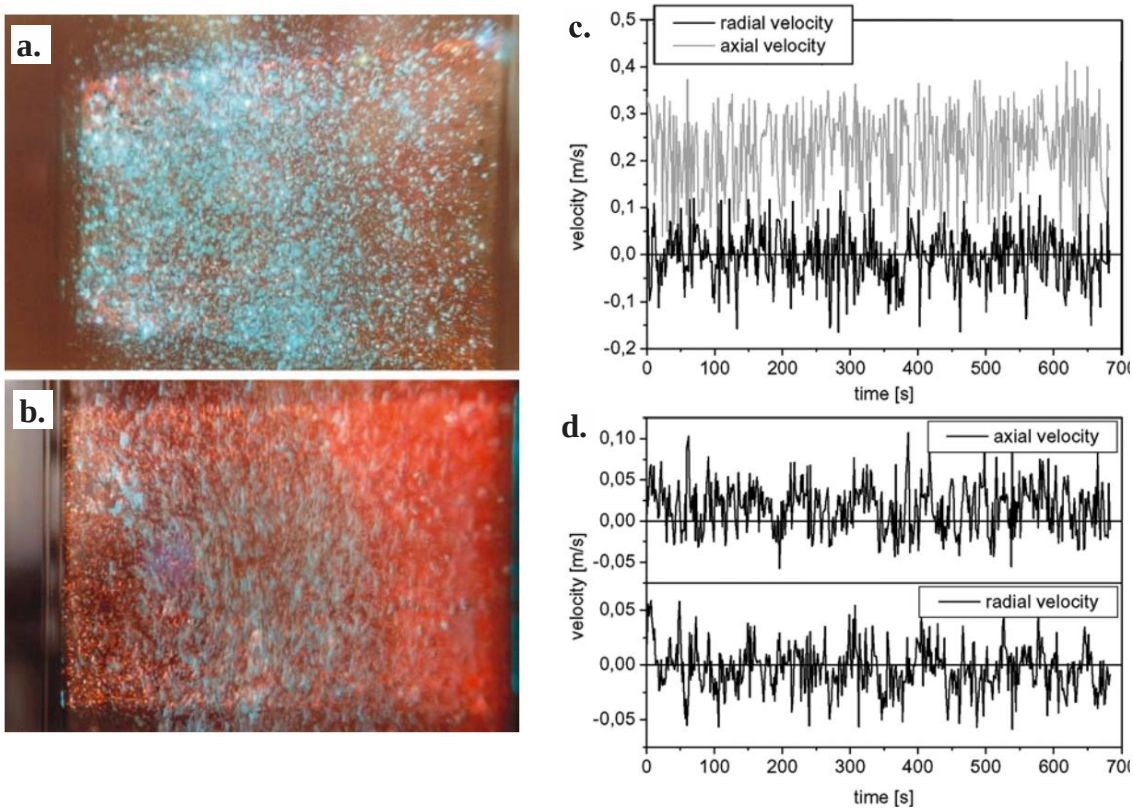

Figure 3.18 – Field-of-view of the camera with the filters (a) 532 and (b) 585 nm. Time series (c) bubble and (d) liquid velocities 500 mm above the aerator (Bröder and Sommerfeld, 2002).

Liu *et al.* (2005) investigated the liquid flow velocity field and pseudo-turbulence induced by a chain of bubbles rising through stagnant liquids using a system similar to Fluorescent –

PIV (Referenced by the authors as laser-induced fluorescence - LIF). The “pseudo-turbulence” is defined as the random velocity field induced by the bubbles when no turbulent production occurs (Lance and Bataille, 1991). This condition enhances multiphase interaction and influences the motion of the bubbles. The PIV system was used to measure the entire field velocity instantaneously to provide an accurate and complete description of the flow field surrounding bubbles. In addition, a digital camera was used to capture the motions of rising bubbles at a rate of 15 fps (Figure 3.19). A single bubble stream was injected into the rectangular column. The observing field was 65.5 × 87.9 mm^2, located 260 mm above the bottom of the column. The frequency of the bubble generation was controlled by a needle valve for different flow rates Q. Gas and four liquids of different viscosity were used: deionized water (S-1), 50 wt% glycerin in water (S-2), 64 wt% glycerin in water (S-3), and 72 wt% glycerin in water (S-4). The authors observed that the bubbles travel upwards in three different trajectories, varying from one- to three-dimensional mode as liquid viscosity reduces (Figure 3.20). In addition, different bubble motions led to different instantaneous liquid velocity fields, turbulent intensity and Reynolds stress (Figure 3.21).

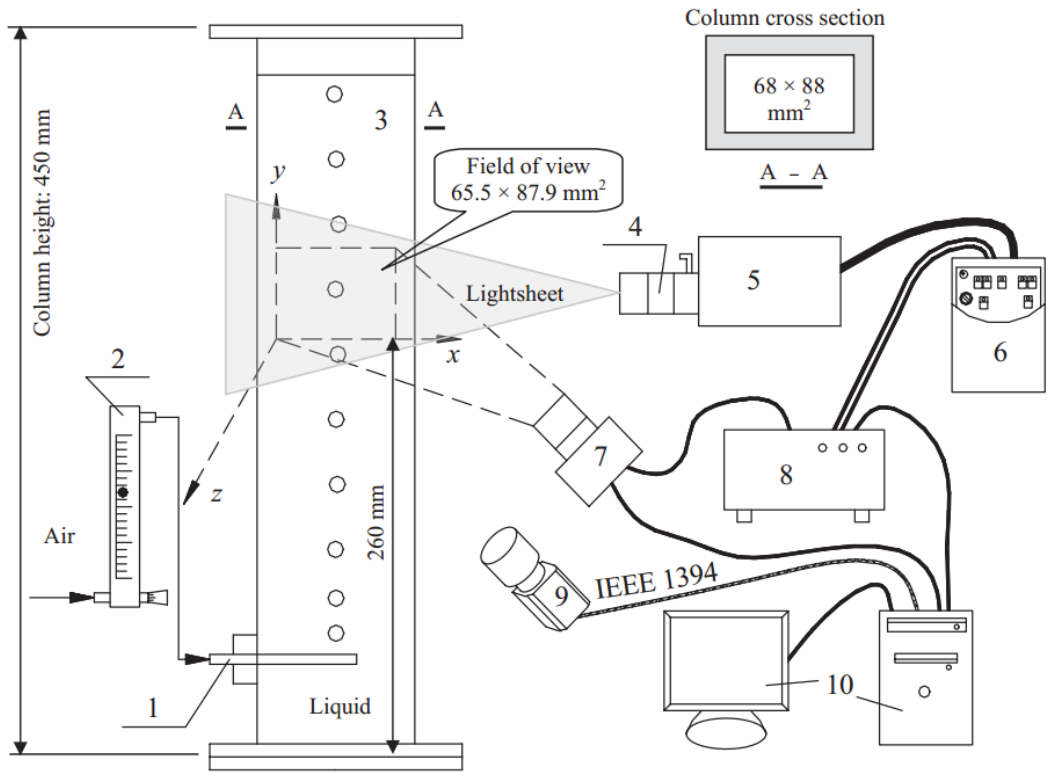

Figure 3.19 - Experimental setup investigated by Liu *et al.* (2005).

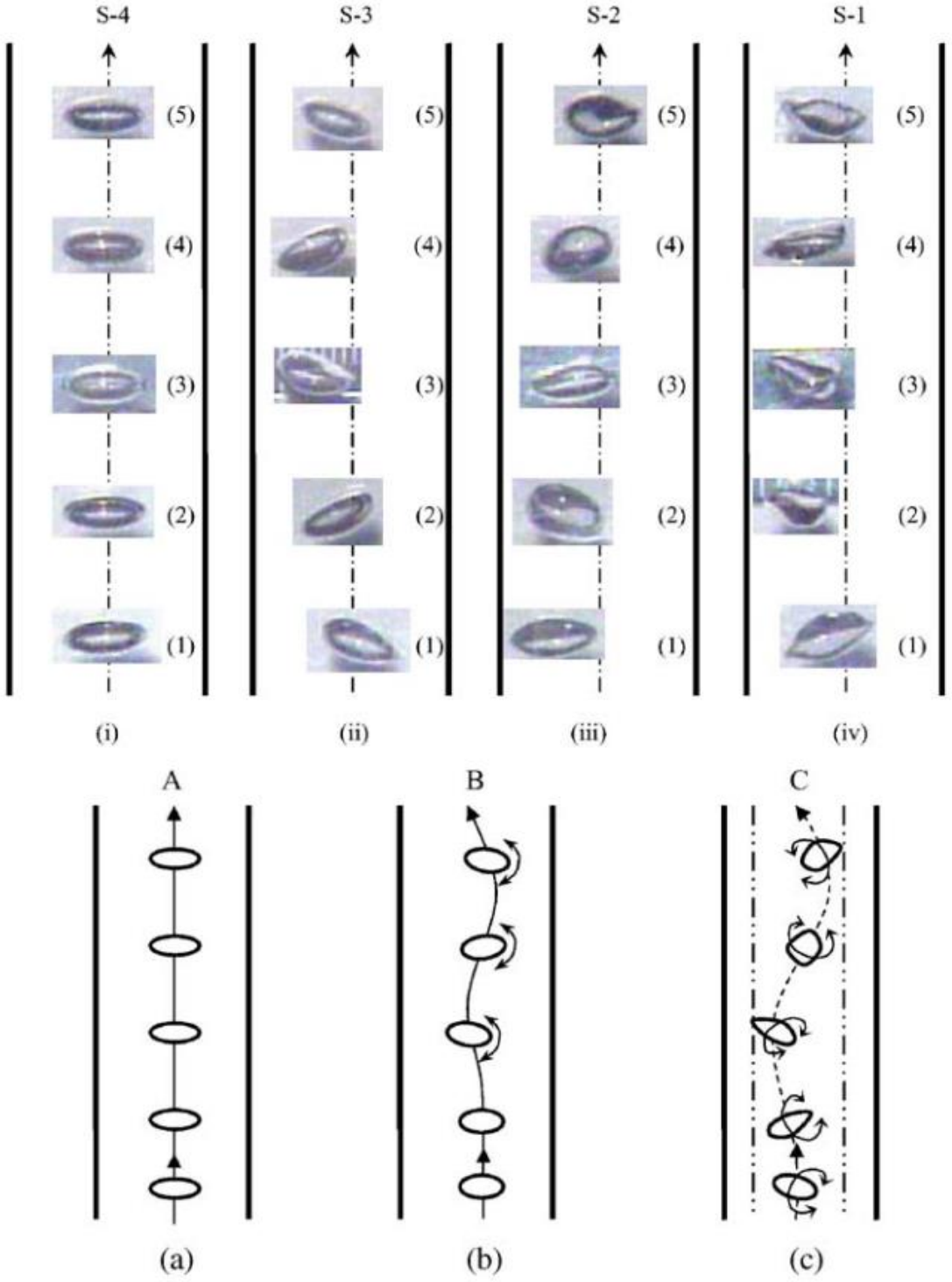

Figure 3.20 - Bubble trajectory captured by digital camera in liquid (i) S-4, (ii) S-3, (iii) S-2, and (iv) S-1; and model trajectory: (a) trajectory A - straight line in liquid S-4; (b) trajectory B - Zigzag in liquid S-3; (c) trajectory C - Spiral in liquids S-2 and S-1 (Liu *et al.*, 2005).

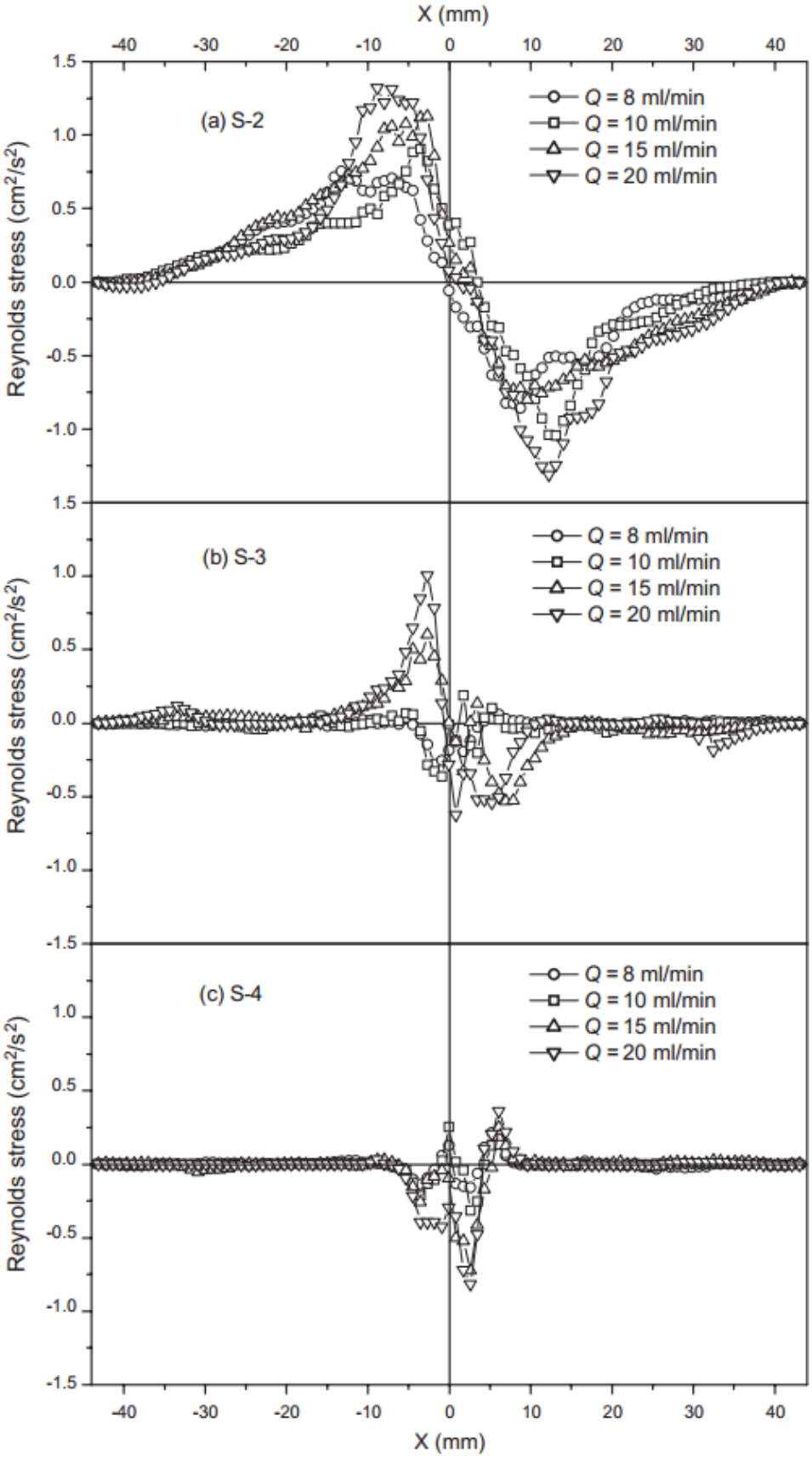

Figure 3.21 - Reynolds stress profiles across the column of liquid (a) S-2, (b) S-3, and (c) S-4 (Liu *et al.*, 2005).

Seol and Socolofsky (2008) developed a simple phase separation method using vector post-processing techniques to measure velocity fields in a bubble plume. The experimental setup is presented in Figure 3.22. The fluorescent particles contained rhodamine 6G and dichlorofluorescein with a size distribution of 20–100 μm were used. Fluorescent-PIV data were used for validation. In addition, a third dataset was derived by applying a digital mask to remove bubbles from the mixed-phase images. All datasets were processed using cross-correlation. The scheme of the vector post-processing algorithm applied for phase discrimination of the mixed-phase PIV vector maps is presented in Figure 3.23. In the mixed-phase vector field, a maximum velocity threshold for the continuous-phase velocities and the median filter to remove bubble-velocity vectors were applied (Figure 3.24b). In investigation of the bubble-velocity, the two-dimensional median filter was applied to a raw image to remove noise and reduce the intensity of the fluorescent tracer particles. An intensity threshold was used to remove the remaining continuous phase tracers. The PTV algorithm was used to obtain the bubbles velocities (Figure 3.24d).

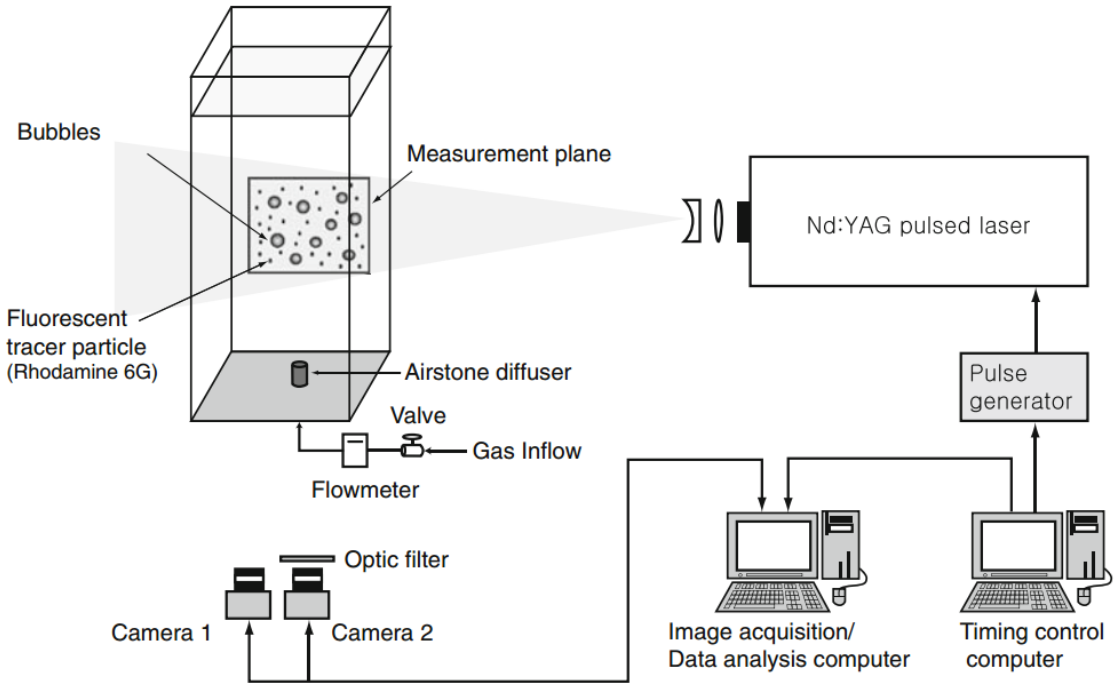

Figure 3.22 -Experimental setup (Seol and Socolofsky, 2008).

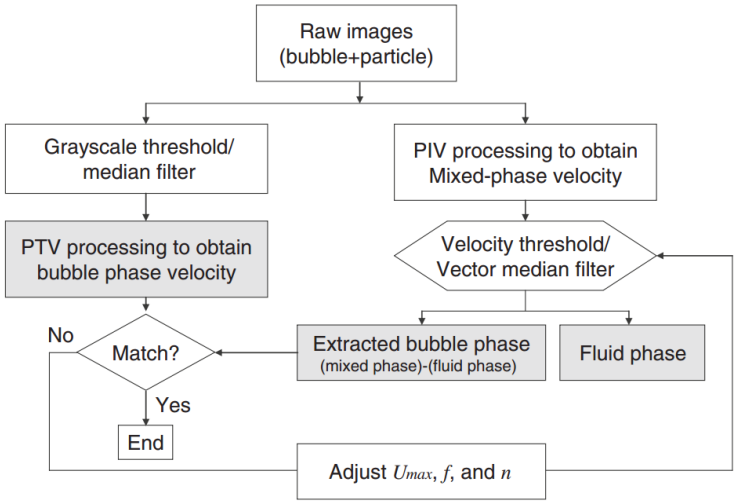

Figure 3.23 – Scheme of the vector post-processing algorithm applied for phase discrimination of the mixed-phase PIV vector maps (Seol and Socolofsky, 2008).

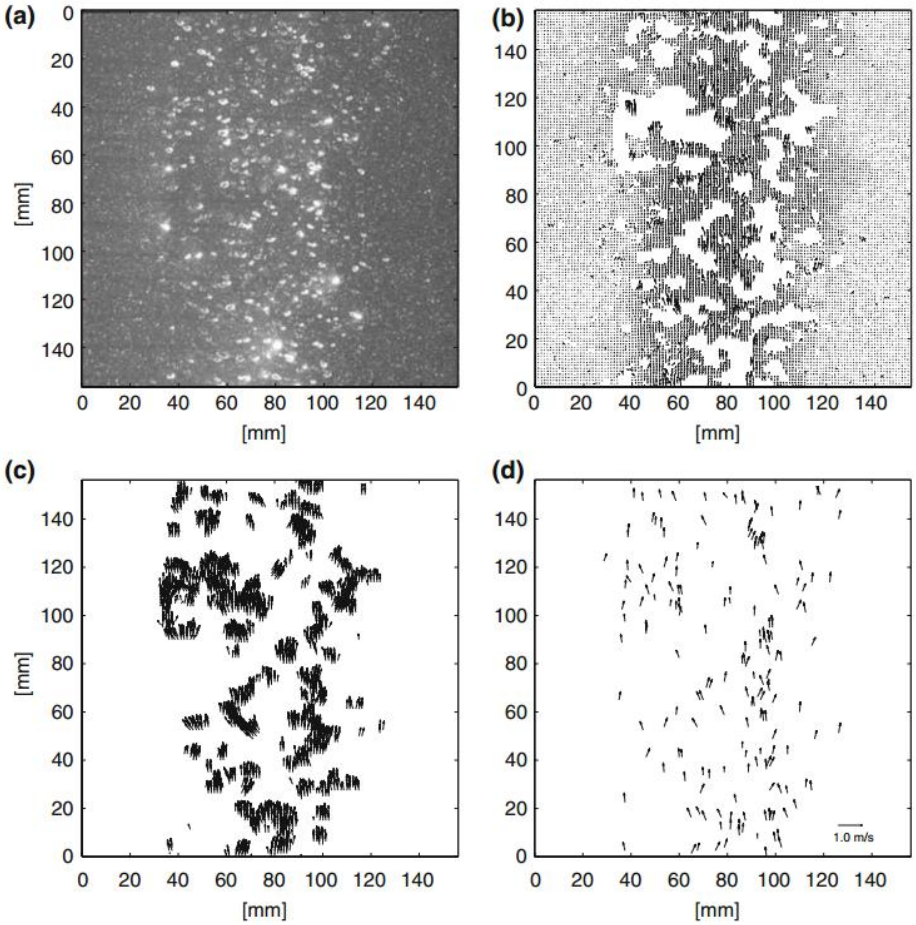

Figure 3.24 – (a) Raw image, (b) post-processed fluid-phase velocity field, (c) post-processed dispersed-phase velocity field, and (d) PTV-processed dispersed-phase velocity vector (Seol and Socolofsky, 2008).

The comparison among the methods shows that the algorithm predicts well both instantaneous and time average statistical quantities for flows having 10% or less of the field of view occupied by bubbles. In addition, the authors observed that the velocity around the bubbles in the post-processed data are higher than nearby continuous-phase vectors and sometimes show significant differences from the optically filtered data. In Figure 3.25, in the regions immediately around a few bubbles (wake regions), some vectors are identified as fluid-phase velocities by the post-processing algorithm, which are much greater in magnitude than corresponding vectors measured in the optically filtered data. In the correlation maps (Figure 3.26), the authors observed that the cross-correlation field for the mixed-phase image showed one distinct displacement peak and two secondary peaks. On the other hand, the cross-correlation field from the optically filtered image had only one peak, and this peak is at the same position as the second highest peak in the mixed-phase image.

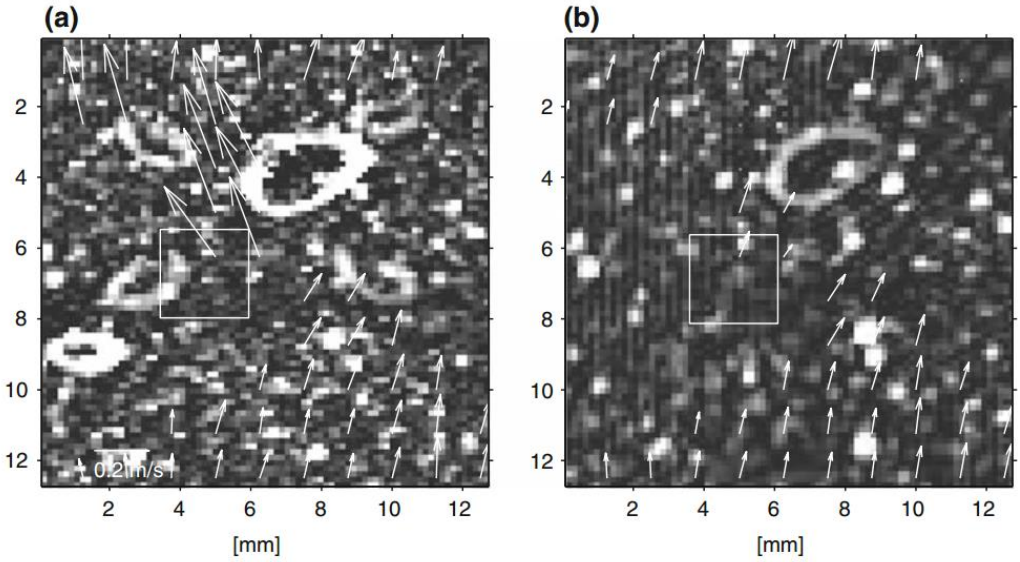

Figure 3.25 - Samples of fluid-phase velocity vector maps: (a) vector post-processed PIV and (b) optic-filtered PIV. The white box is the interrogation window investigated in Figure 3.26 (Seol and Socolofsky, 2008).

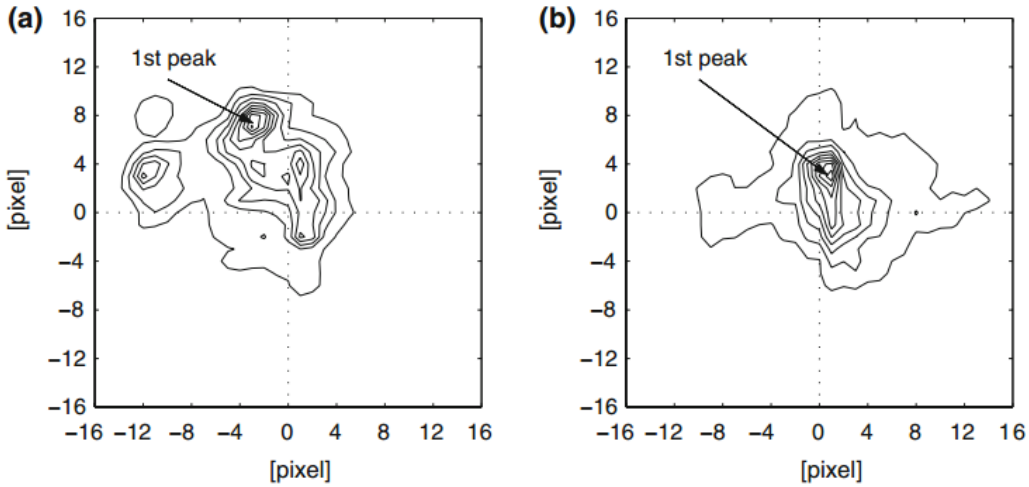

Figure 3.26 – The correlation maps of the interrogation window for (a) mixed-phase image and (b) optically filtered image. The size of interrogation window was 16 x 16 pixels (Seol and Socolofsky, 2008).

Bröder and Sommerfeld (2009) used a planar shadow image velocimetry system to analyze the hydrodynamics and bubble behavior in a bubble column. The system consists of a background illumination utilizing a LED-array and a single CCD-camera which records simultaneously bubble and tracer images (Figure 3.27). The PIV and PTV approaches were used to determine the velocities of the liquid phase and bubbles, respectively.

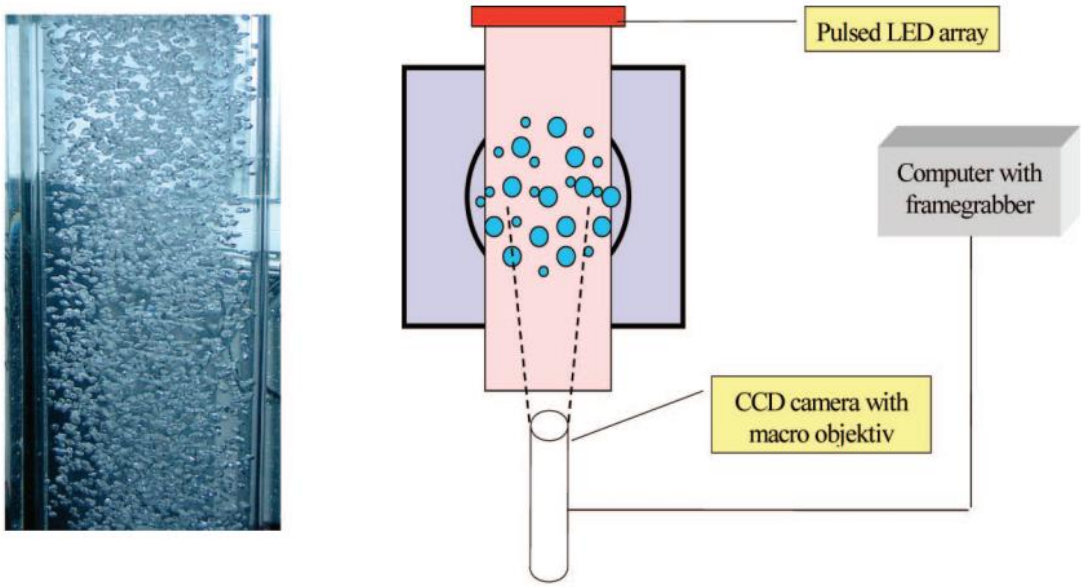

Figure 3.27 - Experimental setup investigated by Bröder and Sommerfeld (2009).

The gas holdup was lower than 5% and the fluctuation energy of the continuous phase was considerably lower than that of the bubble phase. In addition, the bubble mean diameters

were between 2 and 3.8 mm. Filter operations were carried out for phase discrimination (Figure 3.28). The Laplacian of Gaussian (LOG) edge filter was applied with a standard deviation corresponding to the image size of the tracer particles. The resulting image B presented the in-focus tracer images as well as images from the sharply depicted bubbles. An image C was produced applying a 3 × 3 median filter on image B highlighting the edges of the bubbles. Finally, the image B was subtracted from the image C and resulting in an image D which only includes in-focus tracer images. An instantaneous flow field of the continuous phase in the bubble column overlapped onto the raw image containing bubble and tracer is presented in Figure 3.29.

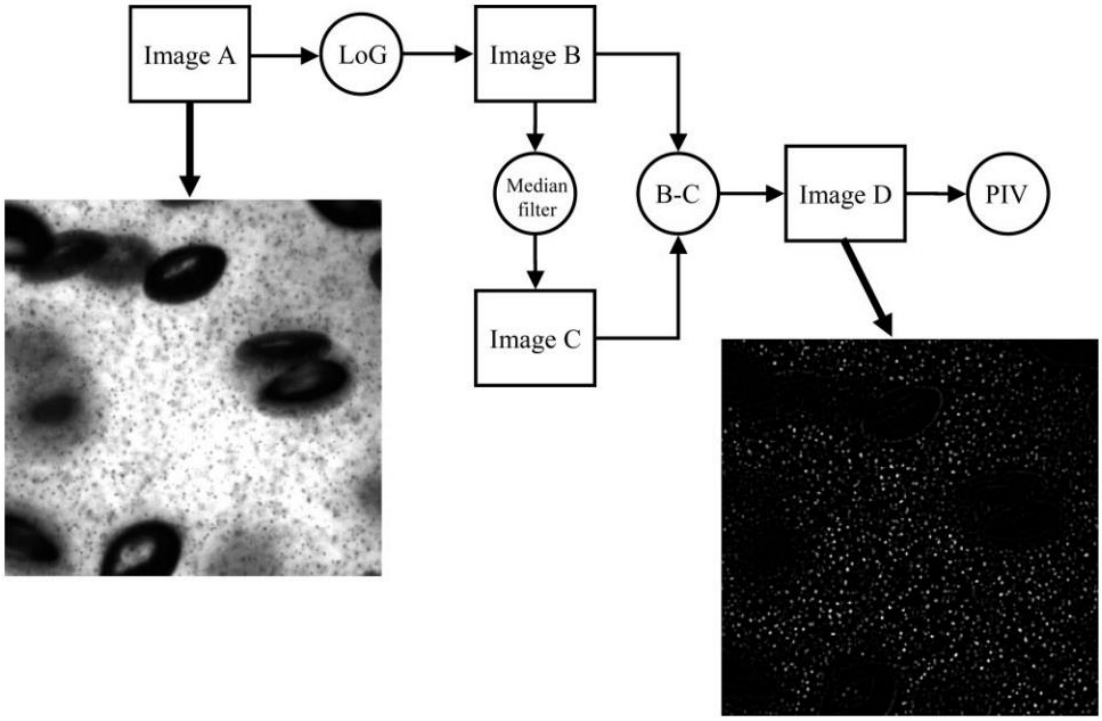

Figure 3.28 - Schematic diagram of the filter operations for phase discrimination by extracting the images of tracer particles from the images of the two-phase flow (Bröder and Sommerfeld, 2009).

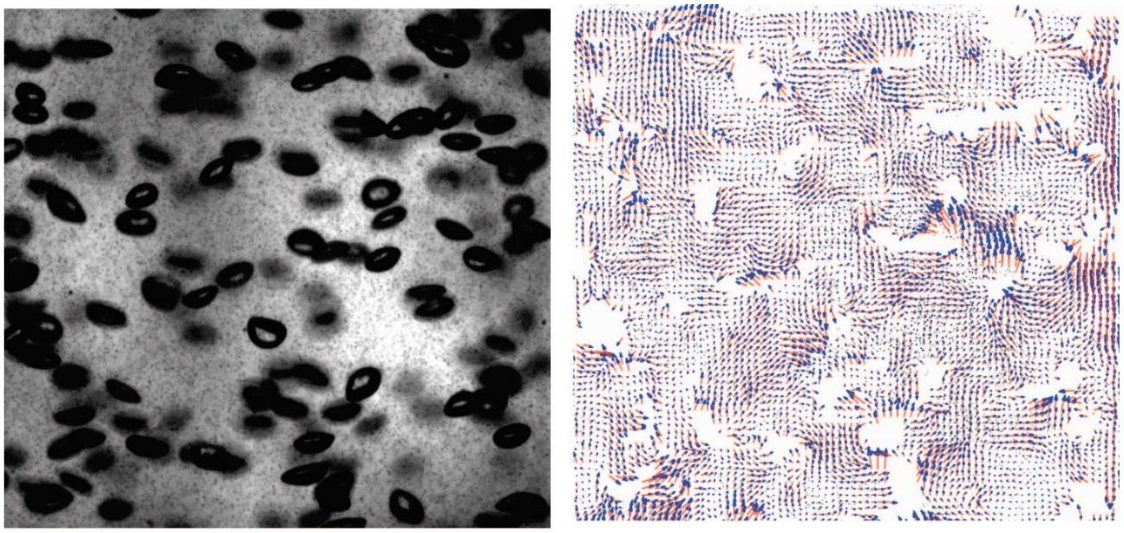

Figure 3.29 – Raw image and instantaneous flow field of the continuous phase (Bröder and Sommerfeld, 2009).

3.2.2. 2D-3C measurements

Ali and Pushpavanam (2011) used 2D-2C and 2D-3C F-PIV measurements to investigate the dynamics of gas-liquid flows in a 2D column (Figure 3.30). In addition, the authors used the PIV measures to validate 2D/3D Euler-Lagrangian simulations. The column used had a square cross-section of 0.2 x 0.2 m, 0.75 m height, and 0.05 m deep. The gas was introduced at the center of the 2D column through a needle. For 2D-2C system, the camera was positioned perpendicular to the plane of the light sheet. For 2D-3C system, both the cameras are mounted on the same side of the light sheet (backward-forward scattering) and the aperture angle between the two cameras was 90º. The calibration error was 0.28 pixel for the 3C-2D system. The authors did not report whether the calibration procedure was also done for the 2D-2C system. Rhodamine was used as tracer particle and an optical filter (λ = 560 nm) was used on camera. Four hundred image pairs were taken for gas flow rates varying from 0.2 to 1 L/min. The results presented by the authors showed that the 2D-2C and 2D-3C measurements did not show the same flow pattern. In velocity component profile of the Figure 3.31, the number of peaks or wave cycles presented was different for both systems. According to the authors, the out-of-plane velocity component (w) is responsible for this difference.

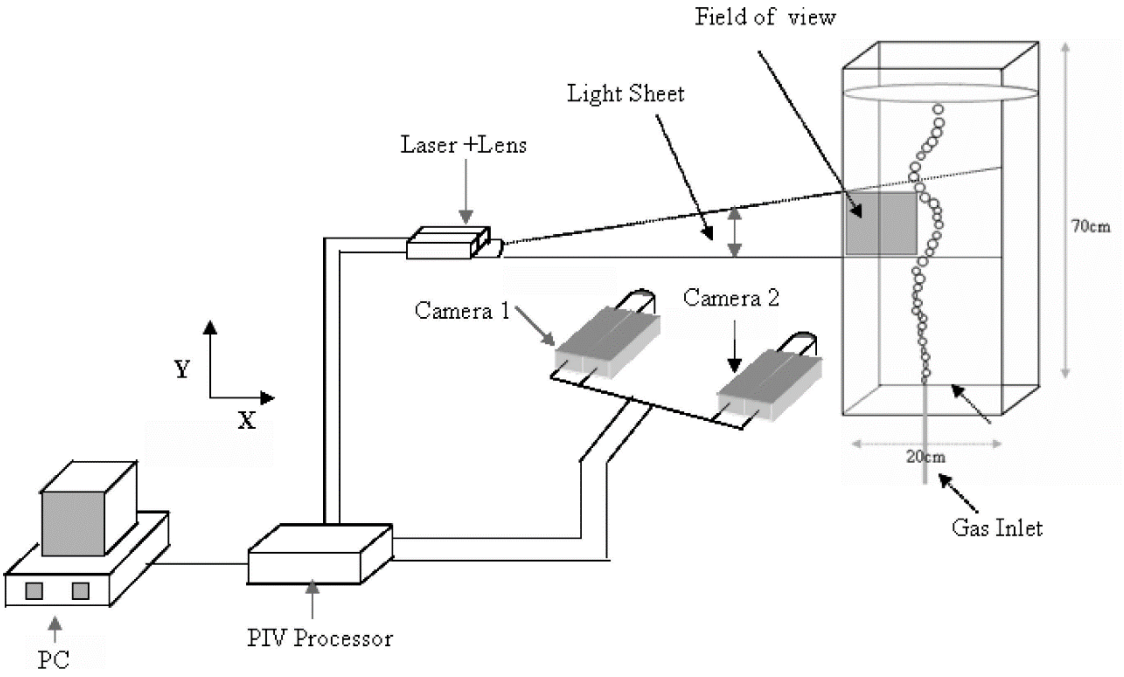

Figure 3.30 - Schematic diagram of experimental setup used by Ali and Pushpavanam (2011).

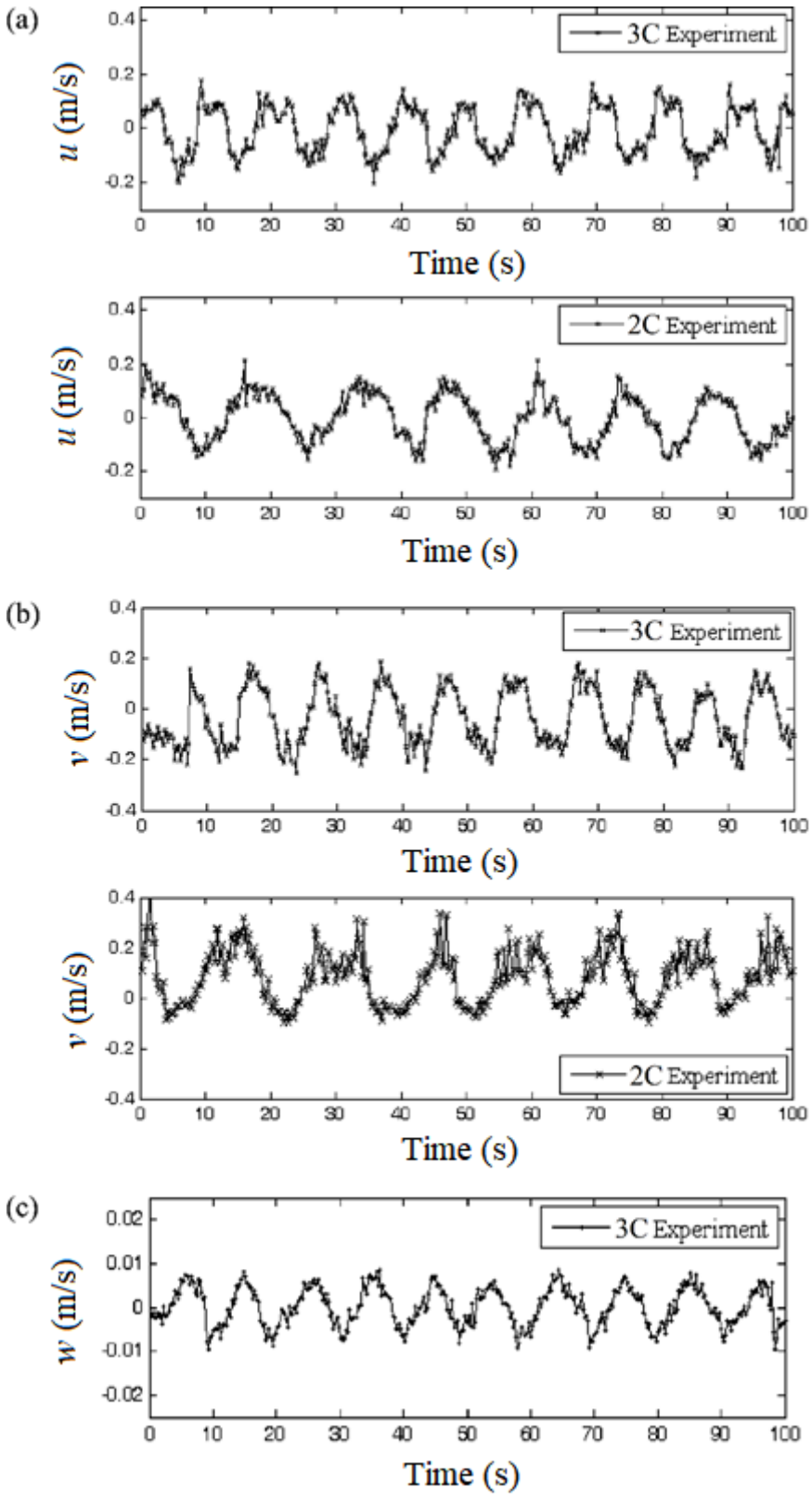

Figure 3.31- Temporal variation of instantaneous liquid velocity at a point obtained using 2D-2C and 2D-3C PIV measurement for a gas flow rate of 0.4 L/min. (a) *u*, (b) *v*, and (c) *w* (Adapted from Ali and Pushpavanam, 2011).

Yoshimoto and Saito (2010) used a 2D-3C F-PIV system to investigate the surrounding liquid motion of the bubble in an acrylic water vessel (0.16 × 0.16 × 0.3 m, Figure 3.32). The liquid phase used was water. In addition, the height of the liquid was 0.23 m. 2D-3C measurements were done at several depth positions sliced by laser sheet to investigate the 3-D structure of the liquid motion around the bubble. Rhodamine B as tracer particle and a sharp cut filter (threshold of 560 nm) to remove the scattering light from the bubble surface were used. Two sets of high-speed video cameras (2000 frames/sec) were used. The angle between the optical axes of the cameras was 45 degrees and the spatial resolution of the imaging system was 12 μm/pixel. LED light was also used to visualize the bubble motion. Furthermore, LIF/HPTS method was used to visualize the wake of a CO_2 bubble. A comparison between the results of the 2D-3C F-PIV and those of the LIF/HPTS is presented in Figure 3.33.

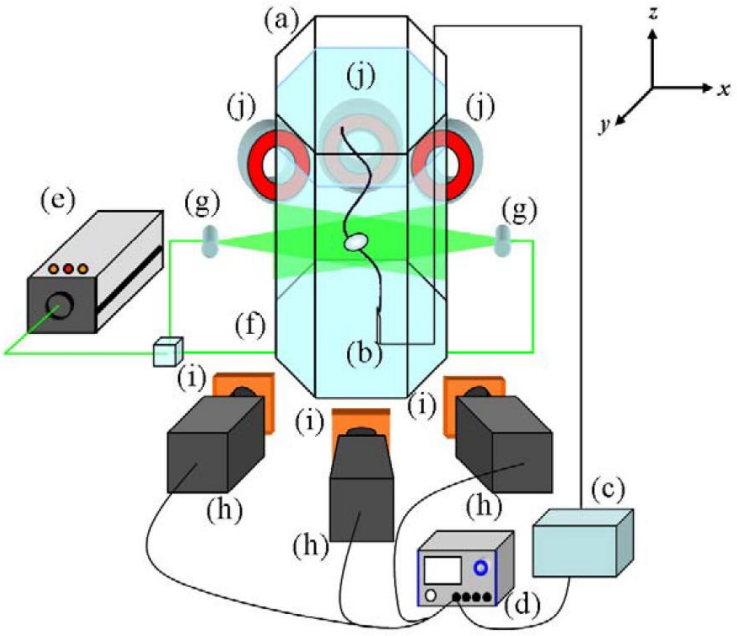

Figure 3.32 - Experimental setup for Stereo PIV used by Yoshimoto and Saito (2010). (a) Water vessel, (b) needle, (c) bubble launch device, (d) function generator, (e) ND: YAG Laser, (f) water and PIV particle, (g) rod lens, (h) Hi-speed video cameras, (i) sharpcut filter, and (j) LED (Yoshimoto and Saito, 2010).

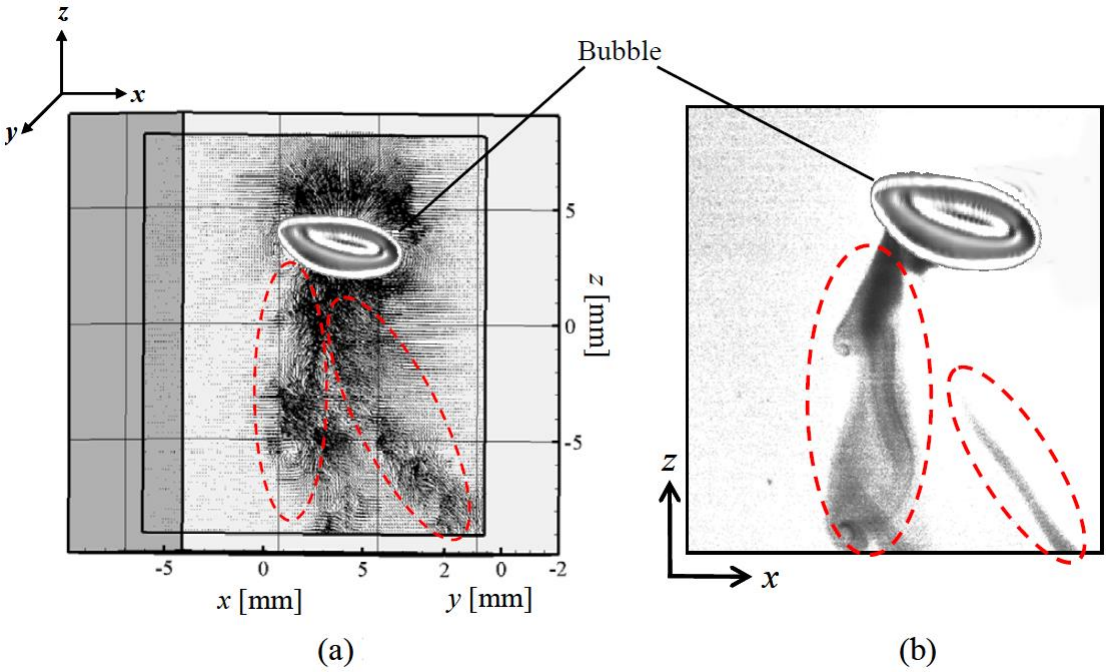

Figure 3.33 - Comparison between the results of the (a) 2D-3C F-PIV and those of the (b) LIF/HPTS (Adapted from Yoshimoto and Saito, 2010).

3.2.3. Quality analysis of the PIV measurements

Although a dewarping function was developed by Soloff *et al*. (1997), the distortions in PIV measurements caused by the wall of the column or by the camera lens were not investigated by the authors presented in section 3.2.1 and 3.2.2. In addition, the effect of variation of the image magnification was not analyzed or compensated, except for Bröder and Sommerfeld (2002).

Most PIV applications were investigated in dilute systems (low bubble concentration - low hold up). In addition, the authors presented in section 3.2.1 and 3.2.2 reported problems related to shadows, light reflections, and the presence of bubbles in the generation of false vectors (outliers). However, the quality analysis of the measurements was non-existent or was not detailed in the studies. Deen *et al.* (2000) used the SNR > 1.2 as a quality factor to eliminate the false vectors in the PIV post-processing. Lindken and Merzkirch (2002) and Bröder and Sommerfeld (2002) also used a SNR criterion, but the limit value was not presented. Seol and Socolofsky (2008) studied the effect of the presence of the bubbles on the correlation peak. However, the authors used the post-processed field as a reference to estimate the measurement error.

In PIV analysis, a limit value of the SNR that guarantees the quality of the measurements has not yet been established. This is because the noise in the correlation plane is more related to the shape of the peak. Although the uncertainty is based on the symmetry of the correlation peak, the CS method (Section 2.3) is not robust to the image noise and out-of-plane motion according to Wieneke (2015).

In the scenario of PIV applications in a bubble column represented in Figure 3.34, this thesis seeks to answer the following questions:

1. Which PIV parameters in the correlation plane or vector field can we use as quality indicators?
2. What are the effects of the dominant noise sources in the experiments?
3. What PIV quality indicators exhibit the same behavior of the dominant noise?
4. In what experimental conditions in the bubble column and PIV processing can we obtain reliable data?
5. How can we compensate or decrease the effect of the dominant noises in velocity fields?

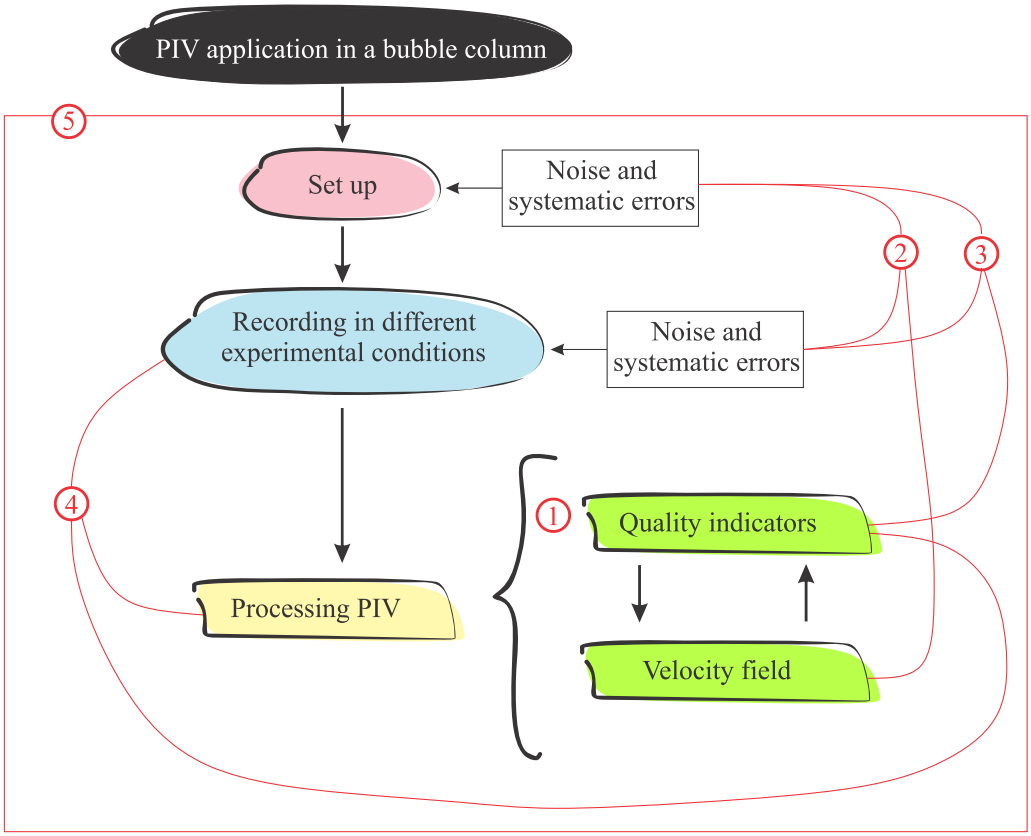

Figure 3.34 - Application scenario of this thesis in the investigation of the quality of the PIV measurements in a bubble column.

CHAPTER 4.

THE BUBBLE COLUMN AND MEASUREMENT SYSTEMS

This chapter presents the characteristics and operating conditions of the bubble column and the configurations of the F-PIV systems used in this work.

The experimental apparatus used to obtain a homogeneous illumination of the laser light sheet and to avoid reflections of the environment are presented.

For the imaging system, a preliminary evaluation of the angle between the cameras and the light sheet based on the best light scattering of the tracer particles is discussed in detail. In addition, the possible configurations and angle of the cameras for 2D-3C F-PIV system are also discussed.

In recording, the interframe time and laser power are displayed for each gas surface velocity.

The optimization of the experimental setup in this chapter is fundamental to ensure the performance of the image processing presented in Chapter 5.

4.1. BUBBLE COLUMN AND F-PIV SYSTEMS

The experimental tests were carried out using an acrylic bubble column of 0.145 m diameter and 1 m height (Figure 4.1a) developed by Silva (2011). The column was filled with water at 298 K and air was fed with a superficial gas velocity (U_G) of 0.152, 0.528, 2.106, and 4.212 cm/s. According to the correlations developed by Shah *et al.* (1982) shown in Figure 3.2, the column presents a homogeneous regime at U_G = 0.152, 0.528, and 2.106 cm/s and homogeneous–heterogeneous regime transition at U_G = 4.212 cm/s. The investigation area was located 0.552 m from the distributor and had a size of 0.14 × 0.10 m. An acrylic box filled with water was used in the investigation area to reduce the distortion effect caused by the curvature of the column. The height of the liquid in the column was 0.8 m. A plane plate with 21 holes (10^{-3} m in diameter) equally distributed was used as the distributor in a square array (Figure 4.1b). In the region immediately before distributor (Figure 4.1c), glass spheres with 2 mm of diameter were positioned to ensure a better distribution of the gas inside the column.

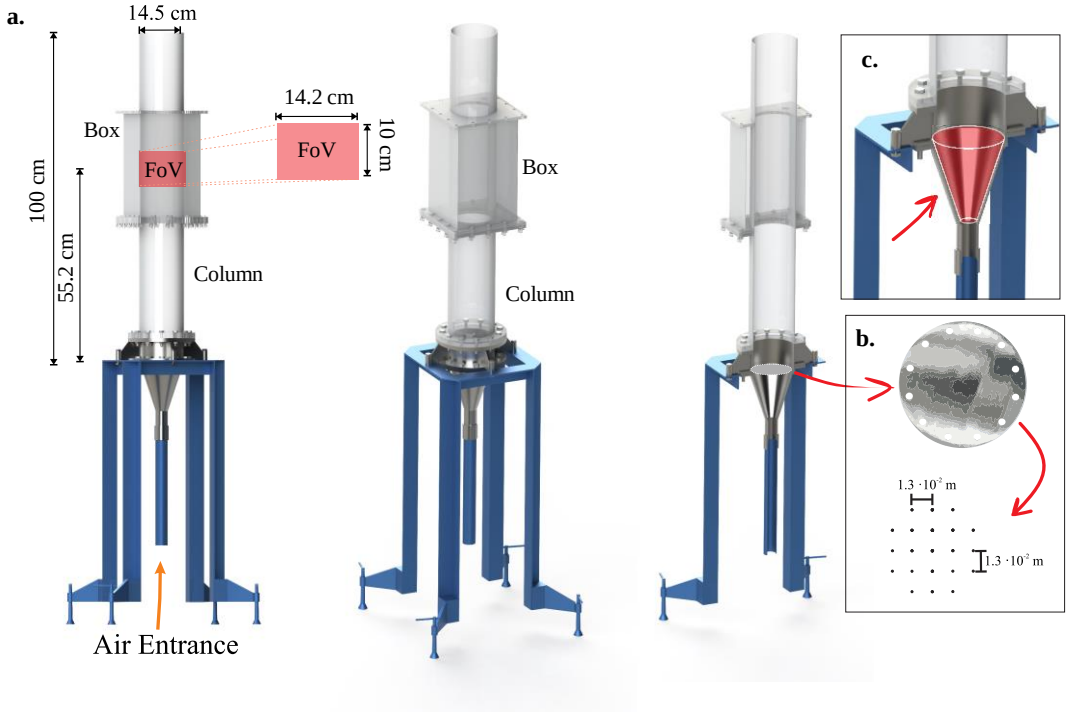

Figure 4.1 – (a) Acrylic bubble column developed by Silva (2011). (b) Air distributor. (c) Region filled with glass spheres.

The F-PIV systems were developed by LaVision. The cameras (two "*Imager Intense cross correlation*" CCD camera 12 bits with 1376 x 1040 pixels and 1376 x 1024 pixels) and laser system (Nd:YAG, 200 mJ/pulse and λ = 532 nm) can be controlled with a programmable time unit (PTU) by Davis 8.2 software. An objective lens with focal distance of 60 mm

(F/2.8D), Rhodamine-B (diameter of 20–50 μm) as tracer particle, and a high-pass filter on the camera that allows only the passage of emitted light by tracer (λ = 620 nm) were used. The fluorescent particles are based on poly(methyl methacrylate) and they were supplied by LaVision. The fluorescent dye was homogeneously distributed over the entire particle volume. The concentration of the tracer particles is limited by its high cost and safety (see Pedocchi *et al.*, 2008).

4.2. ILLUMINATION

The laser head was located 1.2 meters from the column so that the laser beam could be expanded through a cylindrical lens producing a light sheet (Figure 4.2). Before reaching the column, the expanded light sheet (Gaussian distribution) passed through a slit (12 x 0.4 cm) to produce a more homogeneous light intensity profile (top-hat intensity profile). The thickness of the light sheet was 4.2 $\cdot 10^{-3}$ m. In addition, the use of a box with a slit (Figure 4.3) aims to prevent a large amount of light to reach the column. Black cloths were used to avoid reflections of light caused by the wall of the column and screws (Figure 4.4). These reflections can saturate the image and damage the CCD sensor.

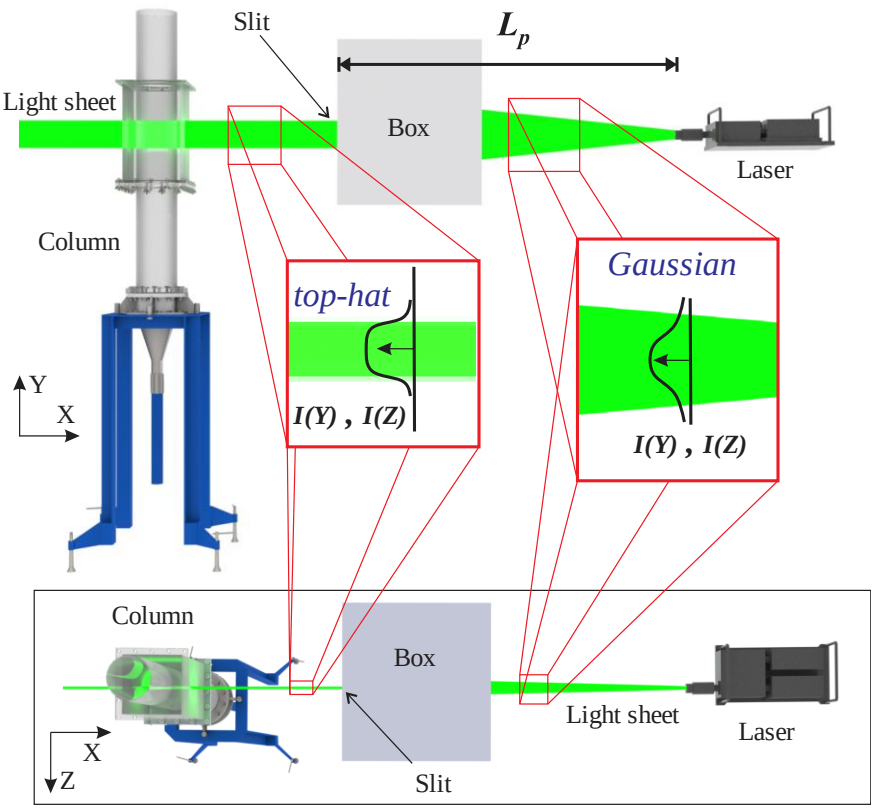

Figure 4.2 - Formation of the top-hat intensity profile by the slit.

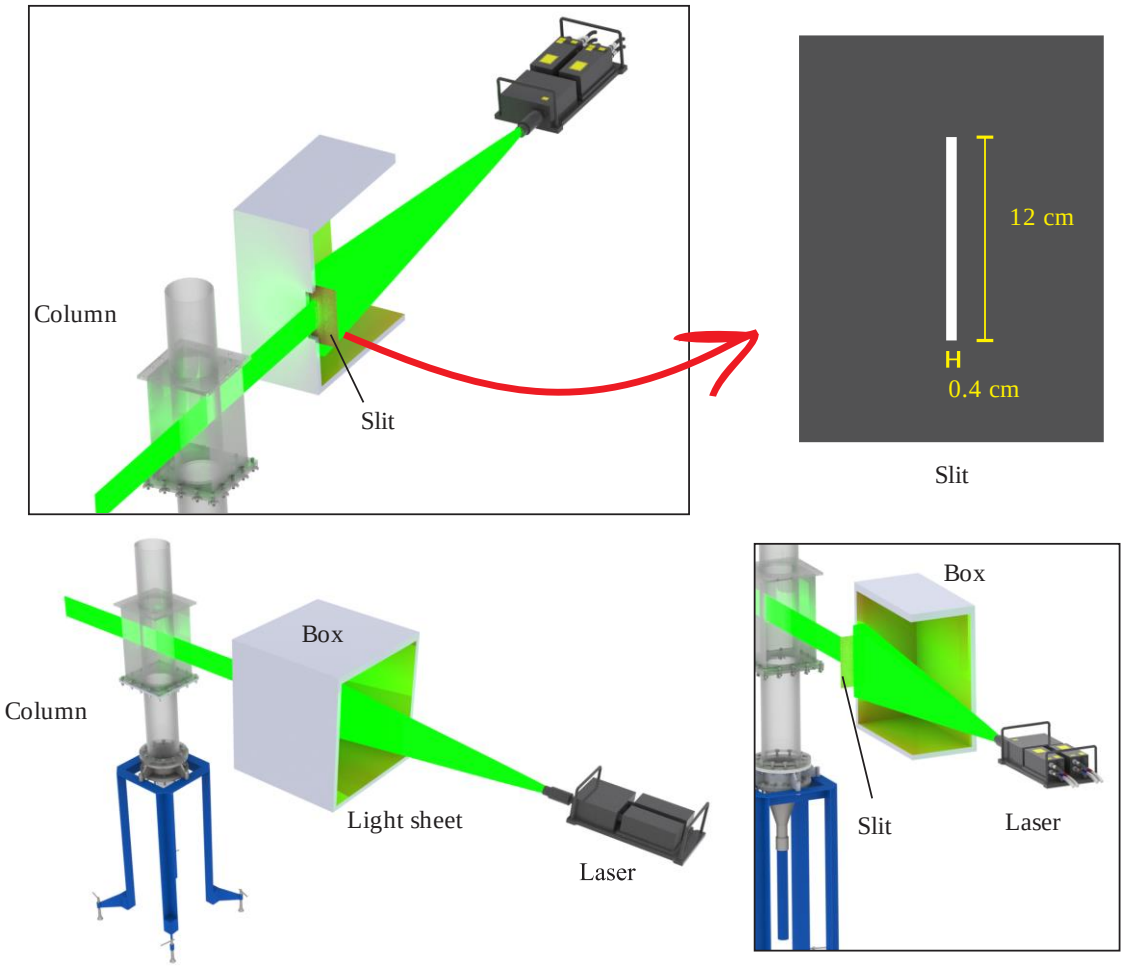

Figure 4.3 – Details of the box with the slot.

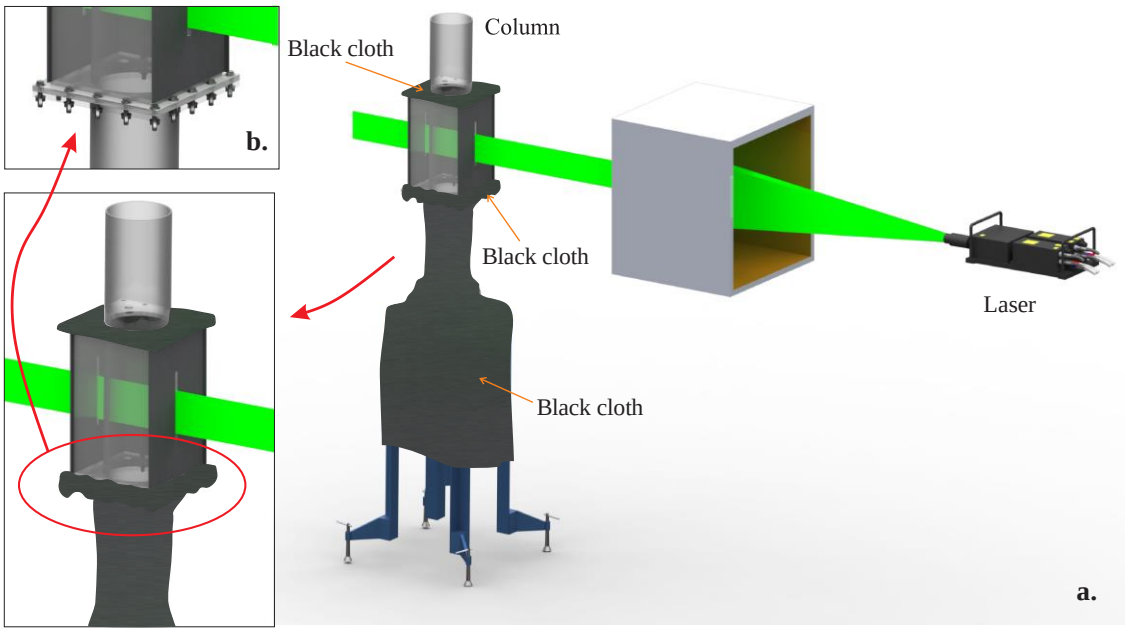

Figure 4.4 – (a) Use of black cloths to avoid reflection of light caused by the wall of the column and (b) screws.

4.3. EVALUATION OF THE CAMERA SETUP

4.3.1. Angle between the light sheet and the camera

The experimental setup used for the evaluation of the camera angle for the 2D-2C PIV system is presented in Figure 4.5. The CCD cameras were placed at an angle β from the light plane in an angular configuration satisfying the Scheimpflug condition. The angle β was chosen based on the study by Broder and Sommerfeld (2002), calibration error and focus of the investigated area. These authors investigated the best angle β to record the smallest amount of light scattered by a cylindrical air bubble in water using geometrical optics. A laser power and interframe time equal to 30 % and $2 \cdot 10^{-3}$ s were used for U_G = 0.105, 0.528, and 1.053 cm/s, respectively. Under these conditions, the bubble column presents a homogeneous regime and the effect of bubble coalescence is not observed.

According to Broder and Sommerfeld (2002), β = 73.9 degrees. However, image distortion and therefore the calibration error are greater when the angle β is smaller. The distortion is minimal when β = 90 degrees and the light reflecting on the column wall is easily registered when $\beta \neq 90$ degrees. A preliminary test evaluating the angles β of 90 and 80 degrees was performed for the camera and 2000 frame pairs were recording. The measurements were made simultaneously. The calibration error for β = 90 and 80 degrees was 0.579 and 0.588 pixel, respectively.

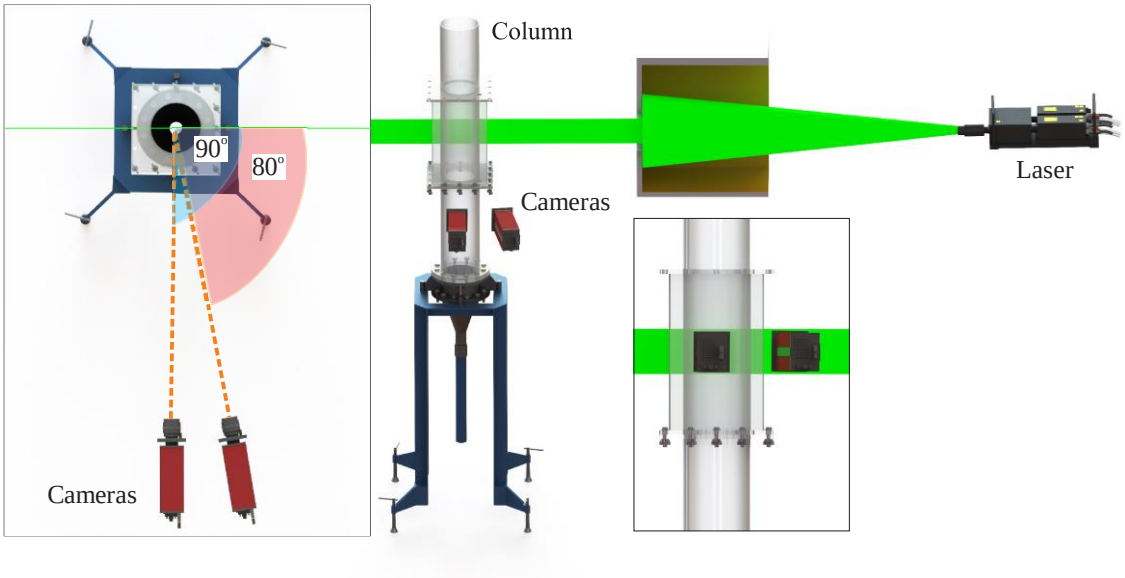

Figure 4.5. Experimental setup used in the evaluation of the camera angle for the 2D-2C PIV system.

The probability density function (PDF) of the time-averaged intensity distribution $\langle I \rangle$ for U_G = 0.105, 0.528, and 1.053 cm/s is presented in Figure 4.6. For 80 degrees, the frame 0 (F0) and 1 (F1) presented a spatial average of $\langle I \rangle, \overline{\langle I \rangle}$, of approximately 61 and 82 counts. On the other hand, for 90 degrees, F0 and F1 presented a $\overline{\langle I \rangle}$ of approximately 40 and 69 counts. Table 4.1 shows the detailed values of $\overline{\langle I \rangle}$ for all U_G. In Figure 4.6, the images were not preprocessed and reconstructed. The frames are presented in Figure 4.7 for U_G = 0.105 cm/s and in Figure A1 and A2 (Appendix A) for U_G = 0.528 and 1.053 cm/s.

The difference between F0 and F1 was approximately 30 counts for β = 90 degrees and 20 counts for 80 degrees. F1 had a larger background illumination due to the light scattering of the first laser pulse. This large light scattering is observed in the width of the PDF curve mainly for β = 90 degrees. Then, the β value chosen was 80 degrees based on the recording of the lowest background illumination.

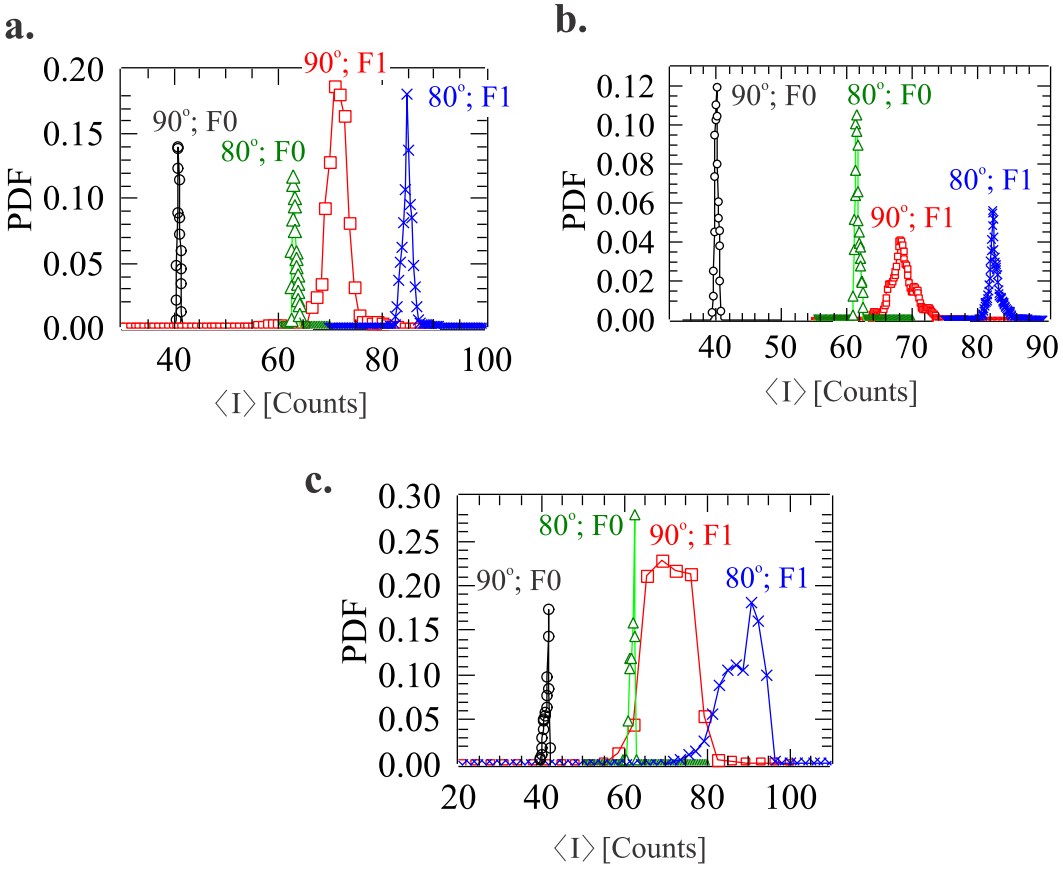

Figure 4.6 – Probability density function (PDF) of the time-averaged intensity distribution $\langle I \rangle$ in frame 0 (F0) and 1 (F1) of the camera A with a 2θ equals to 80 and 90 degrees without PIV preprocessing for U_G = (a) 0.105, (b) 0.528, and (c) 1.053 cm/s.

Table 4.1 - Spatial average of in frame $\langle I \rangle$, $\overline{\langle I \rangle}$, for U_G = 0.105, 0.528, and 1.053 cm/s.

U_G [cm/s]	$\overline{\langle I \rangle}$ [Counts] for 90º		$\overline{\langle I \rangle}$ [Counts] for 80 º	
	F0	F1	F0	F1
0.105	40.952	70.963	62.280	83.659
0.528	40.053	68.568	60.663	81.462
1.053	41.160	70.146	61.067	86.312

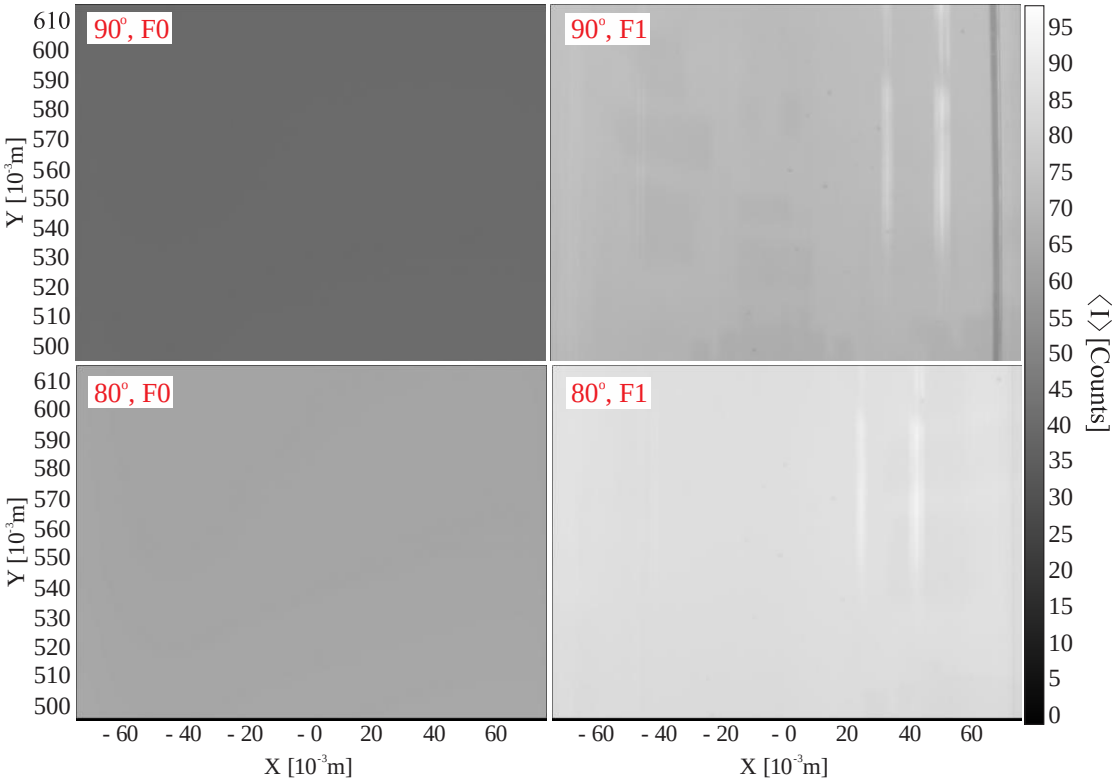

Figure 4.7 - Distribution of time-averaged intensity of the frames 0 and 1 (F0 and F1) for the two camera arrangement presented in Figure 4.5 for U_G =0.105 cm/s.

The scattering of laser light in acrylic wall was observed in recorded images even with the use of black cloths. Some reflections appeared in the second frame mainly due to the light scattering of the environment caused by the first pulse (Figure 4.8).

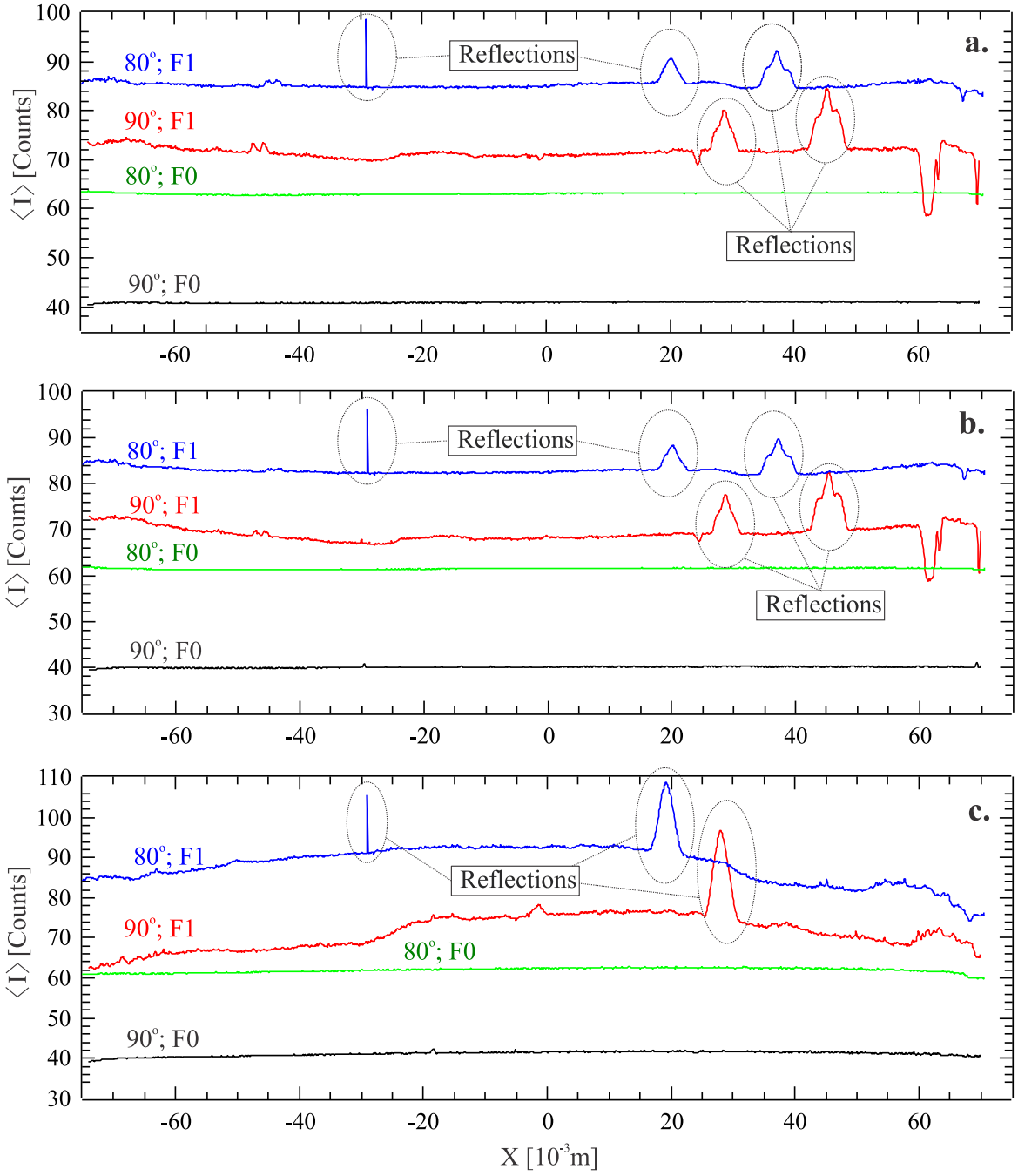

Figure 4.8 - Profile of the time-averaged intensity for the frames 0 and 1 (F0 and F1) at Y = 0.552 m and the two cameras arrangement presented in Figure 4.5 (a) 0.105, (b) 0.528, and (c) 1.053 cm/s.

4.3.2. Aperture angle of the 3C-2D system

The cameras were located in a plane parallel to the axis of the column (Figure 4.9). In addition, the camera plane was 80 degrees from the light sheet (similar to that evaluated in the previous section). An angle $2\beta_{yz}$ = 60 degrees was chosen for the stereo arrangement of the

cameras (camera B) to ensure the quality of the 3C reconstruction based on the investigation carried out by Lawson and Wu (1997). The configuration of the stereoscopic imaging used was angular. In addition, a Scheimpflug adapter was used on each camera to ensure focus in the plane. In Figure 4.9, an angle $2\beta_{yz}$ = 90 degrees (optimal angle) was not chosen due to the large distortion in the bubble column.

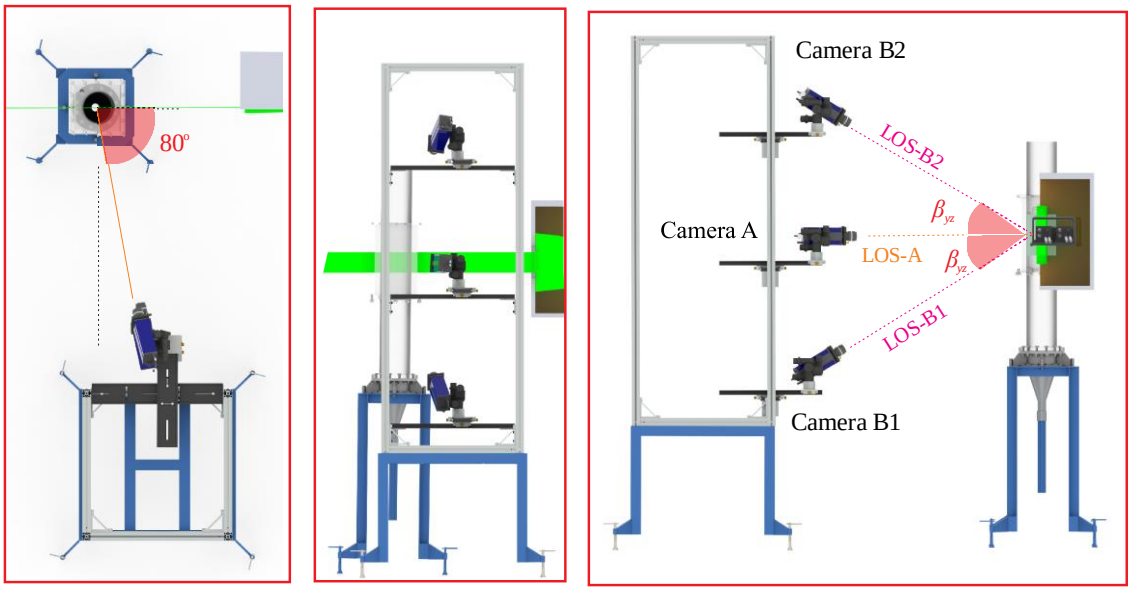

Figure 4.9 - Experimental setup used in the 2D-3C PIV system

The Figure 4.10 presents two possible configurations with the cameras located in a plane cross to the axis of the column. The cameras D observe the tracer particles in a forward scattering direction while the cameras C observe in the backward scattering direction. In stereo configuration, the use of the cameras C1 and D1 (similar to C2 and D2) is not recommended because the cameras C and D register different light scattering directions. The configuration of the cameras D is not ideal because it records large amounts of light from the bubbles and the environment as observed by Broder and Sommerfeld (2002). The disadvantage of using the configuration of the cameras C is mainly in the difficult calibration procedure requiring calibrated two-sided plates. In addition, the light scattering on the wall is more easily observed by the cameras C and D than by cameras B.

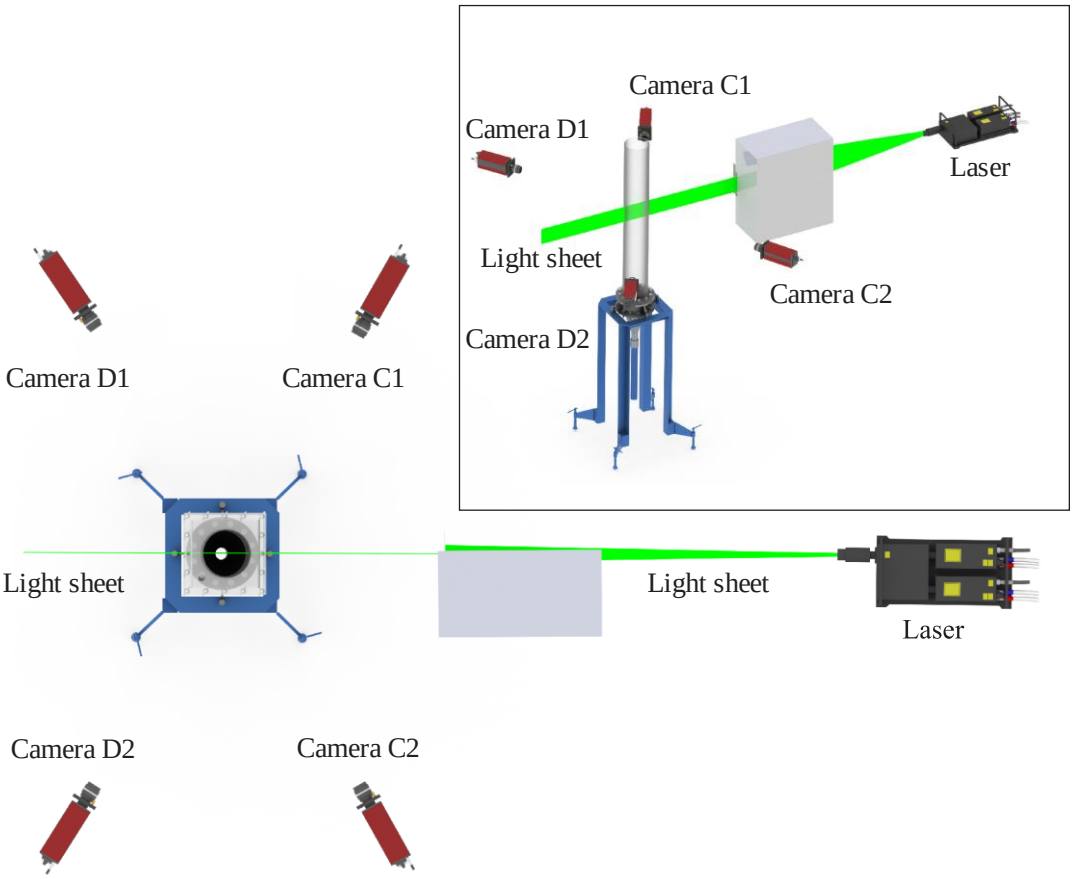

Figure 4.10 – Possible configuration with the cameras located in a plane cross to the axis of the column

4.4. CALIBRATION PROCEDURE

The calibration procedure was performed manually by the previous orientation of the line-of-sight (LOS) of the camera targeting the calibration plate. Two-level calibration plate made of alloy steel developed by LaVision (Figure 4.11) was not used. In addition to presenting a size larger than the diameter of the column, LaVision's plate could scratch the acrylic wall. The calibration plate was created using Inkscape software. The pattern was made with a point diameter and spacing of 0.5 and $2.5 \cdot 10^{-3}$ m, respectively. The real-size calibration plate is presented in Figure B1. The plate was made of plastic corrugated sheet (Figure 4.12). Ideally, the calibration plate should have the maximum points to compensate for the effect of the heterogeneous distribution of the refractive index throughout the plane.

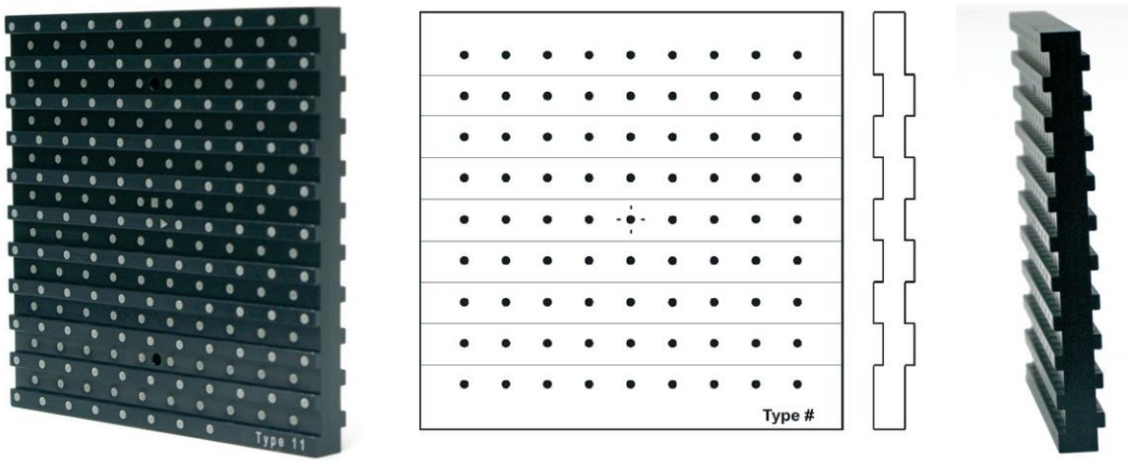

Figure 4.11. Two-level calibration plate made of alloy steel developed by LaVision. (LaVision, 2016)

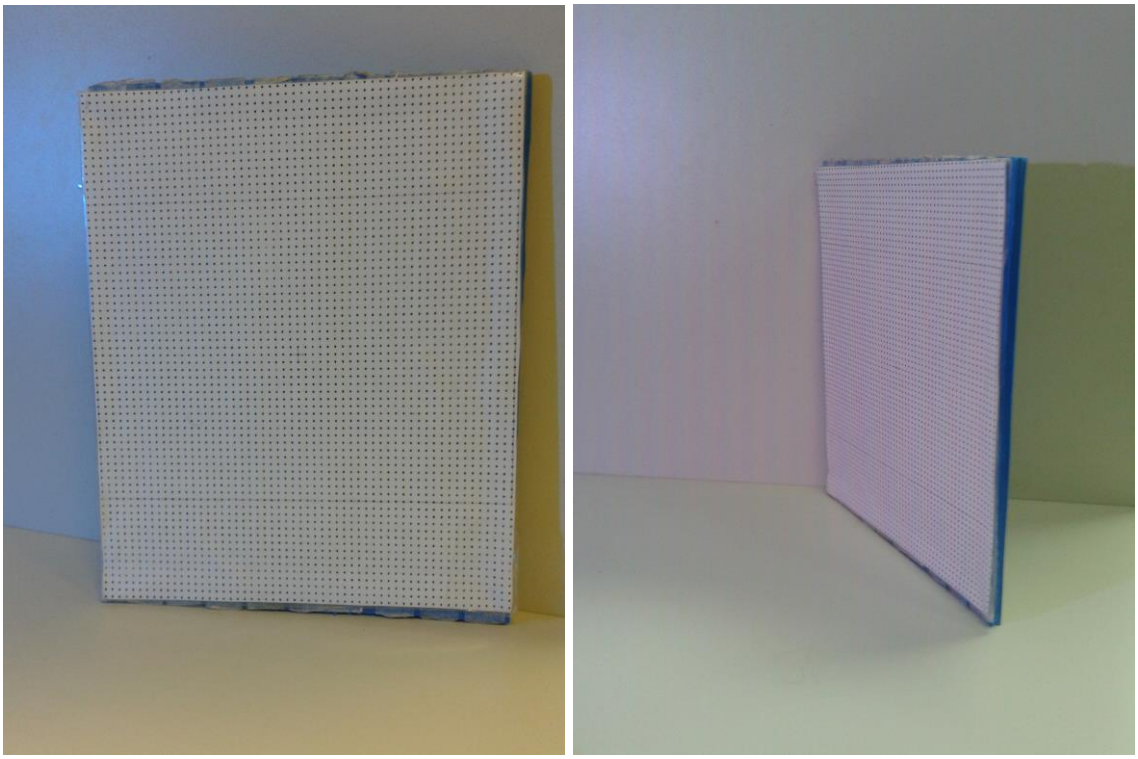

Figure 4.12 - The plate made of plastic corrugated sheet used in the calibration procedure.

A plastic rod and two rubbers were used to support and align the calibration plates with the field of view (Figure 4.13). The calibration plate 1 was fixed on the plastic rod.

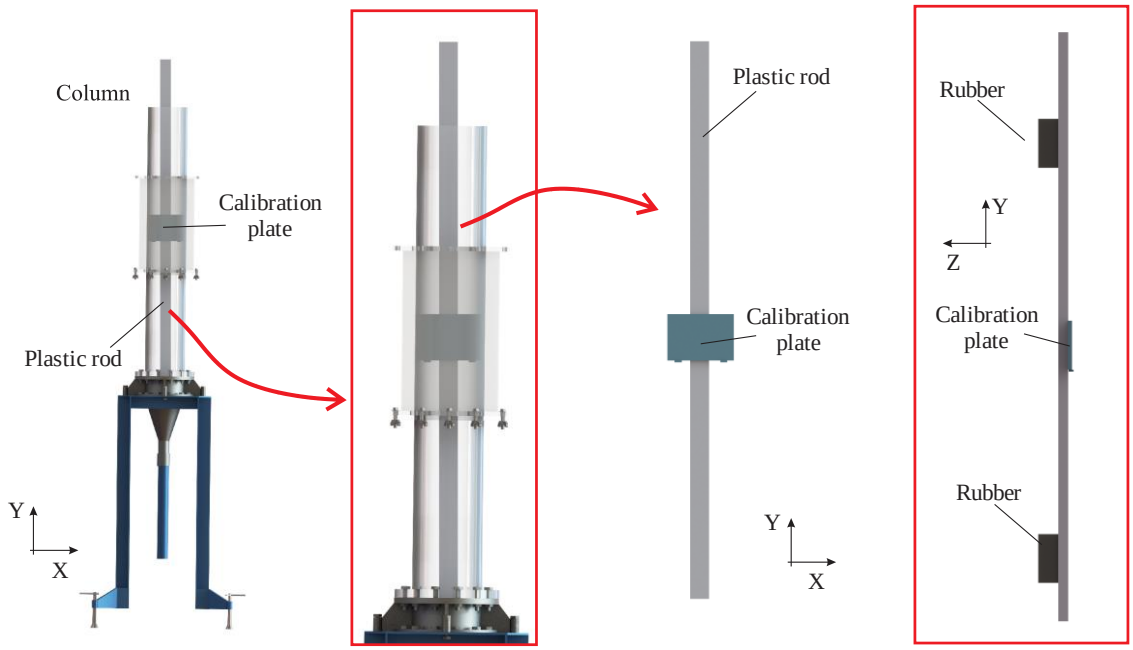

Figure 4.13 - Support and align the calibration plates with the field of view using a plastic rod and two rubbers.

Two Z planes were used for the calibration of the 2D-3C system. The ΔZ variation of the mapping plane was chosen based on the thickness (4.15 mm) of the calibration plate. In Figure 4.14, the calibration plate 1 and 2 represents the plane 0 and -4.15 $\cdot 10^{-3}$ m. After mapping the plane -4.15 mm, the plate 2 was removed with the aid of a string. For the 2D-2C PIV calibration, only the plate 1 (0 mm) was used.

The relation between the physical (X, Y, Z) and the image (x, y, z) coordinates was described by a third order polynomial adjustment (Eq. 4.1), where dX and dY are defined by Eq. 4.2. The dX and dY displacement are determined using the normalized coordinates $s = 2 \cdot (X - X_0)/n_x$ and $t = 2 \cdot (Y - Y_0)/n_y$, where n_x and n_y are the image sizes in pixels. The least squares method was used to determine a mapping function.

The coefficients of the mapping function for the PIV 2D-2C and 2D-3C system are presented in Table 4.2.

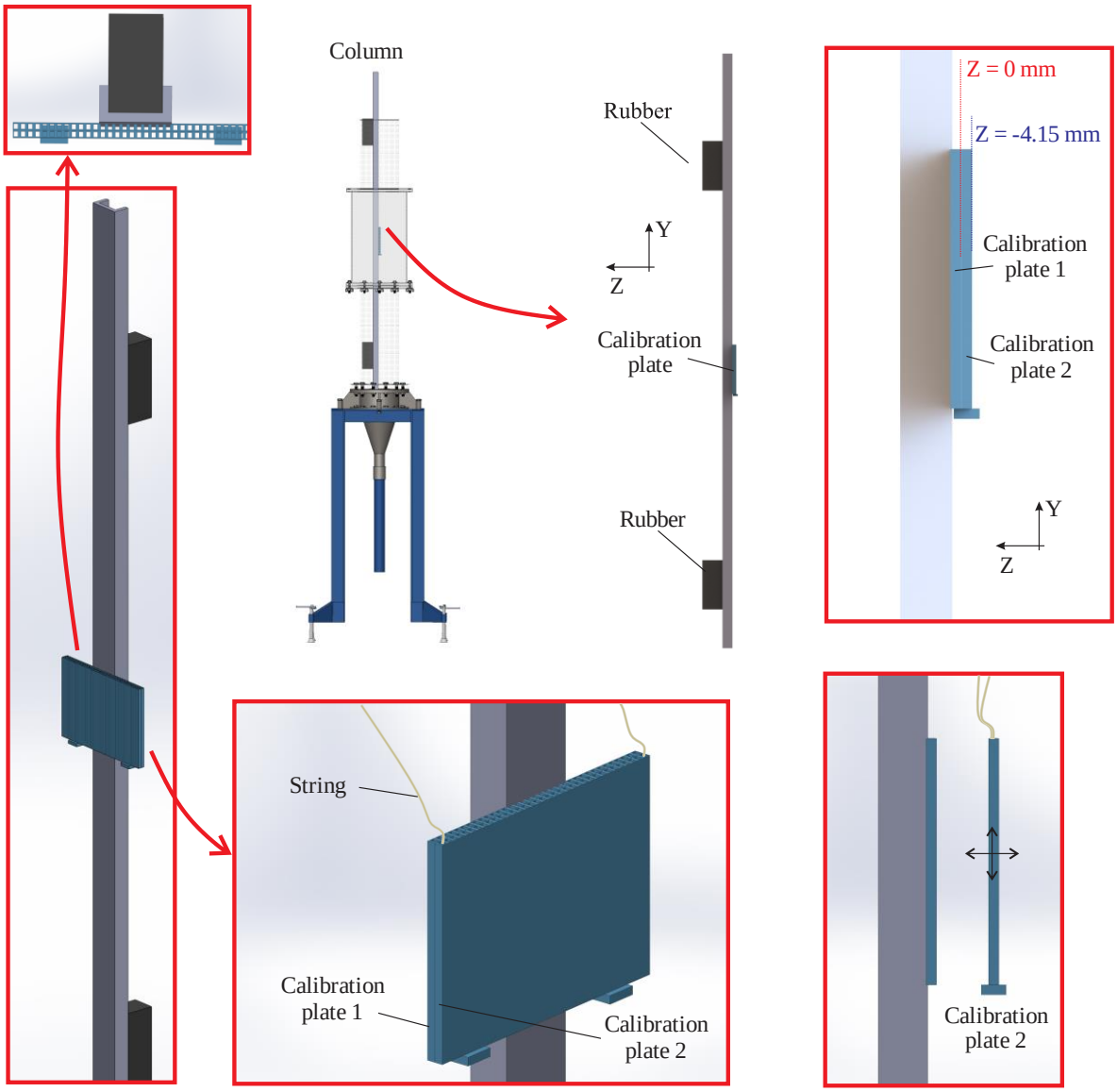

Figure 4.14 - Details of the two-plane calibration for the 2D-3C system.

$$\begin{pmatrix} x \\ y \end{pmatrix} = \begin{bmatrix} X + dX(X,Y) \\ Y + dY(X,Y) \end{bmatrix} \tag{4.1}$$

$$\begin{pmatrix} dX \\ dY \end{pmatrix} = \begin{pmatrix} a_0 + a_1 s + a_2 s^2 + a_3 s^3 + a_4 t + a_5 t^2 + a_6 t^3 + a_7 st + a_8 s^2 t + a_9 st^2 \\ b_0 + b_1 s + b_2 s^2 + b_3 s^3 + b_4 t + b_5 t^2 + b_6 t^3 + b_7 st + b_8 s^2 t + b_9 st^2 \end{pmatrix} \tag{4.2}$$

Table 4.2 - Coefficients of the mapping function for the PIV 2D-2C and 2D-3C system.

Z [10^{-3} m]	Camera A	Camera B1		Camera B2	
	0	0	- 4.15	0	- 4.15
X_0	570.046	721.297	721.297	721.297	721.297
Y_0	619.443	572.144	572.144	572.144	572.144
n_x	1376	1376	1376	1376	1376
ny	1376	1040	1040	1040	1040
a_0	37.117	43.314	34.985	40.109	40.111
a_1	16.887	30.438	31.160	10.984	10.975
a_2	-7.965	-2.061	-1.142	-3.627	-3.617
a_3	-0.030	7.679	13.051	6.537	6.565
a_4	15.164	17.710	12.785	-21.577	-21.591
a_5	1.210	1.573	0.623	1.599	1.568
a_6	0.829	1.928	1.268	2.510	2.589
a_7	-5.045	-16.572	-15.480	12.054	12.066
a_8	0.028	-1.273	-1.449	0.094	0.058
a_9	0.687	2.259	1.907	1.173	1.138
b_0	15.281	41.661	3.270	92.385	92.389
b_1	-3.343	-4.178	-0.493	-17.271	-17.268
b_2	-0.221	4.834	1.196	-7.127	-7.095
b_3	1.625	1.456	1.368	-0.556	-0.563
b_4	2.102	85.724	86.716	69.207	69.167
b_5	-5.330	-11.128	-11.393	9.276	9.186
b_6	1.722	2.981	0.727	0.809	1.043
b_7	-10.984	-1.037	-1.638	-4.668	-4.669
b_8	0.740	-2.458	2.856	4.918	4.810
b_9	1.270	-0.026	-0.154	0.230	0.233

Recorded image of the calibration plate, identification of the marks, and corrected image for the 2D-2C and 2D-3C PIV system are presented in Figure B2 - Figure B5. The average resolution of the imaging system was 10 pixels/mm and calibration error for all the cameras was below 1 pixel (Table 4.3). The ambient light saturated the image of the calibration plate in some regions of different projections. This makes it difficult to identify the points of the calibration plate by the software and contributes directly to the calibration error.

Table 4.3 - Calibration Error

Camera	Plane (10^{-3} m)	Calibration error [pixel]
A	0	0.982
B1	0	0.925
B1	- 4.15	0.925
B2	0	0.976
B2	- 4.15	0.979

4.5. RECORDING PARAMETERS

The 2D-2C and 2D-3C F-PIV measurements were performed separately (not simultaneously). The interframe time and the laser power used in experiments are presented in Table 4.4. The interframe time was chosen to provide a particle image maximum displacement (shift) of 15 - 20 pixels. The laser power was adjusted in each experiment to get the best particle image contrast and to prevent that the reflections of light do not damage the camera even when using the high-pass filter.

Table 4.4 - Interframe time (dt) and laser power used in experiments.

System	2D-2C PIV				2D-3C PIV			
U_G [cm/s]	0.152	0.528	2.106	4.212	0.152	0.528	2.106	4.212
Interframe time (10^{-6} s)	500	1000	1000	1000	1000	1000	1000	1000
Laser power (%)	20	20	35	35	25	35	35	35

Four thousand pairs of frames (N_R) were recorded with a frequency of 4.2 Hz. For $N_R >$ 4000, some instabilities in the PIV system were observed. The effect of these instabilities was observed in the oscillation of the laser system, contributing directly to the heterogeneous distribution of the light intensity in frame. As detailed in Chapter 6, this heterogeneous distribution increases the number of outliers in the vector field. According to Drahoš *et al.* (1991) and Lin *et al.* (1996), the dominant frequency of the flow structures presented in the column is less than 3 Hz for $U_G \leq 4$ cm/s.

CHAPTER 5.

DATA PROCESSING

This chapter presents the image analysis settings used in this work. Parameters and strategies of the PIV preprocessing, processing and post-processing are detailed.

Even using the experimental set up optimized in Chapter 4, some regions with shadows and large scattering of light were observed in the frame. Spatial filters were used and are detailed in preprocessing to reduce the heterogeneous illumination in frame. Moreover, the fluid dynamics effect on recording the light emitted by the tracer particles is discussed.

The interrogation strategies used in this work to provide the highest spatial resolution and best quality of the measurements are presented. In addition, the post-processing filters to correct the noisy fields obtained by the standard cross-correlation (SCC) approach are also detailed.

The quality indicators from the velocity field and the correlation plane are detailed in this Chapter.

5.1. PREPROCESSING

The time-averaged intensity distribution, $\langle I \rangle$, in the 2D-2C and 2D-3C PIV frames for raw image is showed in Figure 5.1. $\langle I \rangle$ is shown for the non-reconstructed images. Besides the cameras with different projections, the bubbles cause an unequal distribution of intensity along the radius and between the frames of each camera. These factors added to the light scattered on the column wall contribute directly to the background illumination. The raw images are showed in Figure 5.2. In PIV preprocessing, two spatial filters are applied to remove the background illumination and improve the particle image contrast. RMS (Root Mean Square) and SSM (Subtract Sliding Minimum) filter of 3x3 pixels were applied sequentially in the recorded images. An upper limit of 50 counts and a pixel intensity lower than 10 counts were used to improve the image contrast. The effect of the PIV preprocessing can be observed by comparing the Figure 5.2 and Figure 5.3.

The bubbles present in the light sheet formed regions with shadows in frame (Figure 5.2, Figure 5.3, and Figure 5.4). This was observed mainly with the increase of U_G. In addition, the region between the cameras and the light sheet was also occupied by the bubbles. These bubbles in front of the light sheet also contribute directly to the shadow regions in the frame by not allowing the light emitted by the tracer particles to leave the column.

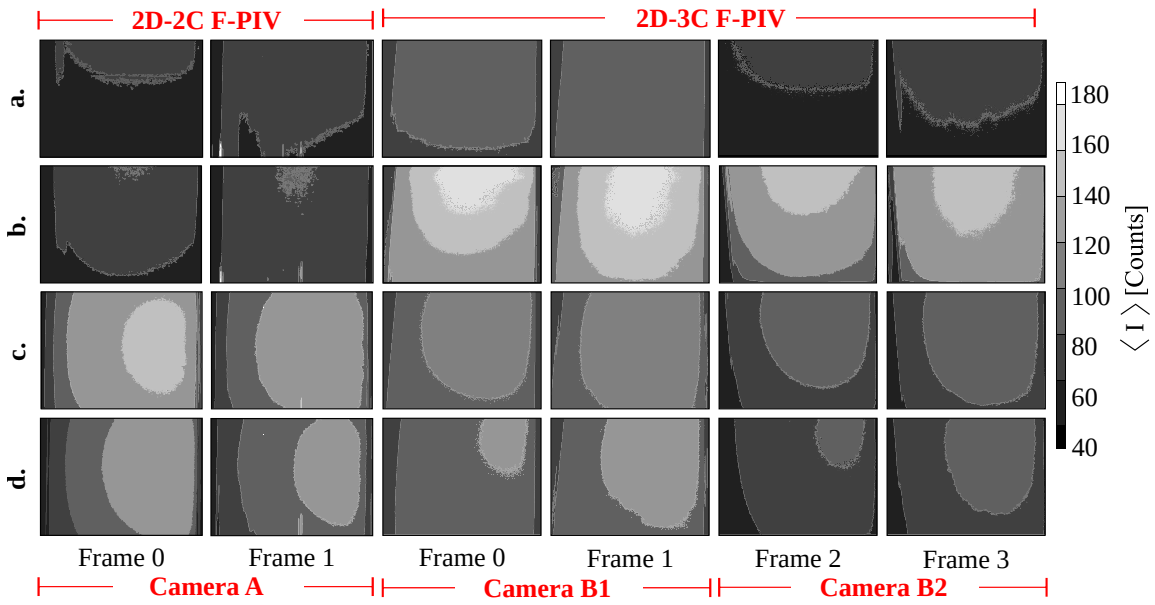

Figure 5.1 - Time-averaged intensity distribution, $\langle I \rangle$, for U_G = (a) 0.152, (b) 0.528, (c) 2.106, and (c) 4.212 cm/s.

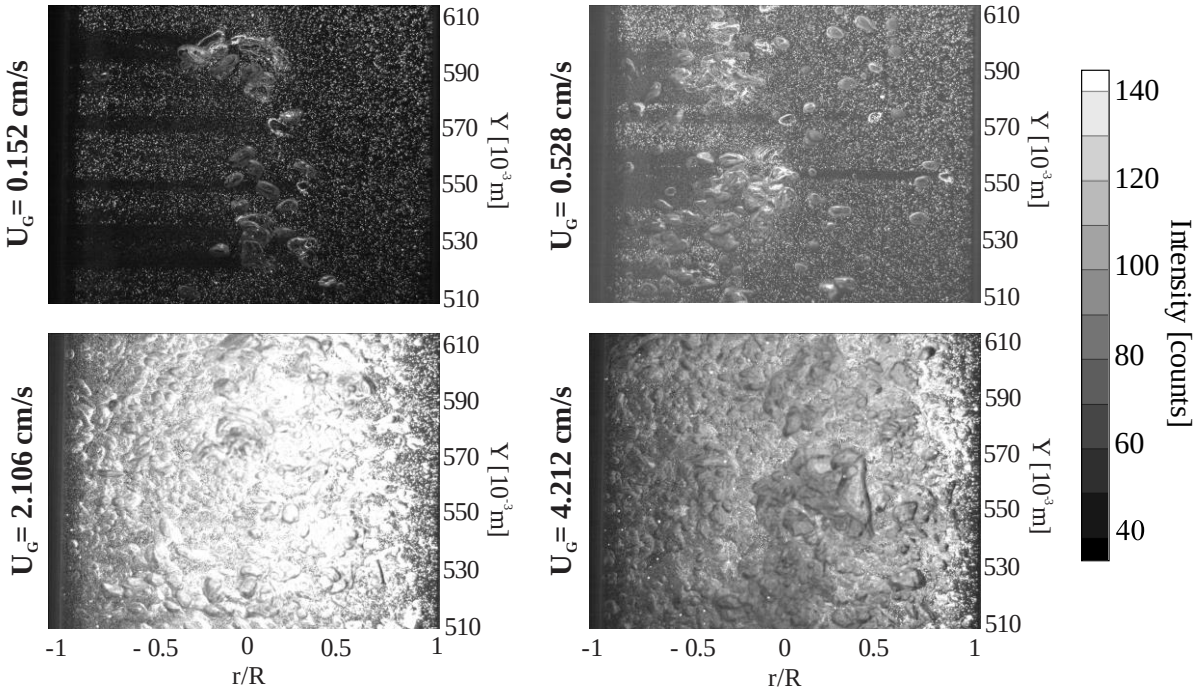

Figure 5.2 - Raw image for U_G = 0.152, 0.528, 2.106, and 4.212 cm/s. Regions with shadows and large light scatters were observed mainly for low and high U_G, respectively.

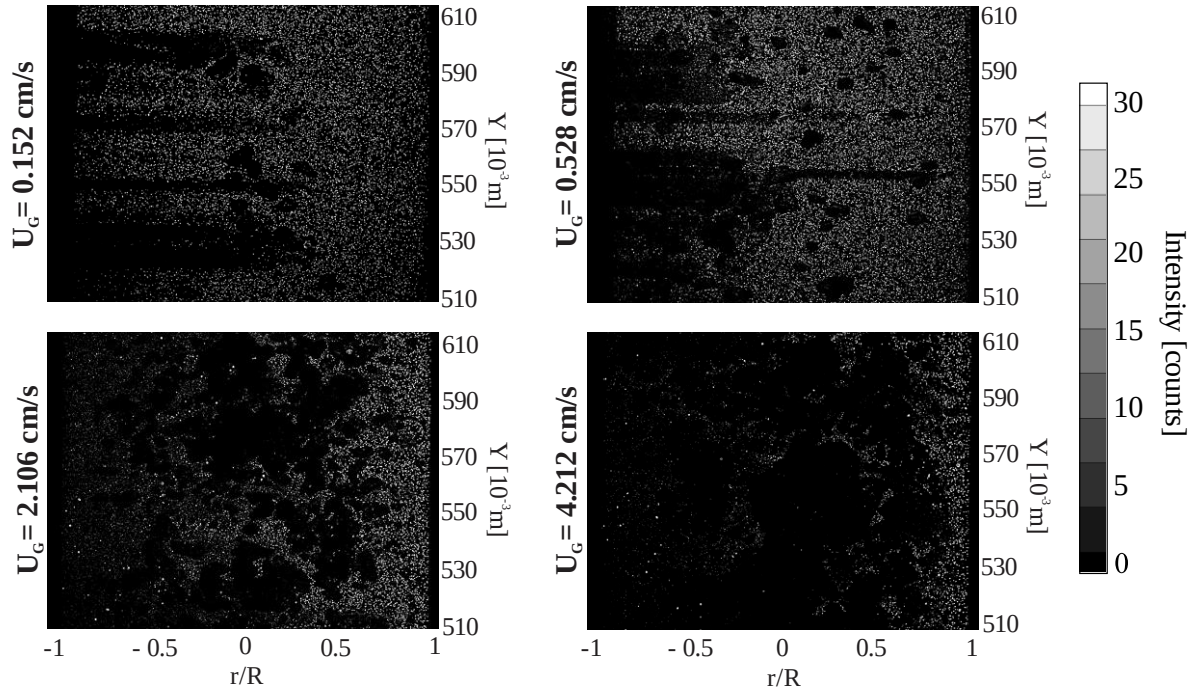

Figure 5.3 - Preprocessed image from the raw image of the Figure 5.2. The large amount of light is practically eliminated by the filters. However, the presence of the bubbles in the light sheet increased the regions with shadows.

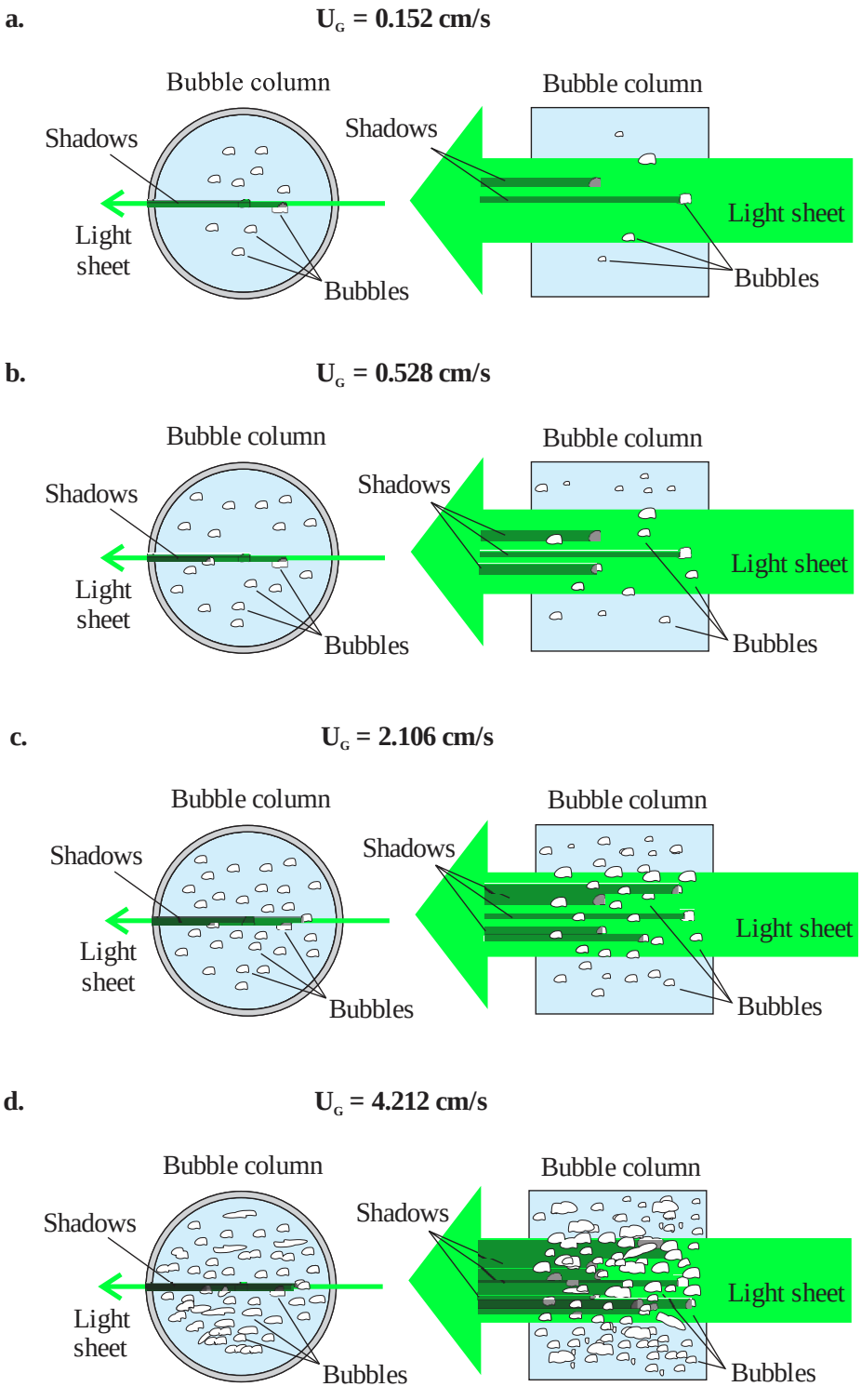

Figure 5.4 - Heterogeneous illumination caused by the bubbles for U_G = (a) 0.152, (b) 0.528, (c) 2.106, and (d) 4.212 cm/s.

For U_G = 4.212 cm/s (homogeneous–heterogeneous flow regime transition), the presence of coalesced bubbles also contributes significantly to the formation of regions with shadows in frame (Figure 5.4d). For U_G = 2.106 cm/s (homogeneous flow regime), the recorded light scattering in frame was greater than for U_G = 4.212 cm/s, even using the same laser power (Figure 5.4c). This shows that increasing the laser power may not contribute to improve the illumination in the column.

5.2. PROCESSING AND POST-PROCESSING

In PIV processing, the standard cross-correlation (SCC) was made using an interrogation strategy with two steps: the first using an interrogation window size of 256 pixels (50% overlap of adjacent windows) and the second of 128 pixels (75% overlap of adjacent windows). The final size of the interrogation window was 32 x 32 pixels ($\simeq$ 3.2 x 3.2 $\cdot 10^{-6}$ m^2). The evaluation of multiple steps and adaptive PIV method were used with decreasing interrogation window size in the PIV correlation. According to Wieneke and Pfeiffer (2010), the adaptive PIV method is used to change the size and shape of the interrogation window automatically according to the particle image density and flow gradients to increase the correlation coefficient and SNR. The initial and final size of the interrogation window was defined using 2 and 3 passes to ensure the convergence in determining the particle image displacement. The overlap of the interrogation window with its neighborhood was used in order to increase the spatial resolution of the vector field.

For the image reconstruction, the particle image displacement information of the first step and the mapping function using a bicubic interpolation were used (Fincham and Delerce, 2000; Scarano and Riethmuller, 2000). The Gaussian function was applied for peak detectability and the correlation peak was fitted by an estimator of three points (Westerweel, 1997). The allowed maximum error of 3C reconstruction ($\varepsilon_{Max3C-R}$) was 5 pixels.

The fields determined by the ensemble correlation (EC) and sliding-average correlation (SAC) approach using 4000 images were used as a reference for the fields obtained by SCC. In addition, a temporal kernel *k* equal to 2 was used for SAC approach. The interrogation strategy was the same as that used in the SCC approach. The EC approach is suitable when the SNR is very low (Meinhart *et al*., 2000). In double-frame images, the loss of temporal resolution is one of the main disadvantages of the SAC approach. Table 5.1 presents an overview of the PIV correlations used in this work.

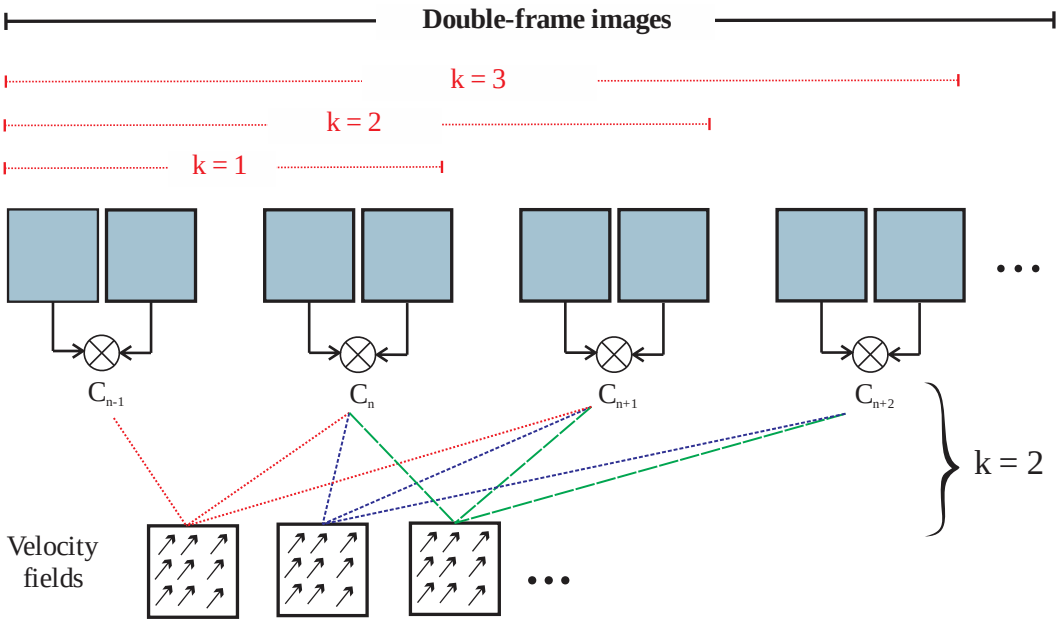

Figure 5.5 – Application of the sliding-average correlation (SAC) approach for k = 2 in double -frame images.

Table 5.1 - Overview of the PIV correlations used in this work.

PIV correlation	Advantage	Disadvantage
Standard cross-correlation (SCC)	- Low computational cost	- Less robust to noise
Sliding-average correlation (SAC)	- More robust to random noise than the SCC approach	- Loss of temporal resolution
Ensemble correlation (EC)	- More robust to noise	- It provides only average fields

In PIV post-processing, the filter developed by Westerweel and Scarano (2005) was used to mainly reduce the outliers of the fields obtained by SCC approach. According to the authors, a removal threshold of 2 is suitable for detecting false vectors in a neighborhood of 3 x 3 pixels. The post-processed fields (SCC*) were compared with those obtained by the EC approach to investigate the correction performance.

Overview of the PIV processing and post-processing used in this work is presented in Figure 5.6.

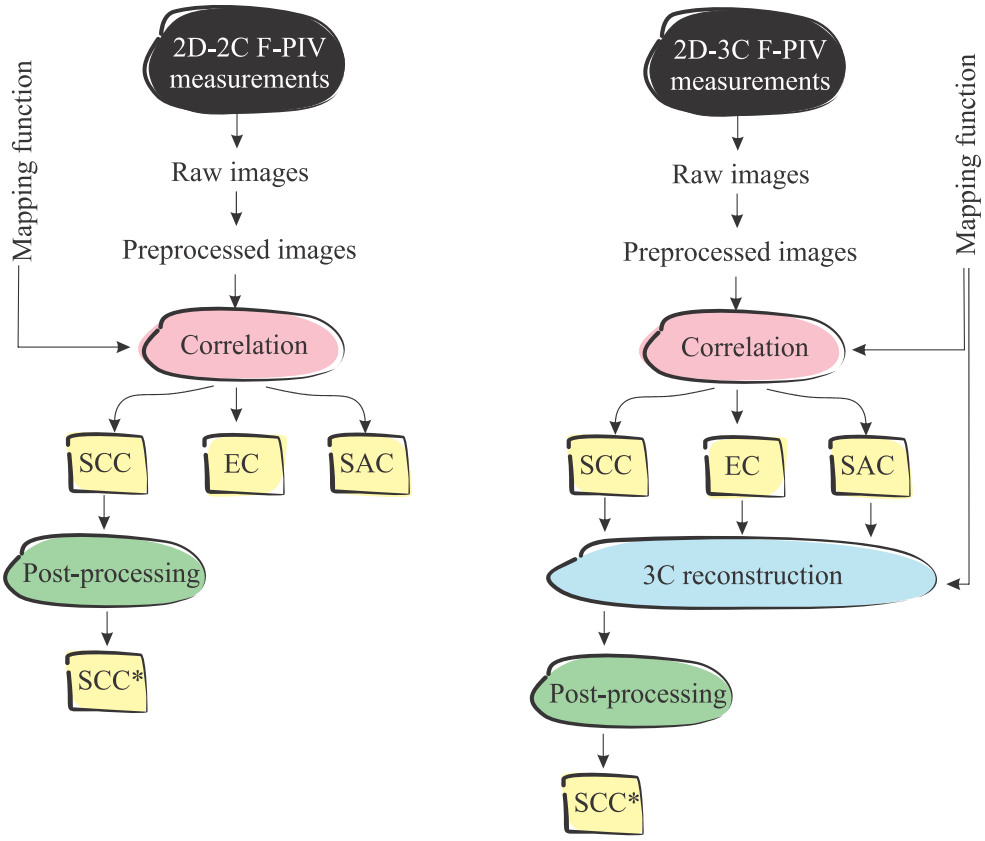

Figure 5.6 – Overview of the PIV processing and post-processing used in this work.

5.3.QUALITY INDICATORS

The quality indicators used in this work were determined from the velocity field and the correlation plane. All of these indicators are found in the Davis 8.2 software. The indicators obtained from velocity field were compared to those obtained from correlation plane to identify behavior patterns and to establish quality ranges.

5.3.1. Indicators from velocity field: *Diff_4* and $\varepsilon_{3C\text{-}R}$

The *Diff_4* (Eq. 5.1) is the average of the velocity difference in the interrogation window and its four spatial neighbors (Figure 5.7). The high values of *Diff_4* can be used as an indicator of outliers in the vector field (Figure 5.8).

$$Diff\_4 = \frac{abs(u_0 - u_a) + abs(u_0 - u_b) + abs(u_0 - u_c) + abs(u_0 - u_d)}{4} \qquad (5.1)$$

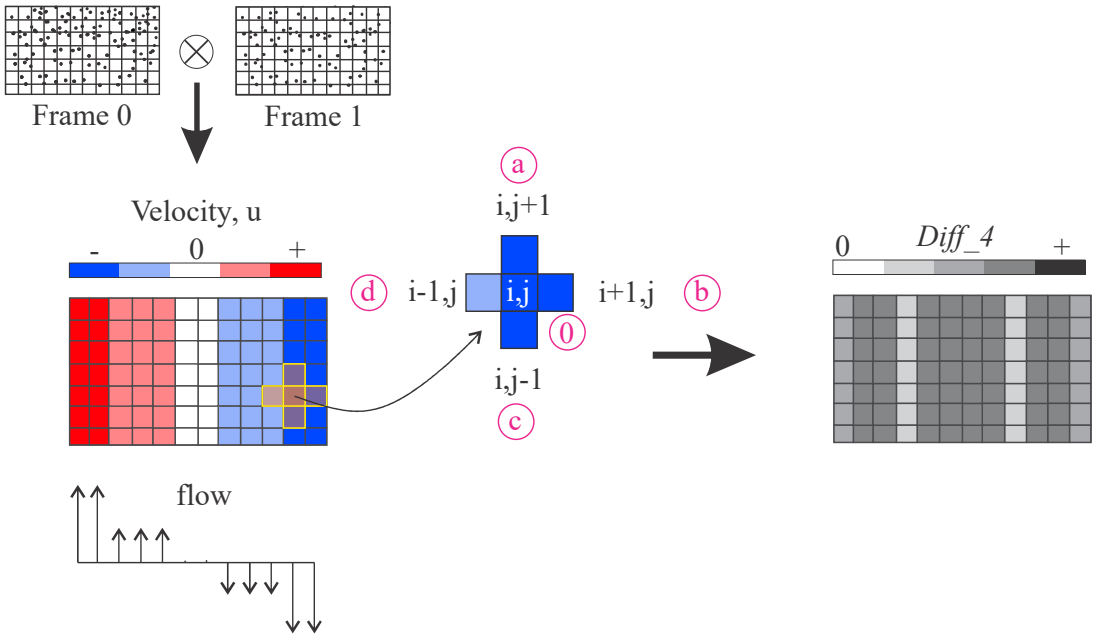

Figure 5.7 – Definition of *Diff_4*

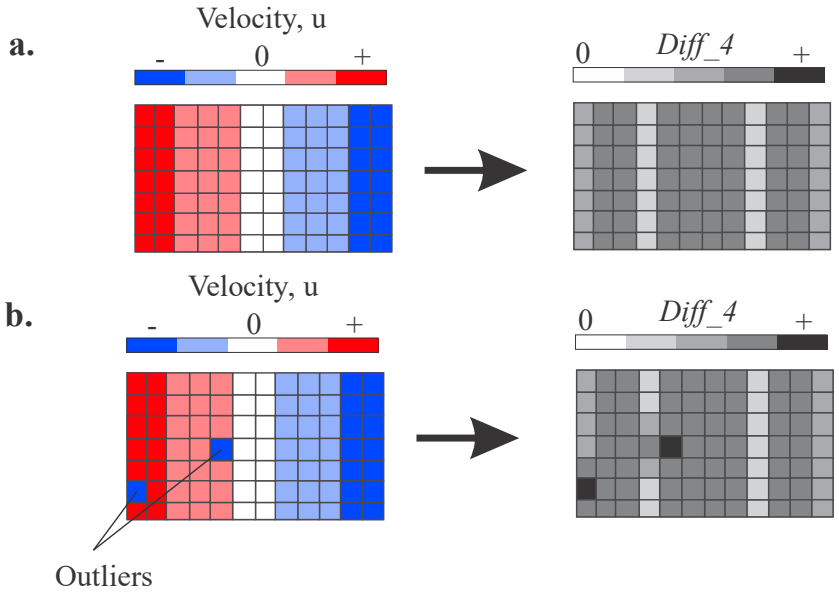

Figure 5.8 – Effect of the outliers on *Diff_4*. Velocity field (a) without and (b) with outliers.

For 2D-3C measurements, the reconstruction error (Eq. 5.2) can also be used as a quality indicator. The 3C reconstruction error (Figure 5.9) is determined from the deviation of the projection of the reconstructed velocities, (u_{i1}, v_{i1}) and (u_{i2}, v_{i2}), and components in 2D-2C fields, (u_1, v_1) and (u_2, v_2). This projection is performed in the image plane of each camera and can be referenced as a "back-reconstruction".

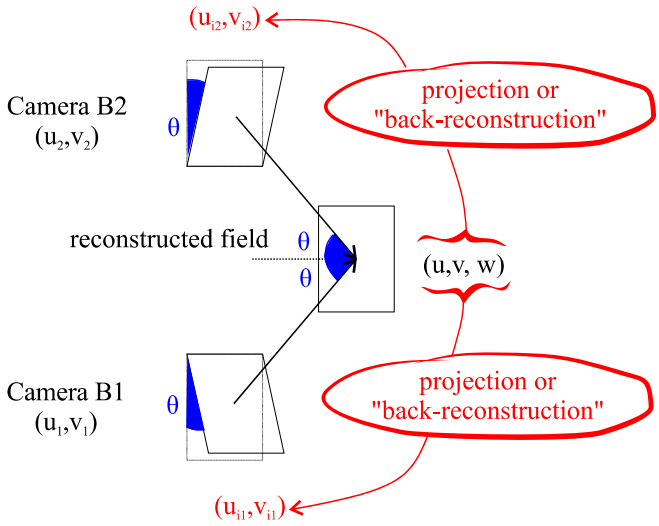

Figure 5.9 - Definition of the 3C reconstruction error

$$\varepsilon_{3C-R} = \sqrt{(u_1 - u_{i1})^2 + (u_2 - u_{i2})^2} \tag{5.2}$$

5.3.2. Indicators from correlation plane: CV, CCC, SNR, and UQ

The cross-correlation value (CV) was determined by Eq. 5.3. The correlation coefficient (Eq. 5.4) was used for the SCC approach. In Eq. 5.1, N_x and N_y are the interrogation area size, μ_0 is the average of the intensity in frame 0 (I_0), and μ_1 is the average of the intensity in frame 1 (I_1). The signal-to-noise ratio (SNR) was determined using the Eq. 5.5, where P_{1st} and P_{2st} are the peak heights of the first and second highest correlation peak and P_{min} is the lowest value of the correlation plane (Figure 5.10). For the 3C-2D measurements, the CCC and SNR values are estimated as the average of the values of each 2D-2C field. The uncertainty quantification (UQ, Section 2.2) was estimated by CS method developed by Wieneke (2014, 2015) as a generic post-processing method.

$$\mathrm{CV} = \sum_{i=0}^{N_x} \sum_{j=0}^{N_y} [I_0 - \mu_0][I_1 - \mu_1] \tag{5.3}$$

$$\mathrm{CCC}=\frac{\sum_{i=0}^{N_x}\sum_{j=0}^{N_y}[I_0-\mu_0][I_1-\mu_1]}{\sqrt{\sum_{i=0}^{N_x}\sum_{j=0}^{N_y}[I_0-\mu_0]^2}\sqrt{\sum_{i=0}^{N_x}\sum_{j=0}^{N_y}[I_1-\mu_1]^2}} \tag{5.4}$$

$$\mathrm{SNR}=\frac{P_{1st}-P_{\min}}{P_{2st}-P_{\min}} \tag{5.5}$$

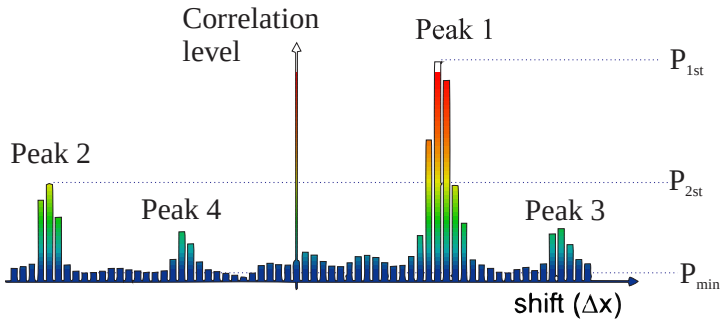

Figure 5.10 – Definition of SNR (Adapted from LaVision, 2016)

CHAPTER 6.

RESULTS AND DISCUSSION

The profiles and vector fields of the liquid phase are presented for different U_G under the conditions of homogeneous and homogeneous-heterogeneous transition regime. The effect of the quality indicators from the vector field and correlation plane is analyzed and quality limits are established.

In addition to the effect of the regions of shadows and presence of the bubbles observed in section 5.1, the quality of the velocity components was individually investigated to identify new noise sources.

The effect of the spatial resolution and allowed maximum error of 3C reconstruction is presented. In addition, the ability of the tracer particles to follow the flow were discussed.

The noise effect on the convergence of the average fields evaluating the number of frame pairs is presented. The velocity fluctuation was investigated to identify the noise effect. In addition, the performance of the sliding-average correlation (SAC) approach in the correction of false vectors is discussed.

An optimization strategy of the PIV processing is presented and discussed based on observed quality limits.

The profile of the time-averaged velocity modulus, $\langle \mathbf{u} \rangle$, using the SCC and EC method for Y = 0.552 m and U_G of 0.152, 0.528, 2.106, and 4.212 cm/s is presented in Figure 6.1. In all cases, the $\langle \mathbf{u} \rangle$ profile is asymmetric and the wall condition is not satisfied ($\mathbf{u} \neq \langle \mathbf{u} \rangle \neq 0$). The asymmetric velocity profile can be result of the recirculation regions in the column or distributor design. In this case, the recirculation regions are influenced by the low height of liquid in the column. The low spatial resolution (DSR) of both techniques can explain the wall condition not satisfied. Moreover, the final size of the interrogation window is greater than the flow structures of the order of the boundary layer thickness. The concentration of bubbles near the wall, vibration of the column, large distortion caused by the curvature of the wall and reflection of tracer particles forming "doublets" can also contribute directly to the correlation noise.

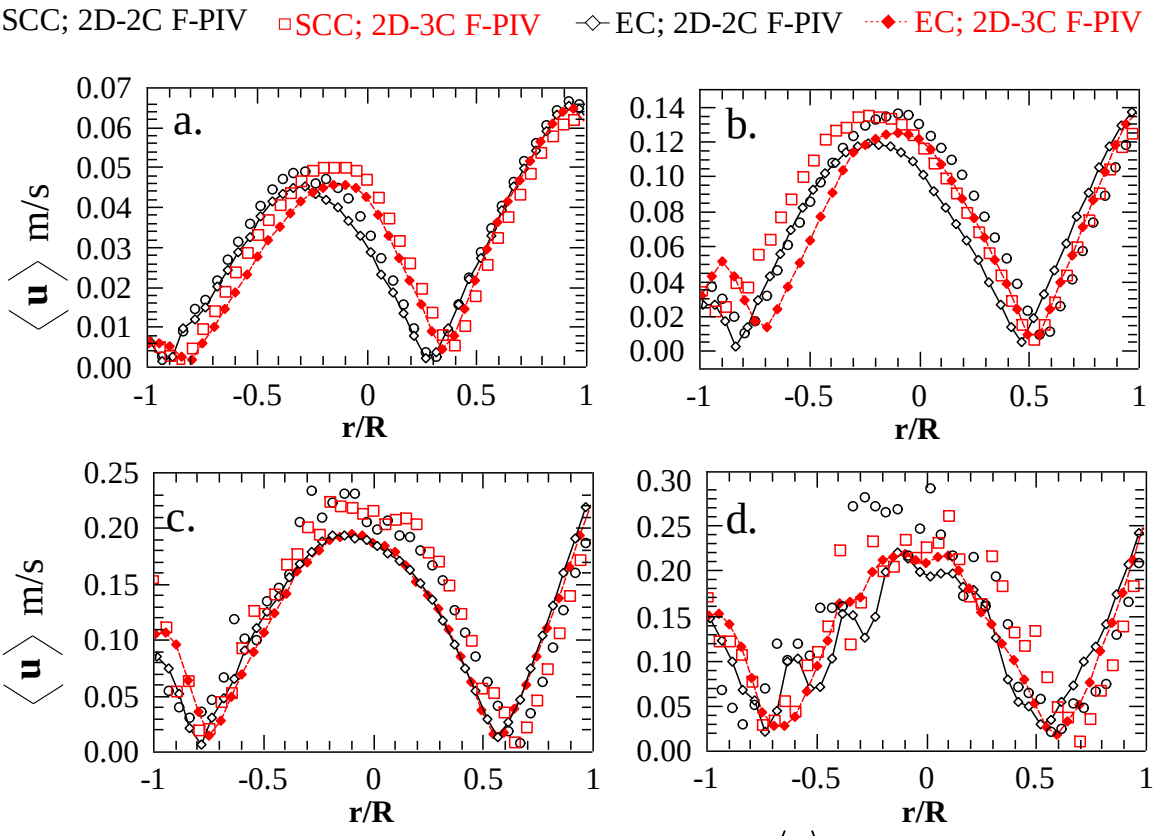

Figure 6.1 – Profile of the time-averaged velocity modulus, $\langle \mathbf{u} \rangle$, using the standard cross-correlation (SCC) and ensemble correlation (EC) method (Y = 0.552 m) for U_G = (a) 0.152 (b) 0.528, (c) 2.106, and (d) 4.212 cm/s.

For SCC, the measurements apparently showed a spatial coherence along the radius for U_G = 0.152 and 0.528 cm/s. However, the measurements were less spatial coherent in -1 < r/R

< 0.5 for U_G = 2.106 cm/s. As discussed in section 2.1, a measurement is said to be spatial coherent when its distribution varies smoothly in space between adjacent interrogation windows. For U_G = 4.212 cm/s, this spatial incoherence was evident mainly in -1 < r/R < 0.75. In Figure C1 and C2, this behavior was also observed for the 2D-3C F-PIV system. However, the vorticity field and profile were smoother compared to the 2D-2C F-PIV system. This behavior can be related to the allowed maximum error of reconstruction, $\varepsilon_{Max3C-R}$, as discussed in Section 6.1.4.

The effect of the low spatial coherence caused by the false vectors is more easily observed in the fields derived from velocity, such as the vorticity field (Eq. 6.1). The vorticity profile and field determined by the standard cross-correlation (SCC), SCC with post-processing (SCC*) and ensemble correlation EC from the 2D-2C F-PIV measurements is presented in Figure 6.2 and Figure 6.3. For standard cross-correlation (SCC) approach, the spatial coherence decreased with increasing U_G in Figure 6.2 and Figure 6.3. A low spatial coherence was observed in -1 < r/R < - 0.25 for U_G = 0.152 and 0.528 cm/s. This behavior was observed in -1 < r/R < 0 for U_G = 2.106 cm/s and across all radius for U_G = 4.212 cm/s. For ensemble correlation (EC) approach, only the measurements for U_G = 4.212 cm/s presented low spatial coherence. Comparing the fields obtained by the SCC and EC approaches, some differences were observed in the regions with high spatial coherence. Comparing the fields obtained by the standard cross-correlation with post-processing (SCC*) and EC approaches, the post-processing filters corrected the outliers for $U_G \leq$ 2.106 cm/s without losing the characteristics of the original field. This can be easily observed in the small difference between the EC and SCC profiles in Figure 6.3. However, this behavior was not observed for U_G = 4.212 cm/s. Beyond the outliers, these differences may be related to the random noises, the limitation of the correlation approaches (discussed in Section 6.1), and the number of frame pairs used to estimate the average field (discussed in Section 6.2).

$$\text{vorticity} = \frac{\partial v}{\partial x} - \frac{\partial u}{\partial y} \qquad (6.1)$$

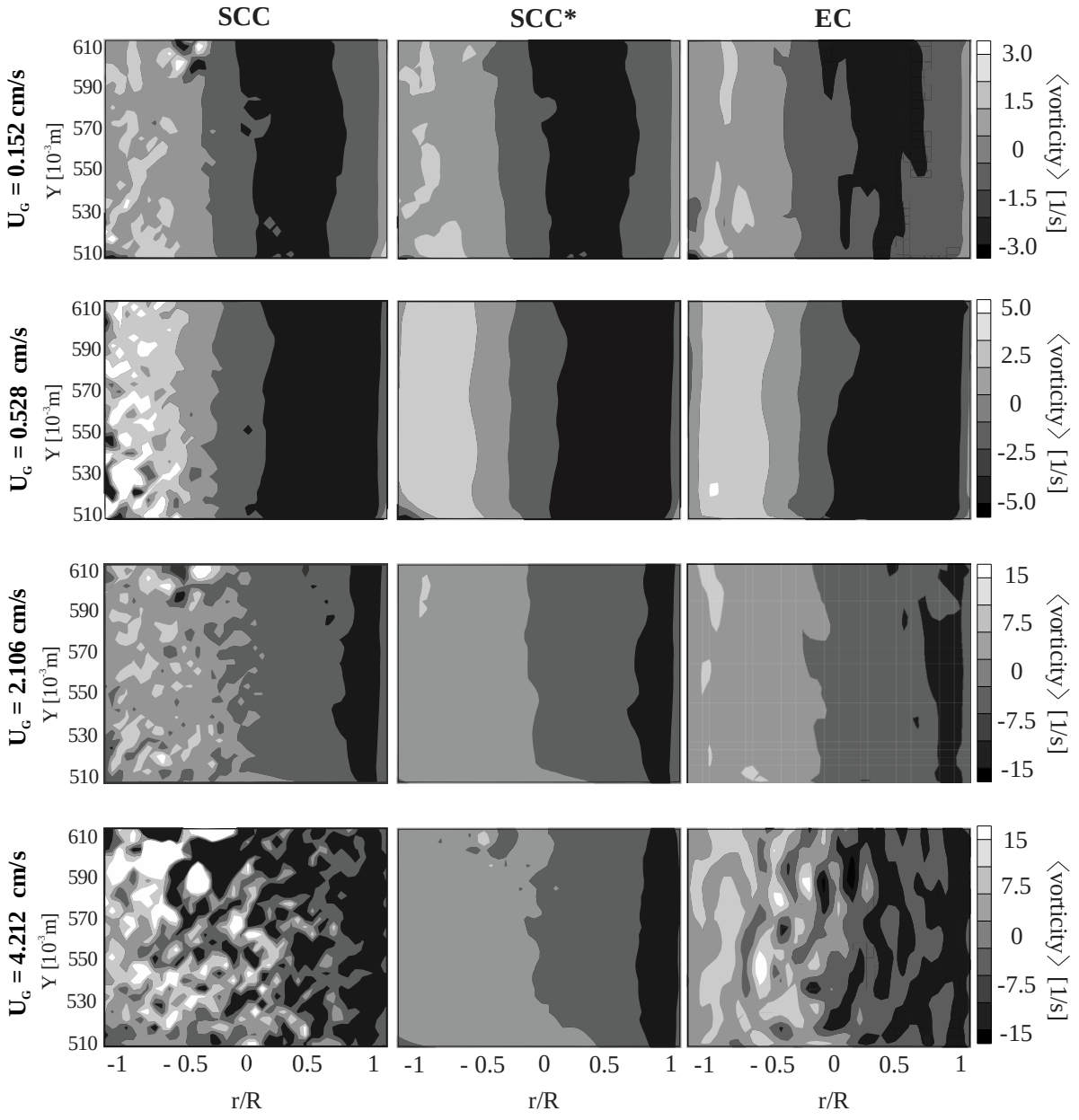

Figure 6.2 – Time-averaged vorticity field determined by the standard cross-correlation (SCC), SCC with post-processing (SCC*) and ensemble correlation (EC) from the 2D-2C F-PIV measurements.

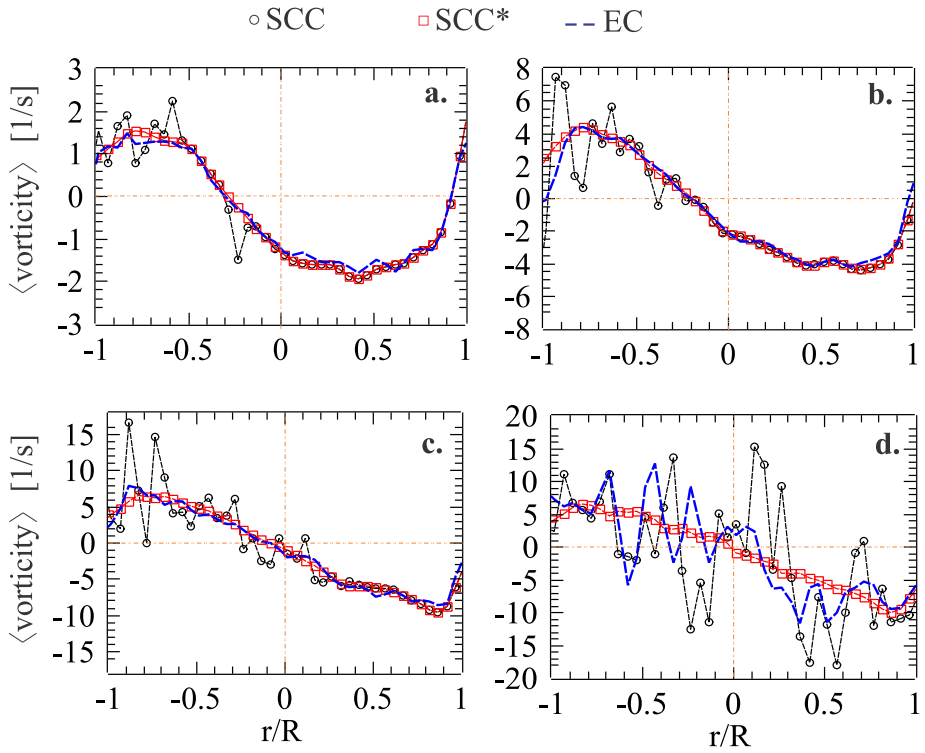

Figure 6.3 – Time-averaged vorticity profile (Y = 0.552 m) determined by the standard cross-correlation (SCC), SCC with post-processing (SCC*) and ensemble correlation (EC) from 2D-2C F-PIV measurements for U_G = (a) 0.152, (b) 0.528, (c) 2.106, and (c) 4.212 cm/s.

Similar to the velocity profile (Figure 6.1), the asymmetry of the vorticity profile for low U_G is clearly observed in Figure 6.3. In addition, the vorticity profile becomes more symmetrical as U_G increases. Becker *et al.* (1999) observed in a 2D column that the bubble plume produced by a single-orifice sparger moved in an undulatory motion due to a lateral movement (Figure 6.4). According to the authors, this behavior was caused by the continuous movement of the bubbles that changed the flow direction of the liquid phase. However, the column investigated in this work presented movements of bubble clusters without the observation of coalesced bubble in the homogeneous regime ($U_G \leq 2.106$ cm/s). This behavior was also observed by Chen *et al.* (1994) analyzing a cylindrical column (10.2 cm ID and 1.2 m high) using PIV for 1.7 cm/s $\leq U_G \leq$ 2.1 cm/s. For 2.1 cm/s $\leq U_G \leq$ 4.9 cm/s, the authors also observed that the bubble clusters and the coalesced bubbles presented upward and laterally oscillatory spiral movements (vortical-spiral flow). In addition, the liquid flows downwardly in the same spiral shape between the column wall and the central bubble stream and it is carried upward by the spiral movement of the central bubble stream. This vortical-spiral frow regime is presented in Figure 6.5. In 2D or 3D bubble columns, the irregular axial movement of vortical

structures through the column was also reported by Sokolichin and Eigenberger (1994), Becker *et al.* (1994), Lin *et al.* (1996), Mudde *et al.* (1997), and Jakobsen *et al.* (2005).

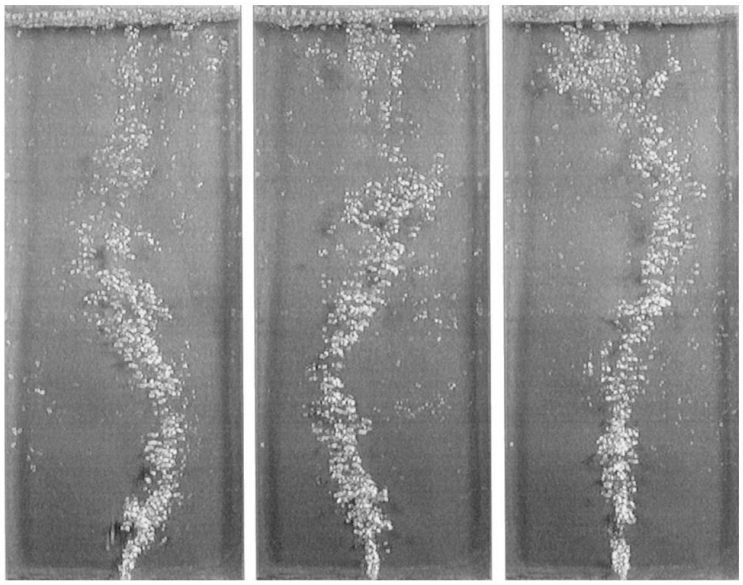

Figure 6.4 - Lateral movement of the bubble plume in the 2D bubble column (gas flow rate: 0.8 L/min) (Becker *et al.*, 1999)

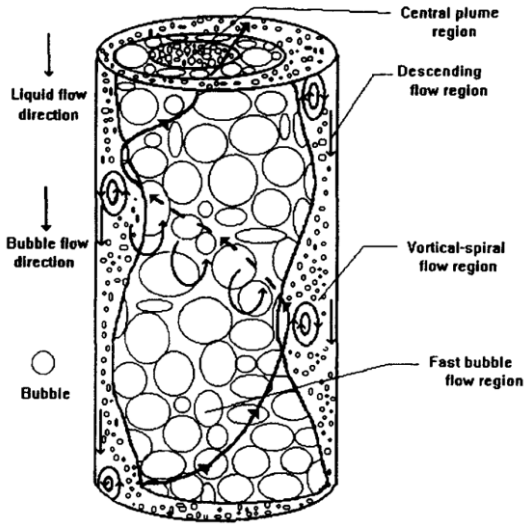

Figure 6.5 - Flow structure in the vortical-spiral flow regime in a 3-D bubble column (Chen *et al.*, 1994)

Figure 6.2 and Figure 6.3 show the importance of the quality analysis of the raw velocity fields before the application of the post-processing filters. The velocity field for U_G = 4.212 cm/s does not represent the phenomenon in the image space based on the analysis of the spatial coherence and the comparison of the different correlation approaches. In addition to ensuring

the representativeness of the analyzed phenomenon, the quality analysis (Figure 6.6) can serve as a reference in the optimization of the PIV system in the physical space (hardware and experimental set up) and in the image space (software). Quality indicators in physical space such as triplicate experiments are often infeasible or do not estimate all error sources (mainly systematic errors). In this case, an investigation of the quality indicators in the imaging space becomes necessary in different experimental conditions.

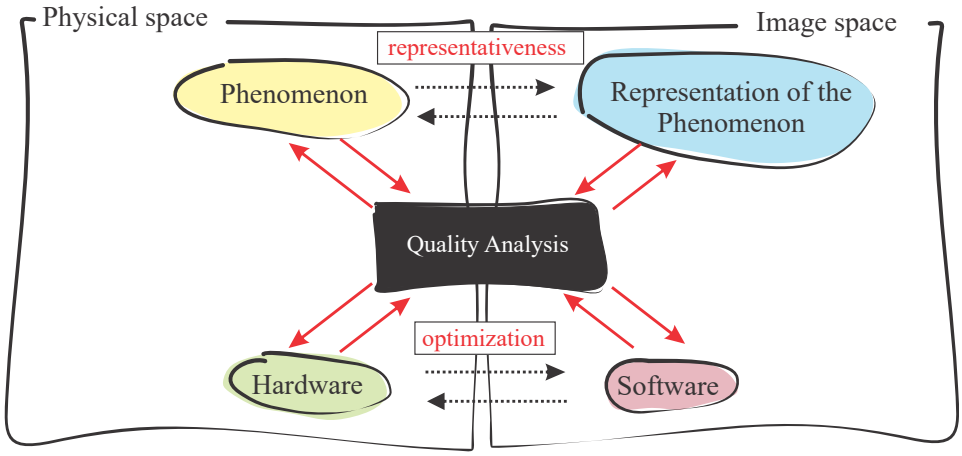

Figure 6.6 – Quality analysis used in the representativeness of the phenomenon and in the optimization of hardware and software.

6.1. QUALITY ANALYSIS OF F-PIV MEASUREMENTS

6.1.1. Quality analysis from velocity field: *Diff_4 and* ε_{3C-R}

Figure 6.7a and b presents the profile of the time-averaged *Diff_4*, $\langle Diff\_4 \rangle$, and *Diff_4* normalized by **u,** $\langle Diff\_4/\mathbf{u} \rangle$, for standard cross-correlation (SCC) approach. For SCC approach, $\langle Diff\_4 \rangle$ and $\langle Diff\_4/\mathbf{u} \rangle$ increased with U_G, where the difference between the 2D-2C and 2D-3C measurements was low. In addition, the left side of the column ($-1 \leq r/R \leq 0$) presented high $\langle Diff\_4 \rangle$ and values in relation to the right ($0 \leq r/R \leq 1$), except for $U_G \leq$ 0.528 cm/s and 2D-3C measurements. Outliers were observed mainly when $\langle Diff\_4/\mathbf{u} \rangle > 0.1$. In addition, the performance of the post-processing filters decreases considerably when $\langle Diff\_4/\mathbf{u} \rangle > 0.4$ (or $\langle Diff\_4 \rangle > 0.2$ m/s). In this case, the resulting vector fields are not reliable.

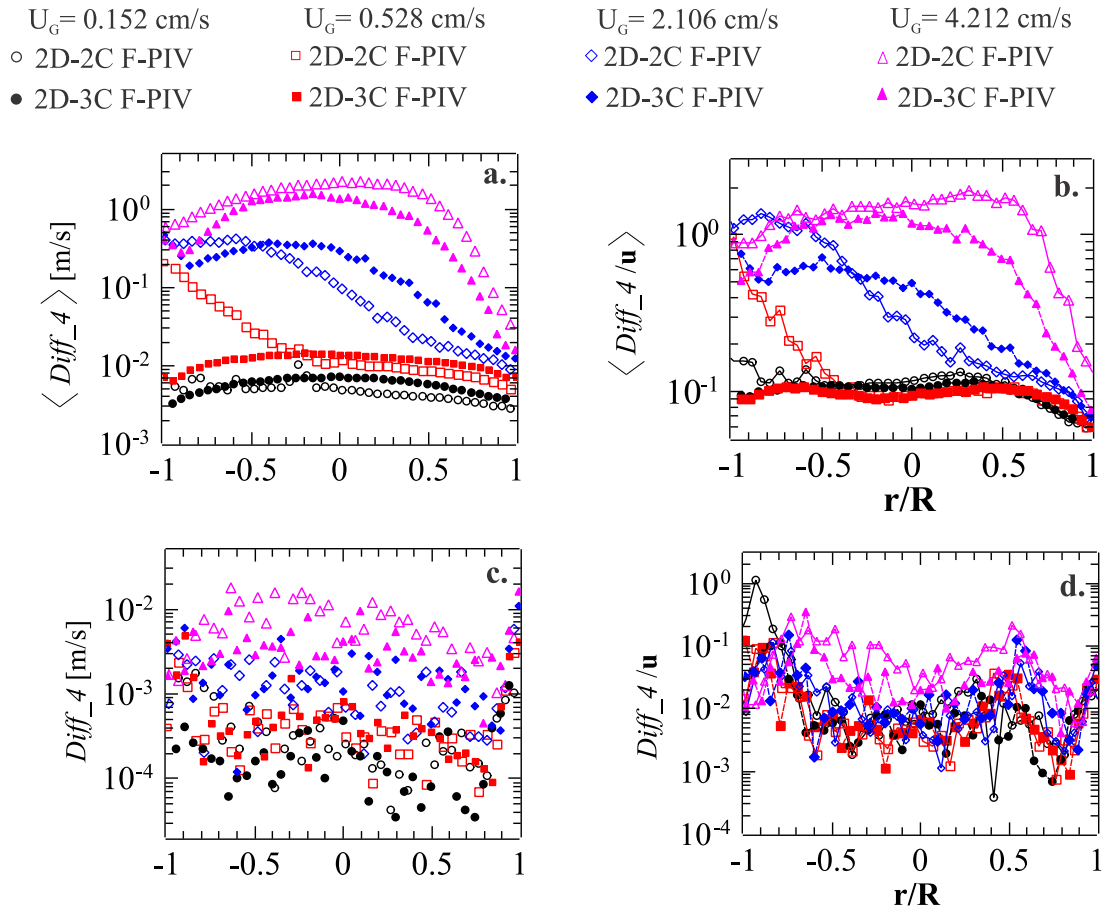

Figure 6.7 – Profile of the time-averaged of (a) *Diff_4*, $\langle Diff\_4 \rangle$, and (b) *Diff_4* normalized by velocity modulus, $\langle Diff\_4/\mathbf{u} \rangle$, for standard cross-correlation (SCC). Profile of (c) *Diff_4* and (d) *Diff_4*/**u** for ensemble correlation (EC). Y = 0.552 m.

As discussed in Chapter 2, the spatial incoherence is mainly caused by the existence of outliers (error > 1 pixel), which arise mainly due to the low particle image concentration (*ppp* – particle per pixel) in the frame. Table 6.1 and Table 6.2 presents the *ppp* of the preprocessed images for 2D-2C and 2D-3C F-PIV. The field of view (FoV) was divided in FoV_1 ($-1 \leq r/R \leq 0$) and FoV_2 ($0 \leq r/R \leq 1$) to analyze in detail the particle image concentration along the radius (Figure 6.8). In Table 6.1 and Table 6.2 it was observed that *ppp* decreased with increasing U_G. In addition, the right side of the column (FoV_2) had a higher *ppp* in relation to the left one (FoV_1) in most of the frames and U_G. As illustrated in Figure 5.2 and Figure 5.3, this can be explained by the heterogeneous illumination caused by the bubbles. The low *ppp* in FOV_1 is mainly due to the presence of bubbles in the light sheet.

Table 6.1 - Particle image concentration (*ppp*) of the preprocessed 2D-2C images $FoV_1 = -1 \leq r/R \leq 0$ and $FoV_2 = 0 \leq r/R \leq 1$.

U_G [cm/s]	*ppp* [10^{-3}]			
	Frame 0		Frame 1	
	FoV1	FoV2	FoV1	FoV2
0.152	19	25	18	25
0.528	16	22	12	22
2.106	9	12	5	10
4.212	≤ 1	3	≤ 1	2

Table 6.2 - Particle image concentration (*ppp*) of the preprocessed 2D-3C images $FoV_1 = -1 \leq r/R \leq 0$ and $FoV_2 = 0 \leq r/R \leq 1$.

U_G [cm/s]	*ppp* [10^{-3}]							
	Frame 0		Frame 1		Frame 2		Frame 3	
	FoV_1	FoV_2	FoV_1	FoV_2	FoV_1	FoV_2	FoV_1	FoV_2
0.152	26	26	25	26	27	25	26	26
0.528	19	18	20	19	17	20	18	19
2.106	3	7	3	7	2	6	2	6
4.212	4	7	4	6	2	6	2	6

In Figure 6.9, the effect of the low *ppp* in the quality indicators can be clearly observed in the instantaneous vector field for image of Figure 5.3, SCC approach, and U_G = 0.528 cm/s. High values of UQ and *Diff_4* were observed in the shadow regions. In addition, the SNR values were the lowest in these regions. In this case, low *ppp* is a dominant source of noise for standard cross-correlation (SCC) approach in the imaging space (Figure 6.10).

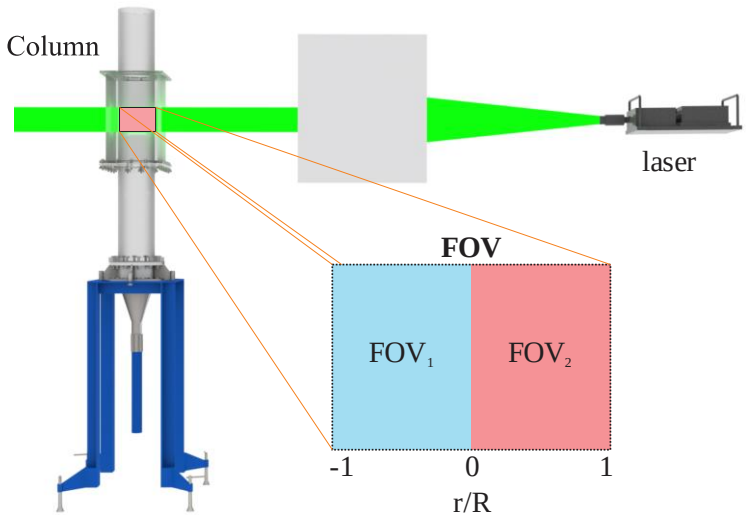

Figure 6.8 - Definition of the field of view (FOV) analyzed in the column. $FoV_1 = -1 \leq r/R \leq 0$ and $FoV_2 = 0 \leq r/R \leq 1$.

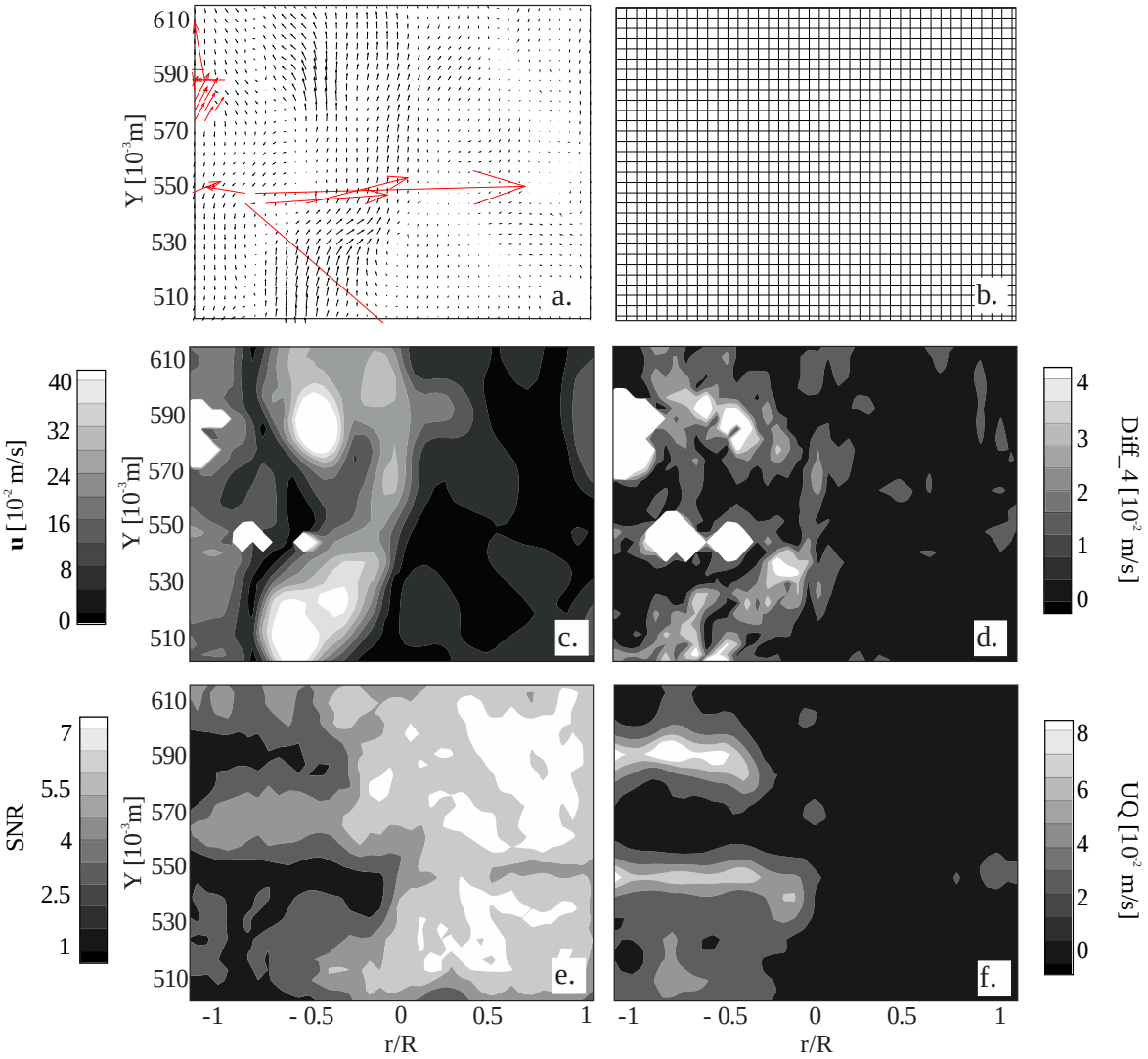

Figure 6.9 - Quality analysis for the PIV processing of Figure 5.3 (U_G = 0.528 cm/s): (a) outliers in the velocity vector field, (b) grid, (c) velocity modulus, **u**, (d) *Diff_4*, (e) SNR, and (f) uncertainty quantification field, UQ, using SCC approach.

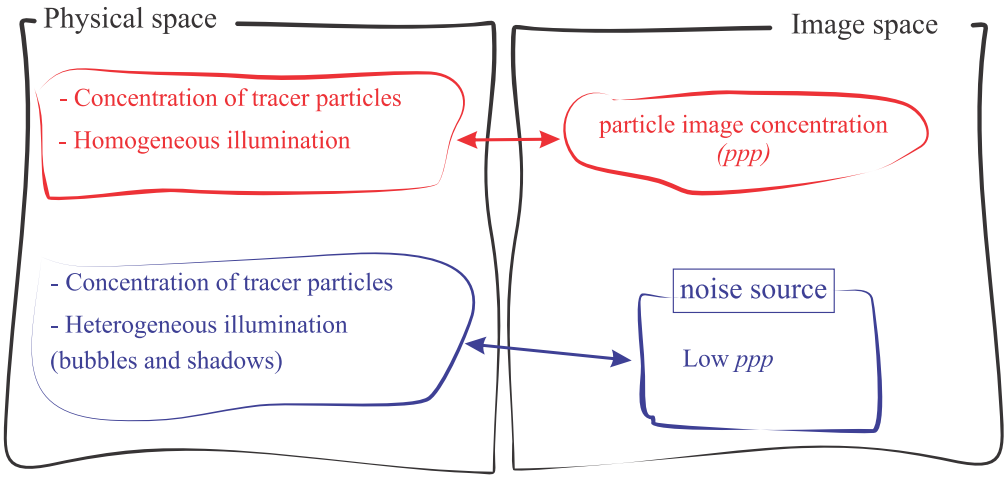

Figure 6.10 – Low *ppp* as a noise source for the standard cross-correlation (SCC) approach.

For 2D-3C measurements, the profile of the 3C reconstruction error did not exhibit the same behavior as $\langle Diff\_4 \rangle$ for the SCC approach (Figure 6.11a). However, the profile of ε_{3C-R} normalized by velocity modulus in pixel ($\mathbf{u}_{shif}$), $\langle \varepsilon_{3C-R}/\mathbf{u}_{shif} \rangle$ presented the same behavior as $\langle Diff\_4 \rangle$ (Figure 6.11b). In addition, outliers were observed mainly when $\langle \varepsilon_{3C-R}/\mathbf{u}_{shif} \rangle > 0.20$. The performance of the post-processing filters decreases considerably when $\langle \varepsilon_{3C-R}/\mathbf{u}_{shif} \rangle > 0.25$ (or $\langle \varepsilon_{3C-R} \rangle > 0.7$ pixel).

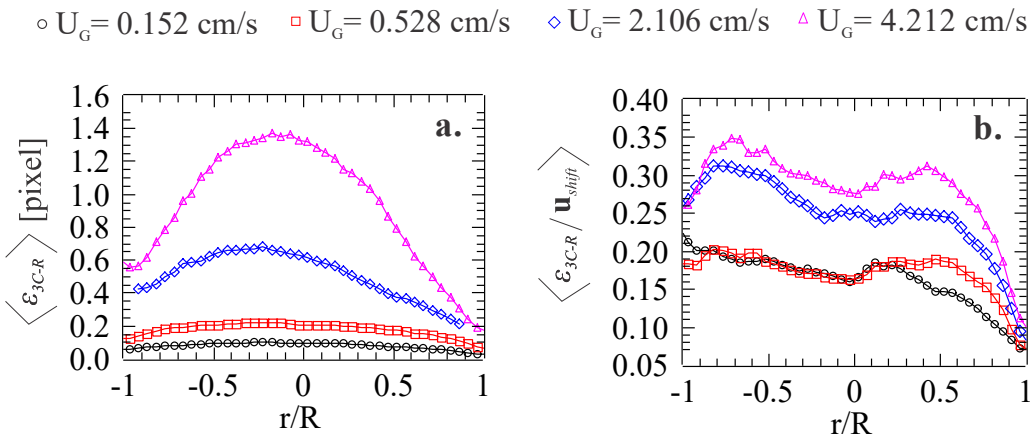

Figure 6.11 - Profile of (a) the time-averaged of the 3C reconstruction error, $\langle \varepsilon_{3C-R} \rangle$ and (b) ε_{3C-R} normalized by velocity modulus in pixel ($\mathbf{u}_{shif}$), $\langle \varepsilon_{3C-R}/\mathbf{u}_{shif} \rangle$ for standard cross-correlation (SCC) and Y = 0.552 m.

A proof that the ensemble (EC) approach is more robust than the standard cross-correlation (SCC) is shown in Figure 6.7, where the *Diff_4* and *Diff_4*/**u** values for EC were smaller than those for SCC (except for U_G = 0.528 cm/s, 2D-2C measurements, and -1 ≤ r/R ≤ - 0.75). In addition, the effect of low *ppp* on *Diff_4* and $\varepsilon_{3C-R}/\mathbf{u}_{shif}$ was not similar to the SCC approach (Figure 6. 12). However, 2D-2C and 2D-3C fields using EC approach presented high *Diff_4* and *Diff_4*/**u** for U_G = 4.212 cm/s and -1 ≤ r/R ≤ 0.75 (Figure 6.7c). In this case, the measurements obtained using the EC approach are not ideal to be used as a reference in the analysis of spatial coherence (Figure 6.1d). This problem may be related to the number of frames used or the presence of noise. One possibility is that 4 000 frames are not sufficient to estimate the average field under these conditions, since the total time of image acquisition is not enough to obtain the steady state of the flow and consequently the average convergence is not obtained. On the other hand, the total time may have been sufficient, but the presence of

noise in the image may deteriorate the field, requiring a greater number of frames. Some tests showed that the average field converged after 3000 frames for all U_G. The average field determined by 4000 frames was used as a reference field to study the convergence. By using 3000 frames it was found a deviation of 3%. The average deviation of the field determined by 3500 frames was of 1.5%. A detailed study of the convergence of the average field is presented in Section 6.2.

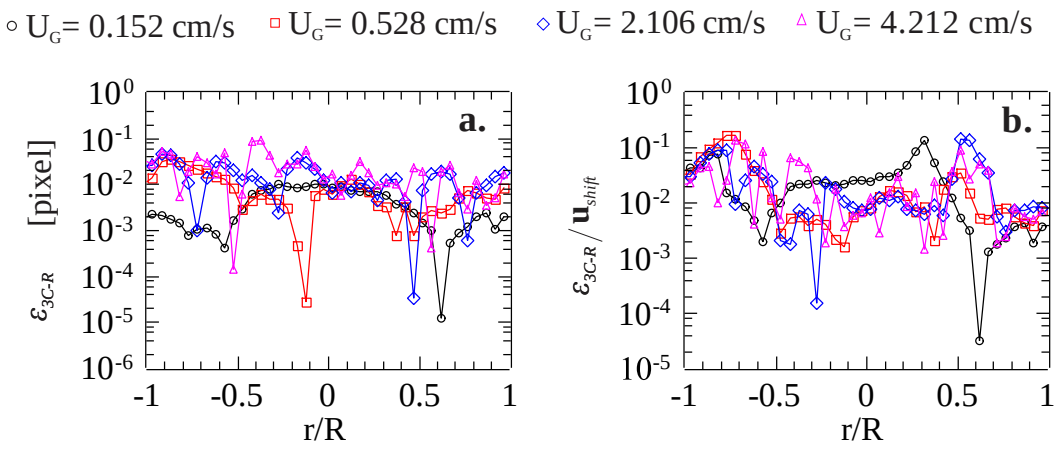

Figure 6. 12 - Profile of (a) ε_{3C-R} and (b) ε_{3C-R} normalized by velocity modulus in pixel ($\mathbf{u}_{shif}$), $\varepsilon_{3C-R}/\mathbf{u}_{shif}$, for ensemble correlation (EC) and Y = 0.552 m.

6.1.2. Quality analysis from correlation plane: CCC, SNR, and UQ.

The time-averaged of the other quality indicators (CCC, SNR_{SCC}, and UQ) for SCC approach are shown in Figure 6.13a-c. Furthermore, Figure 6.13d shows the time-averaged of the uncertainty normalized by velocity $\langle UQ_u/\mathbf{u}\rangle$. In general, the $\langle CCC\rangle$ and $\langle SNR_{SCC}\rangle$ distribution presented a small difference between the 2D-2C and 2D-3C measurements. The $\langle CCC\rangle$ values decreased with U_G, except in some points in -1 < r/R < 0. In this case, some values for U_G = 4.212 cm/s were higher than those for U_G = 2.106 cm/s. The $\langle SNR_{SCC}\rangle$ values also decreased with U_G. On the other hand, the $\langle UQ_{\mathbf{u}}\rangle$ values increased with U_G, where a significant difference was observed between the 2D-2D and 2C-3C measurements for U_G = 2.106 and 4.212 cm/s. In Figure 6.13d, the $\langle UQ_u/\mathbf{u}\rangle$ values were below 0.7, i.e. the measurement uncertainty was less than 70 % of the velocity value. For $\langle UQ_u/\mathbf{u}\rangle$ distributions, it was not possible to establish a direct relationship with U_G.

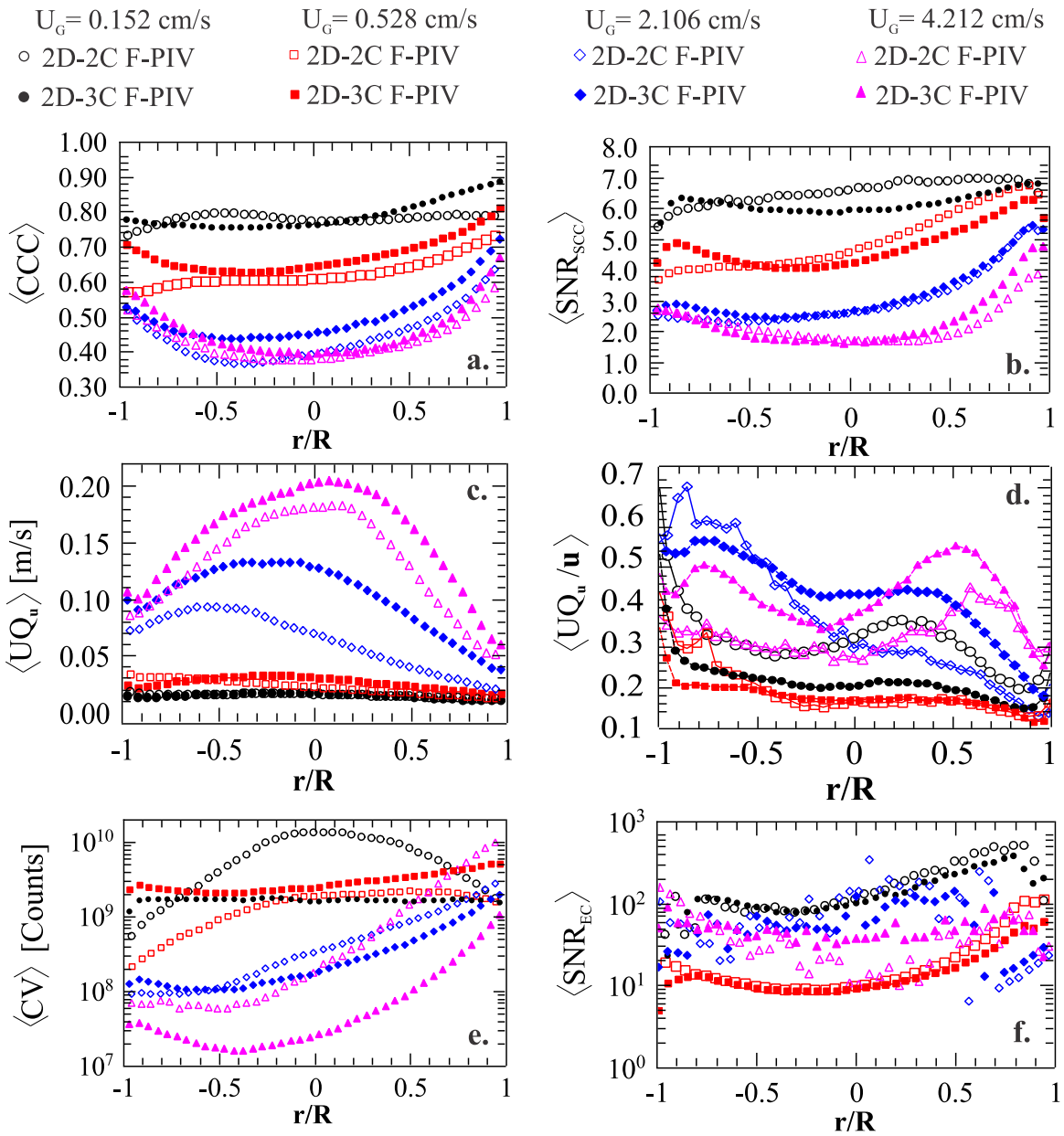

Figure 6.13 – Profile of time-averaged quality indicators (Y = 0.552 m): (a) cross-correlation coefficient, $\langle CCC \rangle$; (b) SNR for SCC, $\langle SNR_{SCC} \rangle$; (c) **u** uncertainty, $\langle UQ_u \rangle$; (d) $UQ_{\mathbf{u}}$ uncertainty normalized by **u,** $\langle UQ_u/\mathbf{u} \rangle$; (e) correlation value, $\langle CV \rangle$; and (f) SNR for EC method, $\langle SNR_{EC} \rangle$.

A large difference between the measurements of the both techniques was observed for U_G = 0.152 cm/s, where the 2D-2C measurements presented the highest values of $\langle UQ_u/\mathbf{u} \rangle$. This can be related directly to the DVR and the choice of dt, since it was chosen a time of 500 μs for the 2D-2C measurements. Apparently, this did not affect the spatial coherence analyzed in Figure 6.1 and Figure 6.7. For U_G = 0.528 cm/s, the $\langle UQ_u/\mathbf{u} \rangle$ values were the lowest in relation

to others U_G, except for the 2D-2C measurements in -1 < r/R < - 0.75. For U_G = 2.106 and 4.212 cm/s, the $\langle UQ_u/\mathbf{u}\rangle$ values were between 0.3 and 0.7, where a considerable difference between both techniques was observed.

For the EC approach, the time-averaged of the correlation value, $\langle CV\rangle$, and SNR, $\langle SNR_{EC}\rangle$, are shown in Figure 6.13e-f. In general, the SNR values were higher than those for SCC, with values between 5 and 700. This confirms the robustness of the EC approach. In addition, the SNR distribution also showed no differences between the 2D-2C and 2D-3C measurements. However, the CV distribution presented a significant difference. Note that a direct relationship between the CV and neighborhood coherence (Figure 6.1) was not established, since the profile for 2.106 cm/s presented a better coherence. But the CV distribution for U_G = 2.106 cm/s was lower than those for U_G = 0.152 and 0.528 cm/s and the SNR values were lower than those for 0.152 cm/s. Moreover, it is not possible to establish a range of CV and SNR_{EC} values where the spatial coherence is high.

For SCC approach, the quality indicators did not exhibit the same behavior of $\langle Diff\_4/\mathbf{u}\rangle$ in relation to the effect of the low particle image concentration (*ppp*). This can be clearly observed by analyzing the value of the indicators on the left side of the column which should be the highest. However, some $\langle UQ_u/\mathbf{u}\rangle$ profiles presented the same trend observed in $\langle Diff\_4/\mathbf{u}\rangle$. As presented in section 2.2, the estimate of UQ is related to the form of the correlation peak.

The particle image diameter d_τ (Eq. 6.1) calculated by Davis 8.2 software can be used to investigate the shape of the correlation peak for standard cross-correlation approach (Figure 6.14), since it is estimated by the standard deviation, σ, of the Gaussian peak fit (Raffel *et al*., 2007, Adrian and Westerweel, 2011). It is important to note that this equation is obtained considering a uniform displacement field.

$$d_\tau \cong 2\sqrt{2}\sigma \qquad (6.1)$$

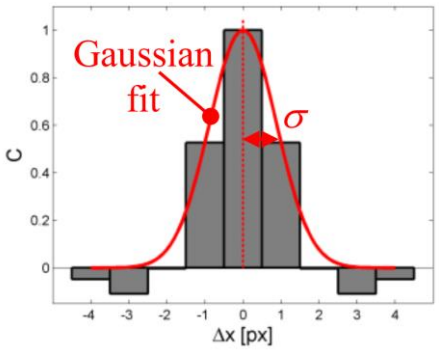

Figure 6.14 - Standard deviation, σ , of the Gaussian peak fit (Adapted from Sciacchitano, 2014).

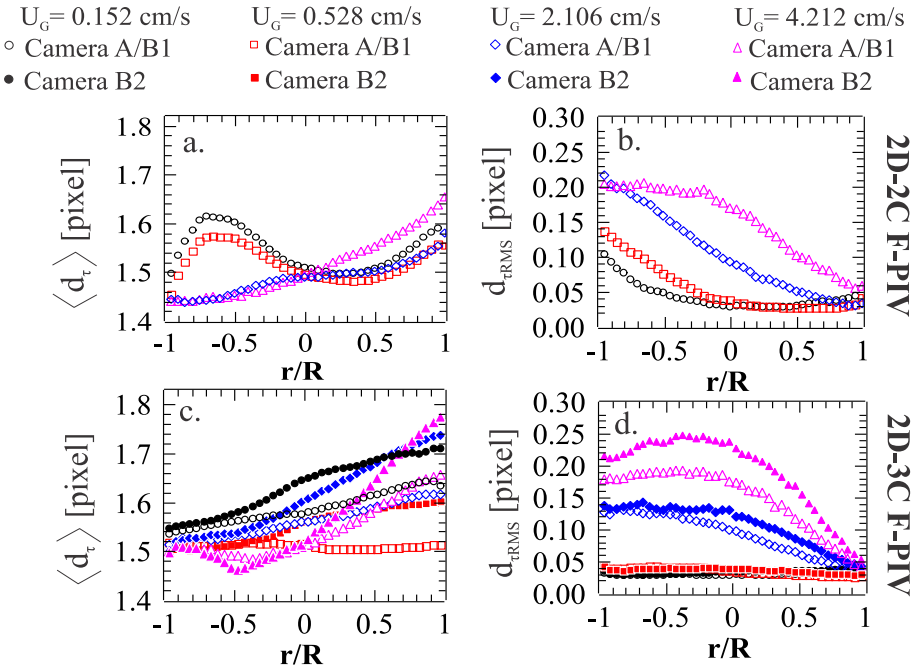

Figure 6.15 – Time-averaged and RMS of the particle image diameter, $\langle d_\tau \rangle$ and $d_{\tau RMS}$, using SCC approach. (a-b) Camera A. (c-d) Camera B1 and B2.

Basically, d_τ increases with the increasing of the correlation peak width. Figure 6.15 shows the time-averaged and RMS of d_τ ($\langle d_\tau \rangle$ and $d_{\tau RMS}$) for the 2D-2C fields of the cameras A, B1, and B2. The $\langle d_\tau \rangle$ values varied along the radius for all cameras and U_G (Figure 6.15a and c). In Figure 6.15b and d, the variation of the $d_{\tau RMS}$ values is directly related to the noise in PIV interrogation (N_I, $|\Delta Z|$, $|\Delta \mathbf{u}|$, and distortion caused by the bubbles), since the d_τ

values for the preprocessed image were 2-3 pixels. The $d_{\tau RMS}$ values can be directly related to low ppp (observed in Table 6.1 and Table 6.2) and therefore, their behavior is similar to *Diff_4* and $\langle Diff\_4/\mathbf{u} \rangle$ in Figure 6.7a and b. The same behavior was observed for $d_{\tau RMS}$ normalized by time-averaged of the particle image diameter, $d_{\tau RMS}/\langle d_\tau \rangle$, in Figure D1. In addition, outliers were observed mainly when $d_{\tau RMS}$ > 0.07 pixel and $d_{\tau RMS}/\langle d_\tau \rangle$ > 0.04.

6.1.3. Quality analysis of the velocity components

The fields of the time-averaged velocity components are shown in Figure 6.16, Figure 6.17, and Figure 6.18. In general, the fields for the axial component ($\langle v \rangle$) presented greater spatial coherence than those for the radial components (in-plane, $\langle u \rangle$, and out-of-plane, $\langle w \rangle$). Regarding the spatial coherence, the fields for standard cross-correlation (SCC) approach are more sensitive to noise than those for ensemble correlation (EC) approach. This behavior was observed previously in Figure 6.1. One can also verify that the fields are deteriorated with the increase of U_G, mainly for $\langle u \rangle$ and $\langle w \rangle$. Note the low spatial coherence caused by low *ppp* (Table 6.1 and Table 6.2) on the left side of $\langle u \rangle$ and $\langle v \rangle$ fields, especially for U_G = 0.528 and 2.106 cm/s. This effect is easily observed when the SCC, SCC* and EC fields are compared. For the SCC fields, the low spatial coherence was also observed when $d_{\tau RMS}$ > 0.07 in Figure 6.19.

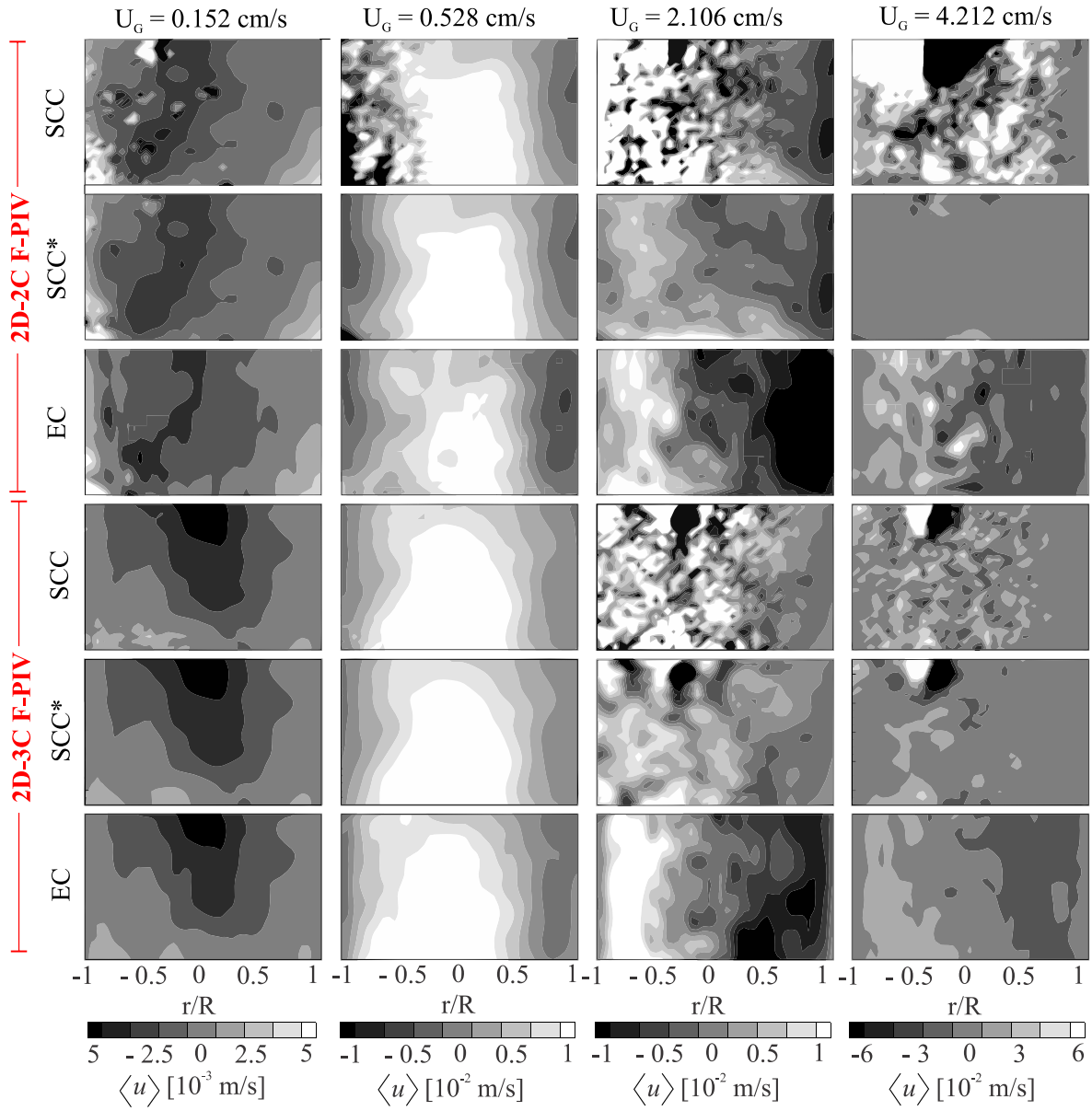

Figure 6.16 – Time-averaged u fields, $\langle u \rangle$, calculated using standard cross-correlation (SCC), SCC with PIV post-processing (SCC*), and ensemble correlation (EC) approach.

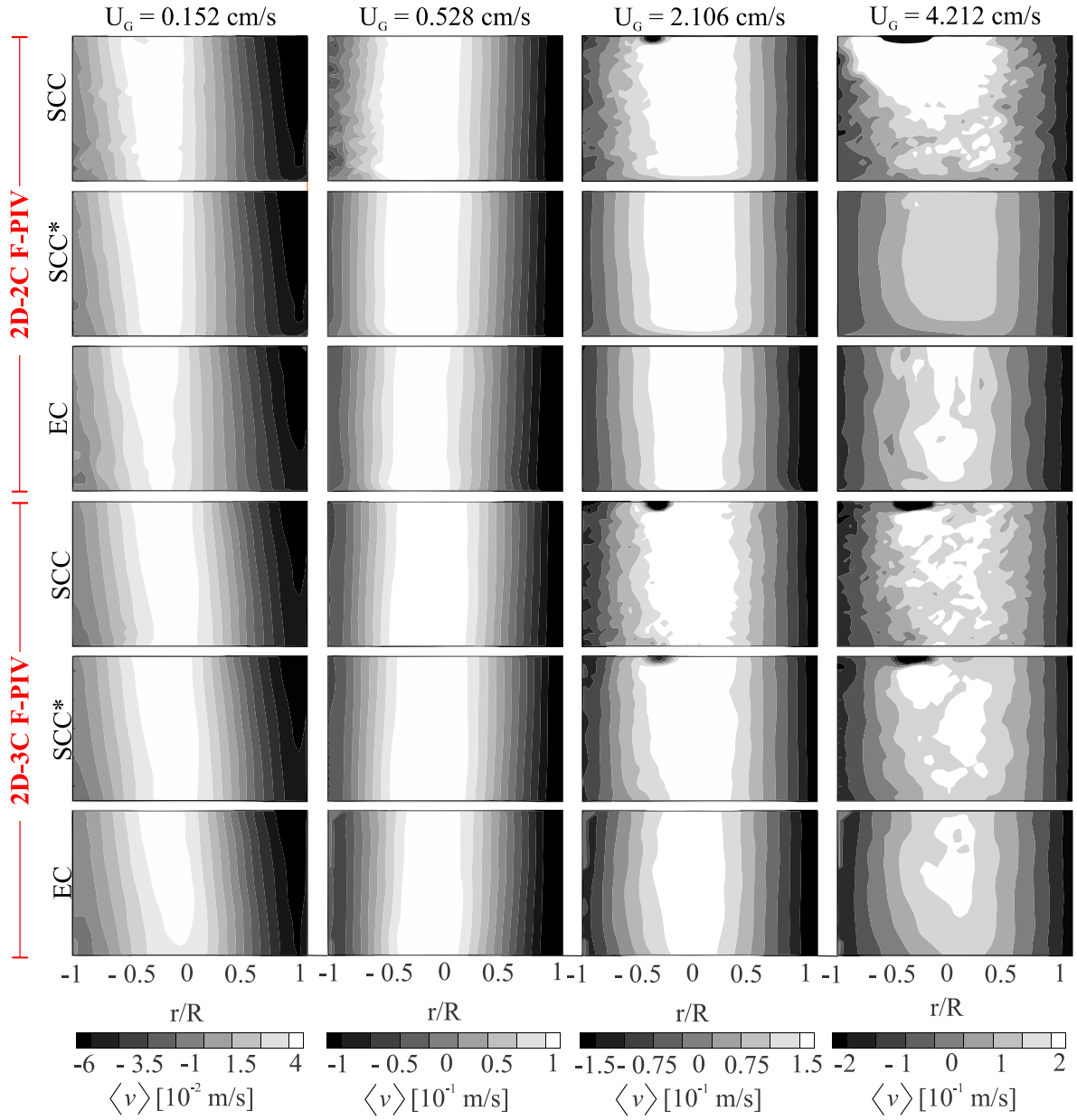

Figure 6.17 – Time-averaged *v* fields, $\langle v \rangle$, calculated using standard cross-correlation (SCC), SCC with PIV post-processing (SCC*), and ensemble correlation (EC) approach.

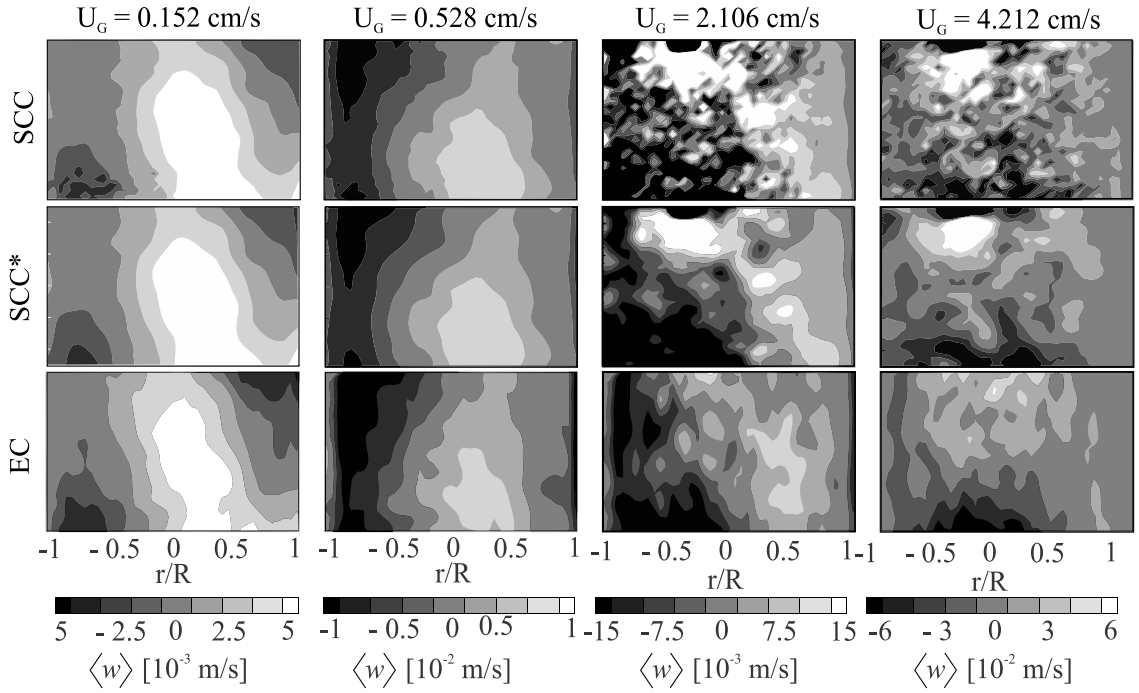

Figure 6.18 – Time-averaged w fields, $\langle w \rangle$, calculated using standard cross-correlation (SCC), SCC with PIV post-processing (SCC*), and ensemble correlation (EC) approach.

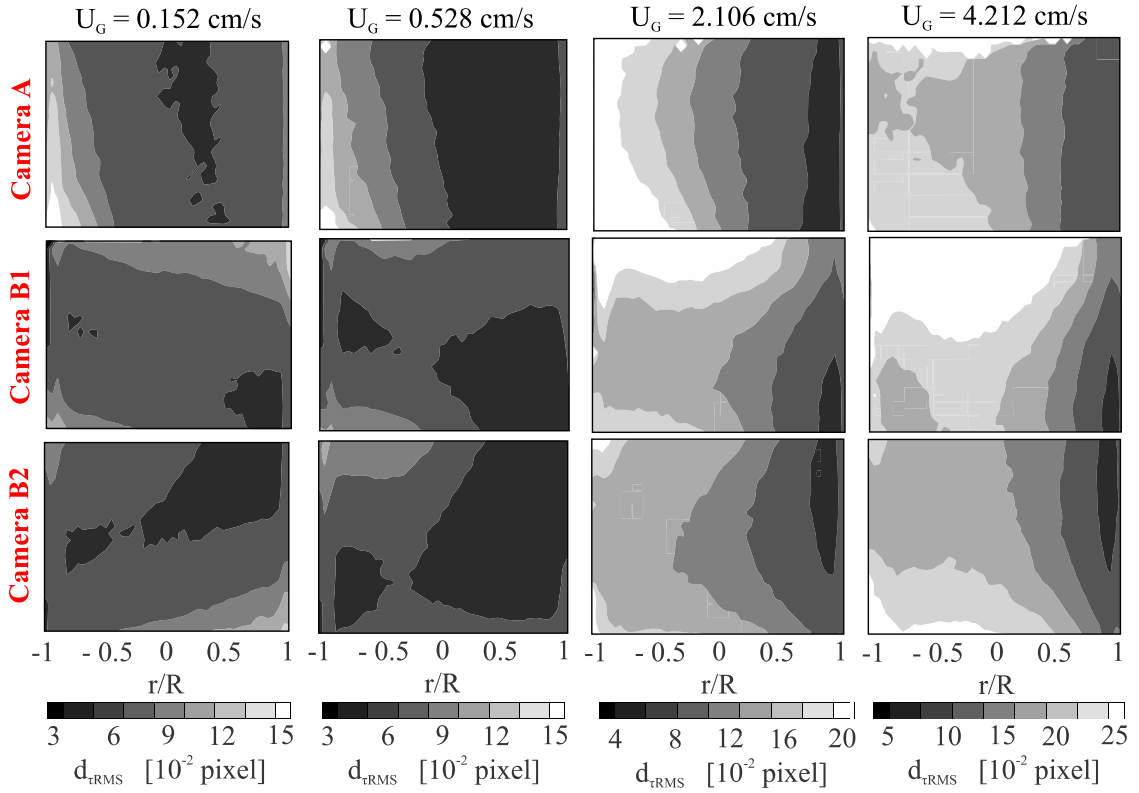

Figure 6.19 – $d_{\tau RMS}$ distribution using SCC approach for camera A, B1, and B2.

If low *ppp* is the dominant noise source in the measurements, then the effect on the components should be the same. However, this was not observed in the velocity fields (Figure 6.16, Figure 6.17, and Figure 6.18). In addition, a large difference was observed between the $\langle u \rangle$ fields of the 2D-2C and 2D-3C measurements. The axial displacement is considerably greater than the radial. This difference makes it difficult to choose a dt for a low-DVR PIV system. For a dt defined in relation to the velocity modulus, the image displacement in the axial direction is easier to determine, i.e., the correlation peak displacement is greater in the axial direction ($ds_y > ds_x$ in Figure 6.20). Table 6.3 presents the maximum and minimum displacement in pixel of the time-averaged velocity components. This can explain the difference between the quality of the fields according to the spatial coherence. The correlation peak displacement, s_D, can be written by Eq. 6.2, where d_r is the pixel pitch, m_0 and n_0 are the displacements related to integer numbers of pixel. ε_X and ε_Y are the fractional displacements (Adrian and Westerweel, 2011).

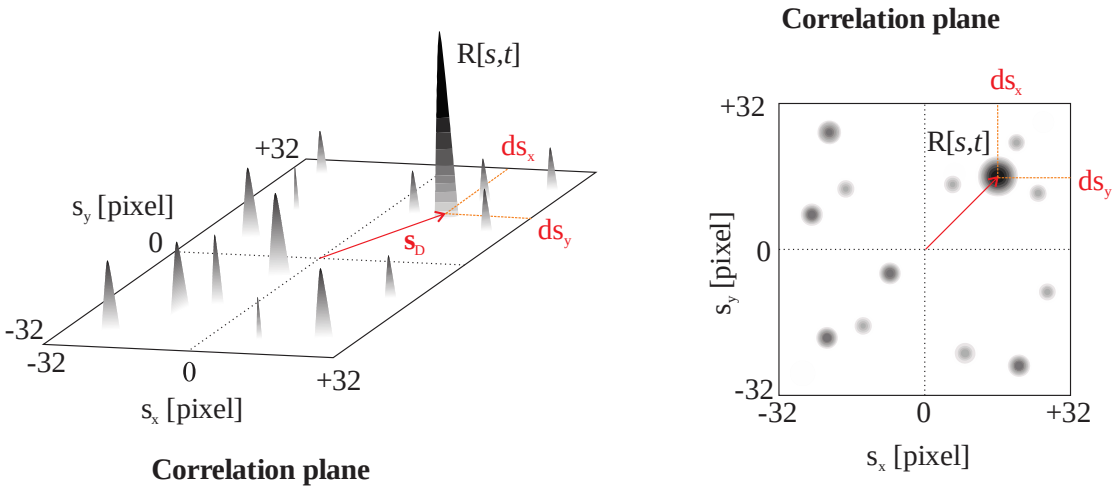

Figure 6.20 – Determination of the correlation peak displacement in the interrogation window (32 x 32 pixels)

$$s_D = \begin{pmatrix} m_0 + \varepsilon_X \\ n_0 + \varepsilon_Y \end{pmatrix} \cdot d_r \tag{6.2}$$

Table 6.3 - Maximum and minimum displacement in pixel of the time-averaged velocity components.

U_G	[pixel]	2D-2C F-PIV				2D-3C F-PIV			
		SCC		EC		SCC		EC	
		min	max	min	max	min	max	min	max
0.152 cm/s	u	-0.084	0.163	-0.025	0.111	-0.059	0.117	-0.056	0.036
	v	-0.365	0.317	-0.221	0.314	-0.503	0.626	-0.435	0.652
	w	-	-	-	-	-0.172	0.073	-0.065	0.056
	u	0.002	0.367	0.003	0.314	0.004	0.627	0.011	0.654
0.528 cm/s	u	-2.361	0.540	-0.050	0.123	-0.069	0.166	-0.016	0.155
	v	-1.267	1.167	-1.144	1.270	-1.268	1.164	-1.177	1.273
	w	-	-	-	-	-0.226	0.136	-0.146	0.080
	u	0.021	2.504	0.011	1.270	0.070	1.277	0.056	1.277
2.106 cm/s	u	-3.285	3.676	-0.155	0.174	-2.595	1.701	-0.135	0.167
	v	-5.245	3.079	-1.810	2.088	-7.185	4.965	-1.910	2.163
	w	-	-	-	-	-4.723	4.502	-0.471	0.169
	u	0.048	5.382	0.040	2.090	0.004	8.617	0.075	2.168
4.212 cm/s	u	-31.649	36.794	-0.615	0.773	-5.654	4.921	-0.283	0.352
	v	-47.798	33.787	-2.782	2.432	-15.513	13.645	-2.167	2.362
	w	-	-	-	-	-11.086	11.252	-1.018	0.644
	u	0.022	51.382	0.062	2.783	0.019	19.667	0.108	2.365

The value of the fractional part in Eq. 6.2 is determined by a three-point Gaussian estimator (as presented in Section 5.2) using a subpixel interpolation. This fractional part is directly related to the correlation value (peak detectability, SNR, and correlation coefficient) and peak shape. Several authors have studied the optimization and performance of subpixel interpolations such as, for example, Westerweel (1993), Willet (1996), Westerweel (2000), Scarano (2002), and Foucaut *et al.* (2004).

The time-averaged absolute value of the velocity normalized by uncertainty for radial ($\left\langle UQ_x^* \right\rangle \equiv \left\langle \mathrm{Abs}\left(UQ_x / u \right) \right\rangle$ and $\left\langle UQ_z^* \right\rangle \equiv \left\langle \mathrm{Abs}\left(UQ_z / w \right) \right\rangle$) and axial ($\left\langle UQ_y^* \right\rangle \equiv \left\langle \mathrm{Abs}\left(UQ_y / v \right) \right\rangle$) components can be used to analyze in detail the quality of the measurements. Table 6. *4* shows the spatial average of $\left\langle UQ_i^* \right\rangle\big|_{i=x,y,z}$, $\overline{\left\langle UQ_i^* \right\rangle}\big|_{i=x,y,z}$, for different U_G. The $\overline{\left\langle UQ_y^* \right\rangle}$ values were the lowest for all U_G. For the 2D-3C measurements, the $\overline{\left\langle UQ_z^* \right\rangle}$ values were the highest. This can be directly related to the loss of correlation due to the out-of-plane motion, peak detectability (SNR), or 3C reconstruction error. Moreover, the bubbles located in the front of the

investigation area can change the refractive index distribution, damaging the performance of the 3C reconstruction.

Table 6. 4 – Spatial Average of $\left\langle UQ_i^* \right\rangle\big|_{i=x,y,z}$ in the area investigated for different U_G.

U_G [cm/s]	2D-2C F-PIV		2D-3C F-PIV		
	$\overline{\left\langle UQ_x^* \right\rangle}$	$\overline{\left\langle UQ_y^* \right\rangle}$	$\overline{\left\langle UQ_x^* \right\rangle}$	$\overline{\left\langle UQ_y^* \right\rangle}$	$\overline{\left\langle UQ_z^* \right\rangle}$
0.152	0.552	0.349	0.448	0.322	0.690
0.528	0.410	0.227	0.428	0.285	0.612
2.106	0.518	0.320	0.548	0.438	0.657
4.212	0.397	0.288	0.450	0.372	0.507

In PIV post-processing, the difference in the quality of the velocity components directly affects the performance of the filters. The effect of the filter developed by Westerweel and Scarano (2005) in the post-processed fields (SCC*) can be observed in Figure 6.16, Figure 6.17, and Figure 6.18. Moreover, the post-processed fields can be compared with those obtained by the ensemble correlation (EC) approach. Except for U_G = 4.212 cm/s, the $\langle v \rangle$ distributions obtained by the SCC* and EC approach were almost the same. This behavior was not observed in the $\langle u \rangle$ and $\langle w \rangle$ distributions. However, the distribution of the radial components obtained by the SCC* and EC approaches also did not show large differences for U_G = 0.152 and 0.528 cm/s. For U_G = 4.212 cm/s, all the velocity components obtained by the SCC* and EC approach were different. This is due to the large amount of false vectors (outliers) reducing the performance of the post-processing filter. In this case, the post-processed fields do not represent the actual flow even these fields with a greater spatial coherence.

6.1.4. Effect of the allowed maximum error of reconstruction $\varepsilon_{Max3C-R}$

For measurements 2D-3C shown in Figure 6.16 and Figure 6.17, the allowed maximum reconstruction error of reconstruction $\varepsilon_{Max3C-R}$ may be the explanation of the high spatial coherence observed in the fields in relation to the 2D-2C measurements. In this case, $\varepsilon_{Max3C-R}$ acts as a post processing filter eliminating the outliers. The difference between the profiles of the time-averaged velocity components with and without $\varepsilon_{Max3C-R}$ is shown in Figure 6.21. The

improvement in the spatial coherence was observed in some cases mainly for U_G = 4.212 cm/s based on $\overline{\langle Diff\_4 \rangle}$ values in Table 6.5.

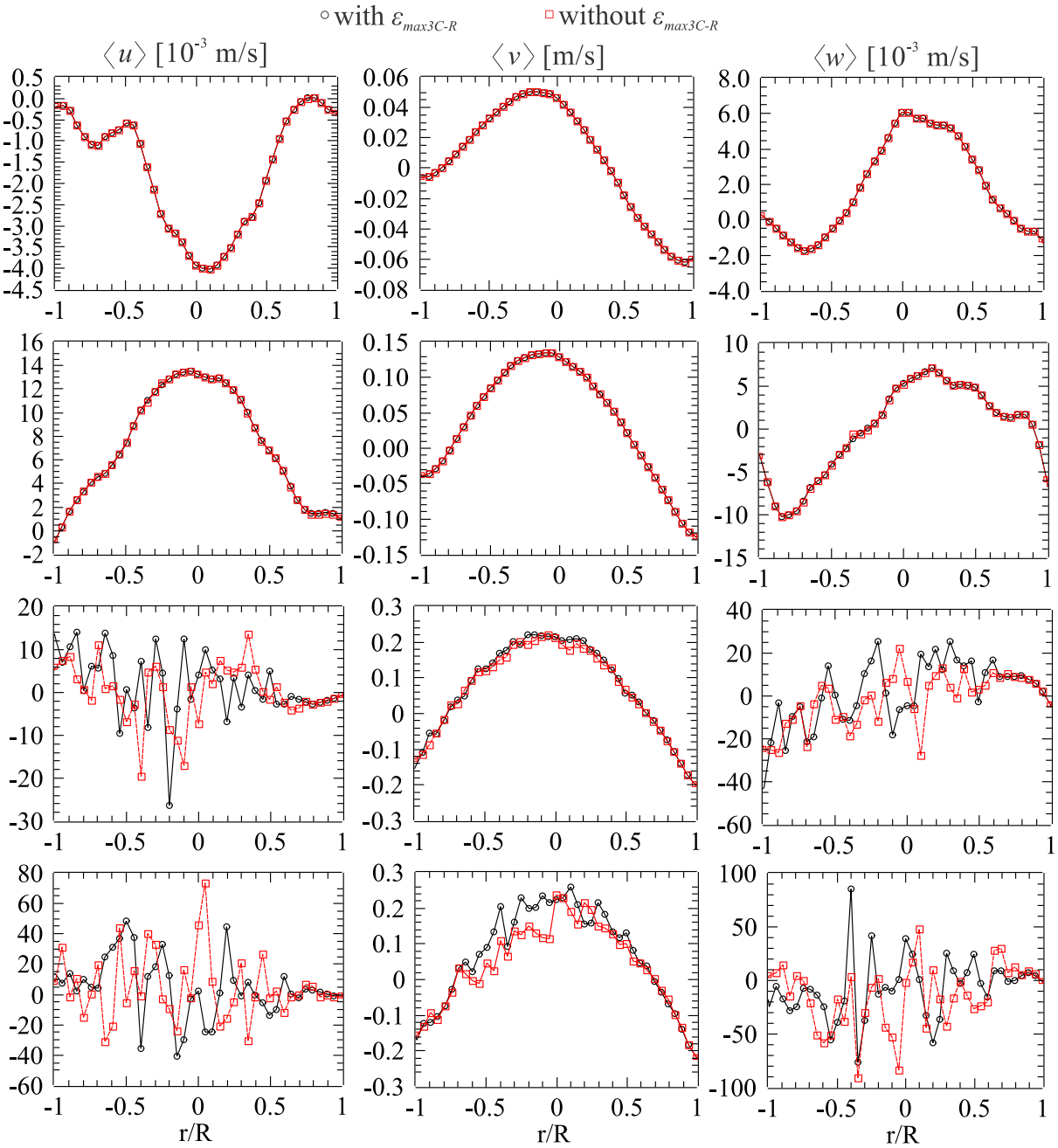

Figure 6.21 - Profiles of the time-averaged velocity components with and without $\varepsilon_{Max3C-R}$

Table 6.5 - Spatial average of $\langle Diff\_4 \rangle$, $\overline{\langle Diff\_4 \rangle}$ [m/s], with and without $\varepsilon_{Max3C-R}$ for different field of view (FOV). FoV = - 1 ≤ r/R ≤ 1, FoV_1 = - 1 ≤ r/R ≤ 0, and FoV_2 = 0 ≤ r/R ≤ 1.

U_G	0.152 cm/s		0.528 cm/s		2.106 cm/s		4.212 cm/s	
$\varepsilon_{Max3C-R}$	with	without	with	without	with	without	with	without
FoV	0.007	0.009	0.013	0.012	0.481	0.441	1.065	1.764
FoV_1	0.008	0.011	0.016	0.014	0.774	0.638	1.368	2.199
FoV_2	0.006	0.006	0.011	0.011	0.225	0.277	0.803	1.418

In Table 6. 4, it was expected that $\overline{\langle UQ_i^* \rangle}\big|_{i=x,y,z}$ values would be the highest for U_G = 4.212 cm/s. These low values can be explained by the large number of outliers and $\varepsilon_{Max3C-R}$ for the 2D-3C measurements. Besides affecting the spatial coherence, the low *ppp* can decrease the CS method performance on the uncertainty quantification. The $\varepsilon_{Max3C-R}$ effect can be observed in Figure 6.22. For all U_G, there was large differences between the $\langle UQ_i^* \rangle\big|_{i=x,y,z}$ values with and without $\varepsilon_{Max3C-R}$. If the 2D-3C field has a vector in the interrogation window with $\varepsilon_{3C-R} > \varepsilon_{Max3C-R}$, then this vector is rejected and a new estimate is made using the second highest correlation peak. The 2D-3C PIV system is more sensitive to the noise than the 2D-2C one mainly because of the 3C reconstruction. The 3C reconstruction error, ε_{3C-R}, can be used as an quality indicator for the 3C-2D measurements.

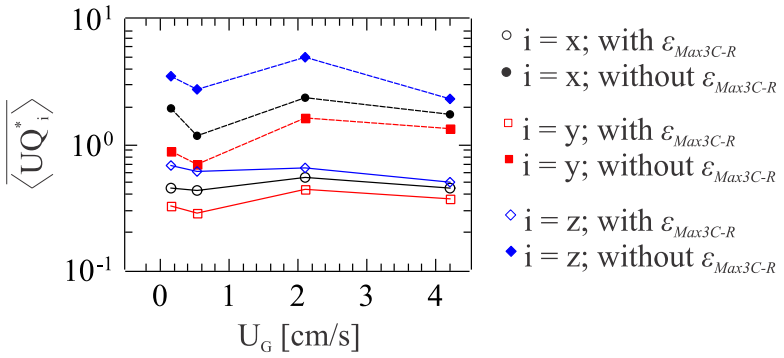

Figure 6.22 - Spatial average of $\langle UQ_i^* \rangle\big|_{i=x,y,z}$ in the area investigated for different U_G with and without $\varepsilon_{Max3C-R}$

The spatial average of the time-averaged 3C reconstruction error, $\overline{\langle \varepsilon_{3C-R} \rangle}$, with and without $\varepsilon_{Max3C-R}$ is presented in the Table 6.6. Small differences between the $\overline{\langle \varepsilon_{3C-R} \rangle}$ values were observed for U_G = 0.152 and 0.528 cm/s. However, the differences are greater for U_G = 2.106 cm/s and especially for U_G = 4.212 cm/s.

Table 6.6 – Spatial average of the time-averaged 3C reconstruction error, $\overline{\langle \varepsilon_{3C-R} \rangle}$, in the area investigated for different U_G.

U_G [cm/s]	$\overline{\langle \varepsilon_{3C-R} \rangle}$ [*pixel*]	
	With $\varepsilon_{Max3C-R}$	Without $\varepsilon_{Max3C-R}$
0.152	0.089	0.109
0.528	0.190	0.194
2.106	0.647	2.554
4.212	1.001	10.730

Table 6.7 - Spatial average of $\langle Diff\_4 \rangle$, $\overline{\langle Diff\_4 \rangle}$ [m/s], with and without $\varepsilon_{Max3C-R}$ for different field of view (FOV). FoV = - 1 ≤ r/R ≤ 1, FoV_1 = - 1 ≤ r/R ≤ 0, and FoV_2 = 0 ≤ r/R ≤ 1.

U_G	0.152 cm/s		0.528 cm/s		2.106 cm/s		4.212 cm/s	
$\varepsilon_{Max3C-R}$	with	without	with	without	with	without	with	without
FoV	0.007	0.009	0.013	0.012	0.481	0.441	1.065	1.764
FoV_1	0.008	0.011	0.016	0.014	0.774	0.638	1.368	2.199
FoV_2	0.006	0.006	0.011	0.011	0.225	0.277	0.803	1.418

6.1.5. Effect of the tracer particle and spatial resolution

Besides the peak detectability, this difference in the measurement quality of the components can be related to the ability of the tracer particles to follow the flow. This capability is guaranteed when the Stokes´ number is less than 0.1, considering that the external forces (gravity, centrifugal and electrostatic) are neglected. The Stokes' number (Eq. 6.3) is defined as the ratio between the relaxation time (τ_p) and the characteristic time scale of the flow (τ_f). The relaxation time (Eq. 6.4) is defined as the response time of the tracer particle to changes in the fluid velocity, where d_p is the diameter of the tracer particle, ρ_p is the tracer particle density,

and ρ and μ is the density and dynamic viscosity of the fluid. The characteristic time scale of the flow, τ_f, can be estimated by Eq. 6.5, where ℓ is the smallest resolved length scale and $\Delta U_{max\text{-}min}$ is the difference between the maximum and minimum velocity of the flow (Samimy and Lele, 1991; Melling, 1997; Westerweel, 1997; Raffel *et al.*, 2007). Table 6.8 presents the ℓ value estimated using the minimum and maximum velocity in the Y direction considering S_k = 0.1 for U_G = 0.152 and 0.528 cm/s. For U_G > 0.528 cm/s, the estimation $\Delta U_{max\text{-}min} = v_{max} - v_{min}$ is compromised by the presence of outliers. In Table 6.8, the ℓ value was at most of the order of 10^{-5} m, i.e., on the order of 10^{-1} pixel (sub-pixel precision).

$$S_K \equiv \frac{\tau_p}{\tau_f} \tag{6.3}$$

$$\tau_p = d_p^2 \frac{(\rho_p - \rho)}{18\mu} \tag{6.4}$$

$$\tau_f = 10 \cdot \ell / \Delta U_{max-min} \tag{6.5}$$

Table 6.8 – Experimental values of $\Delta U_{max\text{-}min} = v_{max} - v_{min}$ and the smallest resolved length scale using rhodamina B for U_G = 0.152 and 0.528 cm/s.

U_G	$\Delta U_{max\text{-}min}$ [m/s]		ℓ [μm]	
[cm/s]	2D-2C	2D-3C	2D-2C	2D-3C
0.152	0.60	0.71	8.31	9.84
0.528	1.60	1.58	22.17	2.91

The effect of the interrogation window size in the measurement quality for 2D-2C PIV was investigated. Figure 6.23 presents the vector field from preprocessed image of Figure 5.3 for U_G = 0.528 cm/s using a size of the final interrogation window (IW*f*) equal to 24 and 16 pixels. The amount of outliers increased with the decrease of IW_f mainly in the shadow regions (low *ppp*). Except for U_G = 4.212 cm/s, this effect of IW_f was observed in the spatial average of $\langle Diff\_4 \rangle$, $\overline{\langle Diff\_4 \rangle}$, in Table 6.9. The spatial coherence for IW_f = 24 and 16 pixels was lower in relation to 32 pixels. For U_G = 4.212 cm/s, in some regions it was not possible to calculate the velocity field due to the absence of particle images.

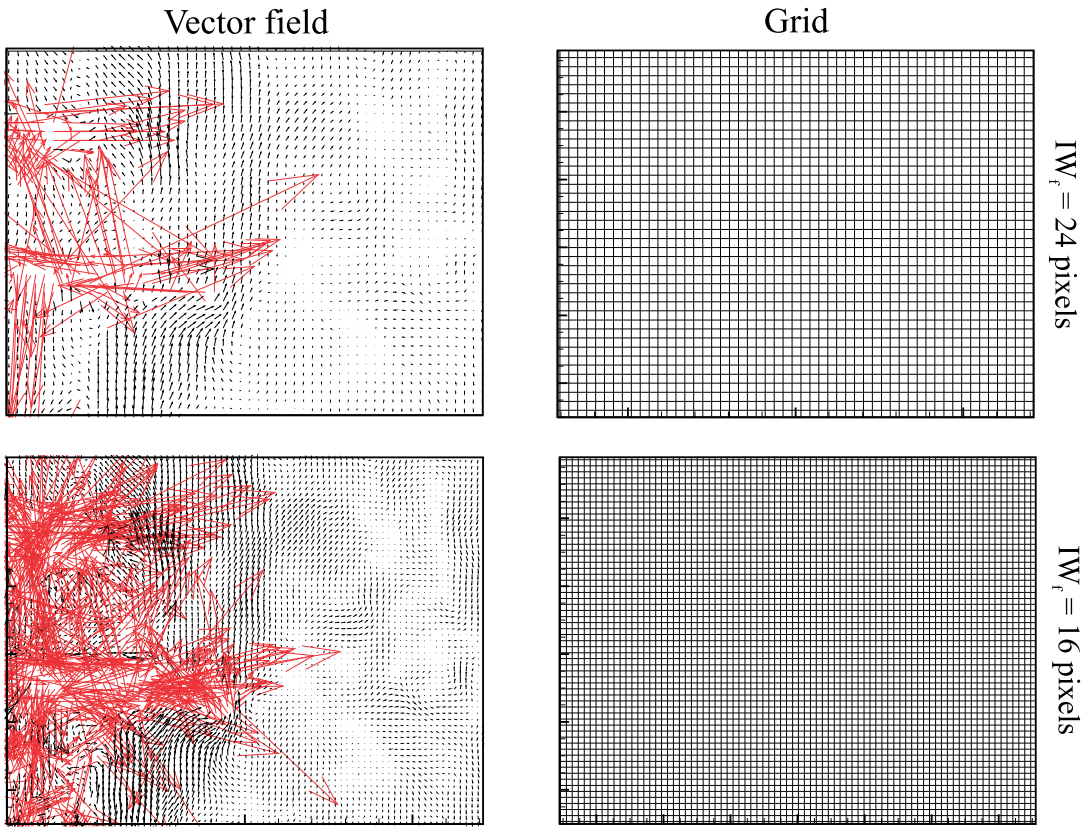

Figure 6.23 – Instantaneous vector field and grid for a size of final interrogation window (IW_f) equal to 24 and 16 pixels from preprocessed image of the Figure 5.3 for U_G = 0.528 cm/s.

Table 6.9 - Spatial average of $\langle Diff\_4 \rangle$, $\overline{\langle Diff\_4 \rangle}$, in frame for different size of final interrogation window (IW_f)

U_G (cm/s)	IW_f (pixel)	IW_f (10^{-3} m)	$\overline{\langle Diff\_4 \rangle}$ (m/s)
0.152	32	3.2	0.010
	24	2.4	0.022
	16	1.6	0.046
0.528	32	3.2	0.064
	24	2.4	0.157
	16	1.6	0.126
2.106	32	3.2	0.252
	24	2.4	0.447
	16	1.6	0.554
4.212	32	3.2	1.523
	24	2.4	1.195
	16	1.6	0.995

6.2. NOISE EFFECT IN CONVERGENCE OF THE AVERAGE FIELD

6.2.1. Analysis of the velocity fluctuation

The fluctuations of the velocity modulus, $\mathbf{u}_{rms}$, were used to identify the noise in the instantaneous fields before calculating the average field. In addition, two approaches were used in the PIV interrogation: standard cross-correlation (SCC) and sliding-average correlation (SAC) approaches. The presence of outliers directly interfered in the time series and consequently in $\mathbf{u}_{rms}$. As discussed in Chapter 2, the SAC approach can reduce the random component of the measurement error increasing the measurement accuracy of $\mathbf{u}_{rms}$ (Figure 2.7). Therefore, the comparison between $\mathbf{u}_{rms}$ obtained by the SCC and SAC approaches can be used to identify sources of noise. Figure 6.24 shows an example of the difference between the time series obtained by the SCC and SAC approach, where the noise effect can be observed. The time-averaged of the series presented in Figure 6.24 was 0.164 and 0.136 m/s for the SCC and SAC approaches, respectively.

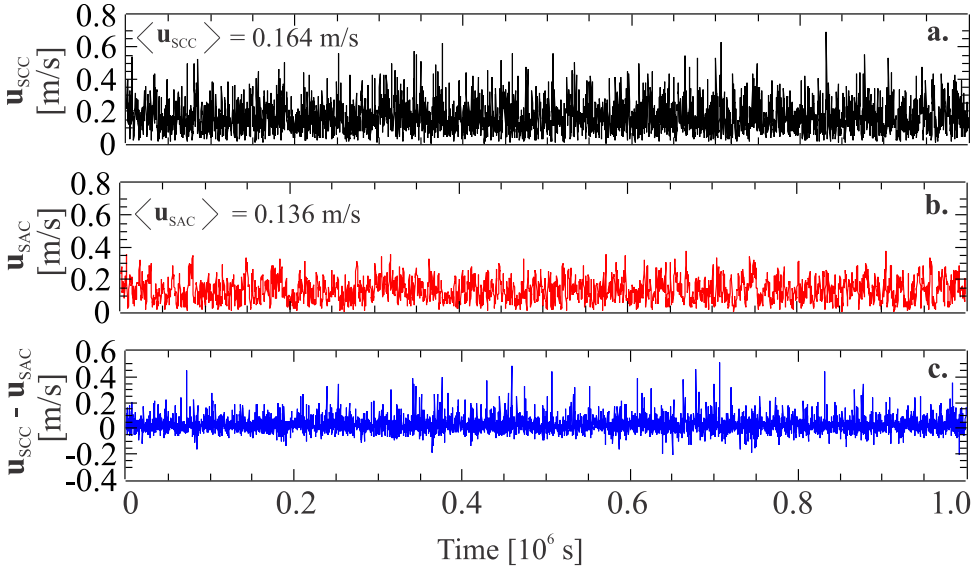

Figure 6.24 – Time series of the velocity modulus, **u**, obtained using the (a) SCC and (b) SAC approach from 2D-2C measurements for r/R = 0, Y = 0.552 cm, and U_G = 0.528 cm/s. (c) Difference between the time series obtained by standard cross-correlation (SCC) and sliding-average correlation (SAC) approaches.

The velocity modulus fluctuation obtained using SCC, $\mathbf{u}_{rms\_SCC}$, and SAC, $\mathbf{u}_{rms\_SAC}$, approaches from 2D-2C and 2D-3C measurements for different U_G is presented in Figure 6.25. A large difference between the $\mathbf{u}_{rms\_SCC}$ and $\mathbf{u}_{rms\_SAC}$ fields was also observed mainly with increasing U_G. The spatial coherence of $\mathbf{u}_{rms}$ field decreased with increasing U_G, where the spatial coherence of $\mathbf{u}_{rms\_SAC}$ was higher than $\mathbf{u}_{rms\_SCC}$ proving that the SAC approach was more robust than SCC. Similar to the effect presented in Table 6.4, the allowed reconstruction maximum error, $\varepsilon_{Max3C-R}$, defined in the 3C reconstruction (Chapter 3) can be responsible for the difference between the $\mathbf{u}_{rms}$ for the 2D-2C and 2D-3C measurements. This difference was observed mainly for 2.106 and 4.121 cm/s. In Figure 6.26, this can be seen more clearly in the $\mathbf{u}_{rms}$ profiles. The behavior of $\mathbf{u}_{rms}$ is also directly related to the low particle image concentration (ppp) in frame as investigated in Table 6.1 and 6.2.

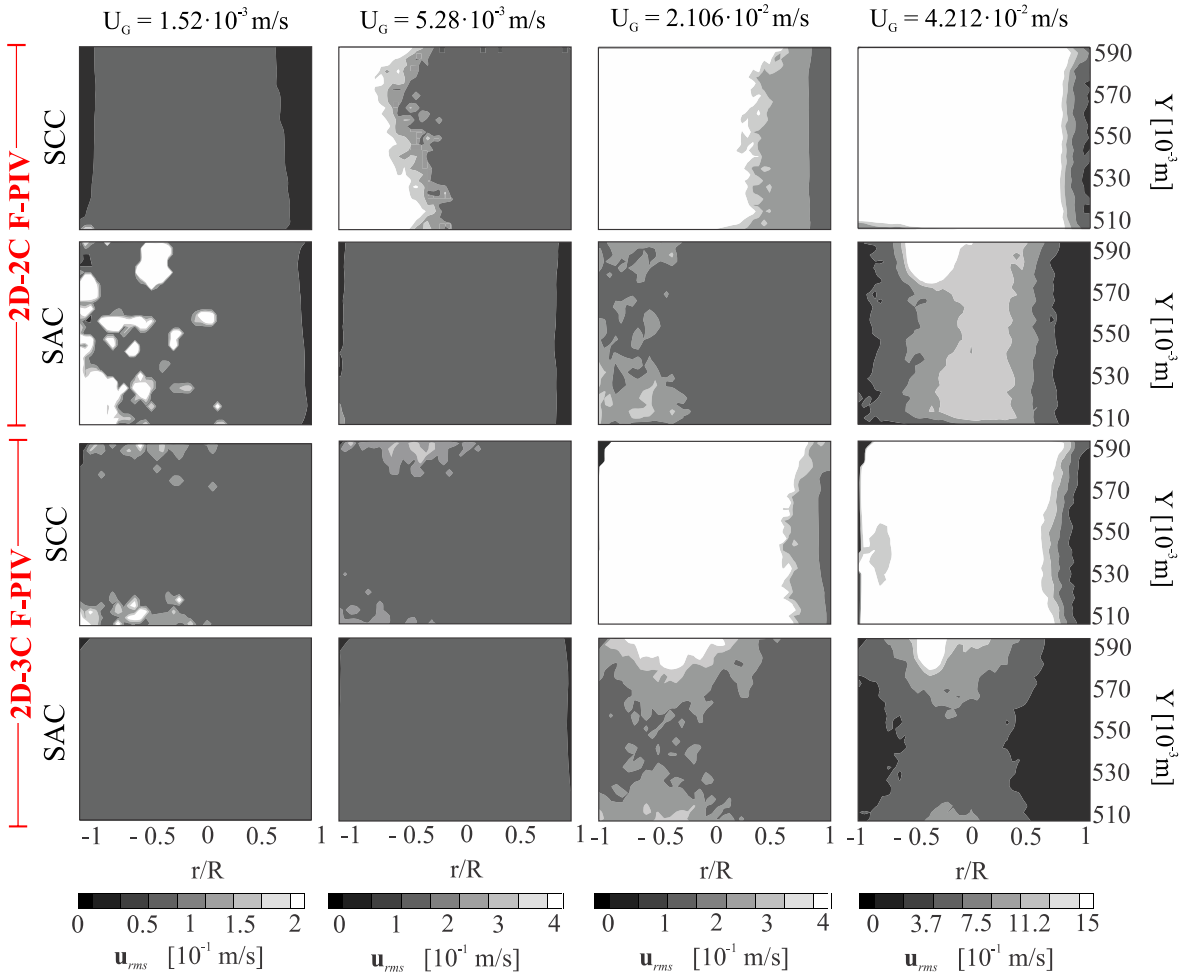

Figure 6.25 – Velocity modulus fluctuation field obtained using standard cross-correlation, $\mathbf{u}_{rms\_SCC}$, and sliding-average correlation, $\mathbf{u}_{rms\_SAC}$, approaches from 2D-2C and 2D-3C measurements for different U_G.

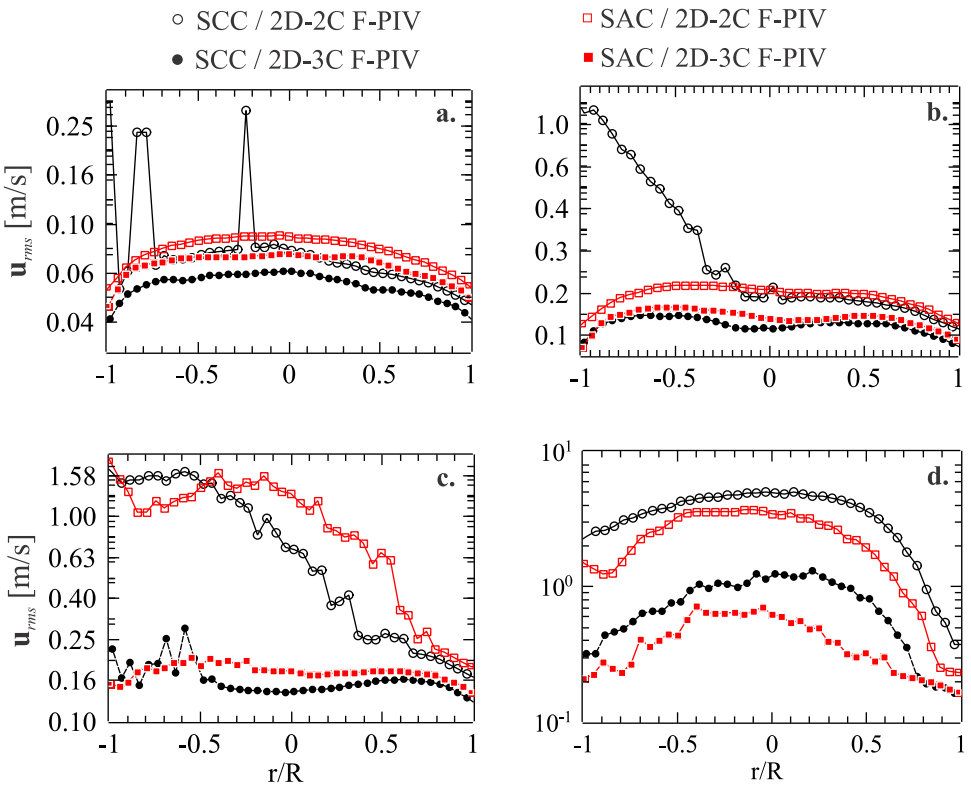

Figure 6.26 - $\mathbf{u}_{rms}$ profiles for Y= 0.552 m and U_G = (a) 0.152, (b) 0.528, (c) 2.106, and (d) 4.121 cm/s obtained by standard cross-correlation (SCC) and sliding-average correlation (SAC) approaches.

6.2.2. Analysis of the convergence of the average field.

Equation 6.6 was used to evaluate if the number of frames N_R was enough to obtain the convergence of the time-averaged velocity. Theoretically, the ideal frame number is obtained when ($\mathbf{u}^*$, u^*, v^*, w^*) = 0. Figure 6.27 shows the values of the spatial average of $\mathbf{u}^*$, u^*, v^*, and w^* ($\overline{\mathbf{u}^*}$, $\overline{u^*}$, $\overline{v^*}$, and $\overline{w^*}$) in the area investigated by the SCC, SAC, and EC approaches. The effect of noise on the convergence of the average field can be observed by the differences of the values of $\overline{\mathbf{u}^*}$, $\overline{u^*}$, $\overline{v^*}$, and $\overline{w^*}$ obtained by the three approaches when $N_R \rightarrow 4000$, in which the values of $\overline{v^*}$ were lower than those of $\overline{u^*}$ and $\overline{w^*}$ in almost all cases (Table E1 and Figure E1). Except for U_G = 4.121 cm/s using the 2D-2C PIV, the values of $\overline{v^*}$ were less than 0.10 (Table E2). This is directly related to large displacement range of the correlation peak as discussed in section 6.1.3. In addition, the behavior of $\overline{\mathbf{u}^*}$ was similar to that of $\overline{v^*}$.

$$i^*_{N_R}\Big|_{i=\mathbf{u},u,v,w} = Abs\left(\frac{\langle i\rangle_{4000} - \langle i\rangle_{N_R}}{\langle i\rangle_{4000}}\right)\Bigg|_{i=\mathbf{u},u,v,w} \tag{6.6}$$

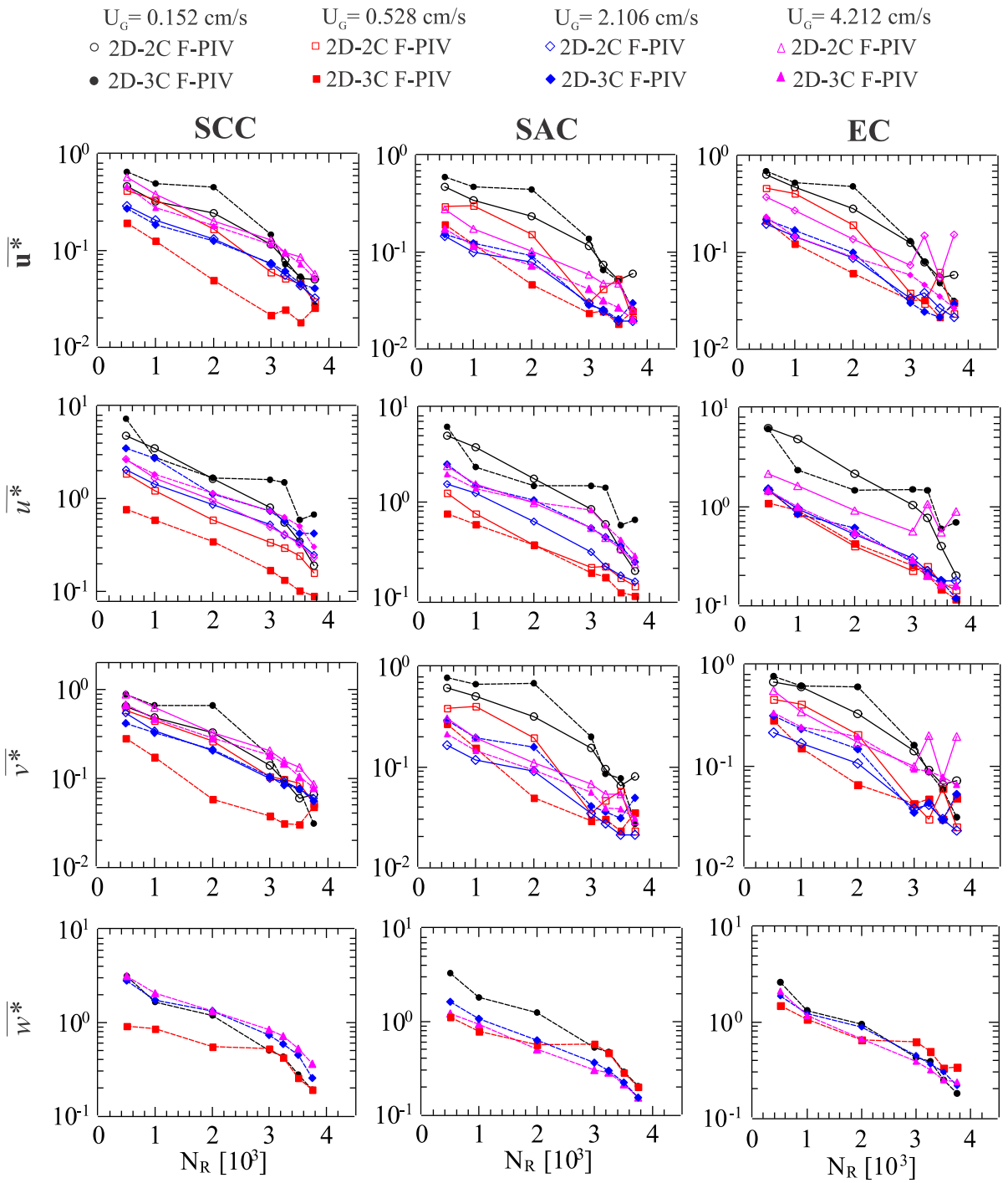

Figure 6.27 – Spatial average of $\mathbf{u}^*$, u^*, v^*, and w^* in function of the number of frames N_R for different U_G and standard cross-correlation (SCC), and sliding-average correlation (SAC), and ensemble correlation (EC) approaches.

The analysis of the spatial coherence can be analyzed by $Diff\_4$ of the time-averaged field ($Diff\_4_{taf}$), where $Diff\_4$ is the spatial average of the velocity difference in the interrogation window and its four neighbors. In Figure 6.28, the noise effect can be clearly seen in the spatial average of $Diff\_4_{taf}$ normalized by the time-averaged of $\mathbf{u}$, $\overline{Diff\_4_{taf}/\langle \mathbf{u} \rangle}$, for different U_G. Ideally, $\overline{Diff\_4_{taf}/\langle \mathbf{u} \rangle} \to 0$ when $N_R \to 4000$. For the EC approach, $\overline{Diff\_4_{taf}/\langle \mathbf{u} \rangle} < 0.1$ when N_R = 4000. In most cases, the $\overline{Diff\_4_{taf}/\langle \mathbf{u} \rangle}$ values were higher for the SCC approach than for the SAC. This can also be observed in the comparison of the profiles of the velocity modulus for the both approaches in Figure 6.29 and Figure 6.30. The profiles of the time-averaged of *Diff_4*, $\langle Diff\_4 \rangle$, and *Diff_4* normalized by velocity modulus, $\langle Diff\_4/\mathbf{u} \rangle$, for sliding-average correlation (SAC) are presented in Figure D2. The $\langle Diff\_4 \rangle$ and $\langle Diff\_4/\mathbf{u} \rangle$ values were lower than for the SCC approach (Figure 6.7).

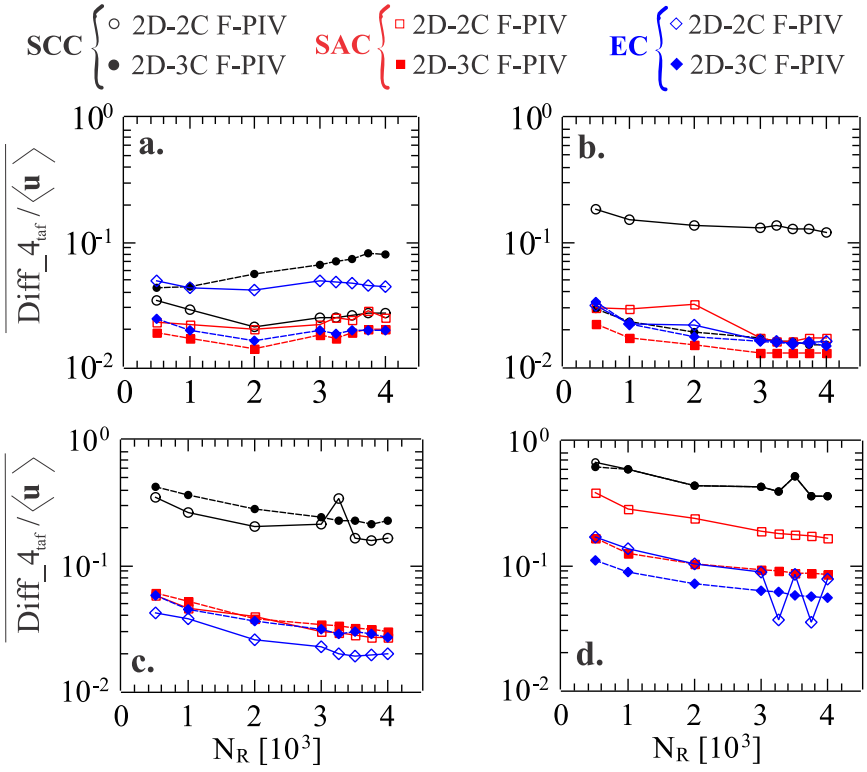

Figure 6.28 - Spatial average of $Diff\_4$ for the time-averaged field, $Diff\_4_{taf}$, normalized by the time-averaged **u**, $\overline{Diff\_4_{taf}/\langle \mathbf{u} \rangle}$, for U_G = (a) 0.152, (b) 0.528, (c) 2.106, and (d) 4.121 cm/s.

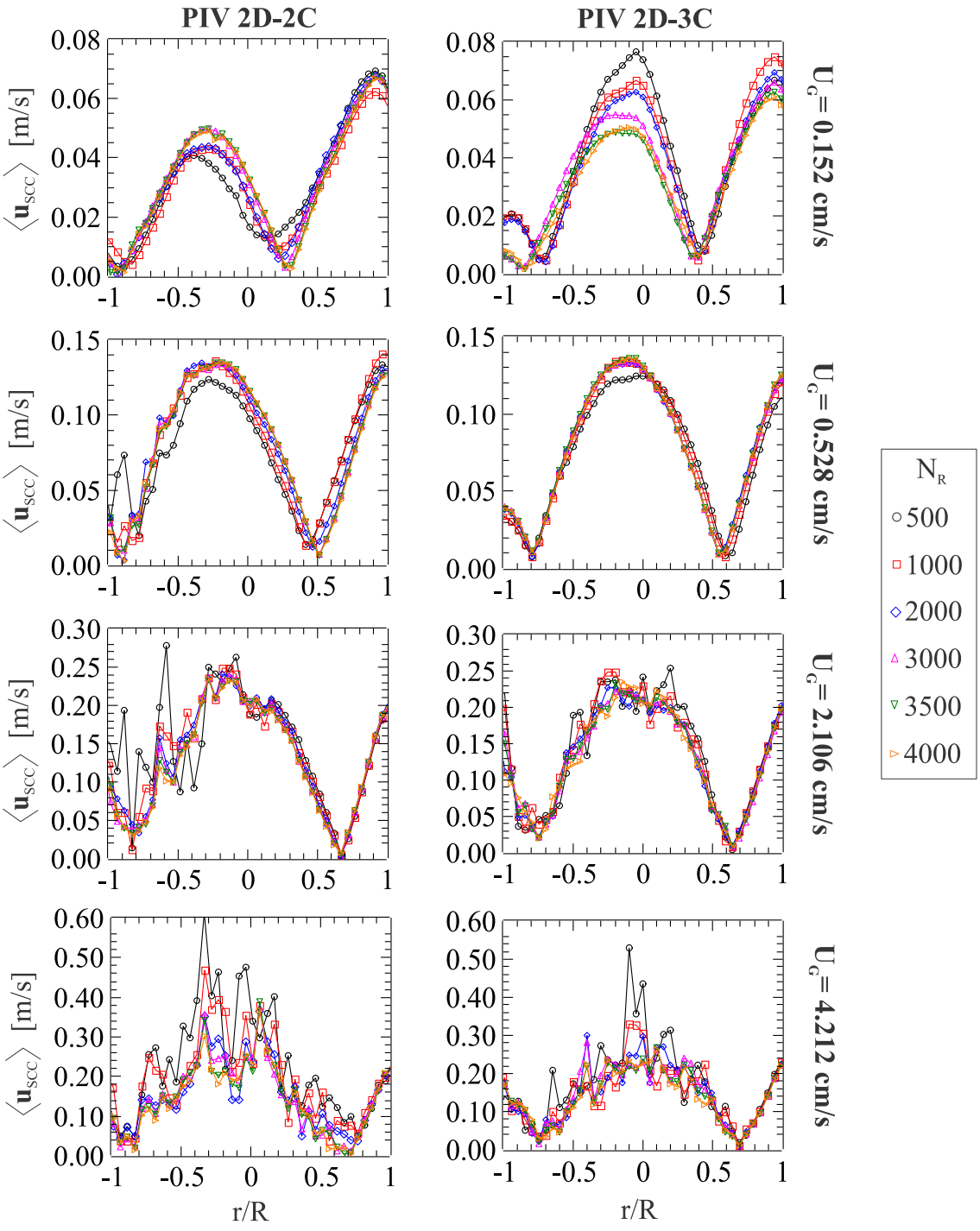

Figure 6.29 - Time-averaged velocity modulus profiles along the radius for different U_G and N_R obtained by the standard cross-correlation (SCC) approach, $\langle \mathbf{u}_{SCC} \rangle$ located at Y = 0.552 m.

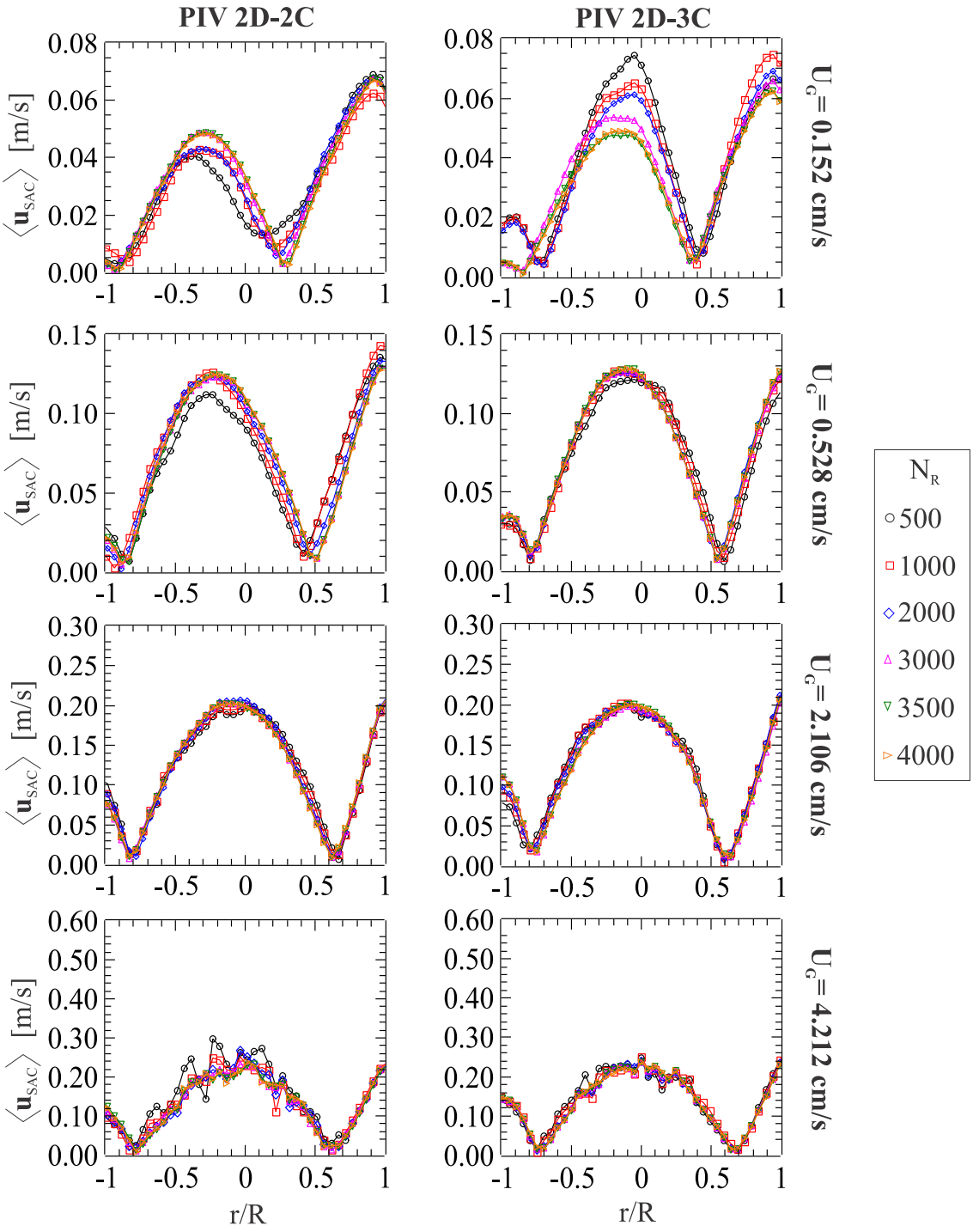

Figure 6.30 – Time-averaged velocity modulus profiles along the radius for different U_G and N_R obtained by the sliding-average correlation (SAC) approach, $\langle \mathbf{u}_{SAC} \rangle$ located at Y = 0.552 m.

For standard cross-correlation (SCC) approach (Figure 6.29), the effect of low *ppp* (Table 6.1 and Table 6.2) can also be observed on the left side of the time-averaged velocity modulus profiles and in the difference between 2D-3C and 2D-2C measurements, respectively.

This low *ppp* effect was not observed for the SAC approach (Figure 6.30). In this case, the SAC approach becomes a good alternative in the low *ppp*. Besides the high cost, there is no guarantee that the increase in the rhodamine concentration can be directly related to the increase of the measurement quality, since *ppp* also depends on the homogeneous illumination and presence of the bubbles in the investigated area (as observed in section 5.1).

6.2.3. Effect of the sliding-average correlation (SAC) on the measurement quality

In general, the spatial average of $\langle SNR \rangle$ and $\langle \varepsilon_{3C-R} \rangle$, that is $\overline{\langle SNR \rangle}$ and $\overline{\langle \varepsilon_{3C-R} \rangle}$, did not vary considerably with N_R for the SCC and SAC approaches (Figure 6.31). For both approaches, the $\overline{\langle SNR \rangle}$ and $\overline{\langle \varepsilon_{3C-R} \rangle}$ values decreased and increased with increasing U_G, respectively. That is, the amount of noise is higher when $\overline{\langle SNR \rangle}$ is lower and $\overline{\langle \varepsilon_{3C-R} \rangle}$ is higher. In addition, there were no significant differences between the $\overline{\langle SNR \rangle}$ values of the 2D-2C and 2D-3C measurements. In Figure 6.31, the SAC approach proved to be more robust than SCC, where $\overline{\langle SNR_{SAC} \rangle}$ was approximately $2 \cdot \overline{\langle SNR_{SCC} \rangle}$ (Table E3) and $\overline{\langle \varepsilon_{3C-R\_SAC} \rangle}$ was approximately $1/2 \overline{\langle \varepsilon_{3C-R\_SCC} \rangle}$.

In Figure 6.32, the uncertainty quantification of the time-averaged velocity modulus and components, $UQ_{\langle i \rangle}\big|_{i=\mathbf{u},u,v,w}$, decreased with U_G for both approaches. In addition, the best quality of the SAC approach in respect to the SCC one can also be observed in the low values of the spatial average of $UQ_{\langle i\_SAC \rangle}\big|_{i=\mathbf{u},u,v,w}$. This behavior can be clearly observed in the $\overline{UQ_{\langle i \rangle}}\big|_{i=\mathbf{u},u,v,w}$ values for both approaches when N_R = 4000 in Figure 6.33, Table E5, and Table E6. According to Sciacchitano (2014), the SAC approach reduces the error by $\sqrt{k}$ assuming that the random error is uncorrelated in time. This can also be observed comparing the uncertainty quantification profiles for both approaches in Figure 6.34 and Figure 6.35. For SCC approach, the effect of low *ppp* can be seen on the left side of the profiles mainly for low U_G = 0.528 and 2.106 cm/s. However, this effect was reduced when using the SAC approach. For the EC approach in Figure 6.31, the $\overline{SNR}$ and $\overline{\varepsilon_{3C-R}}$ values were greater than 10 and smaller than 0.1 pixel, respectively. This shows that for EC approach it is possible to increase the PIV spatial resolution by decreasing the interrogation window if the *SNR* values are greater than 2 and the ε_{3C-R} are

less than 1 pixel. The $\overline{\langle SNR \rangle}$ and $\overline{\langle \varepsilon_{3C-R} \rangle}$ values varied considerably with U_G and N_R for 2.106 and 4.121 cm/s (Table E4). In addition, the effect of the SAC approach can be observed in the low values of $\langle \varepsilon_{3C-R} \rangle$ and $\langle \varepsilon_{3C-R} / \mathbf{u}_{shif} \rangle$ in Figure D3.

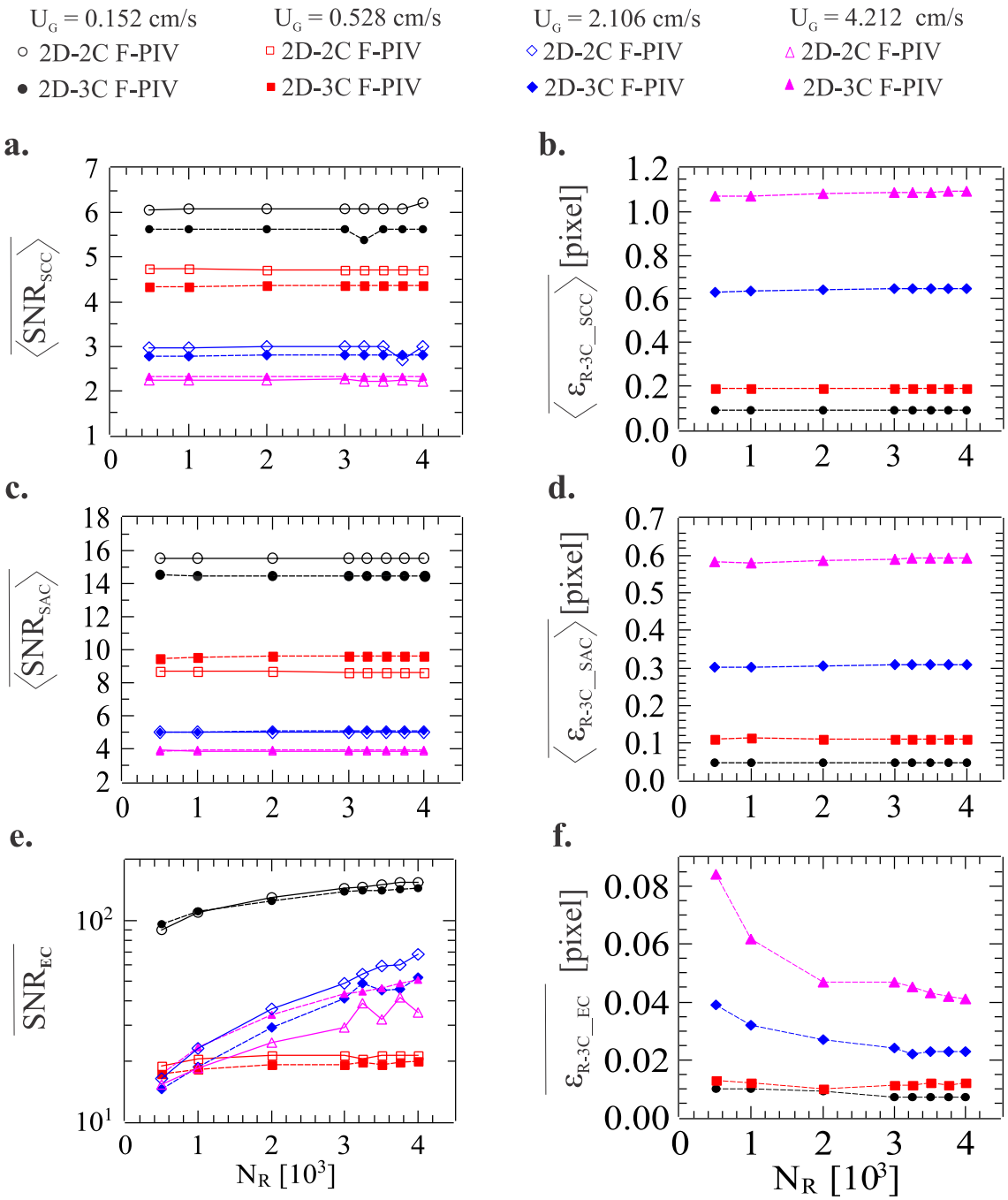

Figure 6.31 – Effect of N_R on the spatial average of $\langle SNR \rangle$ and $\langle \varepsilon_{3C-R} \rangle$ for (a-b) standard cross-correlation (SCC) and (c-d) sliding-average correlation (SAC) approach. (e-f) Analysis of the spatial average of SNR and ε_{3C-R} for ensemble correlation (EC) approach.

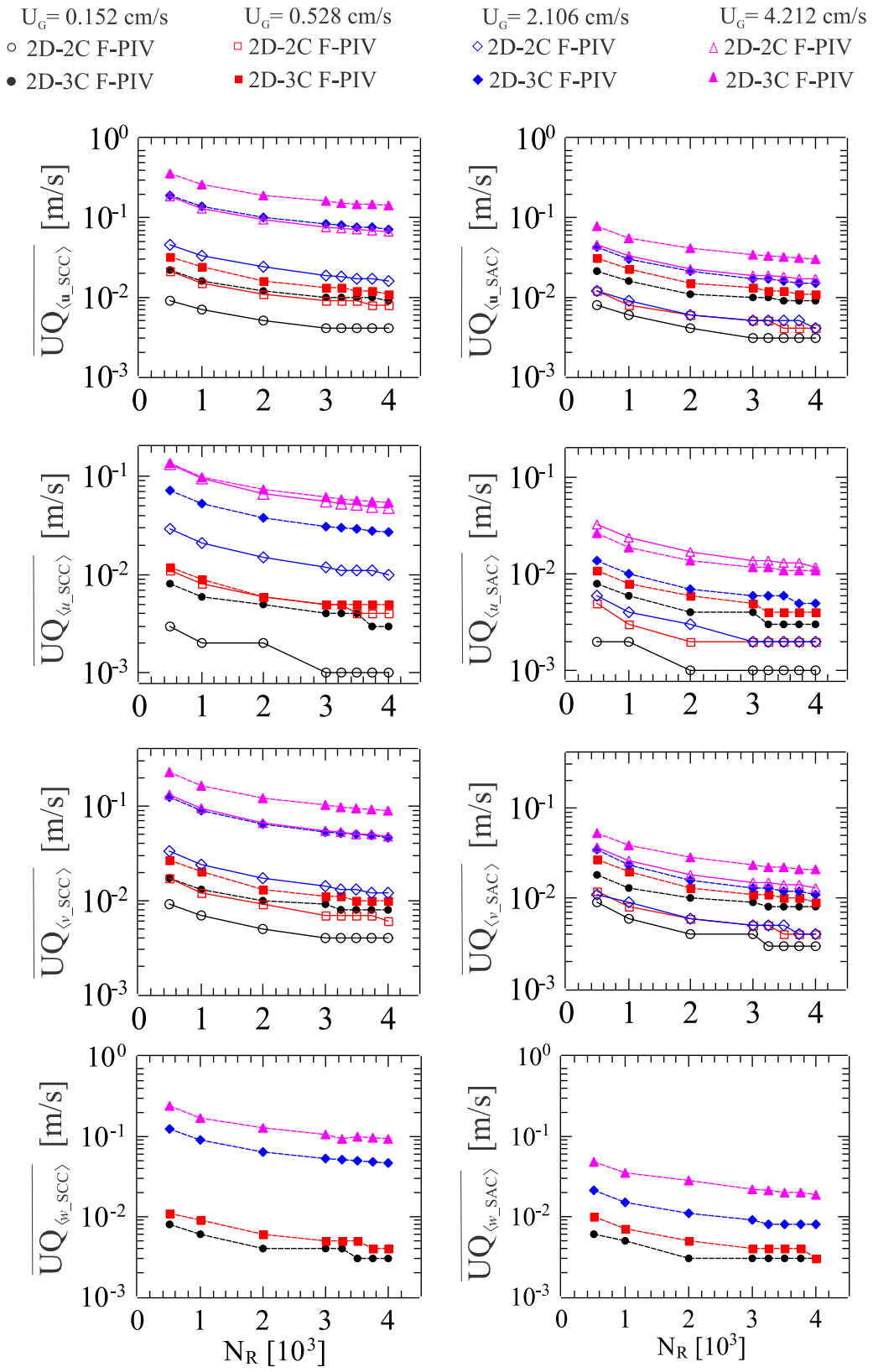

Figure 6.32 – Spatial average of the uncertainty quantification of $\langle \mathbf{u} \rangle$, $\langle u \rangle$, $\langle v \rangle$, and $\langle w \rangle$ obtained by the SCC¨and SAC approach ($\overline{UQ_{\langle i\_SCC \rangle}}\Big|_{i=\mathbf{u},u,v,w}$ and $\overline{UQ_{\langle i\_SAC \rangle}}\Big|_{i=\mathbf{u},u,v,w}$).

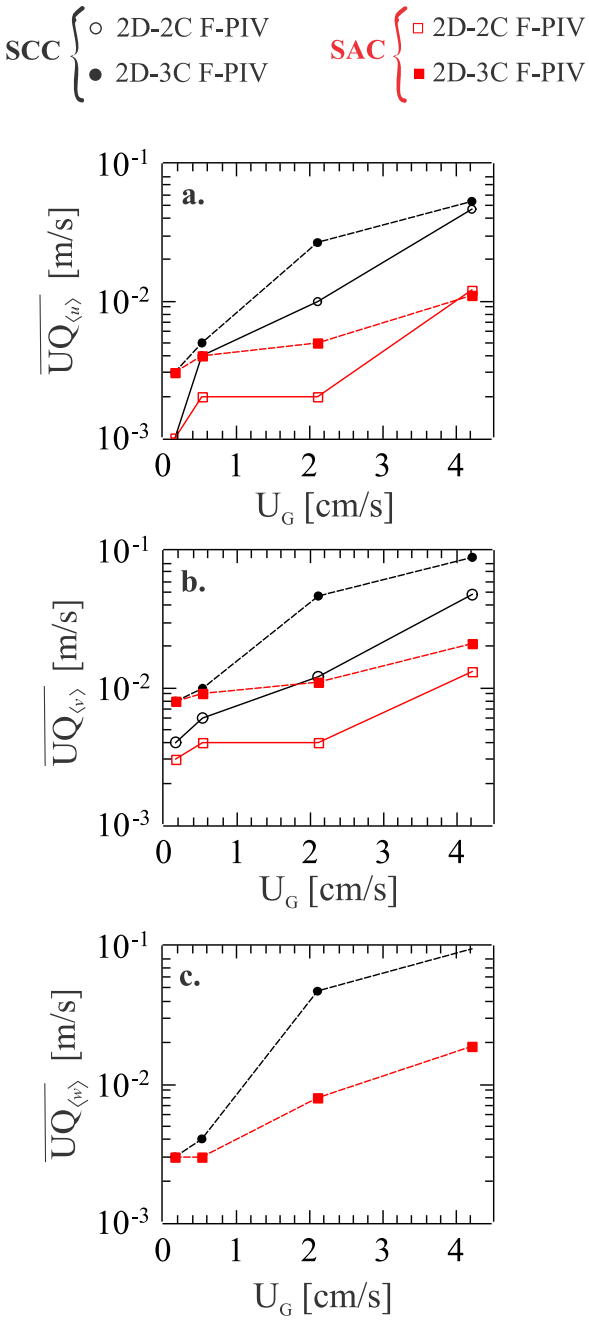

Figure 6.33 – Spatial average of (a) $UQ_{\langle u\rangle}$, (b) $UQ_{\langle v\rangle}$, and (c) $UQ_{\langle w\rangle}$ for N_R = 4000 in function of U_G.

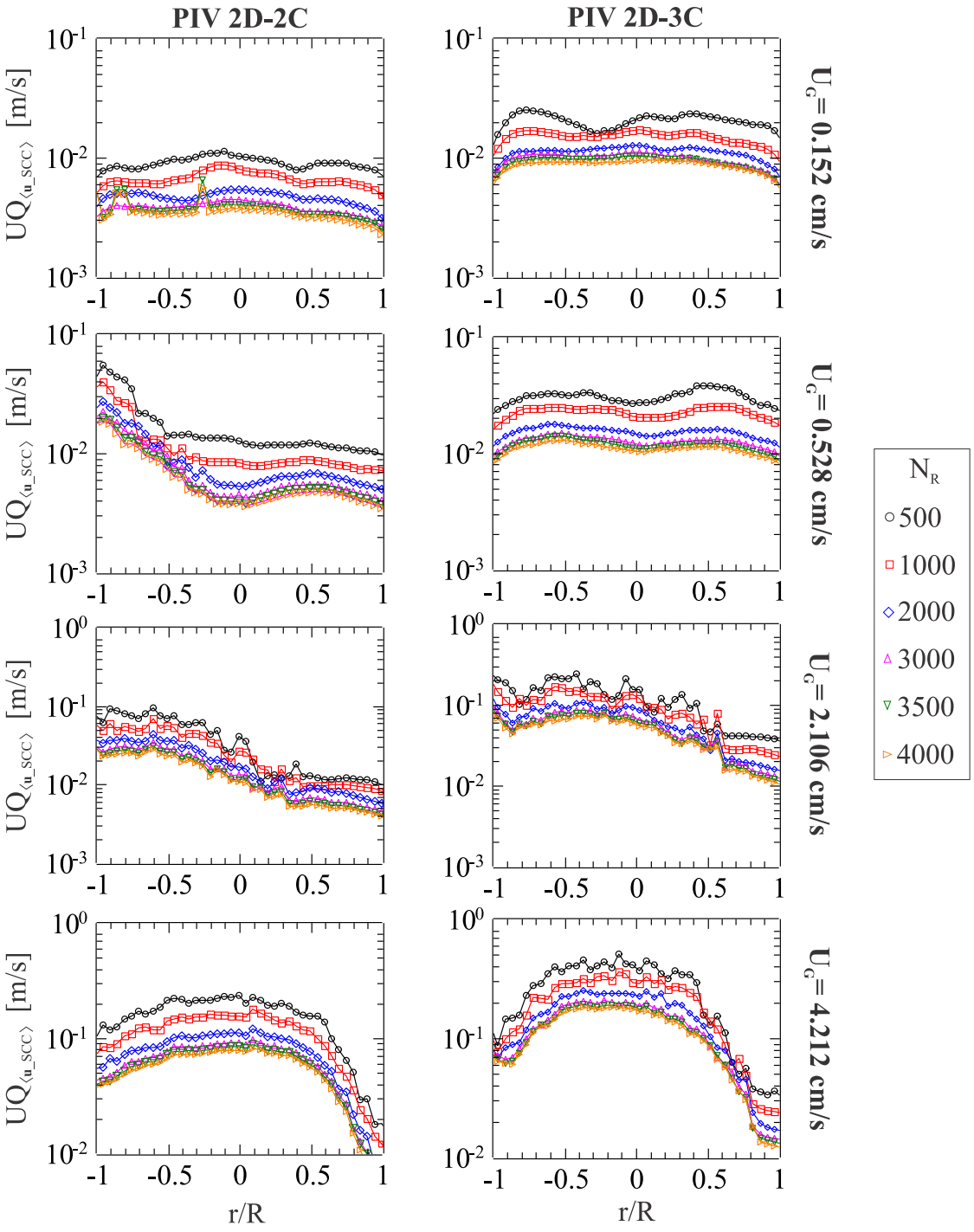

Figure 6.34 –Uncertainty quantification profiles of $\langle \mathbf{u} \rangle$, $\langle u \rangle$, $\langle v \rangle$, and $\langle w \rangle$ along the radius (Y = 0.552 m) for different U_G and N_R obtained by the standard cross-correlation (SCC) approach, $UQ_{\langle i\_SCC \rangle}\Big|_{i=\mathbf{u},u,v,w}$.

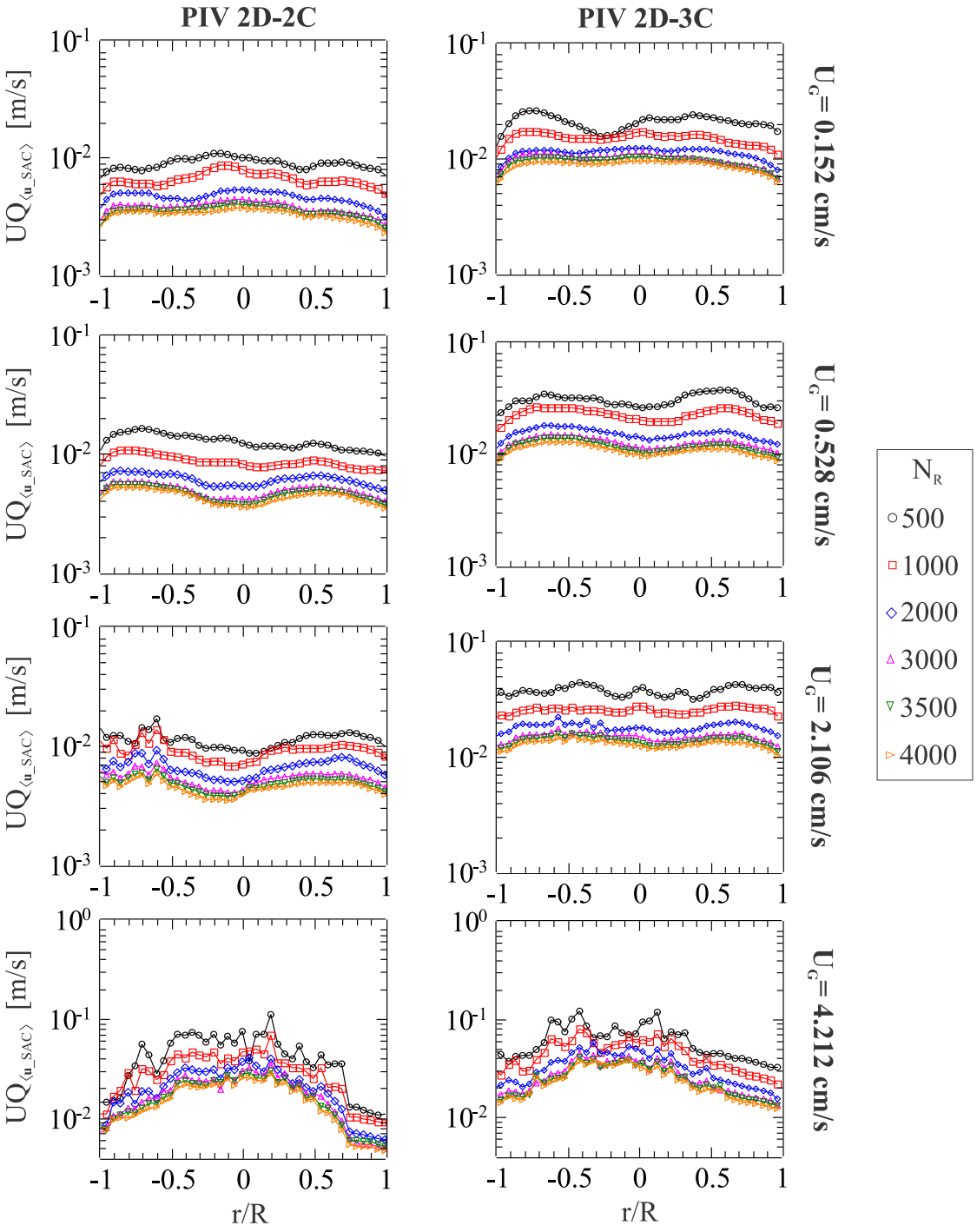

Figure 6.35 - Uncertainty quantification profiles of $\langle \mathbf{u} \rangle$, $\langle u \rangle$, $\langle v \rangle$, and $\langle w \rangle$ along the radius (Y = 0.552 m) for different U_G and N_R obtained by the sliding-average correlation (SAC) approach, $UQ_{\langle i\_SAC \rangle}\Big|_{i=\mathbf{u},u,v,w}$.

The quality of the measurements for the SAC approach can be observed in the smoothing of the vorticity fields and profiles (Figures C3-C6) when compared to the SCC approach (Figures 6.2 and 6.3).

6.3. STRATEGY OF PIV PROCESSING USING THE QUALITY INDICATORS

The optimization strategy of the PIV processing using the quality indicators investigated in sections 6.1 and 6.2 is shown in Figure 6.36.

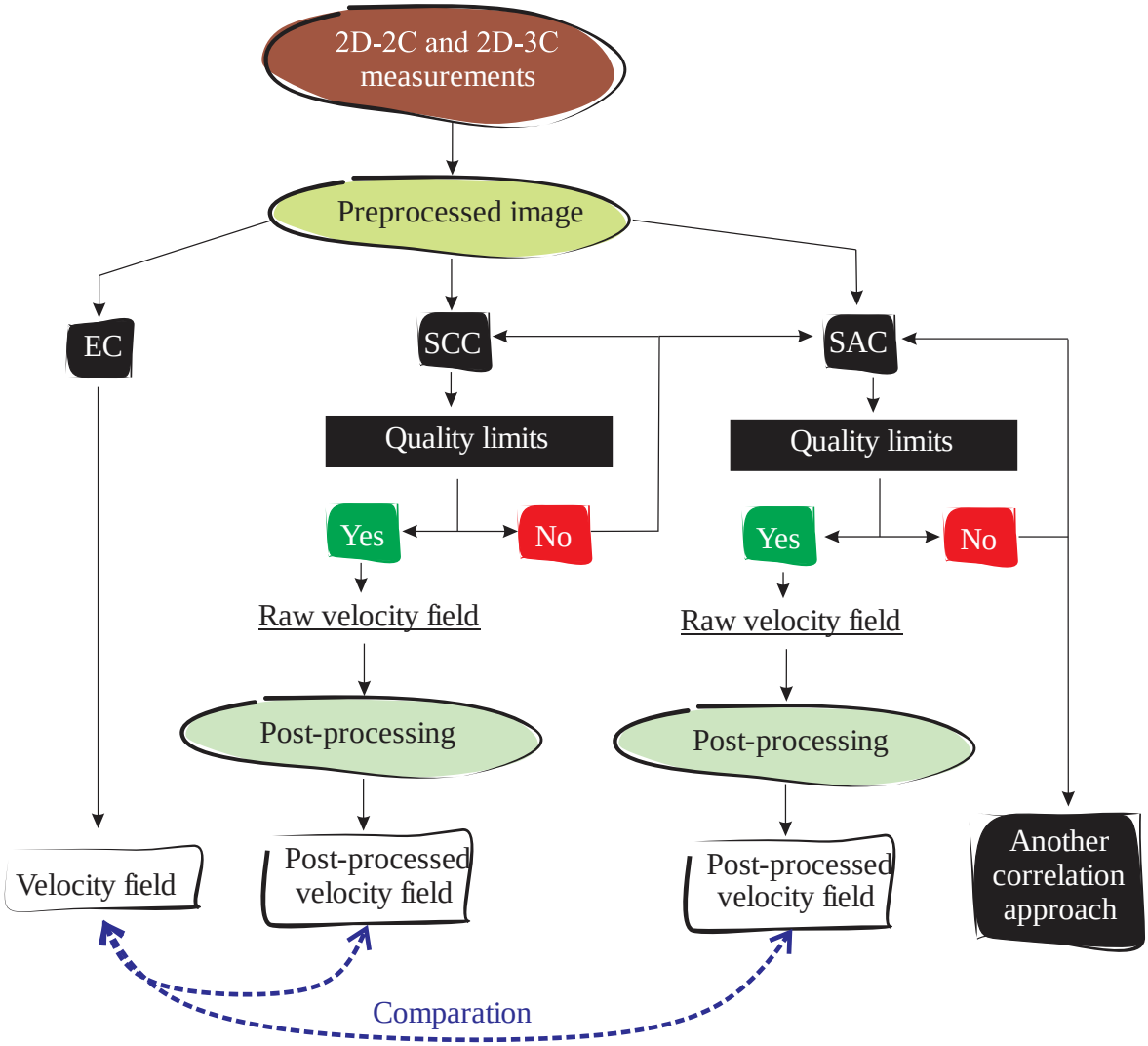

Figure 6.36 - Optimization strategy of the PIV processing using the quality indicators investigated in sections 6.1 and 6.2.

Regarding the quality conditions for standard cross-correlation (SCC) approach, five limits in sections 6.1 and 6.2 were obtained that guarantee that the outliers can be corrected without the vector field losing the representativeness of the flow: $\langle Diff\_4 \rangle < 0.20$ m/s, $\langle Diff\_4/\mathbf{u} \rangle < 0.40$, $\langle \varepsilon_{3C-R}/\mathbf{u}_{shif} \rangle < 0.25$, $\langle \varepsilon_{3C-R} \rangle < 0.70$ pixel, and $d_{\tau RMS} < 0.07$ pixel. For sliding-average correlation (SAC) approach, these quality limits can be applied, except $d_{\tau RMS}$.

If the raw fields obtained by the standard cross-correlation (SCC) approach have values higher than the quality limits observed previously, these fields probably have a high number of outliers that can not be corrected in post-processing. In this case, a new interrogation strategy using the SCC approach can be done or the sliding-average correlation (SAC) approach can be used to decrease or eliminate the outliers. As presented in section 6.2.2, the SAC approach eliminated outliers caused mainly by the low particle image concentration (*ppp*) (Figure 6.37). However, the quality limits should always be analyzed. In addition, the comparison of the post-processed fields with other fields obtained by ensemble correlation or other more robust correlations becomes necessary. In addition, the temporal kernel (*k*) can be optimized in the SAC approach to improve the quality of the measurements.

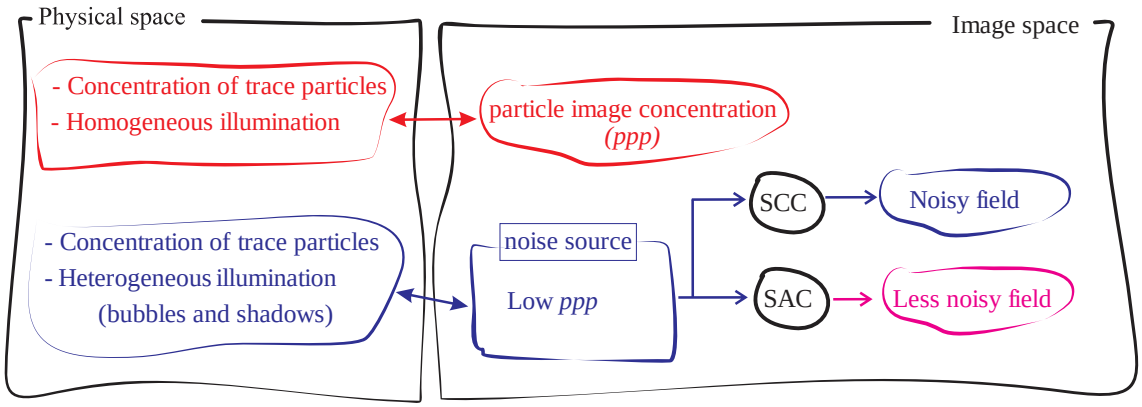

Figure 6.37 – Application of the sliding-average correlation (SAC) approach to decrease or eliminate the effect of the low particle image concentration (*ppp*).

As discussed in section 6.1.3, the quality of the velocity axial component is greater than the radial components mainly in the fields obtained by the SCC approach. This is directly related to the correlation peak displacement. In this case, the displacement in the axial direction is larger and therefore has a smaller error. For PIV systems with low-DVR (conventional PIV or low-DVR PIV), the choice of an ideal interframe time to ensure the quality of the velocity components is difficult (Figure 6.38). The displacement field of the particle images is less

homogeneous due to the passage of few bubbles in the investigated area. This results in a region of maximum and minimum displacement, near and far of the bubbles, respectively.

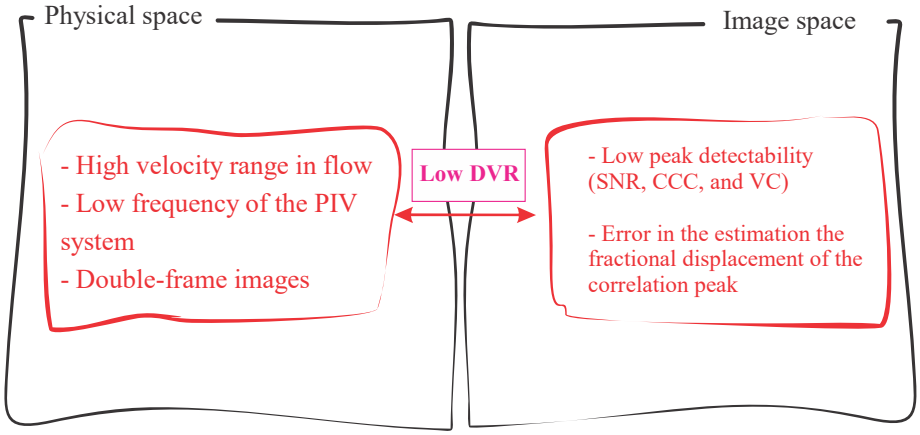

Figure 6.38 - Low DVR as a limiting factor in PIV systems.

A large displacement range in the flow requires a high-DVR of the PIV system (PIV-HDR). For high-DVR PIV, Persoons and O'Donovan (2011) investigated the relationship between the interframe time and SNR using a multi-frame approach. In addition, the use of a high-DVR PIV system allows the application of temporal filters and correlations in the preprocessing, processing, and post-processing. In this case, the temporal and spatial coherence can be used together to increase the quality of the measurements. The drawback is that the high-DVR PIV system is much more expensive than the low-DVR PIV.

Regarding the radial velocity components, the SAC approach presented a higher quality than the SCC approach, as observed in section 6.2.3. However, the development of a correlation that optimizes the particle image displacement using multiple frames in double-frame recording is necessary (like the multi-double-frame (MDF) PIV developed by Persoons *et al.* (2008)).

For investigated correlations in this work, it is only suitable to use the axial velocity, $\langle v \rangle$, to represent the flow up to a superficial gas velocity U_G = 2.106 cm/s (homogeneous flow regime). In the homogeneous-heterogeneous transition regime (U_G = 4.212 cm/s), a more detailed study applying other correlation strategies (correlation approaches, window size and overlap, etc.) becomes necessary.

CHAPTER 7.

CONCLUSIONS AND FUTURE WORK

This chapter presents the conclusions of this Thesis and recommendations for future work.

7.1. CONCLUSIONS

The PIV quality of the liquid phase velocity in the homogeneous and homogeneous-heterogeneous transition flow regime of a bubble column was evaluated. The experimental setup of the 2D-2C and 2D-3C F-PIV system was optimized based on the best recording of light scattering of the tracer particles. In addition, the distortion effect caused mainly by the wall of the column was compensated by using a third-order polynomial as dewarping function.

In general, the quality of the PIV measurements decreased with increasing the superficial gas velocity U_G. This behavior was also related with the low particle image concentration in the frame (*ppp*). The region opposite to the incidence of laser light presented a low *ppp*, causing the increase of outliers (errors > 1 pixel) in the velocity field, particularly with increasing U_G. This can be caused by the large amount of bubbles in the frame, difficulty of penetration of the laser light, and exit of the light emitted by the tracers in column. The effect of the non-uniform illumination (low *ppp*) was observed by the low spatial coherence of the velocity distribution, especially for U_G = 2.106 and 4.212 cm/s (homogeneous-heterogeneous transition flow regime). In addition, a direct relationship between the cross-correlation coefficient (CCC), signal-to-noise ratio (SNR), and uncertainty quantification (UQ) with the spatial coherence of the velocity fields was not established. On the other hand, a low spatial coherence was also observed when the root mean square of the particle image diameter, $d_{\tau RMS}$, was greater than 0.07 pixel. The average of the velocity difference in the interrogation window and its four spatial neighbors (*Diff_4*) was used as a spatial coherence indicator. In addition, outliers were observed mainly when $\langle Diff\_4/\mathbf{u} \rangle > 0.1$, where **u** is the modulus velocity.

The quality of the axial velocity was greater than the radial one. This difference can be directly related to the correlation peak displacement for each component. The axial component had a higher value due to the upward movement of the bubbles. This made it difficult to determine the radial velocity in plane and out-of-plane, since the system used in this work has a low dynamic velocity range (low-DVR). The spatial coherence of the radial distributions was lower than the axial one, even when the post-processing filter was applied. Except for U_G = 4.212 cm/s, the axial velocity distribution was practically the same for the EC and SCC * approaches. Furthermore, a small difference was observed between the axial fields for 2D-2C and 2D-3C measurements, since the perspective error interfered less than the error caused by

the low *ppp* and distortion of the bubbles, especially in 3C reconstruction. For 2D-3C measurements, the in-plane radial velocity showed better quality than the out-of-plane one.

The performance of the post-processing filter in the velocity fields (SCC *) was compromised for U_G = 4.212 cm/s. In this condition, the post-processed fields had high spatial coherence, but did not represent the flow when compared with the fields obtained by EC approach. For the estimation of the average fields, the sliding-average correlation (SAC) approach using a temporal kernel equal to 2 presented higher quality than the SCC approach. Moreover, the noise interfered mainly in the average fields of the radial components. In low-DVR PIV applications, the use of the axial velocity obtained by the standard cross-correlation with post-processing (SCC*) is the most indicated to describe the flow and validate CFD models of the liquid phase velocity in a bubble column for U_G = 0.152, 0.528, and 2.106 cm/s (homogeneous flow regime).

Regarding the quality conditions for standard cross-correlation (SCC) approach, five limits were obtained that guarantee that the outliers can be corrected without the vector field losing the representativeness of the flow: $\langle Diff\_4 \rangle$ < 0.20 m/s, $\langle Diff\_4/\mathbf{u} \rangle$ < 0.40, $\langle \varepsilon_{3C-R}/\mathbf{u}_{shif} \rangle$ < 0.25, $\langle \varepsilon_{3C-R} \rangle$ < 0.70 pixel, and $d_{\tau RMS}$ < 0.07 pixel. Except $d_{\tau RMS}$, these quality limits can be applied for sliding-average correlation (SAC) approach.

The optimization strategy of the PIV processing using the quality indicators investigated in this work is shown in Figure 7.1.

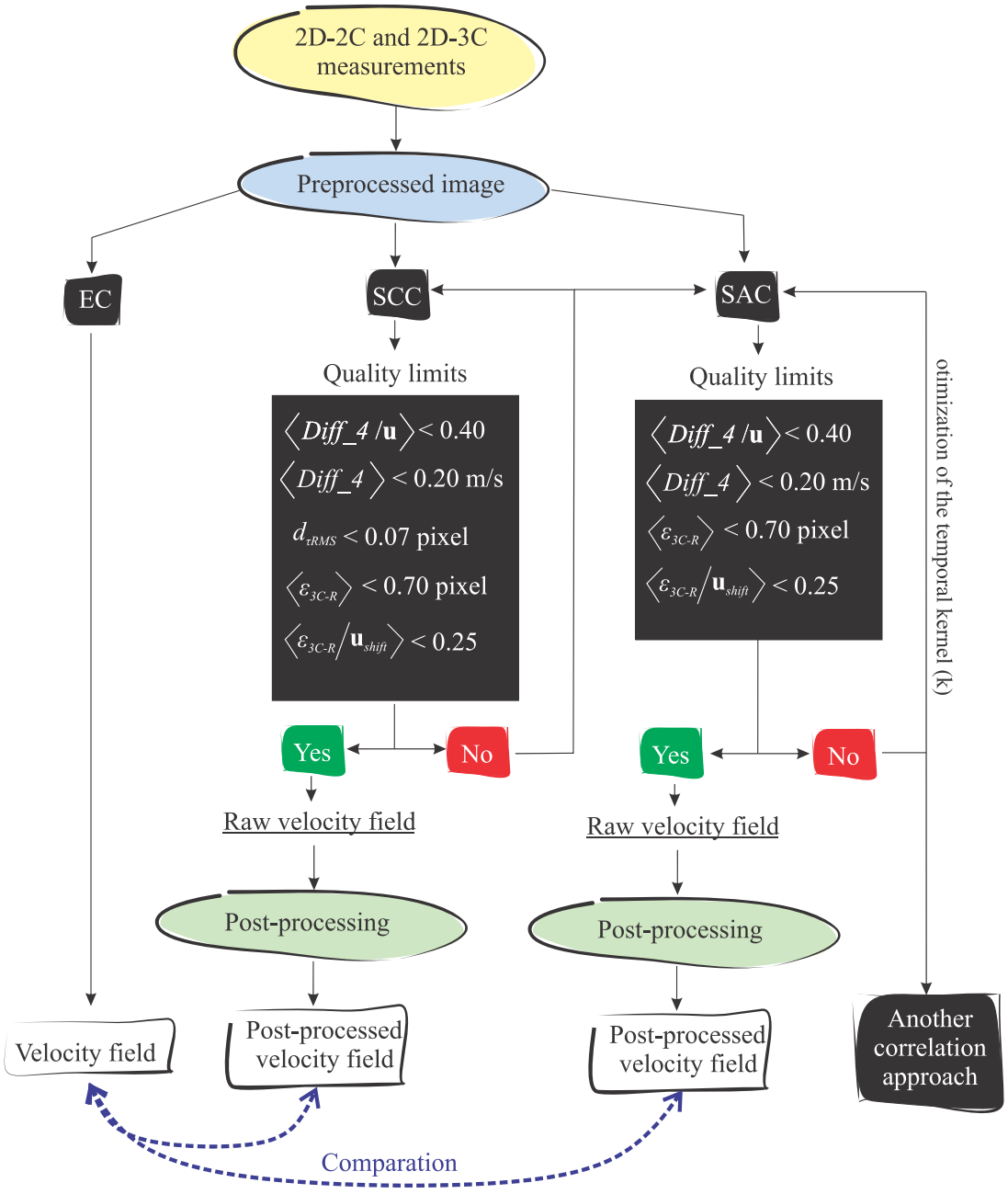

Figure 7.1 - Optimization strategy of the PIV processing using the quality indicators investigated in this work.

7.2. FUTURE WORK

Further research can be performed to improve the quality of the measurements presented along this work. Some suggestions are described below:

- Application of the particle tracking velocimetry (PTV) approach to investigate mainly the regions near the column wall;
- Application of other correlation approaches such as Robust Phase Correlation (RPC);
- Study of the effect of the distortion caused by the bubbles in the velocity field using the self-calibration for 2D-3C system (Wieneke, 2005);
- Investigation of interrogation strategies for the EC and SAC approaches with the aim of increasing the spatial resolution without losing the quality of the velocity fields;
- Application of Synthetic PIV in the investigation of the effects of noise effects for flows with high displacement gradients;
- More detailed investigation of temporal and spatial filters in PIV post-processing;
- Investigation of the intensity distribution in the bubble column using two laser systems.
- A time-resolved PIV system can be used to increase the spatial resolution of the fields using the temporal neighborhood approach to decrease the effect of low *ppp*.
- Development of a PIV software in Matlab.
- Compare the PIV measurements with other techniques.

REFERENCES

Adrian, R. J., 1991. Particle-imaging techniques for experimental fluid mechanics. Annu. Rev. Fluid Mech. 23, 261–304.

Adrian, R.J., 1997. Dynamic ranges of velocity and spatial resolution of particle image velocimetry. Meas. Sci. Technol. 8, 1393–1398. doi:10.1088/0957-0233/8/12/003

Adrian, R.J., Westerweel, J., 2011. Particle image velocimetry. Cambridge University Press, Cambridge; New York.

Becker, S., De Bie, H., Sweeney, J., 1999. Dynamic flow behaviour in bubble columns. Chem. Eng. Sci. 54, 4929–4935. doi:10.1016/S0009-2509(99)00214-6

Becker, S., Sokolichin, A., Eigenberger, G., 1994. Gas—liquid flow in bubble columns and loop reactors: Part II. Comparison of detailed experiments and flow simulations. Chem. Eng. Sci. 49, 5747–5762. doi:10.1016/0009-2509(94)00290-8

Bröder, D., Sommerfeld, M., 2002. An advanced LIF-PLV system for analysing the hydrodynamics in a laboratory bubble column at higher void fractions. Exp. Fluids 33, 826–837. doi:10.1007/s00348-002-0502-z

Calluaud, D., David, L., 2004. Stereoscopic particle image velocimetry measurements of the flow around a surface-mounted block, in: Experiments in Fluids. pp. 53–61. doi:10.1007/s00348-003-0628-7

Charonko, J.J., Vlachos, P.P., 2013. Estimation of uncertainty bounds for individual particle image velocimetry measurements from cross-correlation peak ratio. Meas. Sci. Technol. 24, 65301. doi:10.1088/0957-0233/24/6/065301

Chen, R.C., Reese, J., Fan, L.-S., 1994. Flow structure in a three-dimensional bubble column and three-phase fluidized bed. AIChE J. 40, 1093–1104. doi:10.1002/aic.690400702

Clift, R., Grace, J.R., Weber, M.E., 1978. Bubbles, drops, and particles. Academic Press.

Coleman, H.W., Steele, W.G., 2009. Experimentation, validation, and uncertainty analysis for engineers. John Wiley & Sons.

Deen, N.G., Hjertager, B.H., Solberg, T., 2000. Comparison of PIV and LDA Measurement Methods Applied to the Gas-Liquid Flow in a Bubble Column. 10th Int. Symp. Appl. Laser Tech. to Fluid Mech 1–12.

Deen, N.G., Westerweel, J., Hjertager, B.H., 2001. Upper Limit of the Gas Fraction in PIV Measurements in Dispersed Gas-Liquid Flows, in: 5th Int. Conf. on Gas-Liquid and Gas-Liquid-Solid Reactor Engine. Department of Mechanical Engineering, Aalborg University, Melbourne.

Deen, N.G., Willems, P., van Sint Annaland, M., Kuipers, J.A.M., Lammertink, R.G.H., Kemperman, A.J.B., Wessling, M., van der Meer, W.G.J., 2010. On image pre-processing for PIV of single- and two-phase flows over reflecting objects. Exp. Fluids 49, 525–530. doi:10.1007/s00348-010-0827-y.

Degaleesan, S., Dudukovic, M., Pan, Y., 2001. Experimental study of gas-induced liquid-flow structures in bubble columns. AIChE J. 47, 1913–1931. doi:10.1002/aic.690470904

Delnoij, E., Kuipers, J.A.., van Swaaij, W.P.., Westerweel, J., 2000. Measurement of gas–liquid two-phase flow in bubble columns using ensemble correlation PIV. Chem. Eng. Sci. 55, 3385–3395. doi:10.1016/S0009-2509(99)00595-3

Drahoš, J., Zahradník, J., Punčochář, M., Fialová, M., Bradka, F., 1991. Effect of operating conditions on the characteristics of pressure fluctuations in a bubble column. Chem. Eng. Process. Process Intensif. 29, 107–115. doi:10.1016/0255-2701(91)87019-Y

Elsinga, G.E., van Oudheusden, B.W., Scarano, F., 2005a. Modeling of particle imaging through shock waves. Opt. Model. Perform. Predict. II 5867, 58670M–58670M–11. doi:10.1117/12.616687

Elsinga, G.E., van Oudheusden, B.W., Scarano, F., 2005b. The effect of particle image blur on the correlation map and velocity measurement in PIV, in: Proceedings of SPIE. pp. 588010-588010–12. doi:10.1117/12.616572

Fincham, A., Delerce, G., 2000. Advanced optimization of correlation imaging velocimetry algorithms. Exp. Fluids 29, S13--S22. doi:10.1007/s003480070003

Fincham, A.M., Spedding, G.R., 1997. Low cost, high resolution DPIV for measurement of turbulent fluid flow. Exp. Fluids 23, 449–462. doi:10.1007/s003480050135.

Groen, J.S., Oldeman, R.G.C., Mudde, R.F., van den Akker, H.E.A., 1996. Coherent structures and axial dispersion in bubble column reactors. Chem. Eng. Sci. 51, 2511–2520. doi:10.1016/0009-2509(96)00110-8

Hain, R., Kähler, C.J., 2007. Fundamentals of multiframe particle image velocimetry (PIV). Exp. Fluids 42, 575–587. doi:10.1007/s00348-007-0266-6.

Honkanen, M., Nobach, H., 2005. Background extraction from double-frame PIV images. Exp. Fluids 38, 348–362. doi:10.1007/s00348-004-0916-x.

Hugo A. Jakobsen, *, Håvard Lindborg, and, Dorao, C.A., 2005. Modeling of Bubble Column Reactors: Progress and Limitations. doi:10.1021/IE049447X

Hyndman, C.L., Larachi, F., Guy, C., 1997. Understanding gas-phase hydrodynamics in bubble columns: A convective model based on kinetic theory. Chem. Eng. Sci. 52, 63–77. doi:10.1016/S0009-2509(96)00387-9

Kähler, C.J., Kompenhans, J., 2000. Fundamentals of multiple plane stereo particle image velocimetry. Exp. Fluids 29, S070–S077. doi:10.1007/s003480070009

Kantarci, N., Borak, F., Ulgen, K.O., 2005. Bubble column reactors. Process Biochem. doi:10.1016/j.procbio.2004.10.004

Kaštánek, F., Sharp, D.H. (David H.., Kratochvíl, J., Cermák, J., 1993. Chemical reactors for gas-liquid systems. Academia Praha.

Keane, R.D., Adrian, R.J., 1990. Optimization of Particle Image Velocimeters. Part I: double pulsed systems. Meas. Sci. Technol. Vol. 2pp, 1202–1215. doi:http://dx.doi.org/10.1088/0957-0233/1/11/013

Keane, R.D., Adrian, R.J., 1991. Optimization of particle image velocimeters. II. Multiple pulsed systems. Meas. Sci. Technol. 2, 963–974. doi:10.1088/0957-0233/2/10/013

Keane, R.D., Adrian, R.J., 1992. Theory of cross-correlation analysis of PIV images. Appl. Sci. Res. 49, 191–215. doi:10.1007/BF00384623

Krishna, R., Urseanu, M.I., van Baten, J.M., Ellenberger, J., 1999. Influence of scale on the hydrodynamics of bubble columns operating in the churn-turbulent regime: experiments vs. Eulerian simulations. Chem. Eng. Sci. 54, 4903–4911. doi:10.1016/S0009-2509(99)00211-0

Lance, M., Bataille, J., 1991. Turbulence in the liquid phase of a uniform bubbly air–water flow. J. Fluid Mech. 222, 95--118. doi:10.1017/S0022112091001015

Lawson, N.J., Wu, J., 1997. Three-dimensional particle image velocimetry: experimental error analysis of a digital angular stereoscopic system. Meas. Sci. Technol. 8, 1455–1464. doi:10.1088/0957-0233/8/12/009

Levich, V., 1962. Physicochemical hydrodynamics. Prentice-Hall, Englewood Cliffs N.J.

Lin, T.-J., Reese, J., Hong, T., Fan, L.-S., 1996. Quantitative analysis and computation of two-dimensional bubble columns. AIChE J. 42, 301–318. doi:10.1002/aic.690420202

Lindken, R., Merzkirch, W., 2000. Velocity measurements of liquid and gaseous phase for a system of bubbles rising in water. Exp. Fluids 29, S194–S201. doi:10.1007/s003480070021

Lindken, R., Merzkirch, W., 2002. A novel PIV technique for measurements in multiphase flows and its application to two-phase bubbly flows. Exp. Fluids 33, 814–825. doi:10.1007/s00348-002-0500-1

Liu, Z., Zheng, Y., Jia, L., Zhang, Q., 2005. Study of bubble induced flow structure using PIV. Chem. Eng. Sci. 60, 3537–3552. doi:10.1016/j.ces.2004.03.049

Masullo, A., Theunissen, R., 2016. Adaptive vector validation in image velocimetry to minimise the influence of outlier clusters. Exp. Fluids 57, 1–21. doi:10.1007/s00348-015-2110-8

Meinhart, C.D., Wereley, S.T., Santiago, J.G., 2000. A PIV Algorithm for Estimating Time-Averaged Velocity Fields. J. Fluids Eng. 122, 285. doi:10.1115/1.483256

Melling, A., 1997. Tracer particles and seeding for particle image velocimetry. Meas. Sci. Technol. 8, 1406–1416. doi:10.1088/0957-0233/8/12/005

Mersmann, A., 1978. Design and scale-up of bubble and spray columns. Ger. Chem. Eng. 1, 1–11.

Mudde, R.F., 2005. Gravity-driven bubbly flows. Annu. Rev. Fluid Mech. 37, 393–423. doi:10.1146/annurev.fluid.37.061903.175803

Mudde, R.F., Groen, J.S., Van Den Akker, H.E.A., 1997. Liquid velocity field in a bubble column: LDA experiments. Chem. Eng. Sci. 52, 4217–4224. doi:10.1016/S0009-2509(97)88935-X

Nobach, H., Bodenschatz, E., 2009. Limitations of accuracy in PIV due to individual variations of particle image intensities. Exp. Fluids 47, 27–38. doi:10.1007/s00348-009-0627-4

Northrup, M. a, Kulp, T.J., Angel, S.M., 1991. Fluorescent particle image velocimetry: application to flow measurement in refractive index-matched porous media. Appl. Opt. 30, 3034–3040. doi:10.1364/AO.30.003034

Oberkampf, W.L., Roy, C.J., 2010. Verification and Validation in Scientific Computing. Cambridge University Press, Cambridge. doi:10.1017/CBO9780511760396

Olsen, M.G., Adrian, R.J., 2001. Measurement volume defined by peak-finding algorithms in cross-correlation particle image velocimetry. Meas. Sci. Technol. 12, N14–N16. doi:10.1088/0957-0233/12/2/402

Pedocchi, F., Martin, J.E., García, M.H., 2008. Inexpensive fluorescent particles for large-scale experiments using particle image velocimetry. Exp. Fluids 45, 183–186. doi:10.1007/s00348-008-0516-2

Pereira, F., Ciarravano, A., Romano, G.P., Di Felice, F., 2004. Adaptive multi-frame PIV, in: 12th International Symposium on Applications of Laser Techniques to Fluid Mechanics. Portugal.

Persoons, T., Donovan, T.S.O., Murray, D.B., 2008. Improving the measurement accuracy of PIV in a synthetic jet flow 7–10.

Persoons, T., O'Donovan, T.S., 2011. High dynamic velocity range particle image velocimetry using multiple pulse separation imaging. Sensors 11, 1–18. doi:10.3390/s110100001

Prasad, A. K., Jensen, K., 1995. Scheimpflug stereocamera for particle image velocimetry in liquid flows. Appl. Opt. 34, 7092–7099. doi:10.1364/AO.34.007092

Prasad, A.K., 2000. Particle Image Velocimetry. Curr. Sci. 79, 51–60. doi:10.1007/978-3-540-72308-0

Raffel, M., Willert, C.E., Wereley, S.T., Kompenhans, J., 2007. Introduction, in: Particle Image Velocimetry. Springer Berlin Heidelberg, Berlin, Heidelberg, pp. 1–13. doi:10.1007/978-3-540-72308-0_1

Ruzicka, M.C., Drahoš, J., Fialová, M., Thomas, N.H., 2001. Effect of bubble column dimensions on flow regime transition. Chem. Eng. Sci. 56, 6117–6124. doi:10.1016/S0009-2509(01)00215-9

Samimy, M., Lele, S.K., 1991. Motion of particles with inertia in a compressible free shear layer. Phys. Fluids A Fluid Dyn. 3, 1915. doi:10.1063/1.857921

Scarano, F., 2002. Iterative image deformation methods in PIV. Meas. Sci. Technol. 13, R1–R19. doi:10.1088/0957-0233/13/1/201

Scarano, F., Riethmuller, M.L., 2000. Advances in iterative multigrid PIV image processing. Exp. Fluids 29, S051–S060. doi:10.1007/s003480070007

Sciacchitano, A., 2014. Uncertainty quantification in particle image velocimetry and advances in time-resolved image and data analysis. TU Delft. doi:10.4233/uuid:bfe57561-523f-4e7e-8e28-e804a6f1625e

Sciacchitano, A., Wieneke, B., Scarano, F., 2013. PIV uncertainty quantification by image matching. Meas. Sci. Technol. 24, 45302. doi:10.1088/0957-0233/24/4/045302

Seol, D.G., Socolofsky, S.A., 2008. Vector post-processing algorithm for phase discrimination of two-phase PIV. Exp. Fluids 45, 223–239. doi:10.1007/s00348-008-0473-9

Shah, Y.T., Kelkar, B.G., Godbole, S.P., Deckwer, W.-D., 1982. Design parameters estimations for bubble column reactors. AIChE J. 28, 353–379. doi:10.1002/aic.690280302

Shavit, U., Lowe, R.J., Steinbuck, J. V., 2007. Intensity Capping: a simple method to improve cross-correlation PIV results. Exp. Fluids 42, 225–240. doi:10.1007/s00348-006-0233-7.

Silva, M.K., 2011. Estudo Numérico e Experimental de Colunas de Bolhas Operando em Regime Heterogêneo. Biblioteca Digital da Unicamp.

Sokolichin, A., Eigenberger, G., 1994. Gas—liquid flow in bubble columns and loop reactors: Part I. Detailed modelling and numerical simulation. Chem. Eng. Sci. 49, 5735–5746. doi:10.1016/0009-2509(94)00289-4

Soloff, S.M., Adrian, R.J., Liu, Z.-C., 1997. Distortion compensation for generalized stereoscopic particle image velocimetry. Meas. Sci. Technol. 8, 1441–1454. doi:10.1088/0957-0233/8/12/008

Sommerfeld, M., Bröder, D., 2009. Analysis of hydrodynamics and microstructure in a bubble column by planar shadow image velocimetry. Ind. Eng. Chem. Res. 48, 330–340. doi:10.1021/ie800838u

Theunissen, R., Scarano, F., Riethmuller, M.L., 2008. On improvement of PIV image interrogation near stationary interfaces. Exp. Fluids 45, 557–572. doi:10.1007/s00348-008-0481-9

Timmins, B.H., Wilson, B.W., Smith, B.L., Vlachos, P.P., 2012. A method for automatic estimation of instantaneous local uncertainty in particle image velocimetry measurements. Exp. Fluids 53, 1133–1147. doi:10.1007/s00348-012-1341-1

Tinge, J.T., Drinkenburg, A.A.H., 1986. The influence of slight departures from vertical alignment on liquid dispersion and gas hold-up in a bubble column. Chem. Eng. Sci. 41, 165–169. doi:10.1016/0009-2509(86)85210-1

van Baten, J.M., Krishna, R., 2001. Eulerian simulations for determination of the axial dispersion of liquid and gas phases in bubble columns operating in the churn-turbulent regime. Chem. Eng. Sci. 56, 503–512. doi:10.1016/S0009-2509(00)00254-2

Westerweel, J., 1993. Digital particle image velocimetry: theory and application.

Westerweel, J., 1997. Fundamentals of digital particle image velocimetry. Meas. Sci. Technol. 8, 1379–1392. doi:10.1088/0957-0233/8/12/002

Westerweel, J., 2000. Theoretical analysis of the measurement precision in particle image velocimetry. Exp. Fluids 29, S003--S012. doi:10.1007/s003480070002

Westerweel, J., 2008. On velocity gradients in PIV interrogation. Exp. Fluids 44, 831–842. doi:10.1007/s00348-007-0439-3

Westerweel, J., Scarano, F., 2005. Universal outlier detection for PIV data. Exp. Fluids 39, 1096–1100. doi:10.1007/s00348-005-0016-6

Wieneke, B., 2005. Stereo-PIV using self-calibration on particle images, in: Experiments in Fluids. pp. 267–280. doi:10.1007/s00348-005-0962-z

Wieneke, B., 2014. Generic a-posteriori uncertainty quantification for PIV vector fields by correlation statistics, in: 17th International Symposium on Applications of Laster Techniques to Fluid Mechanics. pp. 1–9. doi:10.1088/0957-0233/26/7/074002

Wieneke, B., 2015. PIV uncertainty quantification from correlation statistics. Meas. Sci. Technol. 26, 74002. doi:10.1088/0957-0233/26/7/074002

Wieneke, B., Pfeiffer, K., 2010. Adaptive PIV with variable interrogation window size and shape, in: 5th Int Symp on Applications of Laser Techniques to Fluid Mechanics. Portugal

Wilson, J.F., Cobb, E.D., Kilpatrick, F.A., 1986. Fluorometric procedures for dye tracing. Tech. Water-Resources Investig.

Zahradník, J., Fialová, M., Ruˇžička, M., Drahosˇ, J., Kasˇtánek, F., Thomas, N.H., 1997. Duality of the gas-liquid flow regimes in bubble column reactors. Chem. Eng. Sci. 52, 3811–3826. doi:10.1016/S0009-2509(97)00226-1

APPENDIX

A. EVALUATION OF THE CAMERA SETUP FOR THE 2D-2C F-PIV SYSTEM

Figures A1-A2 present the distribution of time-averaged intensity of the frames 0 and 1 (F0 and F1) for the two camera setup presented in Figure 4.5 and U_G = 0.528 and 1.053 cm/s.

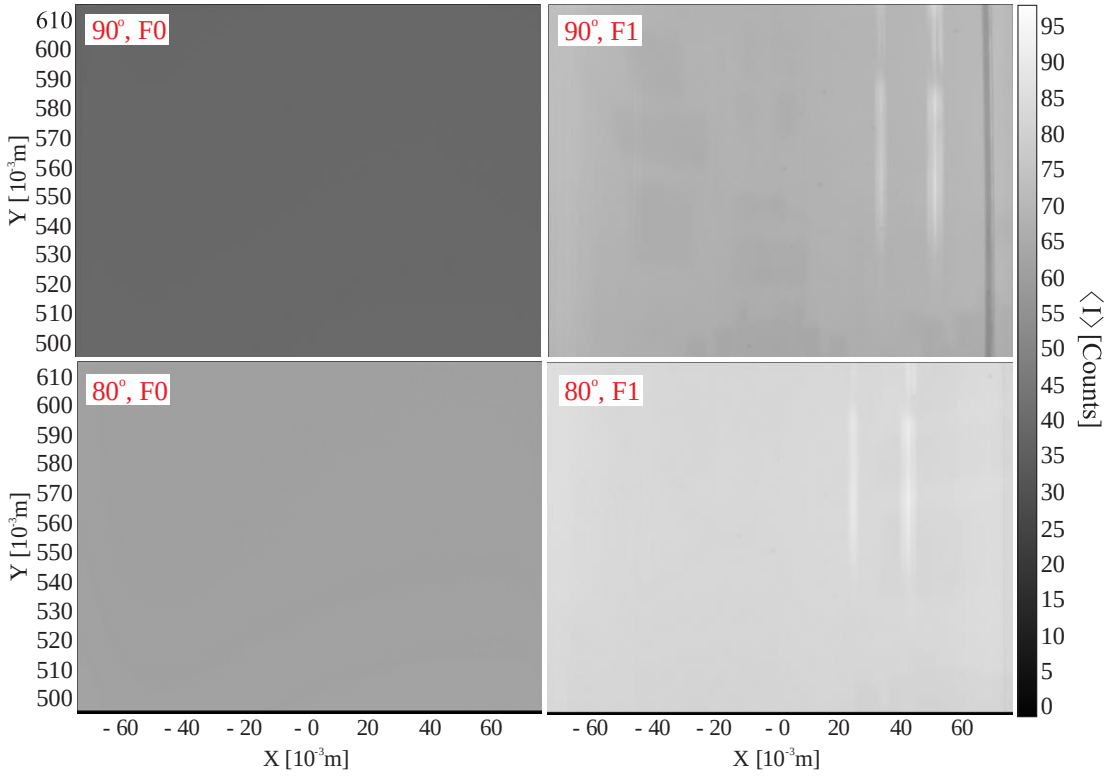

Figure A1 - Distribution of the time-averaged intensity of the frames 0 and 1 (F0 and F1) for the two camera arrangement presented in Figure 4.5 - U_G = 0.528 cm/s.

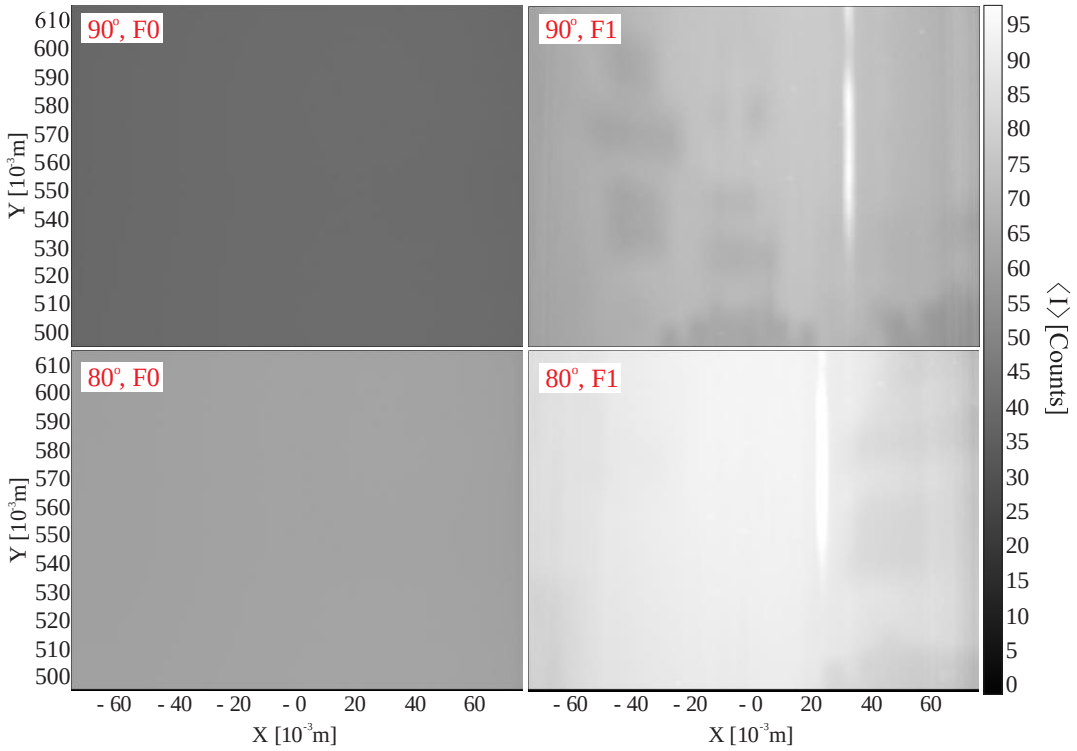

Figure A2 - Distribution of the time-averaged intensity of the frames 0 and 1 (F0 and F1) for the two camera arrangement presented in Figure 4.5 - U_G = 1.053 cm/s.

B. CALIBRATION PROCEDURE

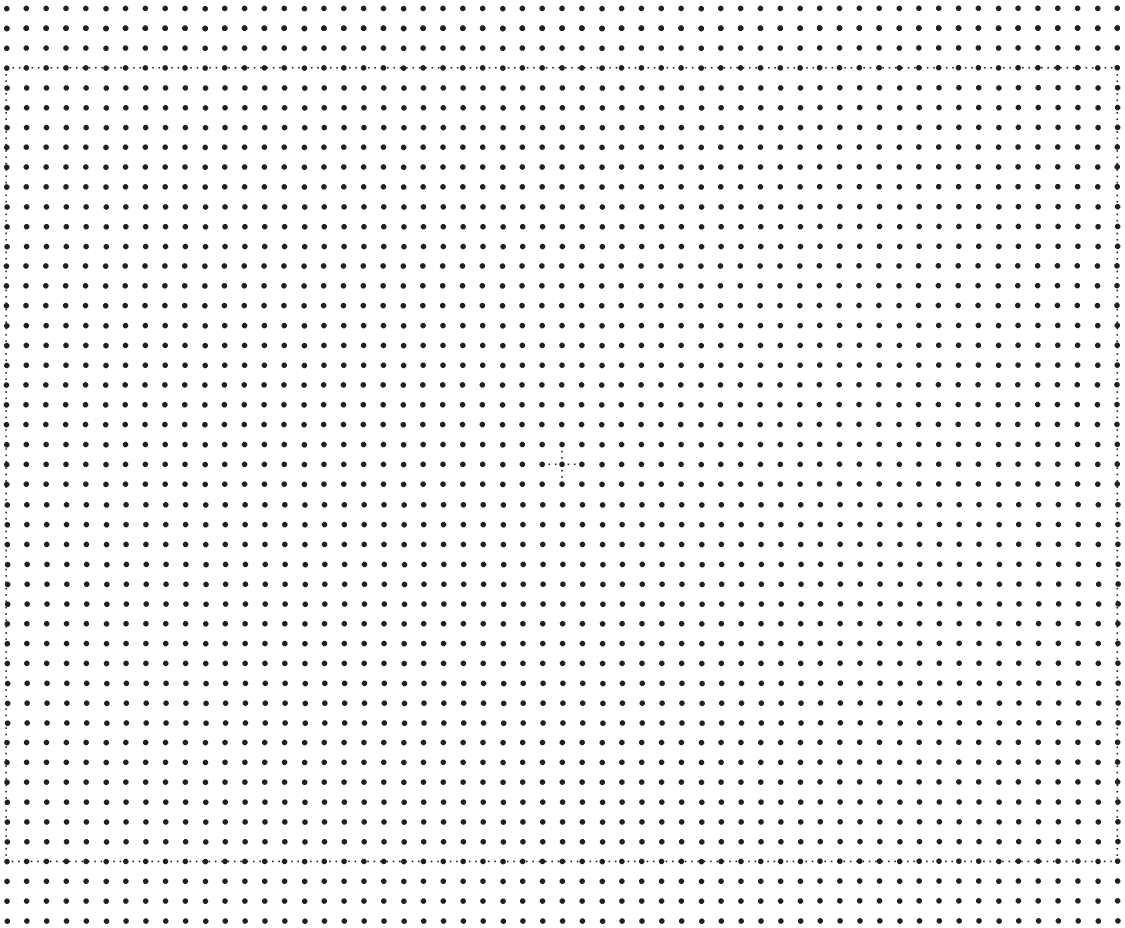

Figure B1 - Real-size calibration plate created in Inkscape.

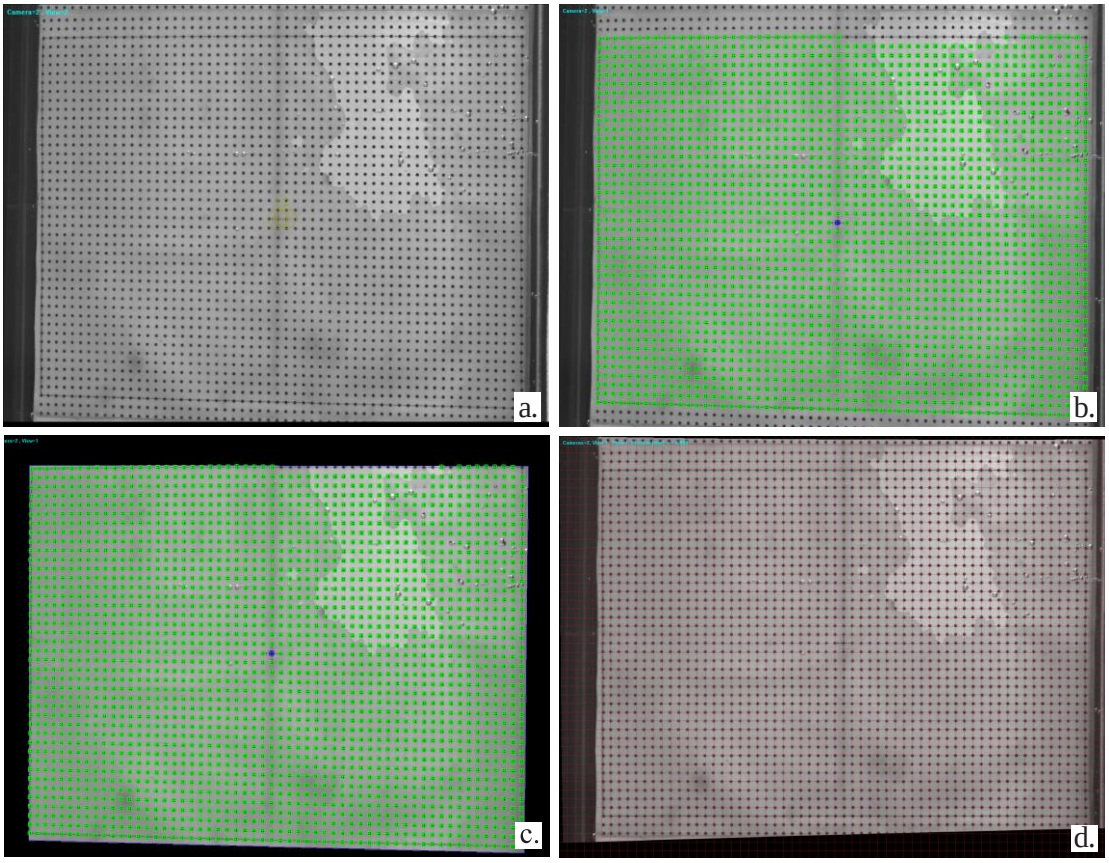

Figure B2 – Calibration procedure for the 2D-2C PIV system: (a) Recorded image of the calibration plate. Identification of the calibration plate marks by Davis software (b) without and (c) with a mask to isolate the investigated region. (d) Corrected image.

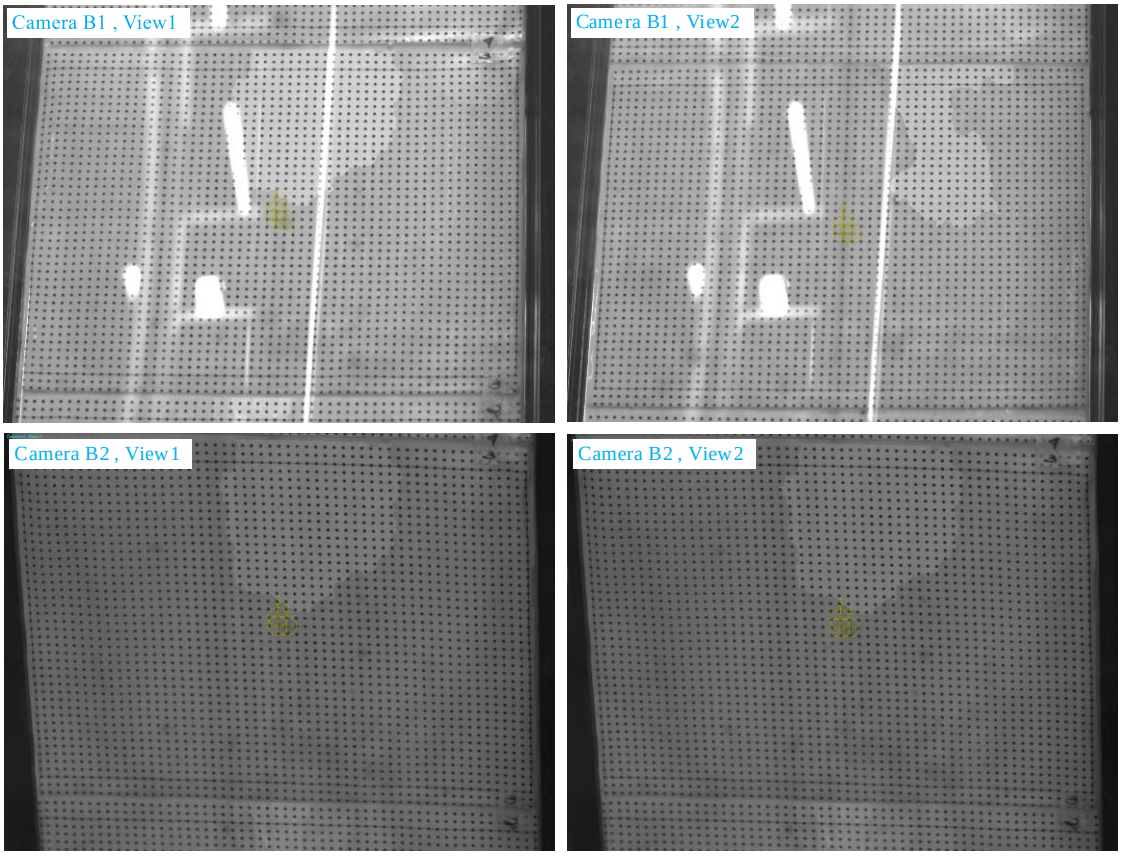

Figure B3 - Recorded image of the calibration plate for the 2D-3C PIV system.

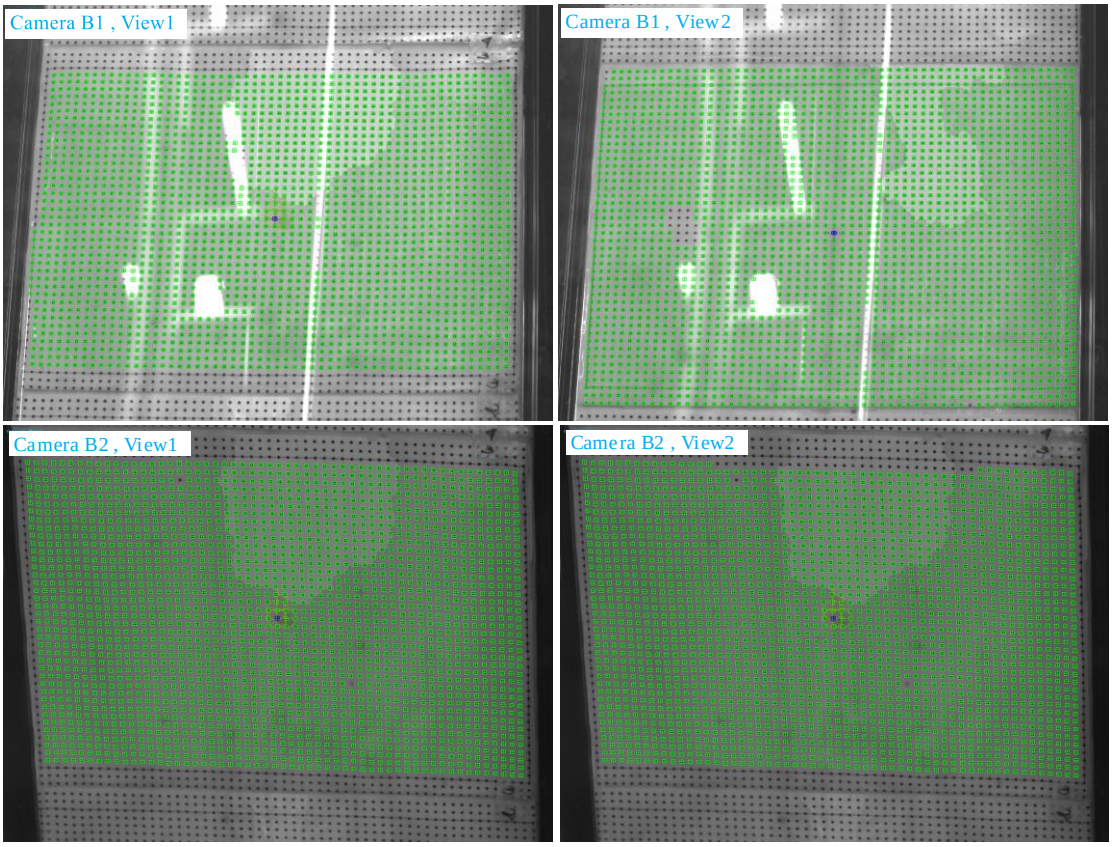

Figure B4 - Identification of the calibration plate marks by Davis software for the 2D-3C PIV system.

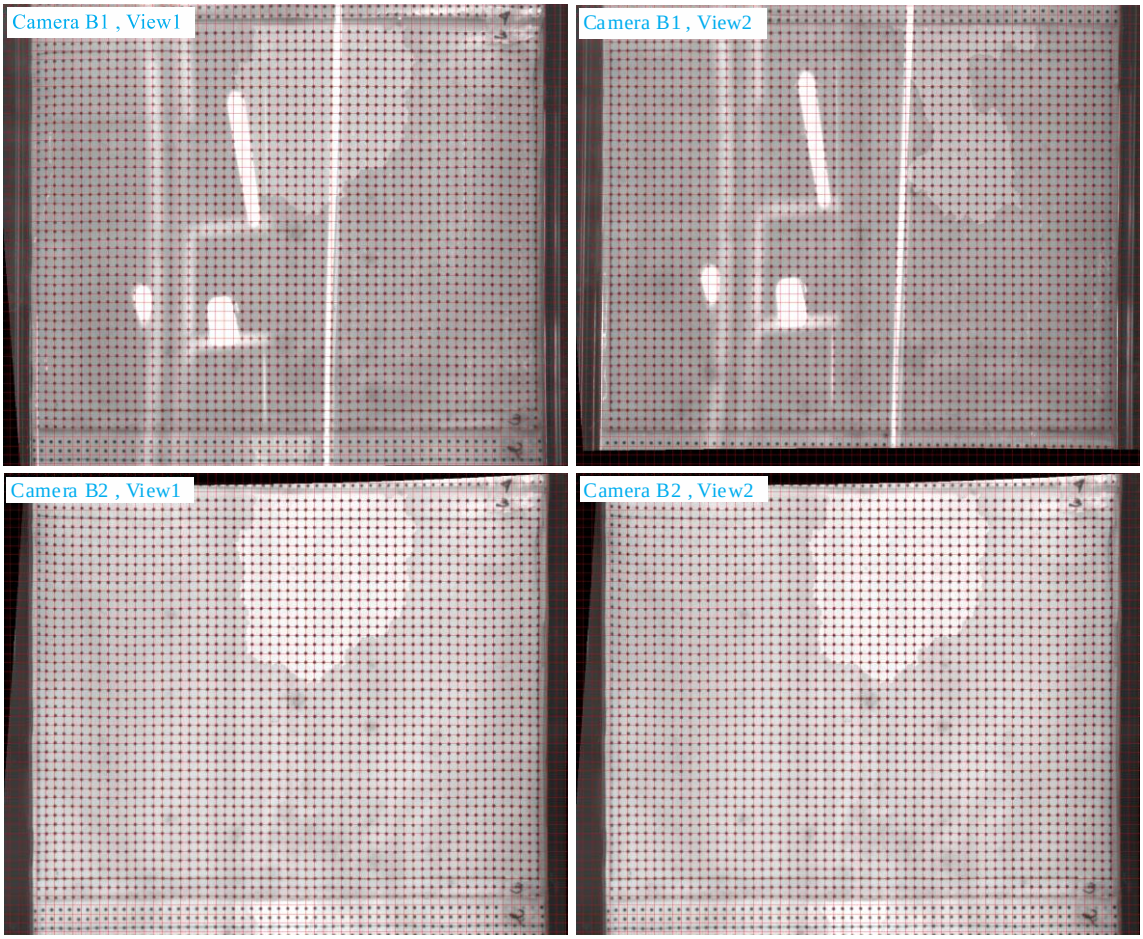

Figure B5 - Corrected image of the calibration plate for the 2D-3C PIV system

C. VORTICITY

From standard cross-correlation (SCC)

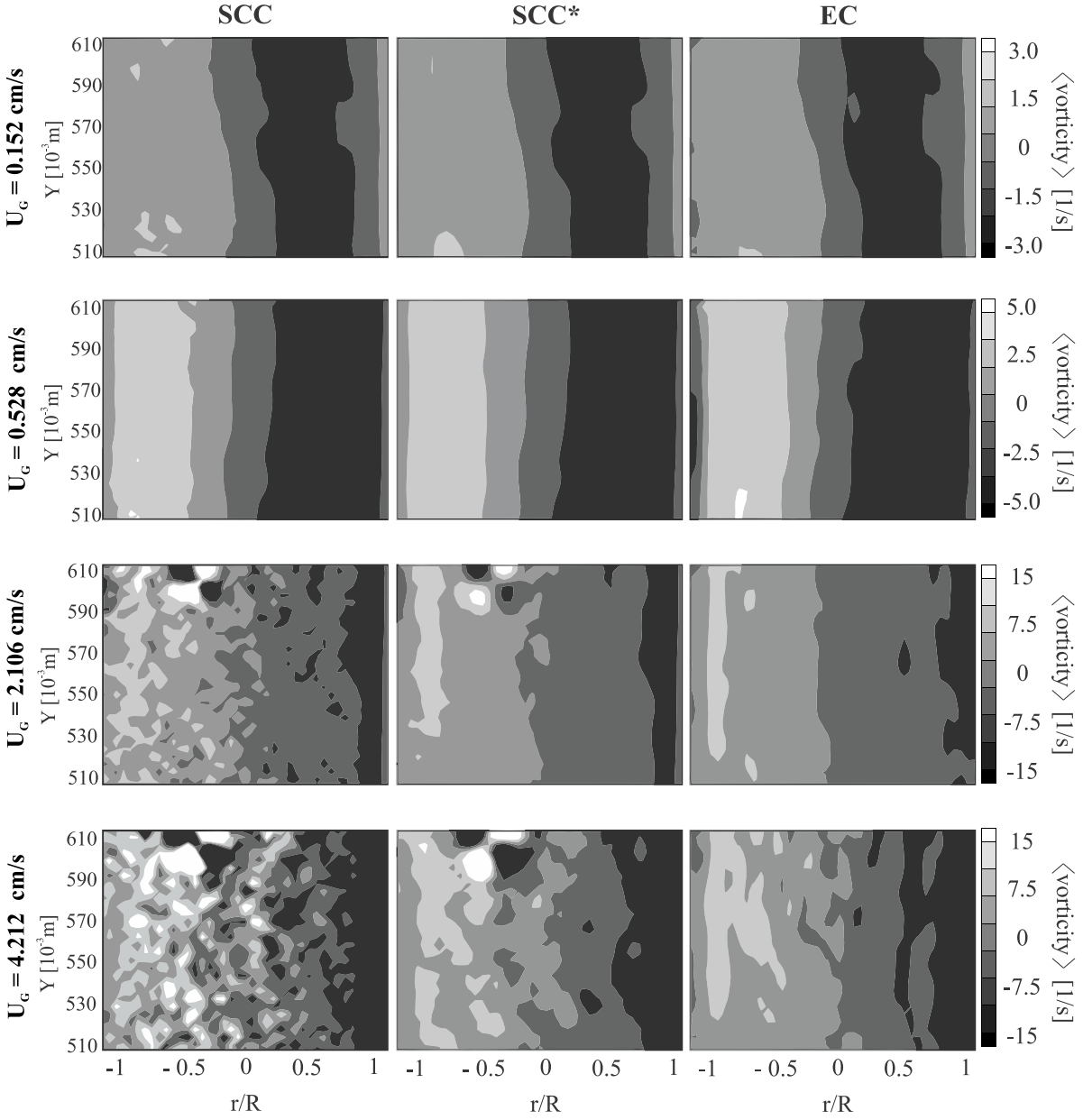

Figure C1 - Time-averaged vorticity field determined by the standard cross-correlation (SCC), SCC with post-processing (SCC*) and ensemble correlation (EC) from the 2D-3C F-PIV measurements.

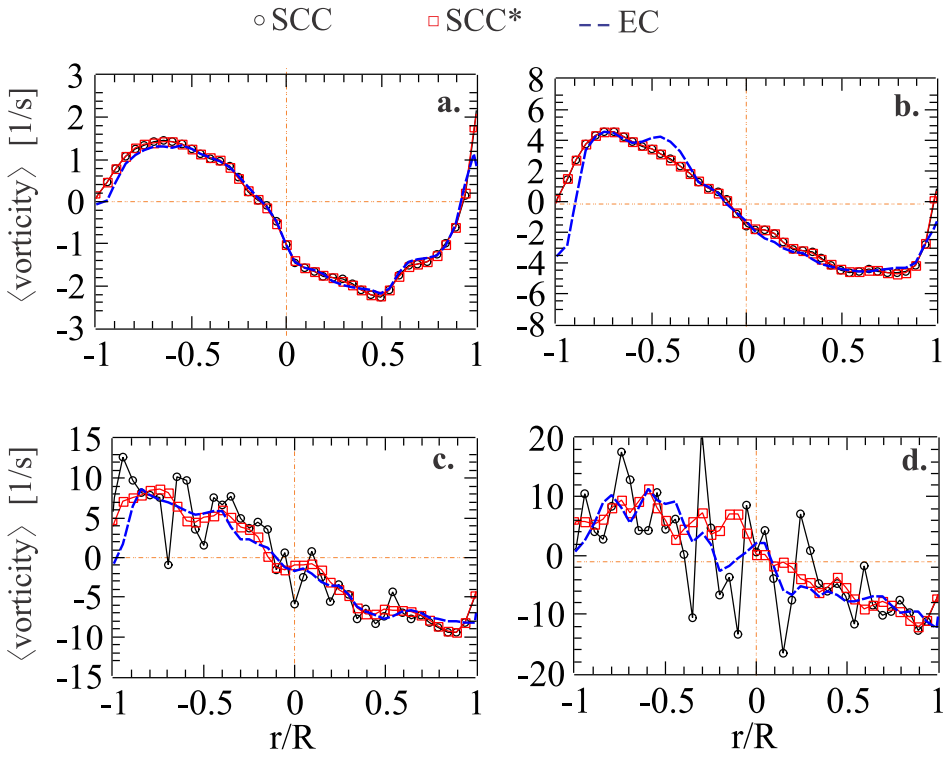

Figure C2 - Time-averaged vorticity profile (Y = 0.552 m) determined by the standard cross-correlation (SCC), SCC with post-processing (SCC*) and ensemble correlation (EC) from 2D-3C F-PIV measurements for U_G = (a) 0.152, (b) 0.528, (c) 2.106, and (c) 4.212 cm/s.

From sliding-average correlation (SAC)

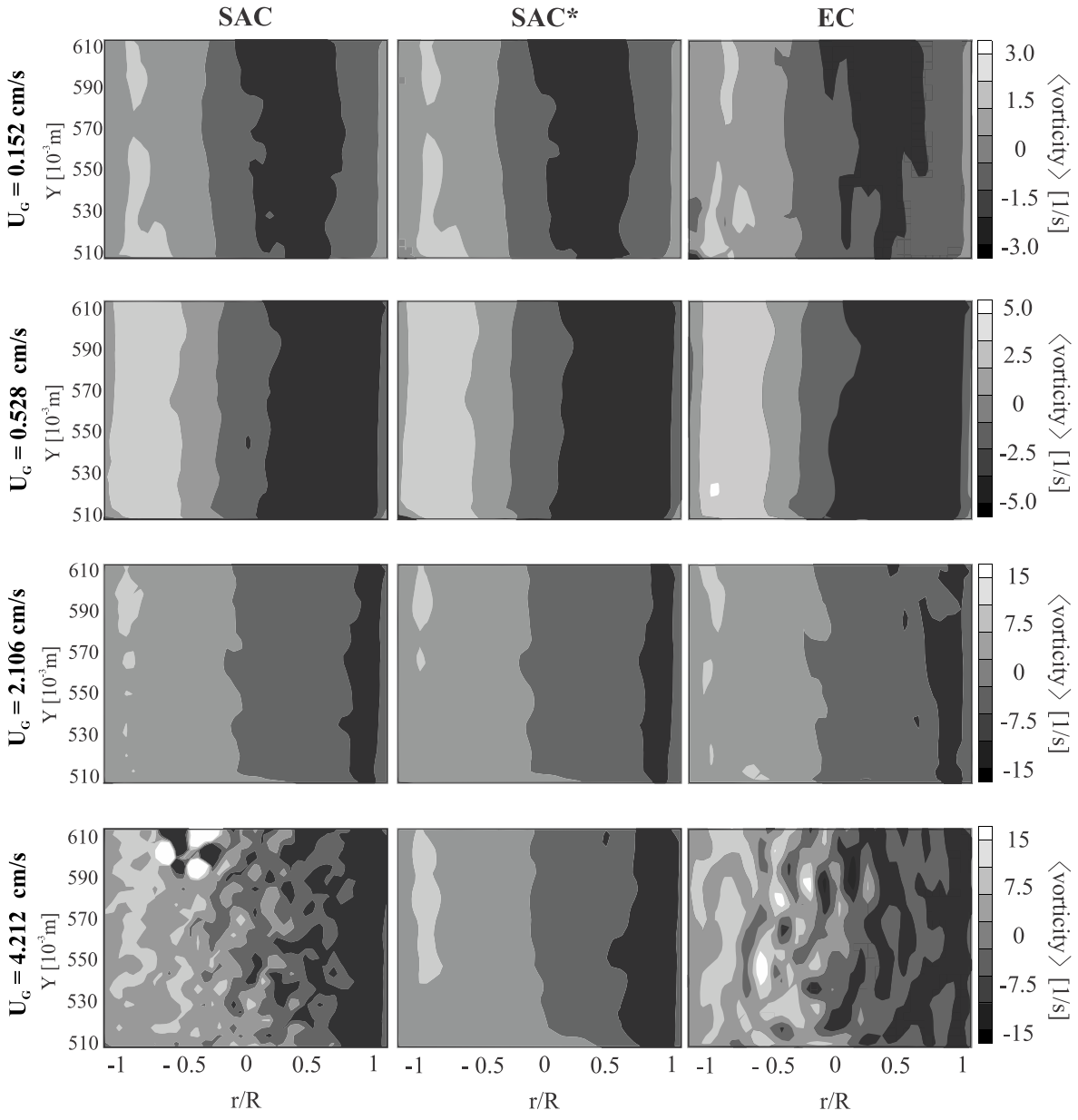

Figure C3 - Time-averaged vorticity field determined by the sliding-average correlation (SAC), SAC with post-processing (SAC*) and ensemble correlation (EC) from the 2D-2C F-PIV measurements.

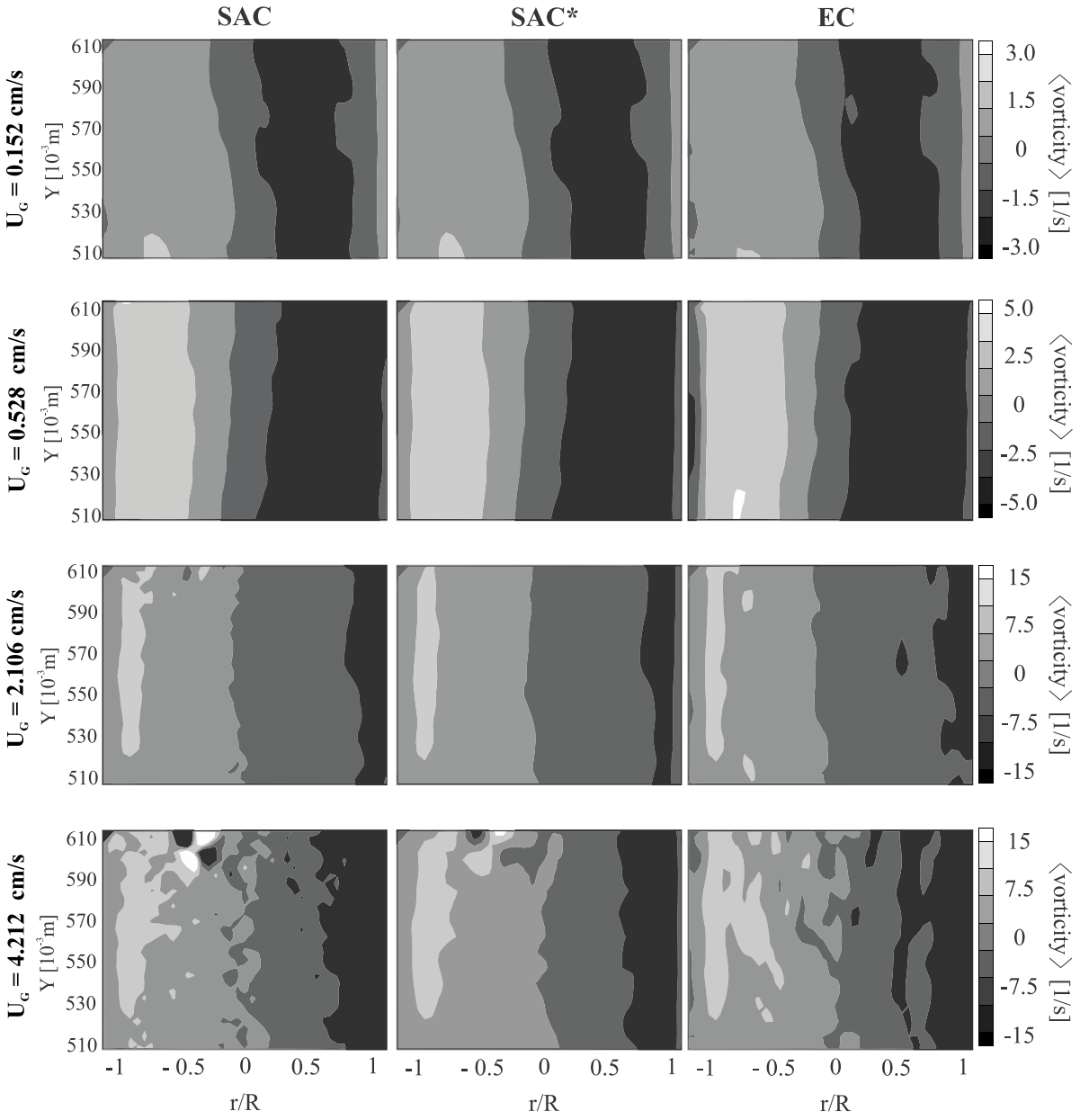

Figure C4 - Time-averaged vorticity field determined by the sliding-average correlation (SAC), SAC with post-processing (SAC*) and ensemble correlation (EC) from the 2D-3C F-PIV measurements.

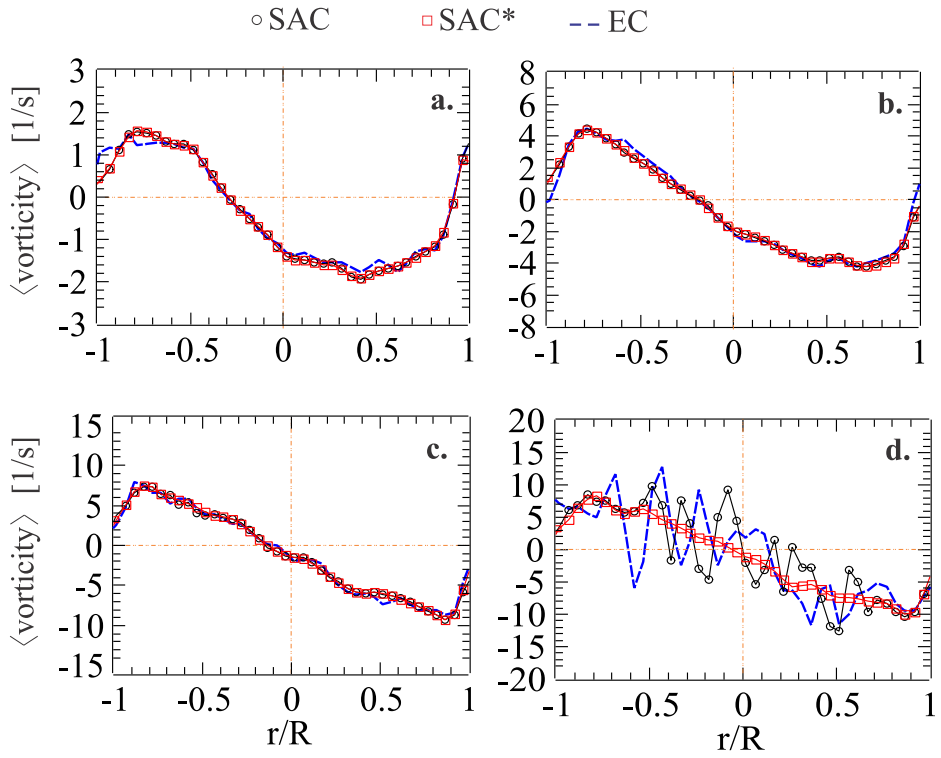

Figure C5 - Time-averaged vorticity profile (Y = 0.552 m) determined by the sliding-average correlation (SAC), SAC with post-processing (SAC*) and ensemble correlation (EC) from 2D-2C F-PIV measurements for U_G = (a) 0.152, (b) 0.528, (c) 2.106, and (c) 4.212 cm/s.

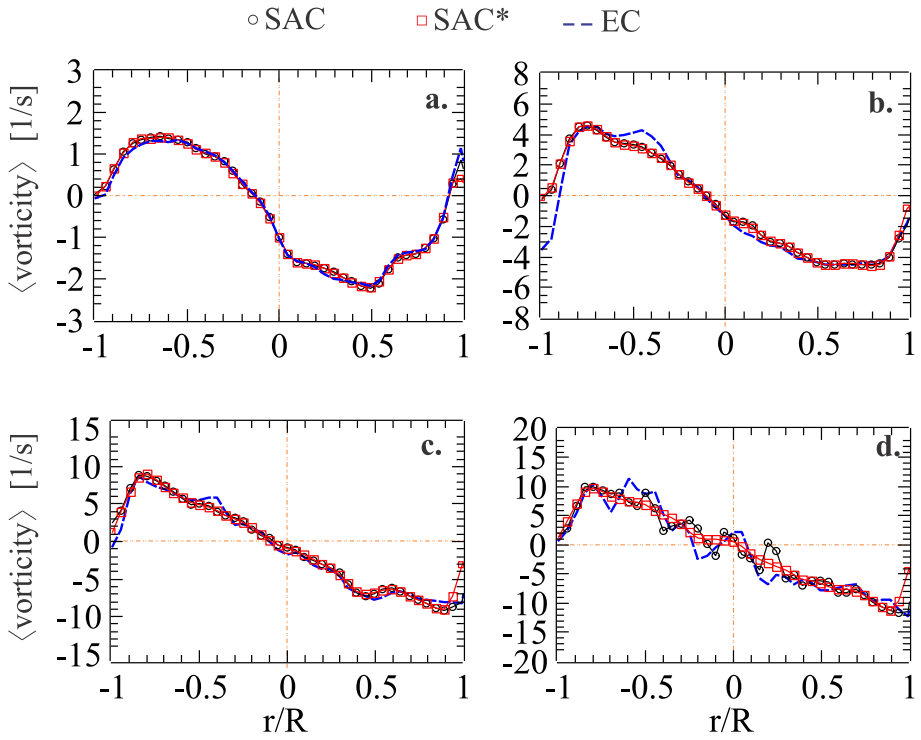

Figure C6 - Time-averaged vorticity profile (Y = 0.552 m) determined by the sliding-average correlation (SAC), SAC with post-processing (SAC*) and ensemble correlation (EC) from 2D-3C F-PIV measurements for U_G = (a) 0.152, (b) 0.528, (c) 2.106, and (c) 4.212 cm/s.

D. QUALITY INDICATORS

Particle image diameter for SCC approach

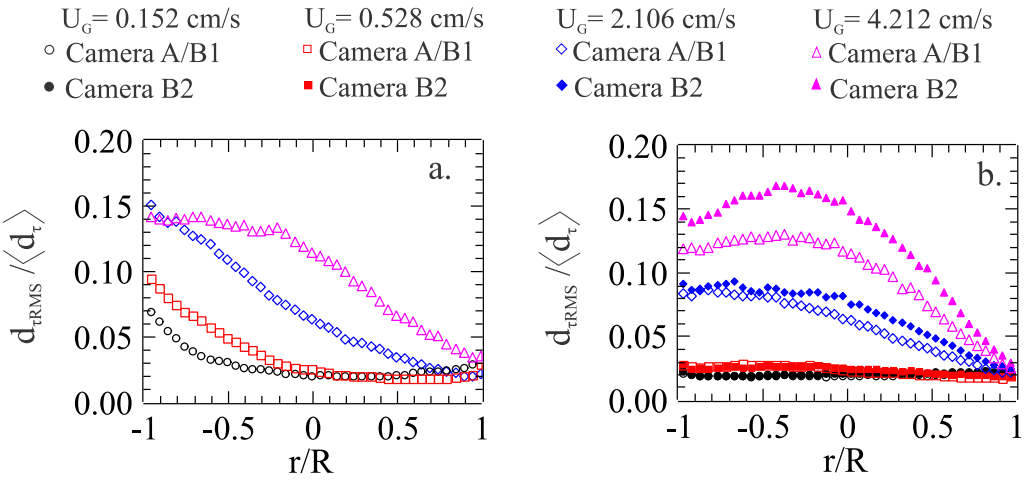

Figure D1 - $d_{\tau RMS}$ normalized by time-averaged of the particle image diameter, $d_{\tau RMS}/\langle d_\tau \rangle$, using SCC approach. (a) Camera A and (b) Camera B1 and B2.

Diff_4 and 3C reconstruction error for SAC approach

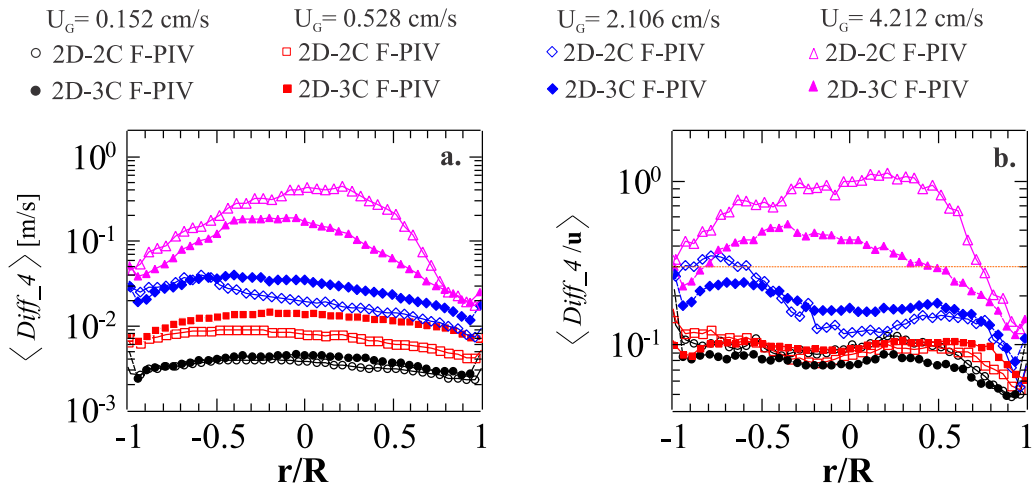

Figure D2 - Profile of (a) the time-averaged of *Diff_4*, $\langle Diff\_4 \rangle$, and (b) *Diff_4* normalized by velocity modulus, $\langle Diff\_4/\mathbf{u} \rangle$, for sliding-average correlation (SAC).

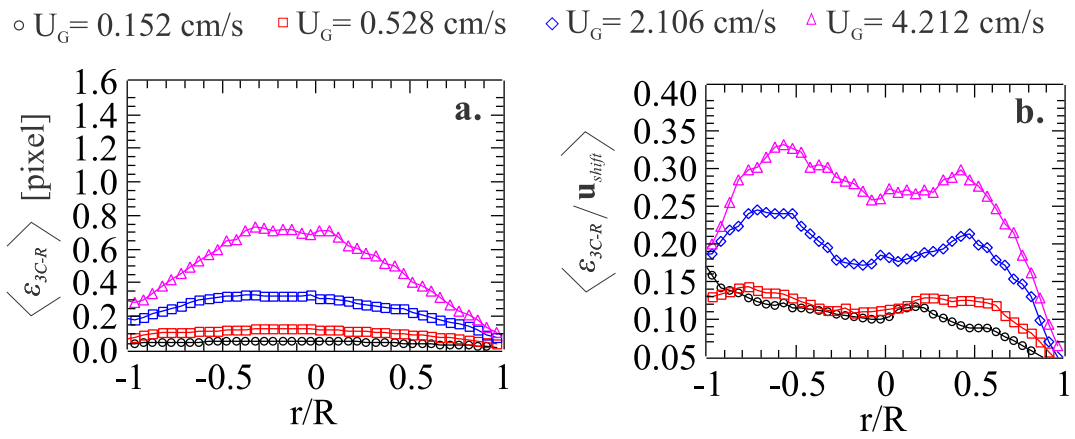

Figure D3 - Profile of (a) the time-averaged of the 3C reconstruction error, $\langle \varepsilon_{3C-R} \rangle$ and (b) ε_{3C-R} normalized by velocity modulus in pixel ($\mathbf{u}_{shif}$), $\langle \varepsilon_{3C-R} / \mathbf{u}_{shif} \rangle$ for sliding-average correlation (SAC) and Y = 0.552 m.

E. STATISTICS OF THE AVERAGE FIELD

Table E1 - Spatial average of u^*, v^*, and w^* for N_R = 3750 and SCC, SAC, and EC approaches.

U_G [cm/s]			0.152	0.528	2.106	4.212
$\overline{u^*}$	SCC	2D-2C	0.192	0.158	0.250	0.235
		2D-3C	0.672	0.090	0.423	0.304
	SAC	2D-2C	0.188	0.129	0.145	0.226
		2D-3C	0.650	0.103	0.236	0.271
	EC	2D-2C	0.197	0.140	0.173	0.880
		2D-3C	0.690	0.114	0.117	0.157
$\overline{v^*}$	SCC	2D-2C	0.065	0.051	0.060	0.085
		2D-3C	0.031	0.048	0.055	0.077
	SAC	2D-2C	0.080	0.023	0.021	0.029
		2D-3C	0.027	0.035	0.049	0.031
	EC	2D-2C	0.071	0.025	0.023	0.195
		2D-3C	0.031	0.048	0.052	0.066
$\overline{w^*}$	SCC	2D-3C	0.191	0.191	0.253	0.362
	SAC	2D-3C	0.205	0.200	0.153	0.153
	EC	2D-3C	0.182	0.338	0.217	0.241

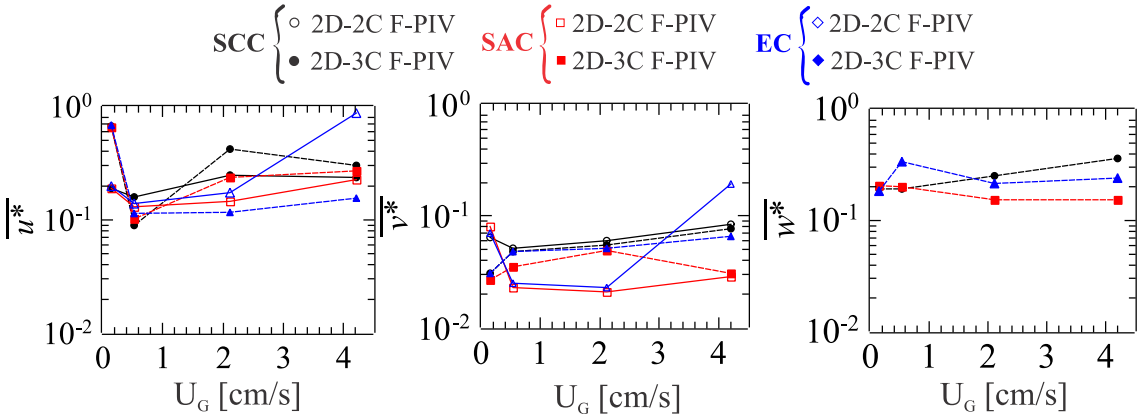

Figure E1 - Spatial average of u^*, v^*, and w^* in function of U_G for N_R = 3750 and SCC, SAC, and EC approaches.

Table E2 - Spatial average of $Diff\_4$ for the time-averaged field, $Diff\_4_{taf}$, normalized by the time-averaged **u**, $\overline{Diff\_4_{taf} / \langle \mathbf{u} \rangle}$.

U_G	N_R [10^3]	SCC		SAC		EC	
		2D-2C	2D-3C	2D-2C	2D-3C	2D-2C	2D-3C
0.152 cm/s	0.50	0.034	0.043	0.023	0.019	0.049	0.024
	1.00	0.029	0.044	0.022	0.017	0.043	0.020
	2.00	0.021	0.056	0.020	0.014	0.041	0.016
	3.00	0.025	0.066	0.022	0.018	0.049	0.020
	3.25	0.025	0.071	0.025	0.017	0.048	0.019
	3.50	0.026	0.073	0.024	0.019	0.047	0.020
	3.75	0.027	0.082	0.028	0.020	0.045	0.020
	4.00	0.027	0.080	0.025	0.020	0.044	0.020
0.528 cm/s	0.50	0.183	0.029	0.030	0.022	0.031	0.033
	1.00	0.151	0.023	0.029	0.017	0.022	0.022
	2.00	0.136	0.019	0.032	0.015	0.022	0.018
	3.00	0.131	0.017	0.017	0.013	0.017	0.016
	3.25	0.136	0.016	0.016	0.013	0.016	0.016
	3.50	0.129	0.016	0.016	0.013	0.015	0.015
	3.75	0.127	0.015	0.017	0.013	0.016	0.016
	4.00	0.119	0.015	0.017	0.013	0.016	0.015
2.106 cm/s	0.50	0.351	0.422	0.058	0.060	0.042	0.058
	1.00	0.266	0.368	0.046	0.052	0.038	0.045
	2.00	0.207	0.284	0.039	0.038	0.026	0.036
	3.00	0.216	0.244	0.030	0.034	0.022	0.031
	3.25	0.343	0.228	0.029	0.033	0.020	0.029
	3.50	0.165	0.228	0.028	0.032	0.019	0.030
	3.75	0.160	0.216	0.027	0.031	0.019	0.029
	4.00	0.164	0.228	0.027	0.030	0.020	0.027
4.212 cm/s	0.50	0.678	0.620	0.383	0.167	0.169	0.109
	1.00	0.591	0.591	0.285	0.125	0.136	0.088
	2.00	0.442	0.442	0.240	0.104	0.102	0.071
	3.00	0.433	0.433	0.190	0.092	0.089	0.062
	3.25	0.396	0.396	0.181	0.090	0.037	0.061
	3.50	0.524	0.524	0.179	0.087	0.084	0.058
	3.75	0.365	0.365	0.174	0.087	0.035	0.057
	4.00	0.359	0.359	0.168	0.085	0.078	0.055

Table E3 - Effect of N_R on the spatial average of $\langle SNR \rangle$ for SCC and SAC approaches.

-	N_R [10^3]	U_G = 0.152 cm/s		U_G = 0.528 cm/s		U_G = 2.106·cm/s		U_G = 4.212 cm/s	
		2D-2C	2D-3C	2D-2C	2D-3C	2D-2C	2D-3C	2D-2C	2D-3C
SCC	0.50	6.054	5.631	4.737	4.337	2.966	2.776	2.251	2.316
	1.00	6.073	5.627	4.727	4.343	2.972	2.784	2.237	2.316
	2.00	6.075	5.622	4.714	4.359	2.981	2.792	2.234	2.315
	3.00	6.076	5.635	4.714	4.359	2.984	2.790	2.256	2.321
	3.25	6.074	5.385	4.714	4.359	2.988	2.792	2.223	2.321
	3.50	6.075	5.635	4.718	4.362	2.988	2.795	2.223	2.322
	3.75	6.073	5.632	4.716	4.360	2.699	2.799	2.229	2.324
	4.00	6.225	5.633	4.717	4.358	2.986	2.798	2.223	2.324
SAC	0.50	15.521	14.513	8.684	9.489	4.987	5.022	3.911	3.849
	1.00	15.563	14.478	8.711	9.554	4.982	5.033	3.882	3.891
	2.00	15.557	14.431	8.677	9.620	5.007	5.071	3.884	3.904
	3.00	15.544	14.471	8.643	9.626	5.009	5.076	3.871	3.925
	3.25	15.536	14.463	8.641	9.625	5.018	5.083	3.868	3.927
	3.50	15.538	14.458	8.648	9.639	5.018	5.091	3.871	3.930
	3.75	15.523	14.444	8.645	9.628	5.013	5.102	3.870	3.941
	4.00	15.517	14.441	8.644	9.613	5.013	5.103	3.873	3.941

Table E4 - Effect of N_R on the spatial average of $\langle SNR \rangle$ for EC approach.

N_R [10^3]	U_G = 0.152 cm/s		U_G = 0.528 cm/s		U_G = 2.106·cm/s		U_G = 4.212 cm/s	
	2D-2C	2D-3C	2D-2C	2D-3C	2D-2C	2D-3C	2D-2C	2D-3C
0.50	90.156	95.941	18.824	17.153	16.384	14.480	15.255	17.302
1.00	110.261	111.657	20.537	18.138	23.131	18.650	18.403	23.450
2.00	131.033	125.942	21.300	19.132	36.155	29.585	24.751	33.952
3.00	144.788	140.089	21.303	19.197	48.770	40.825	29.555	43.073
3.25	148.121	141.488	20.613	19.677	54.093	49.089	38.762	44.698
3.50	151.010	141.831	21.395	19.176	59.700	45.303	32.199	46.477
3.75	154.642	142.959	21.436	19.761	60.361	45.596	41.492	48.618
4.00	155.754	145.386	21.386	19.960	67.928	51.956	34.824	50.532

Table E5 – Spatial average of the uncertainty quantification of $\langle \mathbf{u} \rangle$, $\langle u \rangle$, $\langle v \rangle$, and $\langle w \rangle$ obtained by the SCC approach ($\overline{UQ_{\langle i\_SCC \rangle}}\Big|_{i=\mathbf{u},u,v,w}$).

UQ	N_R [10^3]	U_G = 0.152 cm/s		U_G = 0.528 cm/s		U_G = 2.106·cm/s		U_G = 4.212 cm/s	
		2D-2C	2D-3C	2D-2C	2D-3C	2D-2C	2D-3C	2D-2C	2D-3C
$\langle \mathbf{u} \rangle$	0.50	0.009	0.022	0.021	0.032	0.046	0.190	0.184	0.364
	1.00	0.007	0.016	0.015	0.024	0.033	0.139	0.132	0.259
	2.00	0.005	0.012	0.011	0.016	0.024	0.100	0.094	0.192
	3.00	0.004	0.010	0.009	0.013	0.019	0.083	0.077	0.161
	3.25	0.004	0.010	0.009	0.013	0.018	0.080	0.074	0.155
	3.50	0.004	0.010	0.009	0.012	0.017	0.077	0.071	0.150
	3.75	0.004	0.010	0.008	0.012	0.017	0.075	0.069	0.146
	4.00	0.004	0.009	0.008	0.011	0.016	0.072	0.067	0.142
$\langle u \rangle$	0.50	0.003	0.008	0.011	0.012	0.029	0.071	0.131	0.135
	1.00	0.002	0.006	0.008	0.009	0.021	0.052	0.094	0.097
	2.00	0.002	0.005	0.006	0.006	0.015	0.038	0.066	0.073
	3.00	0.001	0.004	0.005	0.005	0.012	0.031	0.055	0.061
	3.25	0.001	0.004	0.005	0.005	0.011	0.030	0.053	0.059
	3.50	0.001	0.004	0.004	0.005	0.011	0.029	0.051	0.057
	3.75	0.001	0.003	0.004	0.005	0.011	0.028	0.049	0.056
	4.00	0.001	0.003	0.004	0.005	0.010	0.027	0.047	0.054
$\langle v \rangle$	0.50	0.009	0.017	0.017	0.027	0.033	0.124	0.134	0.231
	1.00	0.007	0.013	0.012	0.020	0.024	0.091	0.096	0.164
	2.00	0.005	0.010	0.009	0.013	0.017	0.065	0.067	0.122
	3.00	0.004	0.009	0.007	0.011	0.014	0.054	0.055	0.102
	3.25	0.004	0.008	0.007	0.011	0.013	0.052	0.053	0.098
	3.50	0.004	0.008	0.007	0.010	0.013	0.050	0.051	0.095
	3.75	0.004	0.008	0.007	0.010	0.012	0.049	0.050	0.092
	4.00	0.004	0.008	0.006	0.010	0.012	0.047	0.048	0.090
$\langle w \rangle$	0.50	-	0.008	-	0.011	-	0.123	-	0.243
	1.00	-	0.006	-	0.009	-	0.090	-	0.173
	2.00	-	0.004	-	0.006	-	0.065	-	0.128
	3.00	-	0.004	-	0.005	-	0.054	-	0.107
	3.25	-	0.004	-	0.005	-	0.052	-	0.095
	3.50	-	0.003	-	0.005	-	0.050	-	0.100
	3.75	-	0.003	-	0.004	-	0.049	-	0.097
	4.00	-	0.003	-	0.004	-	0.047	-	0.095

Table E6 – Spatial average of the uncertainty quantification of $\langle \mathbf{u} \rangle$, $\langle u \rangle$, $\langle v \rangle$, and $\langle w \rangle$ obtained by the SAC approach ($\overline{UQ_{\langle i\_SAC \rangle}}\Big|_{i=\mathbf{u},u,v,w}$).

UQ	N_R [10^3]	U_G = 0.152 cm/s		U_G = 0.528 cm/s		U_G = 2.106·cm/s		U_G = 4.212 cm/s	
		2D-2C	2D-3C	2D-2C	2D-3C	2D-2C	2D-3C	2D-2C	2D-3C
$\langle \mathbf{u} \rangle$	0.50	0.008	0.021	0.012	0.031	0.012	0.043	0.045	0.078
	1.00	0.006	0.016	0.008	0.023	0.009	0.030	0.033	0.056
	2.00	0.004	0.011	0.006	0.015	0.006	0.021	0.023	0.041
	3.00	0.003	0.010	0.005	0.013	0.005	0.017	0.019	0.034
	3.25	0.003	0.010	0.005	0.012	0.005	0.017	0.019	0.033
	3.50	0.003	0.009	0.004	0.012	0.005	0.016	0.018	0.032
	3.75	0.003	0.009	0.004	0.011	0.005	0.015	0.017	0.031
	4.00	0.003	0.009	0.004	0.011	0.004	0.015	0.017	0.030
$\langle u \rangle$	0.50	0.002	0.008	0.005	0.011	0.006	0.014	0.033	0.027
	1.00	0.002	0.006	0.003	0.008	0.004	0.010	0.024	0.019
	2.00	0.001	0.004	0.002	0.006	0.003	0.007	0.017	0.014
	3.00	0.001	0.004	0.002	0.005	0.002	0.006	0.014	0.012
	3.25	0.001	0.003	0.002	0.004	0.002	0.006	0.014	0.012
	3.50	0.001	0.003	0.002	0.004	0.002	0.006	0.013	0.011
	3.75	0.001	0.003	0.002	0.004	0.002	0.005	0.013	0.011
	4.00	0.001	0.003	0.002	0.004	0.002	0.005	0.012	0.011
$\langle v \rangle$	0.50	0.009	0.018	0.012	0.027	0.011	0.034	0.036	0.053
	1.00	0.006	0.013	0.008	0.020	0.009	0.023	0.026	0.038
	2.00	0.004	0.010	0.006	0.013	0.006	0.016	0.018	0.028
	3.00	0.004	0.009	0.005	0.011	0.005	0.013	0.015	0.023
	3.25	0.003	0.008	0.005	0.011	0.005	0.013	0.015	0.022
	3.50	0.003	0.008	0.004	0.010	0.005	0.012	0.014	0.022
	3.75	0.003	0.008	0.004	0.010	0.004	0.012	0.014	0.021
	4.00	0.003	0.008	0.004	0.009	0.004	0.011	0.013	0.021
$\langle w \rangle$	0.50	-	0.006	-	0.010	-	0.021	-	0.049
	1.00	-	0.005	-	0.007	-	0.015	-	0.035
	2.00	-	0.003	-	0.005	-	0.011	-	0.028
	3.00	-	0.003	-	0.004	-	0.009	-	0.022
	3.25	-	0.003	-	0.004	-	0.008	-	0.021
	3.50	-	0.003	-	0.004	-	0.008	-	0.020
	3.75	-	0.003	-	0.004	-	0.008	-	0.020
	4.00	-	0.003	-	0.003	-	0.008	-	0.019

LIST OF PUBLICATIONS

Journal articles

DE MOURA, HELDER LIMA; **LIMA AMARAL, RODRIGO DE** ; SÁNCHEZ FORERO, DIANA ISABEL ; DE CASTILHO, GUILHERME JOSÉ ; VENÂNCIO VIANNA, SÁVIO SOUZA ; MORI, MILTON . Using chaos analysis for evaluating the quality of F-PIV measurements in a bubble column. Chemical Engineering Science, v. 160, p. 54-71, 2016.

SANTANA, H. S.; **AMARAL, R. de L.;** TARANTO, O. P. Numerical Study of Mixing and Reaction for Biodiesel Production in Spiral Microchannel. Chemical Engineering Transactions, v. 43, p. 1663-1668, 2015.

Diana I. Sanchez-Forero ; COSTA, K. K. ; **AMARAL, R. L**. ; Taranto, Osvaldir P. ; MORI, M. . Influence of Liquid Viscosity and Solid Load in a Three-Phase Bubble Column using Stereoscopic Particle Image Velocimetry (Stereo-PIV). Chemical Engineering Transactions, v. 43, p. 1579-1584, 2015.

COSTA, K. K. ; Diana I. Sanchez-Forero ; **AMARAL, R. L.** ; Taranto, Osvaldir P. ; MORI, M. . Effect of Solid Phase and Geometry on Liquid Velocity of Three-Phase Bubble Columns. Chemical Engineering Transactions, v. 43, p. 1651-1656, 2015.

Conference proceedings

MOURA, H. L., **AMARAL, R. L.,** FORERO, D. I. S., CASTILHO, G. J., VIANNA, S.S.V., MORI, M. Influência da terceira componente de velocidade na qualidade de medidas F-PIV com base na análise da dimensão de correlação. In: XVI Congresso Brasileiro de Engenharia Química, 2016, Fortaleza-CE. Congresso Brasileiro de Engenharia Química (COBEQ), 2016.

AMARAL, R. L., MOURA, H. L., EMÍDIO, D., FIGUEIRAS, M., CASTILHO, G. J., MORI, M. Utilização do Youtube como ferramenta complementar na pesquisa e ensino da engenharia química: estudo de caso do canal RaTech. In: XVI Encontro Brasileiro sobre o Ensino em Engenharia Química, 2016, Fortaleza-CE. Encontro Brasileiro sobre o Ensino em Engenharia Química (ENBEQ), 2016.

AMARAL, R. L., MOURA, H. L., FORERO, D. I. S., CASTILHO, G. J., VIANNA, S.S.V., MORI, M. Ensemble correlation em medidas F-PIV 2C-2D e 3C-2D de uma coluna de bolhas: efeito do número de pares de frames. In: XVI Congresso Brasileiro de Engenharia Química, 2016, Fortaleza-CE. Congresso Brasileiro de Engenharia Química (COBEQ), 2016.

FORERO, D. I. S., **AMARAL, R. L**., MOURA, H. L., CASTILHO, G. J., VIANNA, S.S.V., MORI, M. Efeito da presença de particulados na qualidade das medidas F-PIV 3C-2D de um fluido não-newtoniano em uma coluna de bolhas. In: XVI Congresso Brasileiro de Engenharia Química, 2016, Fortaleza-CE. Congresso Brasileiro de Engenharia Química (COBEQ), 2016.

R. L. AMARAL, D. I. S. FORERO, G. J. CASTILHO, S.S.V. VIANNA e M MORI. Evaluation of PIV interrogation strategy in the investigation of the liquid phase velocity in a

bubble column section. Congresso Brasileiro de Engenharia Mecânica (COBEM 2015), Rio de Janeiro - RJ. 2015.

R. L. AMARAL, D. I. S. FORERO, G. J. CASTILHO, S.S.V. VIANNA e M MORI. Comparison between Fluorescent PIV and Stereo-PIV measurements of the liquid phase velocity in a bubble column. Congresso Brasileiro de Engenharia Mecânica (COBEM 2015), Rio de Janeiro - RJ. 2015.

H. L. MOURA, **R. L. AMARAL**, D. I. S. FORERO, G. J. CASTILHO, S.S.V. VIANNA, M. Chaos analysis of the PIV measurement quality on the liquid velocity fluctuation in a bubble column section. Congresso Brasileiro de Engenharia Mecânica (COBEM 2015), Rio de Janeiro - RJ. 2015.

R. L. AMARAL, H. L. MOURA, D. I. S. FORERO, G. J. CASTILHO, S.S.V. VIANNA e M. MORI. Incerteza de medidas PIV 2D-2C e 2D-3C: Análise do cenário atual e estudo de caso em uma coluna de bolhas. Congresso Brasileiro de Sistemas Particulados (ENEMP 2015), São Carlos - SP. 2015.

R. L. AMARAL, G. J. CASTILHO, S.S.V. VIANNA e M. MORI. Tomographic Particle Image Velocimetry (Tomographic-PIV): É possível medir concentração de partículas? Congresso Brasileiro de Sistemas Particulados (ENEMP 2015), São Carlos - SP. 2015.

H. L. MOURA, **R. L. AMARAL,** D. I. S. FORERO, G. J. CASTILHO, S.S.V. VIANNA, M. MORI. Análise da entropia de Kolmogorov a partir de medições PIV no escoamento da fase líquida de uma coluna de bolhas. Congresso Brasileiro de Sistemas Particulados (ENEMP 2015), São Carlos - SP. 2015.

BARBUTTI, A. D.; **AMARAL, R. L.;** CASTILHO, G. J.; MORI, M. Efeito do distribuidor de gás de uma coluna de bolhas na velocidade 2D da fase líquida por Fluorescent PIV. In: XX Congresso Brasileiro de Engenharia Química, 2014, Florianópolis. Anais do XX Congresso Brasileiro de Engenharia Química. São Paulo: Editora Edgard Blücher, 2014. p. 5395.

SANCHEZ-FORERO, D. I.; COSTA, K. K. DA ; **AMARAL, R. L.** ; TARANTO, O. P. ; VIANNA, S. S. V. ; MORI, M. . Efeito da vazão de gás na qualidade da medida da velocidade do líquido em uma seção de uma coluna de bolhas com expansão de diâmetro por PIV. In: XX Congresso Brasileiro de Engenharia Química, 2014, Florianópolis. Anais do XX Congresso Brasileiro de Engenharia Química, 2014.

AMARAL, R. L.; FORERO, D. I. S. ; COSTA, K. K. DA ; TARANTO, O. P. ; VIANNA, S. S. V. ; MORI, M. . Efeito da função de mapeamento na distribuição da velocidade da fase líquida na seção de uma coluna de bolhas por PIV. In: XX Congresso Brasileiro de Engenharia Química, 2014, Florianópolis. Anais do XX Congresso Brasileiro de Engenharia Química. p. 5436.

COSTA, K. K. Da; FORERO, D. I. S. ; **AMARAL, R. L**. ; TARANTO, O. P. ; VIANNA, S. S. V. ; MORI, M. . Efeito da autocalibração para Stereo-PIV na distribuição da velocidade 2D3C da fase líquida em uma seção de uma coluna de bolhas. In: XX Congresso Brasileiro de Engenharia Química, 2014, Florianópolis. Anais do XX Congresso Brasileiro de Engenharia Química 2014.

AMARAL, R. L., COSTA, K. K., FORERO, D. I. S., VIANNA, S. S. V., TARANTO, O. P., MORI, M. Efeito do pré-processamento de imagem PIV na velocidade do líquido em uma coluna de bolhas com expansão de diâmetro In: Congresso Brasileiro de Engenharia Mecânica

(CONEM 2014), 2014, Uberlândia. Congresso Brasileiro de Engenharia Mecânica (CONEM 2014). 2014.